

**Electrical and Optical Characterization of Intrinsic and Ion-  
Implantation Induced Defects in 6H- and 4H-SiC**

**Dissertation**

**Michael B. Scott, Major, USAF**

**AFIT/DS/ENP/97-09**

Approved for public release; distribution unlimited

1999 1206 074

DTIC QUALITY INSPECTED 4

ELECTRICAL AND OPTICAL CHARACTERIZATION OF INTRINSIC AND ION-IMPLANTATION  
INDUCED DEFECTS IN 6H- AND 4H-SiC

Michael B. Scott, B.S., M.S.  
Major, USAF

Approved:



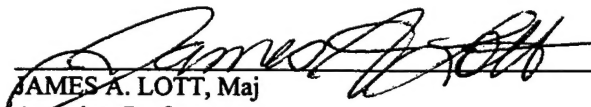
YUNG KEE YEO  
Professor of Physics  
Chairman, Advisory Committee

8 Nov. '99



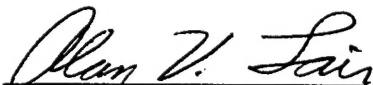
ROBERT L. HENGEGHOLD  
Professor of Physics and Head  
Department of Engineering Physics  
Member, Advisory Committee

8 Nov '99



JAMES A. LOTT, Maj  
Associate Professor  
Department of Electrical Engineering  
Member, Advisory Committee

08 NOV 99



ALAN V. LAIR  
Professor and Head  
Department of Mathematics and Statistics  
Dean's Representative

8 Nov 99

Accepted:



ROBERT A. CALICO, Jr.  
Dean, Graduate School of Engineering and Management

12 Nov '99

**“The views expressed in this dissertation are those of the author and do not reflect the official policy or position of the Department of Defense or the U.S. Government.”**

**ELECTRICAL AND OPTICAL CHARACTERIZATION OF  
INTRINSIC AND ION-IMPLANTATION INDUCED  
DEFECTS IN 6H- AND 4H-SiC**

**DISSERTATION**

**Presented to  
the Faculty of the Graduate School of Engineering  
and Management of the Air Force Institute of Technology  
Air University in Partial Fulfillment of the Requirements for  
the Degree of Doctor of Philosophy**

**Michael B. Scott, B.S., M.S.**

**Major, USAF**

**November 1999**

**Approved for public release; distribution unlimited**



## PREFACE

This research project continues the ongoing Air Force study on wide bandgap semiconductors for use in air and space systems where silicon (Si) and gallium arsenide (GaAs) based electronics cannot be used, due chiefly to their temperature and radiation level limitations.

Silicon carbide's (SiC) physical characteristics give it the potential for superior electronic performance in harsh environments. The SiC material used in this study was of the highest quality available, which unfortunately still possessed high concentrations of device degrading defects, both impurity related and intrinsic crystal defects. Variation in quality elevated the difficulty in characterization of defect centers and their response to ion implantation and subsequent annealing. Understanding the nature of these defects is paramount to improving the quality of this material to the required level mandated for high quality production SiC devices. Ion implantation has been a very successful method for creating such device features as buried channels and insulating layers in Si and GaAs. Before this method can be effectively used for SiC device production, ion implantation and annealing studies are required to gain a clearer understanding of how ion implantation and subsequent annealing of this semiconductor controls both the formation and evolution of various electrically active defect centers. In addition, contacts, surface oxide interfaces, and other issues must be studied and controlled before SiC based electronic devices approach their physical potential. Currently, SiC devices are only available commercially as blue LEDs and poor efficiency UV photodetectors. This limit in commercially available products can be traced back to the lack of fundamental knowledge required for repeatable production of low defect material and for device processing. Both silicon and gallium arsenide have passed through these same stages before arriving at their present level of quality. However, both these materials can be grown and processed at relatively low temperatures and are easily etched. Silicon carbide requires a 2500 °C growth temperature, 1800 °C or higher diffusion temperatures, and is chemically resistant to etching. In this research, I intended to deepen our limited understanding of deep level defects in SiC and assist those working at improving the quality of 6H- and 4H-SiC material.

I thank both the Air Force Research Laboratory and the Air Force Office of Scientific Research for providing the funding of this research. My sincere thanks go out to Dr. Yung Kee Yeo for again allowing me to work under his guidance. His insights into experimental methods and genuine concern for my progress kept me on the right track. I also thank Dr. Hengehold for giving me the chance to complete this doctoral program. I could not have completed this research without the additional assistance and insights of Dr. James D. Scofield. His frequent assistance and suggestions allowed me to make steady progress throughout the research phase. I tried to take full advantage of his thorough knowledge of deep level transient spectroscopic techniques during our numerous conversations. I extend my gratitude to Dr. Matthew and Mr. Greg Smith for his assistance in gathering a portion of the data after my departure. I am also very thankful for

the technical efforts of Belinda Johnson, Greg Smith and Bill Tropp that helped to keep the labs running and assisting in processing many of the test devices.

My deepest gratitude goes to my wife and daughter. This is the second time that Martha has picked up the extra tasks at home while supporting my graduate studies. Her understanding gave me the opportunity to focus on this work. Tina has been extremely understanding of my increased absence from home.

Michael B. Scott

## **TABLE of CONTENTS**

Preface .....	iv
List of Figures .....	ix
List of Tables .....	xvii
Abstract .....	xviii
I. INTRODUCTION .....	I-1
I-1 Goal Statement .....	I-1
I-2 Limits of Silicon .....	I-5
I-3 Characteristics of Wide Gap Semiconductors .....	I-6
I-4 Future Semiconductor Requirements .....	I-8
I-5 Problems with SiC .....	I-11
I-6 Current Status of SiC Material and Devices .....	I-14
II. BACKGROUND: SILICON CARBIDE .....	II-1
II-1 Crystal Structure .....	II-1
II-2 Optical and Electrical Properties .....	II-5
II-3 Defects .....	II-11
III. BACKGROUND: ION IMPLANTATION and ANNEALING .....	III-1
III-1 Introduction .....	III-1
III-2 Ion Implantation Theory .....	III-6
III-3 Defects .....	III-14

IV. CHARACTERIZATION TECHNIQUES .....	IV-1
IV-1 Introduction .....	IV-1
IV-2 Deep Level Transient Spectroscopy .....	IV-4
IV-3 I-V-T Measurements .....	IV-17
IV-4 Hall effect .....	IV-19
IV-5 C-V-T Measurements .....	IV-24
IV-6 Cathodoluminescence .....	IV-30
V. EXPERIMENTAL SETUP .....	V-1
V-1 Devices .....	V-1
V-1-A 6H-SiC Schottky Diodes .....	V-1
V-1-B 4H-SiC p-n Diodes .....	V-5
V-2 DLTS and C-V Setup .....	V-11
V-3 I-V-T Setup .....	V-14
V-4 Hall Effect Setup .....	V-15
V-5 Cathodoluminescence Setup .....	V-16
VI. EXPERIMENT AND RESULTS .....	VI-1
VI-1 Ar-, Cr-, and Mg-Implanted 6H-SiC .....	VI-1
VI-1-A Electrical Properties .....	VI-5
VI-1-B Deep Level Transient Spectroscopy .....	VI-12
VI-1-B-1 DLTS of 6H-SiC:Ar .....	VI-17
VI-1-B-2 DLTS of 6H-SiC:Cr .....	VI-34
VI-1-B-3 DLTS of 6H-SiC:Mg .....	VI-50

VI-1-C Summary .....	VI-69
VI-2 N- and P-Implanted n-type 4H-SiC .....	VI-74
VI-2-A Cathodoluminescence Measurements .....	VI-76
VI-2-A-1 CL Measurements of 4H-SiC:N .....	VI-86
VI-2-A-2 CL Measurements of 4H-SiC:P .....	VI-94
VI-2-B Hall Effect Measurements .....	VI-100
VI-2-B-1 Hall Effect Measurements of 4H-SiC:N .....	VI-101
VI-2-B-2 Hall Effect Measurements of 4H-SiC:P .....	VI-105
VI-2-B-3 Hall Effect Measurements Summary .....	VI-110
VI-2-C Summary .....	VI-112
VII. CONCLUSION AND RECOMMENDATIONS .....	VII-1
Appendix A: Publication Summary .....	A-1
Appendix B: Sample Processing Procedures .....	B-1
Appendix C: Modulating Function Error .....	C-1
Bibliography .....	a

## List of Figures

I-1. The Air Force conceptual view of a more electric aircraft showing the various subsystems being replaced with electrical subsystems including the conversion of hydraulic actuators to electrical actuators. ....	I-10
II-1. Bonding Planes in SiC. ....	II-1
II-2. The two possible stacking sequences for the basal planes of SiC molecules viewed along the c-axis. ....	II-3
II-3. Representation of the stacking sequence of 3C, 4H, 6H, and 15R-SiC using the Ramsdell zigzag notation. ....	II-14
III-1. Stopping power $S_e$ and $S_n$ as a function of ion energy (arbitrary scale). ....	III-8
III-2. Damage generation dependence on mass of implanted ion, (a) light ion and (b) heavy ion relative to semiconductor constituent atoms. ....	III-9
III-3. Order of formation and loss of defects in n-type silicon. ....	III-17
IV-1. DLTS sample configuration where the Schottky contacts were formed on 6H-SiC material and ohmic contacts used on 4H-SiC material ....	IV-7
IV-2. Sequence of a DLTS measurement. ....	IV-8
IV-3. Emission and capture processes in n-type material ....	IV-10
IV-4. Deep level transient spectroscopy laboratory setup. ....	IV-16
IV-5. Hall sample configuration for 4H-SiC:N and :P samples. ....	IV-20
IV-6. Shift in depletion width as a function of sample temperature. ....	IV-27
IV-7. The effect of partial ionization of donor atoms on capacitance as a function of temperature. ....	IV-27
IV-8. Schottky barrier energy band diagram (n-type) with a deep trap level. ....	IV-28
IV-9. Various Radiative Transitions. ....	IV-32

IV-10. Spectrometer/Detector Response Curve using a 1000 °C Blackbody Source.	IV-35
IV-11. Cathodoluminescence Setup.	IV-36
V-1. 6H-SiC diode design used for electrical measurements.	V-3
V-2. Profile of the 6H-SiC diode design used for electrical measurements.	V-3
V-3. Typical Implantation Concentration Profile for the 6H-SiC material used in this study.	V-4
V-4. 4H-SiC diode design used for electrical measurements.	V-7
V-5. Typical implanted ion concentration profile for the 4H-SiC material used in this research.	V-10
V-6. Sample mount used in cold head for DLTS, I-V-T, and C-V measurements.	V-11
V-7. Lab setup for DLTS and C-V measurements.	V-13
VI-1. Typical forward-bias I-V-T curves for ion implanted 6H-SiC diodes chosen for DLTS measurements. The voltage range shown is where tunneling effects dominate the current. Most of the diodes used in this study had this "leaky" tunneling current. Above this voltage range, diffusion and recombination currents became the dominant current components. The theoretical tunneling current is plotted for reference.	VI-6
VI-2. Typical reverse-bias I-V-T curves for ion implanted 6H-SiC diodes chosen for DLTS measurements. The 6H-SiC Schottky diodes showed this consistent performance over the temperature range of 150 to 700 K. The theoretical $V^{1/2}$ reverse-current dependency is shown for comparison.	VI-7
VI-3. Typical C-V curve for the diodes used in this study (plotted $1/C^2$ vs $V_{REV}$ ). A changing slope indicates a changing net doping concentration. The reduced slope near $V = -3$ volts indicates an significant increase in the net doping concentration at the peak ion implantation depth (2500 Angstroms).	VI-8
VI-4. Arrhenius plot of Cr implanted 6H-SiC Schottky diode showing three generation centers dominating the reverse current ( $V_{REV} = -1.5V$ ). The deepest level is at the midgap, the shallowest near 20 meV, and the middle value at 250 meV.	VI-11

VI-5. Principles of Deep Level Transient Spectroscopy - 1) Collapse and re-establishment of depletion region using alternating filling and reverse biases 2) Corresponding transient capacitance due to trapping and detrapping. ....	VI-14
VI-6. Principles of Deep Level Transient Spectroscopy - 3) Arrhenius plot showing "trap signature" of two deep level and 4) Rate window plot showing trap peaks. ....	VI-15
VI-7. Rate window (CV-DLTS) plot of two 6H-SiC:Ar diodes annealed at 1200 and 1400 °C. Also shown is the CV-DLTS response of the unimplanted-unannealed 6H-SiC diode. The peaks labeled E1 and E2 correspond to traps similarly identified by Pensl. (Pensl and Choyke, 1993). The $T_A = 1400$ °C curve has been enlarged 20 times for clarity. ....	VI-18
VI-8. Composite curve fitting of rate window curve using DLTS rate window peaks for the sample 6H-SiC:Ar, annealed at 1200 °C. ....	VI-20
VI-9. Two rate window plot illustrating to effect of increasing the implantation dose on the concentration of the 615 meV trap level in argon-implanted 6H-SiC. Note the change in peak heights as the ion implantation dose is increased by two orders of magnitude. ....	VI-22
VI-10. Donor concentration effect on the DLTS rate window plots. Shown are the normalized rate window plots for three n-type 6H-SiC:Ar diodes. The consistent peak height for the 615 meV trap indicates that the concentration of the trap is changing proportionally with the changing donor concentration. This implies that one of the constituents of the 615 meV trap is substitutional nitrogen. ....	VI-25
VI-11. Rate window plot of argon-implanted n-type 6H-SiC at 475 °C. The two $\phi = 2 \times 10^{14} \text{ cm}^{-2}$ curves have been offset for clarity. Also note that the $\phi = 2 \times 10^{14} \text{ cm}^{-2}$ , 1400 °C curve has been enlarged 20 times to show its features. ....	VI-28
VI-12. Two Arrhenius plots produced from DLTS data from two different diodes on a single 6H-SiC:Ar sample. The nearly overlapping linear sections illustrate the repeatability of the DLTS measurement. The slope of the linear section and position on the graph establishes the trap parameters $E_t$ and $\sigma_t$ . The legend indicates the date of measurements. ....	VI-31



VI-13. Arrhenius plot of the strongest trap peaks for three high temperature (475 °C) implanted 6H-SiC:Ar samples. Note the pair of trap levels (615 & 576 meV and 510 & 476 meV) and the near overlapping of the 262 and 260 meV curves as well as the 307 and 310 meV curves.	VI-33
VI-14. Rate window plots of three high temperature (475 °C) implanted 6H-SiC:Cr samples annealed at 1200, 1400, and 1600 °C. Also shown is the rate window plot of the unimplanted 6H-SiC sample annealed at 1400 °C.	VI-35
VI-15. Rate Window curves for four high temperature (475 °C) implanted 6H-SiC:Cr samples. The upper two curves have been shifted upward for clarity. Note the effect of anneal temperature ( $T_A$ ) and implantation dose on the trap peaks.	VI-39
VI-16. Rate window plot for room temperature (23 °C) and 475 °C implanted 6H-SiC:Cr annealed at 1200 °C illustrating the effect of the implantation temperature on the formation/evolution of damage- and chromium-related traps. Also shown are the rate window plots for unimplanted 6H-SiC and high temperature (475 °C) implanted 6H-SiC:Ar.	VI-42
VI-17. Double-correlated DLTS (DDLTS) rate window plots are five different areas from a high temperature (HT) implanted 1200 °C annealed 6H-SiC:Cr sample. The plot illustrates the depth dependence of the trap concentrations. The upper left inset shows the relative location of the regions measured.	VI-45
VI-18. Graph of trap concentrations at a function of anneal temperature from high temperature (475 °C) implanted ( $2 \times 10^{14} \text{ cm}^{-2}$ ) 6H-SiC:Cr. Most of the trap levels had peak concentrations following the 1400 °C anneal. The only exception was the 427 meV damage-related trap.	VI-47
VI-19. Graph of trap concentrations at a function of anneal temperature from high temperature (475 °C) implanted ( $5 \times 10^{12} \text{ cm}^{-2}$ ) 6H-SiC:Cr. Most of the trap level concentrations decreased or remain constant following the 1400 °C anneal. The only exceptions were the two damage-related trap pair (381 and 332 meV) which increased by about 350 %.	VI-48
VI-20. Rate window plots of three high temperature (475 °C) 6H-SiC:Mg samples annealed at 1200, 1400, and 1600 °C. Also shown is the rate window plots of the 1400 °C annealed unimplanted 6H-SiC sample.	VI-51

VI-21. Rate Window curves for four high temperature (475 °C) implanted 6H-SiC:Mg samples. The upper curves have been shifted upward for clarity. Note the effect of anneal temperature ( $T_A$ ) and implantation dose on the trap peaks. ....	VI-55
VI-22. Two rate window plots for two high temperature (HT) implanted 6H-SiC:Mg samples having different donor concentrations. The lower donor concentration level sample formed a minority carrier trap peak (near 460 K), which distorts the position of the majority carrier trap peak near 500 K. ....	VI-60
VI-23. Rate window plots showing the effect of ion implantation temperature on the formation and evolution of trap levels in magnesium-implanted n-type 6H-SiC. Compare this figure to Figure VI-16 to witness the difference of room temperature ion implantation between Cr- and Mg-implantation. ....	VI-62
VI-24. Rate window plot from double-correlated DLTS (DDLTS) measurements showing the trap concentration depth dependence. The 474/424 meV trap pair concentrations increase significantly in the region of the ion implantation peak. ....	VI-65
VI-25. Rate Window plot from double-correlated DLTS (DDLTS) measurements showing the trap concentration depth dependence. Note the dramatic decrease in concentration of the Mg-related traps when probing beyond the implantation peak of 2500 Angstroms. ....	VI-66
VI-26. Graph of trap concentrations as a function of anneal temperature from the heavier implanted ( $1 \times 10^{14} \text{ cm}^{-2}$ ) 6H:SiC:Mg ( $T_i = 475 \text{ °C}$ ). Most of the damage-related traps concentrations increased in concentration following a 1400 °C anneal followed by a slight changes with a 1600 °C anneal. The Mg-related traps concentrations initial decreased when the anneal temperature was raised to 1400 °C then dramatically increased following a 1600 °C anneal. ....	VI-67
VI-27. Cathodoluminescence spectra of as-grown, unimplanted/annealed ( $T_A = 1800 \text{ °C}$ ), and ion implanted/annealed ( $T_A = 1600 \text{ °C}$ ) epitaxial n-type 4H-SiC. Inset shows the above bandgap peaks observed from the as-grown samples. The spectra have been offset for clarity. ....	VI-77

- VI-28. Cathodoluminescence spectra of n-type 4H-SiC epilayer annealed at  $T_A = 1800^\circ\text{C}$ . The first ten phonon replicas are labeled. The P-series denotes hexagonal sites and the Q-series denotes cubic sites with the subscripts denoting the phonon energies in meV involved in the recombinations. The cubic-site zero-phonon line (ZPL) dominates the spectrum due to a higher recombination probability for the tighter bound exciton. .... VI-80
- VI-29. Shown are the calculated phonon energies of 37, 68, 95, and 108 meV (shown along the right hand side of the graph) from cathodoluminescence measurements of n-type 4H-SiC. The curves shown are those reported by Feldman for the phonon energies for SiC along the c-axis.(Feldman, 1968) ..... VI-81
- VI-30. Cathodoluminescence spectra of n-type 4H-SiC epilayer – unannealed and annealed at  $T_A = 1800^\circ\text{C}$ . Note the effect of annealing on the N-associated zero-phonon line pair and associated phonon-replica line pairs. Spectrum of annealed sample is offset for clarity. Inset shows the above bandgap peaks observed only from the unannealed (as-grown) sample. .... VI-83
- VI-31. Sample temperature dependent cathodoluminescence spectra of unimplanted 4H-SiC annealed at  $1800^\circ\text{C}$ . Spectra are offset for clarity. Note proportional intensity reduction of ZPLs and associated phonon replica lines. .... VI-84
- VI-32. CL spectra of N-implanted ( $500^\circ\text{C}$ ) n-type annealed 4H-SiC annealed at 1400, 1600, and  $1800^\circ\text{C}$ . Note the dramatic increase in intensity of peaks following an  $1800^\circ\text{C}$  anneal. .... VI-87
- VI-33. Sample temperature dependent cathodoluminescence spectra of 4H-SiC:N sample annealed at  $1800^\circ\text{C}$ , showing the shifting of the peaks to lower energy with increasing sample temperature. Also shown are the phonon replica corresponding to previously calculated values. Note that, unlike the exciton peaks these peaks are not as quickly thermally quenched indicating a free-to-bound transition. .... VI-89
- VI-34. Shift of the 2.6376 (at 6.5 K) ZPL in 4H-SiC:N ( $T_A = 1800^\circ\text{C}$ ) with sample temperature. Inset shows the square dependence of the peak position with temperature, which corresponds to the square dependence of the bandgap with temperature. This indicates that the transition is band-related. .... VI-91
- VI-35. Cathodoluminescence spectrum of 3.63 eV ZPL pair and associated phonon-replica for 4H-SiC:N ( $\phi = 3 \times 10^{13} \text{ cm}^{-2}$ ,  $T_A = 1600^\circ\text{C}$ ) at four different electron beam energies (5, 6, 8, and 10 keV). .... VI-93

- VI-36. Cathodoluminescence spectrum for the high temperature (500 °C) P-implanted ( $\phi = 3 \times 10^{13} \text{ cm}^{-2}$ ) n-type epitaxial 4H-SiC samples annealed at 1400, 1600, and 1800 °C. The inset shows the presence of the ZPLs detected in the unimplanted samples and related to the exciton bound to at substitutional nitrogen. The curves are offset for clarity. .... VI-95
- VI-37 Cathodoluminescence spectrum for 4H-SiC:P ( $\phi = 3 \times 10^{13} \text{ cm}^{-2}$ ) annealed at 1400, 1600, and 1800 °C. The inset shows the ZPLs dependence on anneal temperature. Note the slight shifting in the ZPL peaks and the changes in intensity with anneal temperature. Curves have been offset for clarity. .... VI-96
- VI-38. Cathodoluminescence spectrum of 1400 oC annealed 4H-SiC:P and 4H-SiC:Ar samples. Spectrum of 4H-SiC:P is offset for clarity. Identical ZPLs and associated phonon-replicas suggests this defect to be damage-related and that phosphorus is not one of the defect constituents. The electron-beam energy used for both spectra was 10 keV. .... VI-98
- VI-39. Sheet carrier concentration measurements of three N-implanted n-type 4H-SiC samples annealed at 1400, 1600, and 1800 °C. A computed value of 63 meV is determined from the sheet carrier concentration slope and is associated to the shallow nitrogen donor level. .... VI-102
- VI-40. Hall mobility measurements of three N-implanted n-type 4H-SiC samples annealed at 1400, 1600, and 1800 °C. Increasing the anneal temperature had only the effect of slightly improving the mobility by approximately 20%. The negative slope is determined by the lattice scattering effect. .... VI-104
- VI-41. Sheet carrier concentration measurements of three P-implanted n-type 4H-SiC samples annealed at 1400, 1600, and 1800 °C. A computed value of 46 meV is determined from the sheet carrier concentration slope and is associated to the shallow phosphorus donor level. .... VI-106
- VI-42. Computed sheet carrier concentration curves for an ideal 4H-SiC sample containing a single donor level at 46 meV, and containing two donor levels at 46 and 300 meV. The concentration of the 300 meV levels was set at 10 times the concentration of the 46 meV level to  $6 \times 10^{13} \text{ cm}^{-2}$ . .... VI-107
- VI-43. Hall mobility measurements of three P-implanted n-type 4H-SiC samples annealed at 1400, 1600, and 1800 °C. .... VI-109

VI-44. Activation efficiency and mobility dependence on anneal temperature on N- and P-implanted (500 °C) n-type 4H-SiC. Both implant type show improved mobility with increased anneal temperature. However, activation is dramatically reduced when the anneal temperature is raised to 1800 °C. .... VI-111

VI-45. Observed levels in high temperature (500 °C) ion implanted and annealed 4H-SiC:N and 4H-SiC:P by Hall effect and cathodoluminescence measurements. .... VI-114

## List of Tables

II-1. Comparison of SiC Properties to Silicon and Gallium Arsenide.....	II-7
II-2. Johnson and Keyes Order of Merit Values (Davis, 1994).....	II-9
II-3. Summary of Deep Levels Observed in 4H-SiC.....	II-16
II-4. Summary of Deep Levels Observed in 6H-SiC.....	II-17
VI-1. List of n-type epitaxial 6H-SiC Schottky diodes used in the DLTS study. Note that all of the ion implanted samples were implanted at 475 °C except for two, which were implanted at room temperature (23 °C).....	VI-2
VI-2. Computed trap parameters for n-type 6H-SiC implanted with argon at 475 °C. The uncertainties are: $\Delta E_t = \pm 0.05 * E_t$ ; $\Delta \sigma_t = \pm 0.50 * \sigma_t$ ; and $\Delta N_t = \pm 0.02 * N_t$ .....	VI-24
VI-3. Computed trap parameters for high temperature (475 °C) implanted 6H-SiC:Cr annealed at 1200 °C. The uncertainties are: $\Delta E_t = \pm 0.05 * E_t$ , $\Delta \sigma_t = \pm 0.50 * \sigma_t$ , and $\Delta N_t = \pm 0.02 * N_t$ .....	VI-40
VI-4. Computed trap parameters for high temperature (475 °C) implanted 6H-SiC:Cr annealed at 1400 °C. The uncertainties are: $\Delta E_t = \pm 0.05 * E_t$ , $\Delta \sigma_t = \pm 0.50 * \sigma_t$ , and $\Delta N_t = \pm 0.02 * N_t$ .....	VI-41
VI-5. Computed trap parameters for high temperature (475 °C) implanted 6H-SiC:Mg annealed at 1200 °C. The uncertainties are: $\Delta E_t = \pm 0.05 * E_t$ , $\Delta \sigma_t = \pm 0.50 * \sigma_t$ , and $\Delta N_t = \pm 0.02 * N_t$ .....	VI-58
VI-6. Computed trap parameters for high temperature (475 °C) implanted 6H-SiC:Mg annealed at 1400 °C. The uncertainties are: $\Delta E_t = \pm 0.05 * E_t$ , $\Delta \sigma_t = \pm 0.50 * \sigma_t$ , and $\Delta N_t = \pm 0.02 * N_t$ .....	VI-59
VI-7. Dominant trap level detected in DLTS measurements of n-type 6H-SiC implanted at 475 °C with either argon, chromium, or magnesium.....	VI-70
VI-8. List of n-type epitaxial 6H-SiC p-n diodes used in the Hall effect (Hall) and cathodoluminescence (CL) studies. Ion implantations were made at 500 °C.....	VI-75

### Abstract

Intrinsic and ion-implantation induced defects were investigated and characterized using deep level transient spectroscopy, Hall effect, and cathodoluminescence (CL) techniques on n-type silicon carbide epitaxial material. The polytypes of SiC studied were 6H and 4H. Currently, these two polytypes are considered the best candidates for high-power, high-temperature, and high-frequency electronic device applications. The epitaxial material was ion-implanted at elevated temperatures (475 and 500 °C) to investigate the effect of a "hot" implant on the formation and evolution of deep level defects, and the activation of ion-implanted donor and acceptor atoms. Material quality, although improving, is not at a sufficient level, and high concentrations of near-midgap traps and micropipes limited the investigation of these polytypes.

In the 6H-SiC samples, twelve new deep level defect pairs were observed ranging in electron trap energy from 0.250 to 1.1 eV. Also observed were the previously reported  $E_1$  and  $E_2$  350 meV defect levels and the 615 meV defect level. From this study, the 615 meV trap was assigned to a  $V_{si}$ -N complex. The remaining trap pairs, due to the inequivalent lattice sites, were identified as either damage- or species-related (Cr and Mg). The high-temperature ion implantations partially annihilated several of the damage-related defects, and thermal anneals from 1200 to 1800 °C resulted in a significant alteration of the trap populations and modest improvement in the rectification of the test devices. High-temperature implantation and annealing also resulted in the activation of several species-related defects.

Cathodoluminescence and Hall effect measurements of 4H-SiC:N indicated that, although the ion-implanted nitrogen was activated, the local environment of the substitutional nitrogen was not fully restored to its pre-implanted state. The electrical activation efficiency of 90 % has been obtained for the sample implanted at 130 keV to a dose of  $1 \times 10^{13} \text{ cm}^{-2}$  after annealing at 1400 °C for 30 minutes. Anneal-resistant 250 and 626 meV deep level traps were also detected. The radiative 626 meV trap appeared to be nitrogen-related. In addition, a higher-energy conduction band minimum, 130 meV above the lower-energy conduction band minimum, was indicated by an above bandgap CL peak pair from as-grown 4H-SiC. This is only the second reported observation of this higher-level conduction band minimum in 4H-SiC.

Analysis of the 4H-SiC:P samples indicated the formation of a phosphorus-related shallow 46 meV donor level, and an anneal-resistant radiative 346 meV deep level defect, which appeared to be a damage-complex not involving phosphorus. The electrical activation efficiency of 30 % has been obtained for the sample implanted at 130 keV to a dose of  $1 \times 10^{13} \text{ cm}^{-2}$  after annealing at 1600 °C for 30 minutes. Argon-implanted samples were tested in both polytypes and aided in characterizing the detected defects.



## I INTRODUCTION

### I-1 Goal Statement

The goal of this study was to electrically and optically characterize n-type 4H- and 6H-polytype silicon carbide (4H-SiC and 6H-SiC) semiconductor epitaxial layers both as-grown and ion implanted at high temperature with nitrogen, phosphorus, chromium, magnesium, and argon. The ion species phosphorus and nitrogen were implanted into 4H-SiC polytype to investigate donor doping by ion implantation. Chromium is a transition metal and was implanted to investigate deep levels that may be used in producing compensated SiC. Magnesium was also investigated for deep levels in 6H-SiC, as it should act as an amphoteric implant. Argon was used as an inert damage-generating implant species in both 6H- and 4H-SiC polytypes.

Implantation methods are not established for SiC and are required for devices which need precise control of the impurity profile; total dose and area uniformity; and for producing ohmic contacts via tunneling. Room-temperature ion-implantation of SiC has been shown to produce anneal resistant deep level defects (Scofield, 1996) (Suttrup, 1990) (Anikin, 1985). Even small concentrations of deep level defects in device material can significantly degrade its electrical performance. Ion implantation is extensively used to improve device performance. Improvements in field-effect transistors include reducing the overall capacitance by self-aligned source and drain; adjusting the threshold voltages by a shallow dopant at the oxide interface; reducing 'punch-through' between source and drain by a channel implant on a lightly doped substrate; and creating buried-channel de-

vices by incorporating an opposite type impurity into the surface region (Sze, 1985:456). Once ion-implantation techniques have been fully developed for SiC, SiC-based field-effect transistor designs will include these ion-implantation based improvements. Such devices include metal-oxide-semiconductor field-effect transistors (MOSFETs), high performance metal-oxide-semiconductors (HMOS), and double-drift IMPATT diodes.

The requirement also exists for semi-insulating SiC material for buffer layers in such devices as metal-semiconductor field-effect transistors (MESFETs). Deep level defects have been used in other semiconductors to make semi-insulating material. Transition metals are known to produce deep levels and it may be feasible to use them in SiC for this effect (Strack, 1967). For example, Cr doping in GaAs is used to compensate in both n- and p-type material. Damage defects can also serve this purpose. In addition, epitaxially grown SiC material has not been well characterized in 4H-, and 6H-SiC. This material should be of much better quality than bulk material allowing better interpretation of test results. This includes the identification of the fundamental electrical characteristics such as drift mobility, carrier concentrations, compensation densities; and the measurement of the energy levels, capture cross sections, and concentrations of deep levels due to impurities and defects.

In this study, I chiefly used Deep Level Transient Spectroscopy (DLTS) to quantify activation energies, capture cross-sections, concentrations, and concentration profiles associated with the dopant-related and damage-related deep level defects. I also used Hall effect to measure electrical parameters such as resistivity, Hall mobility, free carrier density, and total impurity density to assess the effect of nitrogen and phosphorus implanted

and annealed 4H-SiC. In addition, I employed cathodoluminescence (CL) on the 4H-SiC samples to further understand the effect of implantation/annealing on the crystalline defects. I related electrical performance to the deep level defects, and implantation/annealing parameters. These parametric relationships to implantation and annealing are critical for the successful fabrication of high-temperature high-power electronic devices, high electron-mobility transistors and heterostructure bipolar transistors, high temperature detectors, and shorter-wave optoelectronic devices such as blue/UV LEDs and detectors. By understanding these dependencies on implantation and annealing parameters, techniques may be developed for implanting SiC to produce the required electrical and optical properties for these devices. There still exist very little information on the mechanisms involved in the formation and activation of deep levels in SiC. Several experimental results from previous research of defects in SiC, diamond, and other semiconductors can be used to suggest possible kinetics. By evaluating both as-grown and ion-implanted samples, these trap levels can be characterized, allowing device designs to minimize or exploit these levels. For example, once the analysis of temperature-dependent mobility and carrier concentration data has been completed for a sufficient number of samples using the Brooks-Herring formula for ionized impurity scattering, the total impurity density ( $N_d + N_a$ ) can be accurately estimated from a single measurement of the mobility, instead of, from a series of Hall coefficient ( $R_H$ ) measurements (Wolf, 1970:504). This empirical relationship would then allow a much quicker way to check the quality of future samples.

The three main measurement methods used were deep level transient spectroscopy (DLTS), Hall effect, and Cathodoluminescence (CL). To aid in selecting and characterizing the test devices, capacitance-voltage-temperature (C-V-T) and current-voltage-temperature (I-V-T) measurements were also accomplished and analyzed. DLTS techniques included differential deep level transient spectroscopy (DDLTS) and constant voltage deep level transient spectroscopy (CVDLTS). Hall effect was completed on nitrogen- and phosphorus-implanted 4H-SiC samples to assess the dominant donor level, activation of the implanted species, and electron mobility. Cathodoluminescence (CL) was also accomplished on select samples to examine radiative recombinations, correlate to electrical performance and to provide additional or supporting information.

## **I-2 Limits of Silicon**

Many applications (including military) of electronic devices require operation in high temperature, severe radiation and caustic environments. However, the use of semiconductor devices in these harsh environments is currently limited by the physical limits of silicon and gallium arsenide. Silicon-based devices are thermally limited to about 250 °C and are highly susceptible to radiation damage and corrosion. Although thermal cycling has been shown to repair some of the radiation damage in silicon, the leakage current in silicon minority carrier devices doubles with each 10 °C increase in temperature at elevated temperatures due to the dominating effect of the increasing intrinsic carrier concentration.

Carrier mobility is also reduced due to increased scattering (lattice and ionized impurity). In addition, heat generation and the inefficient heat dissipation of silicon forces the use of costly coolant systems that also cost in terms of weight, space and reliability (Swonger, 1992). For the U.S. military, the next generation aircraft will be designed with more electrically powered controllers and sensors. This will remove much of the hydraulic systems that also serve as the coolant. These future electrically powered units will experience higher temperatures, a wider operating temperature range, and reduced heat sinks. To make this a viable 21<sup>st</sup> century design, semiconductor devices will have to be developed from semiconductors other than silicon and gallium arsenide that reliably operate in these demanding environments.

### **I-3 Characteristics of Wide Gap Semiconductors**

Fortunately, wide bandgap semiconductors, like SiC, GaN (gallium nitride), and AlN (aluminum nitride), exist that have the needed physical characteristics for high-power high-temperature use. These properties include large bandgap, physical hardness, radiation hardness, large heterojunction offsets, high carrier saturation velocity, low dielectric constants, high thermal conductivity, and high chemical, thermal, and mechanical stability. Order of Merit values have been computed by Johnson and Keyes showing the relative potential performance of these wide gap materials (Davis, 1991). These order-of-merit values relate to the potential speed of free carriers and field strengths in these materials. Unfortunately, the extraordinary properties of these semiconductors also make them extremely difficult to produce with high quality and to fabricate into high quality devices.

As a wide bandgap semiconductor, SiC does not allow a significant increase of intrinsic carriers, even at very high temperatures. This means that SiC minority carrier devices can operate at high temperatures without temperature sensitive current/voltage fluctuations. This wide bandgap also allows fabrication of blue/UV range LEDs and optical detectors. This is currently being done with both GaN and SiC. Its radiation hardness makes SiC ideal for space-borne optical detector systems. Also, SiC has excellent thermal conductivity and a large breakdown voltage, giving it better heat dissipation for high power device use and increased integrate circuit (IC) packing density. Productive use in negative affinity devices is also possible due to its lower electron affinity. Compensated

SiC is a requirement for a high resistivity layer in such devices as MESFETs. Near mid-gap energy levels generated by transition metal dopants might be used to produce such semi-insulating material. It has also been suggested that non-volatile random-access-memory (RAM) could be produced using SiC. At room temperature the lifetime of the 'on' state once the bias is removed would be extended out to several million years compared to the millisecond lifetime in silicon based RAM due to the thermally excited carrier rates (Morkoc, 1994).

#### **I-4 Future Semiconductor Requirements**

High temperature high power electronics are primarily required in the extreme operating environments of the controls and sensors of aircraft, automobile engine, and spacecraft. These electronics must be able to reliably operate, not only at elevated temperatures and high radiation fluxes, but also in repeated thermal cycling and rapid changing temperature conditions. Device thermal and power limits can be traced back to the physical properties of the semiconductor material. The temperature levels that will be encountered in future systems will exceed the current 125 °C technology limit of silicon. In addition, many of the DOD/DOE thermal requirements for military and space systems extend up to 500 °C and higher (Thome and King, 1988). Presently, these requirements are met by the incorporation of large environmental control units (ECUs) into these systems or using remote monitoring equipment. Size and weight constraints limit the redundancy of ECUs, so that system reliability is critically dependent on the failure rate of these units. Remote monitoring has the shortcomings of increased signal noise and increased maintenance. Future military systems will have increased capabilities, which will increase the thermal loads thus requiring even larger ECUs. Present ECU costs are quite significant and will only increase with larger units (Przybylko, 1990). The military is currently investigating the use of wide-bandgap semiconductor devices to increase the role of electrical systems for control and monitoring of various airborne components and thus reduce the ECU requirement. This concept is known as the "more electric aircraft" for the Air Force. Figure I-1 illustrates how extensive this concept will be integrated into



future aircraft design. Typical failure mechanisms for high temperature electronics include disserviceable reductions in breakdown voltage, cutoff frequency, switching speed, and transistor gain; and increases in leakage current, device resistance, and latch-up events in both switching and logic devices related to degradation in contacts and dielectric layers through liftoff and peeling effects. All of these issues must be researched and understood before reliable production line electronics can be produced for these applications. The designs for these future systems call for electronic performances that do not currently exist. Materials such as SiC, diamond, GaN, and AlGaN have the physical properties to potentially meet these performance levels. However, material and device research of these semiconductors is still in their initial phases with limited demonstration of superior high-temperature performance.

## More Electric Initiative VISIONARY CONCEPT

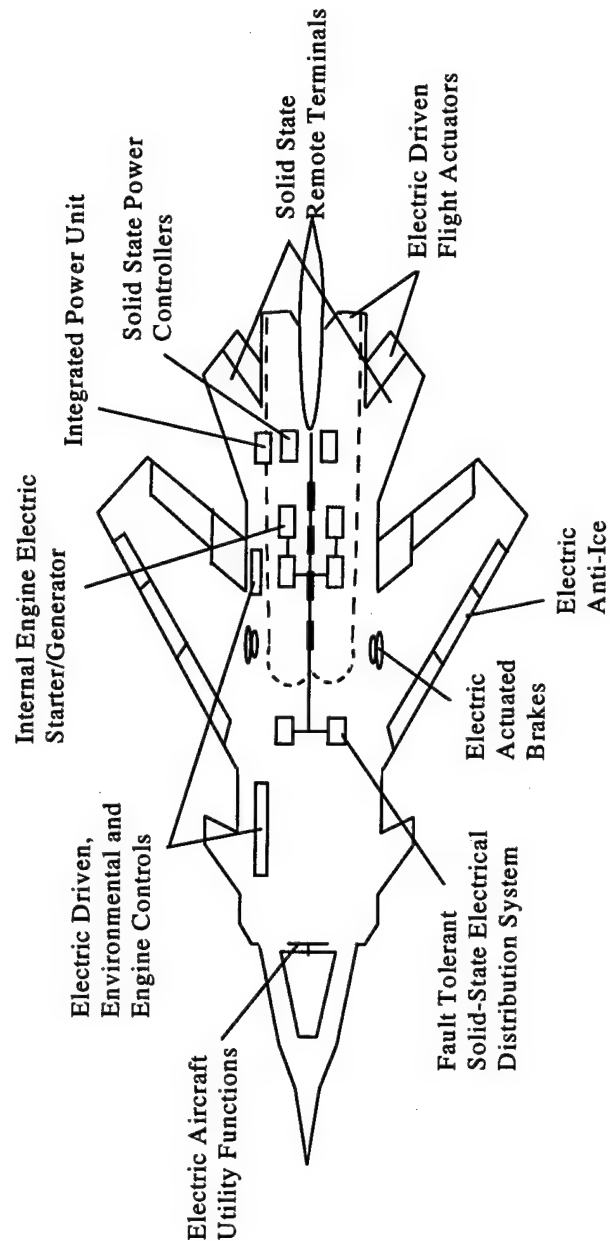


Figure I-1. The Air Force conceptual view of a more electric aircraft showing the various subsystems being replaced with electrical subsystems including the conversion of hydraulic actuators to electrical actuators.

## I-5 Problems with SiC

Although SiC has many favorable physical characteristics, there are also many problems with SiC materials and devices. Large bandgap materials, such as diamond, SiC, AlN, and GaN, are chemically very inert and have low dopant diffusivities due to their large cohesive bonding energies. This makes it difficult to control doping levels and conductivity type and makes them difficult to grow. Furthermore, there are obstacles in obtaining thermally stable Schottky contact and low resistivity ohmic contact metallizations, especially at elevated temperatures. Thermal stability studies of both types of contacts have not been thoroughly accomplished and room temperature contacts may not be usable at higher temperatures. Currently, contacts rely on tunneling as the mechanism for ohmic behavior and thus require high doping, at least at the surface, of the semiconductor. Another issue is the intrinsic n-type nature of SiC due to intrinsic nitrogen donors and double-donor carbon vacancies ( $V_C$ ). This makes p-type material harder to grow and the material is highly compensated. Many devices will require semi-insulating SiC, perhaps achievable with a controllable near midgap point defect or impurity level. A few studies have shown this effect through the incorporation of vanadium (Jenny, 1995) (Hobgood, 1995) (Evwaraye, 1994). Extended void defects along the c-axis, known as micropipes, are formed in SiC during growth. Micropipes are a source for premature electrical breakdown and currently, micropiping densities are too high for high power device use. Deep level defects also exist in sufficient concentrations to affect the electrical properties in SiC devices. Deep level defects have been suggested as another mechanism

for triggering breakdown in 6H-SiC p-n junctions (Neudeck, 1996). These defects and impurities can form deep energy levels in the SiC bandgap that also severely limit minority carrier lifetimes. Additionally, there are severe uniformity issues from wafer to wafer and across a single wafer surface that result in significant performance variations in fabricated devices.

For p-type SiC, aluminum is the most common dopant element used ( $\text{Al}_{\text{Si}}$ ). Unfortunately, aluminum has the problem of degrading the oxide interface. Since device fabrication requires differing doped regions, methods must be developed to dope SiC with different elements and concentrations. Diffusion and ion implantation are the two methods used for narrower gap semiconductors. However, diffusion into SiC is too slow at workable temperatures. Diffusion temperatures must be in the 1880-2200 °C range to produce diffusion rates acceptable for manufacturing layered devices. Unfortunately, these high temperatures prohibit using passivating oxide layers to mask against diffusion. Although SiC p-n junction have been produced using growth methods, they require long times, high temperatures and device dimensions must remain prohibitively large for high speed applications.

The alternative method to diffusion is ion implantation. However, ion implantation causes significant damage that must be repaired by some annealing procedure. Ion implantation techniques have yet to be developed for SiC. A few nitrogen and aluminum implantation and anneal studies have been done. It was shown that 50 % of the implanted nitrogen could be activated by a 1200 °C three hour or 1450 °C three minute anneal (Campbell, 1974). Hall mobility of nitrogen-implanted layers in 3C-SiC continues to in-

crease with annealing up to 1700 °C, showing a continued reduction in the density of scattering centers (Marsh, 1971:285). This research was accomplished on low quality material and should be revisited using today's higher quality semiconductors. High temperature implantation has also been investigated as a method to reduce damage during implantation in other semiconductors. Results have indicated some significant damage reduction. Laser annealing is another method that is employed to activate ion implants and repair damage (Ahmed, 1995). Implantation studies have also been accomplished using low temperature implantation. Recently, a low dosage ion implantation using the p-type dopant boron into low temperature diamond has produced the highest mobility for that implanted material to date (Fontaine, 1996). Another area recently studied in wide bandgap semiconductors is neutron-generated damage which is a critical area for space and reactor applications (McLean, 1994).

## I-6 Current Status of SiC Material and Devices

Recent advances in SiC crystal growth have enabled a renewed pursuit of material device technology. SiC is now commercially available in 2.0 inch diameter wafers, p-, n-type, and highly resistive. Epitaxial layers can now be grown as thin as 0.1  $\mu\text{m}$  and a net donor or acceptor concentration as low as  $5 \times 10^{15} \text{ cm}^{-3}$ . The cost, however, is extremely high compared to Si and even GaAs, significantly impacting the extent of research test matrices. High-temperature device technology is currently in the exploratory and development phases, though a number of promising device results have been reported, including a SiC field-effect transistor (FET) operating up to 650  $^{\circ}\text{C}$  (Palmour *et al.*, 1997). Although currently limited, these initial laboratory results have demonstrated a potential for high temperature applications. Unfortunately, there still exist a wide variation in material quality not only between runs but also across a single wafer indicating the infancy of this material technology. Significant concentrations of micropipes, yet unidentified impurities, and defects still plague the material and greatly limit the quality of test devices. One area that is hindering the advancement of this material is the lack of understanding of both the electrical and optical properties of these materials. Device development has been the driving force in recent material research and crucial device parameters such as Hall and drift mobilities, electron saturation drift velocity, and carrier lifetimes have not been well characterized. Measuring these basic parameters would also serve as a feedback to growers. Another area that will greatly enhance our ability to produce and improve electronic and optoelectronic devices is characterization of doped SiC via ion im-

plantation. Ion implantation is a well-established method for precision spatial control of the doping of silicon. Implanted dopants in SiC, for the most part, are not well studied and so the resulting electrical and optical properties are not well understood. Higher doping levels needed to form ohmic contacts may be achieved through proper ion implantation. Thus, in order to develop promising high temperature electronic and opto-electronic devices, a fuller understanding is needed about the nature of the doped impurities; defects present in the materials, before and after processing; contact metallization properties; interface states and ion implantation/annealing techniques to control damage and activation.

## II BACKGROUND: SILICON CARBIDE

### II-1 Crystal Structure

The crystal structure of silicon carbide (SiC) exhibits a one-dimensional type polymorphism known as polytypism. In fact, polytypism in crystals was first discovered in SiC. The various SiC polytypes are characterized by their stacking sequence of the Si-C bilayers. Polytypes are identical in the close-packed plane (basal) dimensions but differ in the normal dimension (c-axis). The bond between the two semiconductor elements is tetrahedral with each carbon atom bonded to four silicon atoms and, likewise, each silicon atom bonded to four carbon atoms (Verna and Krishna, 1966:81-82). SiC has a strongly homopolar or covalent bonding character (88-90% using Pauling's method) (Linus, 1988). This bonding configuration results in a silicon face and carbon face to each wafer cut normal to the c-axis since the weaker bonding plane is between the silicon and carbon atoms in each bilayer where there is only a single bond per atom (Figure II-1).

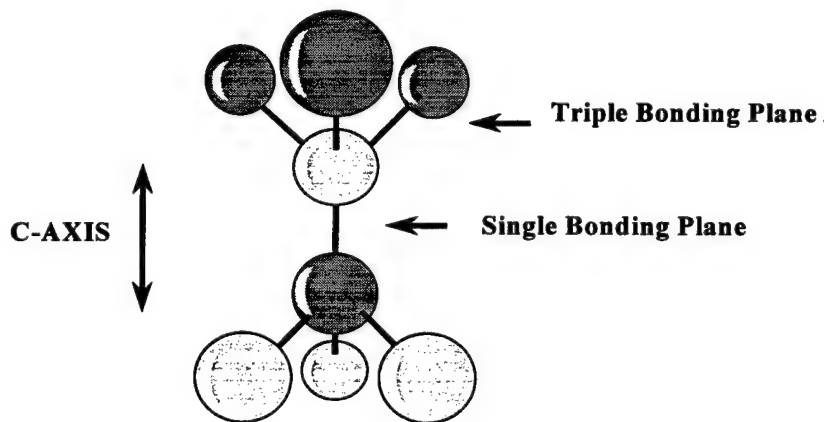


Figure II-1. Bonding Planes in SiC



1).

The crystal can form as a zincblende or wurtzite structure depending on the stacking sequence of the SiC bilayers. In addition, the crystal can grow as a polytype that contains both zincblende and wurtzite stacking sequences, hence the name polytypism. To date, there are over two hundred known polytypes of SiC. Polytypism can be easily understood by considering the stacking sequence along the c-axis. Each stacking bilayer of SiC molecules forms as an equilateral triangular (hexagonal) grid, so that the next bilayer must be offset in order to place its molecules over half the centers of the triangles of the previous bilayer. After that second bilayer is grown, the third bilayer can go down just one of two ways. It can either mirror the first layer, forming the ABA... stacking sequence or it can be offset so that its molecules are directly over the centers of the triangles of the second layer that are not directly over the first layer molecules, forming the ABC... stacking sequence. One can better understand this stacking option by studying Figure II-2. The ABA form is the wurtzite structure with the B sites being hexagonal sites, while the ABC form is the zincblende structure with the B sites being cubic sites. Only for the purely zincblende or wurtzite structure are those sites purely cubic or hexagonal, respectively. All other polytypes can have only quasi-cubic and/or quasi-hexagonal sites. The purely zincblende structure is also known as 3C-SiC or  $\beta$ -SiC. The purely wurtzite structure is known as 2H-SiC. Mixed states are collectively referred to as  $\alpha$ -SiC and are designated by the Ramsdell notation where the number gives the repeating unit of the SiC bilayer and the letter stands for: C for cubic; H for hexagonal; and R for rhombohedral. For example 6H-SiC has the repeated layers ABC ACB; 4H-SiC has the ABAC pattern

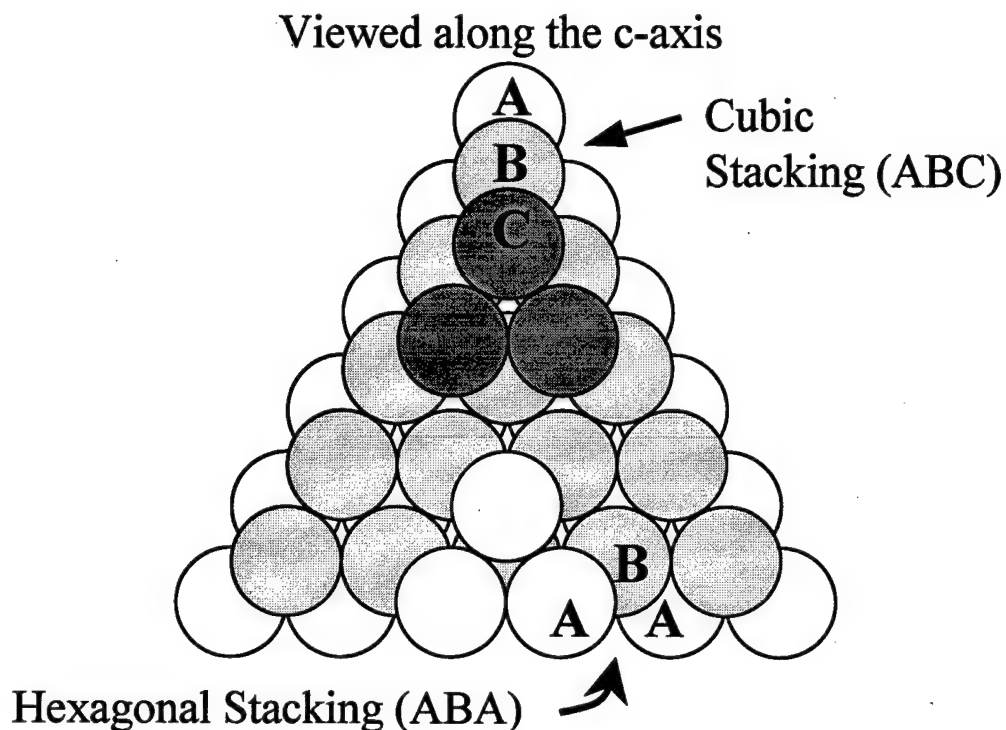


Figure II-2. The two stacking-sequences for the basal planes of SiC molecules viewed along the c-axis.

and 15R-SiC has the ABC BAC ABA CBC ACB pattern (O'Connor and Smiltens, 1960).

The rhombohedral polytypes differ from the hexagonal polytypes by a nonnormal growth axis to the basal plane. The most important polytypes for devices are 6H-, 4H-, and 3C-SiC. 6H-SiC is the most commonly occurring polytype and currently is being produced with the highest quality. However, 4H-SiC has better fundamental electrical properties and should eventually provide superior high power devices. 3C-SiC was originally thought to be a low temperature phase of SiC, but it was empirically shown that 3C-SiC

was metastable over the entire solid phase temperature range (Knippenberg, 1966). 3C-SiC also has the highest electron saturation velocity and mobility of the polytypes. 2H-SiC does not occur naturally and must be synthesized. Currently, 6H- and 4H-SiC can be grown in bulk, while 3C-SiC must be epitaxially grown on a different substrate material. The growth plane is slightly offset from the basal plane to provide the polytype template for the next layers. 3C-SiC has a lattice constant of 4.35 Angstroms ( $\text{\AA}$ ) at room temperature, while all the hexagonal and rhombohedral polytypes have hexagonal unit cell dimensions of  $a = b = 3.078 \text{ \AA}$ , and  $c = n \times 2.518 \text{ \AA}$ , where  $n$  is the identity period of the stacking sequence in the structure. The axial ratio  $c/a = n \times 0.817$  and is nearly equal to the theoretical value of  $n \times 0.8165$ .

## II-2 Optical and Electrical Properties

The electrical properties of SiC were first measured by Busch and Labhart in the late 1940's. Small and highly impure samples were obtained by picking through tons of commercial material found in coal furnaces. The samples varied widely in color due to defects and impurities. Robert Pohl and others studied the electrical properties of small  $\beta$ -SiC crystals as part of an Air Force contract in the 1950's. Optical properties of doped and undoped SiC were measured by J. A. Lely and others during the same period. Except for some of the IR absorption peaks that were common in most samples, the properties of these samples varied widely due to the poor quality of the crystals (Pensl and Choyke, 1993).

The optical and electrical properties of SiC are polytype dependent since the interatomic spacing varies with polytype. This variation of the periodicity of the lattice creates a variation in the associated crystal wave functions and resulting energy band structure. The arrangements of the next neighbors are the same in all polytypes. It is the second and third neighbors that are slightly altered between polytypes that result in the crystallographically inequivalent lattice sites (Morkoç, 1994). The higher symmetries of 3C-SiC and 2H-SiC express themselves in their higher electron saturation velocities and electron mobilities. 3C-SiC has the highest symmetry and accordingly its electron saturation velocity and mobility are the highest (due to reduced phonon scattering). 2H-SiC has the widest bandgap at 3.3 eV. 6H-SiC and 3C-SiC are well lattice-matched which is a critical feature for heterostructure device design and epitaxial growth of 3C-SiC on bulk 6H-SiC. SiC is intrinsically n-type mainly due to nitrogen background levels (on carbon

sites). SiC can also possess n-type defects such as double-donor carbon vacancies ( $V_c$ ) and perhaps other yet undefined point defects. SiC's strong covalent bonds makes it electrically stable up to 1200K, 1580K and 1740K for 3C, 6H and 4H-SiC, respectively. The Si-C bond is so strong that it was initially mistaken as an element (the bond could not be broken) when first discovered in 1824 by Berzelius. At the time, Berzelius was trying to synthesize diamond (Morkoç, 1994). Table II-1 compares the bandgap, lattice constants and other properties of 3C, 6H, and 4H-SiC to Si and GaAs. 4H-SiC has a bandgap nearly three times wider than silicon, operates over 1,000 degrees higher, conducts heat over three times faster, holds off voltages ten times larger, has over twice the electron saturation velocity, and has a lower dielectric constant. The only unfavorable property listed in table II-1 is its significantly lower carrier mobilities. The absorption edges of all SiC polytypes are due to indirect phonon assisted transitions, which produce large numbers of excitons (Choyke and Patrick, 1962). These excitons are important to the low temperature absorption and photoluminescence spectra. In SiC, excitons are more important than in other indirect semiconductors such as silicon and germanium due to their larger binding energy, which comes from the greater effective masses in the large bandgap material. The large number of excitons generated by UV illumination prevents direct measurement of the indirect absorption bandedge. Therefore, reported energy gap values are related to the measured excitonic bandedge (Madelung, 1991). A complex optical spectrum results from this large number of exciton recombinations at defect centers and the multiple phonon branches, due to the large unit cell. For 6H-SiC, there are 12 atoms in the unit cell, producing 36 phonon branches. 4H-SiC has 24 phonon branches.

Property	Si	GaAs	3C-SiC	4H-SiC	6H-SiC
Bandgap (eV @ RT)	1.1	1.4	2.2	3.2	2.9
Lattice Constant-a (Angstroms @ RT)	5.43	5.65	4.36	3.08	3.08
Max. Operating Temperature (K)	600 ?	760 ?	1200	1740	1580
Melting Point (K)	1690	1510	----- Sublimes above 2100 K -----		
Electron/Hole mobility RT, cm <sup>2</sup> /Vs	1400/600	8500/400	1000/40	720/40	600/40
Breakdown Field 10 <sup>6</sup> V/cm (@ 10 <sup>3</sup> V)	0.3	0.4	2.3	4	3
Thermal Conductivity W/cm	1.5	0.5	4.9	4.9	4.9
Electron Saturation Velocity 10 <sup>7</sup> cm/s	1	2	2.5	2.2	2
Dielectric Constant K	11.8	12.8	9.7	9.7	9.7

Table II-1. Comparison of Silicon Carbide Properties to Silicon and Gallium Arsenide

Therefore, characterization, modeling, and identification of the defects become extremely difficult. For example, nitrogen impurities in 6H-SiC have been shown by Choyke and Patrick to generate a photoluminescence spectrum of about 50 resolvable lines due to exciton recombination at neutrally charged nitrogen donors (Choyke and Patrick, 1968). This illustrates the inherent difficulties in characterizing the physical mechanisms governing the optical and electrical properties in SiC. The large bandgap makes intrinsic conduction effects negligible even up to high temperatures. This large bandgap also means that band-to-band and near band-to-band radiative transitions are in the blue and UV wavelengths for LED and detector use. Since it has an indirect bandgap, band-to-band

transitions in SiC are limited and it is only possibly to make LEDs and optical detectors but not laser diodes. These devices could emit or detect from the IR into the UV with appropriate energy level formation through doping or defect generation. The high electric field breakdown means that SiC can handle a voltage gradient 8 to 10 times higher than that of silicon or gallium arsenide allowing such devices as diodes, power transistors, thyristors, and surge suppressors to be fabricated with improved performance. SiC has both high breakdown voltage and excellent heat conductivity, which are two needed qualities for increased integrated circuit (IC) packing densities. The excellent heat conductivity and electronic insulating capability of compensated SiC make it a good choice for electronic packaging material. For comparison, ZnSe also has a large bandgap (2.7 eV) but has poor heat conductivity. SiC's thermal conductivity is higher than all the metals at room temperature. The higher saturation electron drift velocities mean higher frequency device operation into the microwave region. Material order-of-merit values were developed by Johnson and Keyes for semiconductor material used in devices (Davis, 1994). Table II-2 illustrates the potential increase in performance of SiC over Si and GaAs by comparing of order-of-merit values. In fact, it was the measured saturation velocity of 3C-SiC that revitalized much as the interest in SiC.

Included in table II-2 are GaN and diamond, two additional materials currently being studied for high power, high speed device use. The Johnson value is a measure of the frequency and power potential of the material while the Keyes value is a measure of the switching speed potential. Higher values are preferred. The Johnson, Keyes, and breakdown field values have been normalized to the silicon values and are listed in the three

Material	Johnson $(E \cdot v_s)^2 \cdot (W\Omega/s)^2$	Keyes $\sigma_t(v_s/K)^{1/2} \cdot (W/(cm \cdot s)^{-1/2})$	Breakdown Field (V/cm)	Ratios to Silicon		
				J	K	BF
Si	$9 \times 10^{23}$	$1.38 \times 10^3$	$4 \times 10^5$	1	1	1
GaAs	$6.25 \times 10^{24}$	$6.3 \times 10^3$	$5 \times 10^5$	6.9	0.4	1.25
6H-SiC	$6.25 \times 10^{26}$	$7.07 \times 10^3$	$4 \times 10^6$	694	5.2	10
3C-SiC	$1.02 \times 10^{27}$	$8.03 \times 10^3$	$3 \times 10^6$	1138	5.8	7.5
GaN	$2.53 \times 10^{27}$	$2.43 \times 10^3$	$4 \times 10^6$	281	1.8	10
Diamond	$7.39 \times 10^{27}$	-----	$1 \times 10^7$	8206	-----	25

Table II-2. Johnson and Keyes Order of Merit Values (Davis, 1994)

right-most columns labeled J, K, and BF, respectively. As can be seen from the table, these large bandgap materials have excellent order-of-merit values for high power, high frequency, and fast switching. It is mainly the high dielectric strengths ( $E > 10^6$  V/cm) and large electron saturation velocities ( $v_s > 2 \times 10^7$  cm/s) that makes SiC a candidate for high power devices.

For ideal crystals, SiC polytypes would be transparent to energies below their bandgaps (ignoring levels created in the forbidden region by defects and impurities). These semiconductors could be used for quarter wave stack ( $\lambda/4$ ) reflectors and laser cavities in the near UV and below. Some of the polytypes are well lattice-matched and have matching thermal expansion coefficients not only to other SiC polytypes but also to other semiconductors such as GaN, a material that must be epitaxially grown. This would allow



their use as substrates, QW barriers, and confinement material. Potential SiC devices include IR opto-isolators; UV and blue emitters, detectors; fiber optic communication devices; RGB displays; high power devices; wide range optical wavelength devices; high-speed switching devices; and secure space-to-space communication and coatings. The secure space-to-space communication is accomplished at an UV frequency that the ozone layer of the earth absorbs. In addition, these devices are being designed for use in high temperature and caustic environments such as the inside of internal combustion engines, oil wells, military aircraft, satellites, space vehicles and chemical processing plant equipment. Since defects are not mobile in these materials unless they are at very high temperatures ( $> 1,000^{\circ}\text{C}$ ), research is currently underway to produce radiation tolerant devices for space. Devices that could operate in these hostile environments could replace hydraulic and mechanical control systems as heat tolerant in situ control electronics, reducing weight, size, complexity, and fire hazards while increasing reliability.

### II-3 Defects

Defects in SiC can be divided into two groups: shallow and deep. Shallow defects can be modeled hydrogenically and can act as either donors or acceptors depending on their electronic attractive/repulsive nature. Deep level defects lie deeper in the bandgap, are hard to thermally ionize, and cannot be hydrogenically modeled. To date, there are no accurate models for computing the energy levels and capture cross-sections of deep level defects. Therefore, experimental results cannot be compared to theory and must be parametrically studied to identify deep levels. Deep levels can exist in different charge states and excited states leading to multiple energy levels in the bandgap including shallow levels. Site inequivalencies multiply the number of levels, further complicating data analysis. The plethora of sources for deep levels again increases the complexity of studying defects in semiconductors. Defects include point defects such as vacancies, antisites, interstitials, dislocations, substitutional and interstitial impurities, and complexes. Defects can also be created at interfaces and be formed by extended flaws. Complexes include Frenkel pairs, vacancy pairs, and impurity-vacancy defects. To study these defects in SiC, high quality material is essential in order to study intentionally created defects. It has only been in the last few years that the quality of SiC wafers and epitaxy has improved enough to permit limited systematic deep level defect research.

Critical developments in SiC technology have led to a rapid advancement in material quality permitting the fabrication of numerous SiC based electronic test devices. The first major breakthrough was the development of a modification to the Lely sublimation process that allowed fabrication of relatively good quality, single polytypes 6H boules of

substrate material (Lely, 1955). This modification used a porous graphite to pass the sublimated vapor. The current method of boule growth employs a high/low temperature sublimation technique without a graphite filter and produces an even higher quality crystal. These improvements in quality in turn revived the investigation of SiC electronic defects. The improved quality of bulk SiC has also allowed the growth of lattice-matched higher quality epilayers. Epitaxial growth is done by several different methods. The most common methods are variations on chemical vapor deposition (CVD).

The high cost of the bulk and epitaxy SiC material, however, has caused SiC device applications to be restricted to areas where Si or GaAs devices cannot be used due to extreme environmental factors such as high temperature. Since the bulk of SiC research is focused on device development, there is a deficiency in characterizing fundamental properties as well as characterizing the impurities and defects existing in both as-grown and doped material. This deficiency is making it difficult to fabricate SiC devices, which exhibit the superior performance promised by the material's properties.

Early research on the SiC Lely platelets was concentrated mainly on the luminescent properties of various introduced impurities to determine the short wavelength potential of the material as an emitter. The majority of this work was done in the former Soviet Union, where little of this work was published in the West. Early photoluminescence research of 6H-SiC by Choyke and Patrick, and Choyke, Hamilton, and Patrick revealed two series of zero-phonon lines (ZPL) (Choyke and Patrick, 1968). One was a near band-edge (2.99 eV) series of three ZPLs which was determined years later to be due to radiative decay of bound excitons at neutral nitrogen donors. The other series was a deeper

series (2.8 eV) which was studied by Maier *et al.* in 1992 through electron spin resonance (ESR). Maier associated this series to intrinsic titanium complexing with nitrogen and acting as deep trap levels (Maier, 1992).

Since SiC polytypes have inequivalent lattice sites, each donor or acceptor has multiple site-dependent energy levels making defect characterization more complicated. It is the second and third neighbors that are slightly altered causing the crystallographically inequivalent lattice sites. This can be understood by examining Figure II-3, where four polytypes are displayed using the Ramsdell zigzag notation (Verna and Krishna, 1966:87-88). Note the high symmetry of the 3C-SiC polytype and that the 15R-SiC polytype has a shifting stacking sequence unlike polytypes 4H and 6H, whose stacking sequences return to their initial positions after 4 and 6 layers, respectively. The 4H polytype has an equal number of cubic and hexagonal sites while the 6H polytype has twice as many cubic sites than hexagonal sites. Different electronic properties were shown by Choyke and Patrick, (Choyke and Patrick, 1957) Dean and Hartman, (Dean and Hartman, 1979) and Woodbury and Ludwig (Woodbury and Ludwig, 1973) to result from the three inequivalent lattice sites in 6H-SiC. For example, there are three distinct zero phonon lines (ZPLs) associated with exciton recombination at a single impurity type. Two of the sites are nearly equivalent cubic sites (k-sites), so the energy levels can only be distinguished between donor atoms at these quasi-cubic sites (k-sites) and at hexagonal sites (h-sites). The two quasi-cubic sites are labeled  $k_1$  and  $k_2$  and the h-site is labeled h on the 6H-SiC zigzag drawing in Figure II-3. The k-sites exhibit deeper donor levels than the h-site. Acceptor energy levels do not follow the same site dependency. The reason is not yet

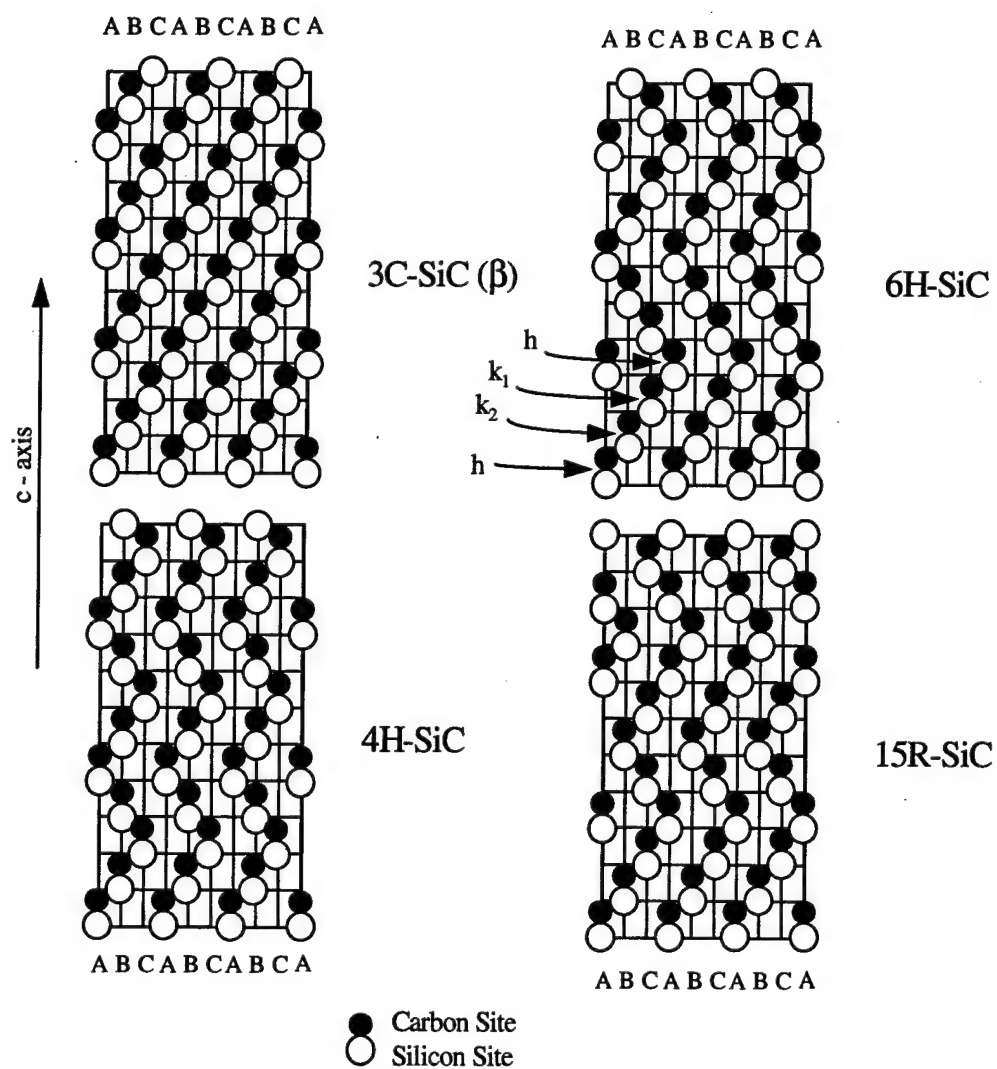


Figure II-3. Representation of the stacking sequence of 3C, 4H, 6H, and 15R-SiC using the Ramsdell zigzag notation with indications of cubic and hexagonal sites.

known. Valley-orbit splitting of nitrogen donors at h-sites and the energy levels of both the ground and excited states at all three electronic sites in 6H-SiC have been measured using Hall effect and IR absorption by Suttrop, Pensl, and Choyke (Suttrop *et al.*, 1992).

Deep level states have also been studied in both n- and p-type SiC. However, most of the measured levels have not been well-characterized, nor correlated to specific defects or impurities and little is known about the defect with energy levels greater than about one electron-volt. Tables II-3 and II-4 give a summary of the published deep levels in 4H- and 6H-SiC to date, respectively. Note that a significant portion of this body of work is for vanadium levels in bulk n-type material. It is also important to note that the different techniques used to characterize these defects can result in significantly different deep level quantities being estimated and it is expected that these deep level defect assignments and values will change with further research.

Even in small concentrations, deep level defects can have significant effects on the electrical and optical properties. They can act as traps or scattering sites, seriously altering the mobility and thermal velocity of free carriers and increase the resistivity of the material. They can act as recombination sites, significantly changing minority carrier lifetimes. The formation and evolution of the defects in SiC are not well understood. No complete systematic studies appear in the literature on defects in SiC. The limited defect studies measure only bits and pieces of information about these defects. Therefore, controlling and exploiting defects in SiC is not yet feasible. This research attempts to clarify and expand on the current knowledge of the formation, evolution, and identification of defects generated through ion implantation and subsequent annealing.

Energy Level	Cross Section	Technique	Defect/ Impurity	Materials	Reference
$E_c - 1.73 \text{ eV}$	n/a	OAS	V	PVT bulk (n)	Evwaraye 1996
$E_c - 1.17 \text{ eV}$	n/a	OAS	?	PVT bulk (n)	Evwaraye 1996
$E_c - 1.13 \text{ eV}$	n/a	OAS	?	PVT bulk (n)	Evwaraye 1996
$E_v + 0.54 \text{ eV}$	--	DLTS/EL	D-center		Anikin 1994
$E_v + 0.5 \text{ eV}$	--	DLTS/EL	i-center		Anikin 1994
$E_c - 0.8 \text{ eV}$	$1.8 \times 10^{-16} \text{ cm}^2$	DLTS/Hall	V	PVT bulk (n)	Jenny 1996
$E_c - 0.60 \text{ to } -0.67 \text{ eV}$	$1 \times 10^{-15} \text{ cm}^2$	DLTS	?	CVD epi (n) Si	Kimoto 1995
$E_c - 0.62 \text{ to } -0.68 \text{ eV}$	$2 \times 10^{-15} \text{ cm}^2$	DLTS	?	CVD epi (n) C	Kimoto 1995
$E_c - 0.6 \text{ eV}$	n/a	Hall	?	epi (n)	Schaffer 1994
OAS – Optical Admittance Spectroscopy			EL – Electroluminescence		
DLTS – Deep Level Transient Spectroscopy			Hall – Hall Effect		
PVT – Physical Vapor Transport			CVD – Chemical Vapor Transport		

Table II-3. Summary of Deep Levels Observed in 4H-SiC

By reviewing the study of deep levels in well-researched semiconductors such as silicon and gallium arsenide, one quickly observes that what first appears as a correct conclusion about a deep level is often changed as more research is accomplished. This evolving understanding forces all initial deep level research results to be viewed as tentative at best. One example of this is the case of the EL2 defect in GaAs. Nearly simultaneously, two articles were published where one concluded that EL2 is the isolated As antisite defect while the other concluded EL2 is not the isolated As antisite defect. In addition to studying deep levels, shallow dopant levels were also studied to gain an understanding of

Energy Level	Cross Section	Technique	Defect/ Impurity	Materials	Reference
$E_v + 1.3 \text{ eV}$	n/a	ESR	$V^{4+}/V^{5+}$ ( $D^0/D^+$ ) (h)	Lely bulk (n)	Schneider 1993
$E_v + 1.6 \text{ eV}$	n/a	ESR	$V^{4+}/V^{5+}$ ( $D^0/D^+$ ) (k)	Lely bulk (n)	Schneider 1993
$E_c - 0.71 \text{ eV}$	$6 \times 10^{-20} \text{ cm}^2$	DLTS	V	sub. bulk (n)	Evwaraye 1993
$E_c - 0.7 \text{ eV}$	n/a	Theory	V	n/a	Stainsy 1992
$E_v + 1.45 \text{ eV}$	n/a	Theory	V	n/a	Stainsy 1992
$E_c - 0.6 \text{ eV}$	n/a	ESR	$Ti_{Si}^{3+}-N_c$ ( $D^0/D^+$ )	Lely bulk (n)	Schneider 1993
$E_c - 0.39 \text{ eV}$	$2 \times 10^{-15} \text{ cm}^2$	DLTS	?	Lely bulk (n)	Jang 1994
$E_c - 0.43 \text{ eV}$	$4 \times 10^{-16} \text{ cm}^2$	DLTS	?	Lely bulk (n)	Jang 1994
$E_c - 0.69 \text{ eV}$	$2 \times 10^{-17} \text{ cm}^2$	DLTS	?	Lely bulk (n)	Jang 1994
$E_c - 0.68 \text{ eV}$	$2 \times 10^{-14} \text{ cm}^2$	DLTS	?	sub. bulk (n)	Uddin 1993
$E_c - 0.71 \text{ eV}$	$5 \times 10^{-14} \text{ cm}^2$	DLTS	?	LPE p/n	Uddin 1993
$E_v + 0.53 \text{ eV}$	--	C-V, I-V-T	Al, C	$SiO_2/p\text{-SiC}$	Raynaud 1994
$E_c - 0.4 \text{ to } -0.54 \text{ eV}$	--	DLTS	Polishing Damage	sub. bulk (n)	Evwaraye 1993
$E_v + 0.61 \text{ eV}$	$1.5 \times 10^{-14} \text{ cm}^2$	DLTS	Al irradiation	Al implant LPE ( $p^+/n$ )	Anikin 1985
$E_v + 0.66 \text{ eV}$	$3 \times 10^{-14} \text{ cm}^2$	DLTS	B	B diffused ( $p/n$ )	Anikin 1985
$E_v + 0.39 \text{ eV}$	--	TSC	B	V doped (p)	Jenny 1995
$E_v + 0.3 \text{ eV}$	$1 \times 10^{-13} \text{ cm}^2$	DLTS	B	B implant epi (p)	Suttrop 1990
$E_v + 0.58 \text{ eV}$	$5 \times 10^{-15} \text{ cm}^2$	DLTS	D-center	B implant epi (p)	Suttrop 1990
$E_v + 0.55 \text{ eV}$	--	--	--	--	Ballando- vich 1991
DLTS – Deep Level Transient Spectroscopy    TSC – Thermally Stimulated Current ESR – Electron Spin Resonance    LPE – Liquid Phase Epitaxy					

Table II-4. Summary of Deep Levels Observed in 6H-SiC



the effectiveness of using ion implantation to dope n-type SiC. Past studies demonstrated 50% activation of nitrogen implants with subsequent anneals up to 1700 °C (Campbell, 1974). It has also been demonstrated that p-type material could be produced by ion implantation of aluminum into n-type material (Palmour, 1993). These implants were performed at room temperature. The properties of the acceptor level formed in the aluminum-implanted material were not investigated. That study was aimed at merely creating a p-n junction through ion implantation. To date, there have not been studies on the effects of high-temperature implantation and annealing on the activation of donor and acceptor implants and on the formation and evolution of deep level defects in epitaxial SiC.

### III ION IMPLANTATION AND ANNEALING

#### III-1 Introduction

Since diffusion of dopants into SiC would require temperatures above 1800 °C (Kroko and Milnes, 1966), thus prohibiting the use of currently available masking techniques, another method is required for the incorporation of foreign ion species into this wide bandgap semiconductor. One doping alternative for SiC is to introduce the dopants during growth. This is fine for producing heterojunctions. However, this technique cannot be used for patterning integrated circuits or other highly geometrically-defined devices. In addition, this method does not permit the controlled formation of defects that may be used to produce compensated material. In addition, masking and etching techniques used in silicon device technology is severely hampered in SiC due to SiC's extremely high resistance to chemical etching. The only remaining method for doping this wide bandgap semiconductor is ion implantation.

In ion implantation, ionized atoms or molecules are accelerated and implanted into a solid. The variation in ion species, dose, and energy create a wide range of possible implantations. Since implantation is a nonequilibrium process, implant concentrations can exceed chemical solubility limits. The ion implant energies can range from less than a thousand electron-volts (keV) to hundreds of millions of electron-volts (MeV). The depth of ion penetration depends on both the mass and energy of the ion species as well as the target material. Implant peak concentration depths can range from less than 100 Å

to several microns. As the dose of the implanted ions is increased, most of the target's properties will be altered at and near the surface.

Over the past three decades, ion implantation has been developed into an effective method for doping semiconductors such as silicon and gallium arsenide, replacing some of the more common processes like doping during epitaxy, diffusion, and alloying. Ion implantation has the advantages of being nearly independent of chemical solubility limits and surface dopant concentration. For relatively narrow bandgap material ( $< 2$  eV), ion implantation is insensitive to implant temperatures being raised several hundreds of degrees Celsius above room temperature. However, implantation temperature may be an important parameter for SiC, a strongly bonded wide bandgap semiconductor. Research has shown that implantation temperature can have a significant effect on damage recovery rates during implantation on diamond - another strongly bonded wide bandgap semiconductor (Prins, 1991 and 1992).

The concentration profiles of the implanted species have a general Gaussian distribution, with an average projected range  $R_p$  and a standard deviation  $\Delta R_p$ . Skewing of the distributions does occur and profiles can be estimated using available validated models.

The advantages of ion implantation over other doping methods include:

1. Speed, homogeneity, and reproducibility of the doping process
2. Exact controllability of the number of doping atoms introduced, by simple current integration, which is especially important for low concentrations (e.g., threshold-voltage adjustment of MOS transistors).

3. Lower requirements for the purity of the dopants, since they are separated according to their mass.
4. Avoidance of high processing temperatures during implantation.
5. Simple masking methods, for example, with the use of thick layers of oxide, nitride, metal or photoresist.
6. Possibility of doping through thin passivating layers (e.g.,  $\text{SiO}_2$ ,  $\text{Si}_3\text{N}_4$ ).
7. Low penetration depth of the ions (in general, less than a few microns); it is possible to dope shallow layers with very high doping gradients (e.g., IMPATT diodes, microwave transistors, Ohmic contact formation).
8. Multiple implantations by changing the accelerator voltage during implantation makes possible a relatively free choice of the doping profile, whereby one is not limited to the near Gaussian shape.
9. Because of the minimal lateral scattering, it is possible to fabricate devices with very small dimensions and to keep parasitic capacitance low. (Ryssel and Ruge, 1986)

This doping method is not, however, without its difficulties. Ion implantation has several disadvantages that must be accounted for:

1. As a result of bombardment with heavy particles, radiation damage is produced. This damage is normally undesired since it causes changes in the semiconductor's electrical properties.

2. Most of the doping atoms do not come to rest after implantation on regular lattice sites, and are not usually electrically active. This necessitates a suitable high temperature treatment (annealing) to restore the crystal lattice and reposition the introduced atoms to electrically active lattice sites.
3. Doping by implantation is limited to layers near the surface. Although greater penetration depths can be achieved with higher acceleration voltages, the electrical properties of the layers thus produced are not yet satisfactory.
4. Due to additional effects during or after implantation (e.g., channeling, diffusion), it is not always possible to obtain the theoretically predicted profile. In most cases, such effects are manifested by a deeper than desired penetration of the doping atoms (Ryssel and Ruge, 1986).

Currently available processes for repairing damage and activating sites include furnace, laser, and rapid-thermal annealing (RTA). The temperature, energy, environment and duration parameters for these different processes must be investigated and characterized before ion implantation procedures can be as effective in doping SiC as is currently the case for silicon and gallium arsenide. Another technique for controlling the formation and effects of deep level defects is co-doping. Co-doping is the process of incorporating multiple ion species into the semiconductor. This method has been used in other semi-

conductors to create complexes with deep level defects thus altering their energy level and electrical effects.

When investigating ion implantation of SiC, important questions need to be answered, including: "What is the formation and evolution of radiation damage?"; "What is the optimum procedure to electrically activate the implanted atoms?"; "What is the resulting dopant profile?"; and "What are the effects of implantation on fundamental electrical material properties such as mobility and lifetime?". Ion implantation has been developed for other uses besides doping semiconductors. However, those areas won't be discussed here since they are outside the area of this dissertation research.

As a historical footnote, the first patented ion implantation technique was obtained by Shockley in 1957 where he pointed out for the first time the requirement for post annealing to restore the crystal lattice (Shockley, 1957). Additional work on implantation soon followed including phosphorus-implanted silicon used in nuclear-radiation detectors; implantation of solar cells; theoretical profiles of ions in solids; and channeling studies. Currently, ion implantation is quite common in device fabrication such as GaAs integrated circuits.

### III-2 Ion Implantation Theory

The investigations of the range of implanted ions in solids goes back to Lenard and Rutherford in 1900, which gave the first indications of the nucleus and shell structure of the atom. Bohr went on to calculate the energy loss for heavy particles based on particle-bound electron collisions (Bohr, 1915). He obtained, the energy loss per path length to be:

$$-\frac{dE}{dx} = \frac{4\pi Z_1^2 q^4 N Z_2}{m_e v^2} \left[ \ln \frac{1.123 M m_e v_1^3}{\bar{\omega} Z_1 q^2 (M_1 + m_e)} - \ln(1-\beta^2) - \beta^2 \right],$$

where  $Z_1$  and  $v$  are the charge number and the ion velocity, respectively,  $Z_2$  and  $N$  are the atomic number and the atomic density of the target atoms, respectively, and  $m_e$  and  $q$  are the electron mass and charge, respectively. Also,  $\ln \bar{\omega} = \sum f_i \ln w_i$ , where  $f_i$  and  $w_i$  are the strength of the oscillator and frequency of the  $i^{\text{th}}$  electron, respectively, and  $\beta = v/c_0$ , where  $c_0$  is the velocity of light. Later work by and Blocke developed more realistic expressions including quantum-mechanical considerations (Bethe, 1932:325). However, both expressions considered only the stopping by collisions with electrons excluding the effect of collisions with nuclei or whole atoms.

The different types of collisions occurring during implantation are:

1. Inelastic collisions with bound electrons of the stopping medium. The energy loss in such collisions takes place by excitation or ionization of atoms or molecules.

2. Inelastic collisions with nuclei. These lead to *bremßstrahlung*, nuclear excitation, or nuclear reactions.
3. Elastic collisions with bound electrons.
4. Elastic collisions with nuclei or whole atoms, whereby a part of the kinetic energy is transferred to the particles absorbing the impact.
5. Cerenkov (CEPEHKOB) radiation. This is produced by particles that pass through the medium faster than the phase velocity of light (Ryssel and Ruge, 1986).

The dominating collision process depends chiefly on the energy and the mass of the ion species, and the mass and atomic number of the target atoms. For the energy ranges used for the ion implantation of semiconductors, the only significant collision types are inelastic collisions with electrons and elastic collisions with nuclei. Figure III-1 shows the relative stopping power for electronic and nuclear collisions with both free and bound electrons. As seen from the figure, it is not until the implanted ions have slowed down significantly that the dominating stopping process switches to collisions with the nuclei.

In 1963, the energy range of ion implantation was theoretically investigated by Lindhart, Scharff, and Schiøtt (LSS) (Lindhart, Scharff, and Schiøtt, 1963). Their theory (LSS theory) gives the implanted ions a Gaussian distribution around an average projected range  $R_p$ , with a standard deviation  $\Delta R_p$ . Others have expanded on this theory, calculating the energy distribution for the stopping process instead of developing integral expressions for the range distribution and standard deviation. This makes the model more use-



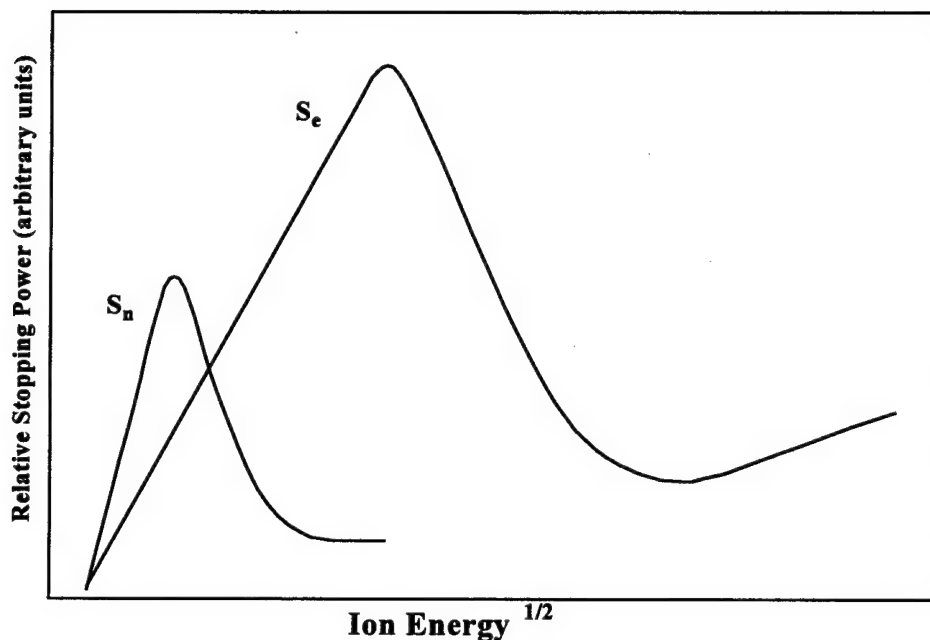


Figure III-1. Stopping powers  $S_e$  and  $S_n$  as a function of ion energy (arbitrary scale)

ful for multi-layered structures, but diffusion effects are still ignored (Brice, 1971) (Furukawa, 1972). These models also do not deal with the effects of the stopping process upon the semiconductor target.

During the stopping process, the target material undergoes 'radiation damage' through the destruction of the lattice. This alteration of the material manifests itself in the material properties (e.g., density, elasticity, resistivity, etc.). In this research, we are only concerned with changes in the target material's electrical and optical properties.

Not only is there a distribution of the stopped ions, there is also a distribution of radiation damage. Not surprisingly, these two distributions need not coincide since the position at which the maximum energy is deposited need not be the position at which the

ions also come to rest. We can expect the maximum of the radiation damage distribution to be nearer the surface than the ion distribution peak. The separation distance of these two distribution peaks will depend on the relative mass of the ion compared to the target atom.

Figure III-2 illustrates the formation of radiation damage where (a) represents the damage formation from a lighter implanted ion than the target atoms and (b) represents the damage formation from a heavier implanted ion than the target atoms. The lighter

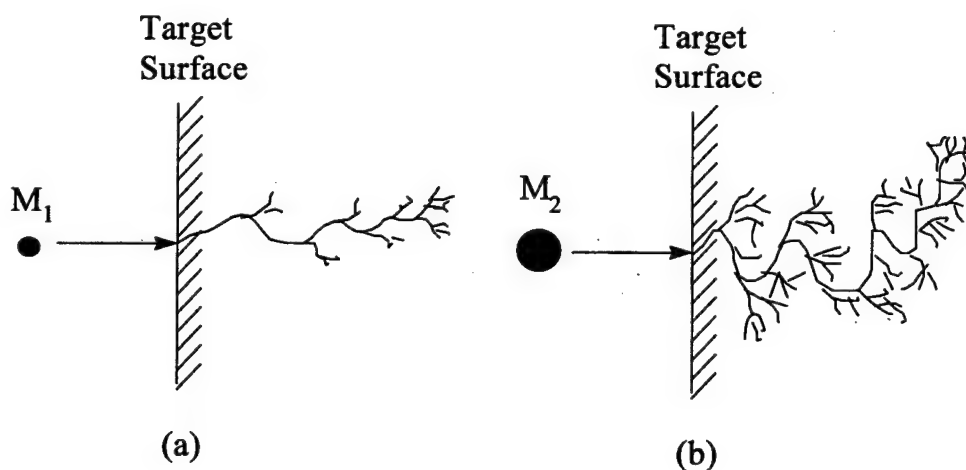


Figure III-2. Damage generation dependence on mass of implanted ion, (a) light ion and (b) heavy ion relative to semiconductor constituent atoms.

ions mostly produce discrete damage sites while the heavier ions produce additional nearby damage forming damage paths or clusters. As the implantation dose is increased, the concentration can become so high that these damage regions overlap and the crystal

loses its long-range order. For this study, the implantation doses were kept at least two orders of magnitude below the amorphous limit. The displaced atoms can also displace additional target atoms resulting in a cascade effect. If the displacement distance is not too great, the vacancy and the displaced atom can interact through coulombic forces forming a Frenkel pair defect.

Considering the independence of only the two significant types of collisions (ions with free and bound electrons and ions with atomic nuclei), we obtain the energy loss per unit length as:

$$-\frac{dE}{dx} = N[S_n(E) + S_e(E)]$$

where  $N$  is the atomic density of the target material, and  $S_n$  and  $S_e$  are the stopping power of the nuclei and electrons, respectively. Integrating from the implant energy ( $E$ ) to zero would produce:

$$R = \frac{1}{N} \int_0^E \frac{dE}{S_n(E) + S_e(E)}$$

where  $R$  is the average range of a particle of energy  $E$  (Ryssel and Ruge, 1986).

For nuclear collisions, the energy loss  $dE$  in a layer  $dx$ , is proportional to the atomic density  $N$  and to the total energy transferred in all individual collisions  $T_n$  (Ryssel and Ruge, 1986):

$$S_n(E) = -\frac{1}{N} \left( \frac{dE}{dx} \right)_n = \int_0^\infty T_n(E, p) 2\pi p dp = \int_0^{T_n} d\sigma(E, T_n)$$

where  $d\sigma$  is the differential cross-section ( $d\sigma = 2\pi p dp$ ), and  $p$  is the impact parameter, and the value  $T_m$  is the maximum transferable energy for a central collision. Using well-

known classical mechanics equations for scattering, analytical solutions for the power potentials, and taking into account electron screening (since the ions are relatively slow), experimentally agreeable values are obtained for the energy dependent stopping power  $S_n$  for all ion-target combinations. The differential cross-section for nuclear scattering is given by the approximating function (Ryssel and Ruge, 1986):

$$\frac{d\sigma}{dt} = 2\pi a^2 t^{3/2} f(t^{1/2}),$$

where values for the universal scattering function,  $f(t^{1/2})$ , are given by LSS in tabular form.

For electronic collisions, stopping decreases with increasing ion velocity at high energies as shown in Fig. III-1. In the lower energy region, the electrons are modeled as a free electron gas, and the stopping cross-section is proportional to the ion velocity or the square root of the energy (Ryssel and Ruge, 1986):

$$S_e(E) = -\frac{1}{N} \left( \frac{dE}{dx} \right) = k'E^{1/2},$$

$$k' = \frac{kC_R}{C_E^{1/2}N}, \text{ and}$$

$$k = \xi_e \frac{0.0793 Z_1^{1/2} Z_2^{1/2} (A_1 + A_2)^{3/2}}{(Z_1^{2/3} + Z_2^{2/3})^{3/4} A_1^{3/2} A_2^{1/2}},$$

where  $\xi_e$  is a dimensionless constant of the magnitude  $Z^{1/6}$ ,  $C_R$  and  $C_E$  are obtained from the scattering parameter, and  $A_1$  and  $A_2$  are the atomic weights of the ion and target, re-

spectively. The values of  $k$  are generally between 0.1 and 0.25. From these two collisional models, range distributions can be calculated (Ryssel and Ruge, 1986).

Additional effects should be taken into account to improve the accuracy of the calculated distribution. These include channeling, surface sputtering, and the back-scattering of ions. For this study, the LSS distribution model was used by running a previously developed Fortran code (called P87.exe) which also computes skewness, kurtosis and takes into account both channeling and surface sputtering. The departure from the Gaussian profile is modeled through the incorporation of the higher order moments leading to a more realistic profile. One effect that is neglected in the code is the back-scattering of ions. Fortunately, the error caused by this effect is minimal for the energies used in this study. Back-scattered ions can be significant for much lower energy implantations. Accounting for this effect would require a Monte Carlo approach and for most cases, it can be neglected. Another effect not accounted for is ion diffusion. For this study, the implanted ions do not diffuse significantly below 1800 °C. Secondary ion mass spectroscopy (SIMS) performed on a few samples validated the implant distributions predicted using the P87.exe code.

Ion implantation has been developed into an alternative method for the incorporating of dopants and point defect into semiconductor material such as silicon and gallium arsenide. By appropriate masking, complex device structure can be produced. Unfortunately, when ions are implanted two, usually undesirable, conditions are generated. The first condition is that the implanted ions do not come to rest at electrically active sites. The second condition is that significant concentrations of undesirable damage defects are

generated in the semiconductor. These conditions necessitate a post-implantation process to activate the implanted species and repair the lattice structure.

### III-3 Defects

Even before the ion implantation process, the target material contains various point and extended defects. These intrinsic defects are the result of the lack of purity in the growth materials, impurity in the growth environment and an imperfect growth process. Efforts are continuously made by the growers to improve these three areas to lower the concentration of undesired defects in the semiconductor. After ion implantation is completed, the target material contains an increased concentration of various types of defects in the near-surface region. Not only are there substitutionally and interstitially positioned implanted ions, but there are also antisite defects and interstitial host atoms due to recoiling host atoms from nuclear interaction. In addition, these interactions create vacancies and complexes during implantation. The variety of defects increases the difficulty in identification of the deep level defects created by ion implantation.

These vacancy, interstitial, and substitutional defects are disruptions to the periodicity of the lattice and thus form defect energy levels, some of which can lie within the band gap. The activation energies of these defects can vary from a few millielectron-volts (meV) to several electron-volts (eV). Those levels that lie close to either the conduction or valence band can be approximated by a hydrogenic model. Unfortunately, no model currently exists that can accurately model the deeper levels. This inability to model deeper levels is the major reason why extensive research must be accomplished before a deep level's true identity is revealed.

To create a vacancy, sufficient energy must be added to a host atom to overcome the binding energy of the lattice. This can be viewed as a potential well of depth  $E_{v.f.}$ . By increasing the temperature of the semiconductor, the lattice vibrations may be amplified until the vibratory excursions surmount this barrier energy. Using Maxwell-Boltzmann statistics for occupancy of a given energy level at a defined temperature, the frequency of success can be computed as (Ryssel and Ruge, 1986):

$$\nu_f = \nu_{f0} \exp \frac{-E_{v.f.}}{kT},$$

where  $\nu_{f0}$  is the zero temperature frequency. There also exists a rate of refilling for these thermally generated vacancies which is proportional to the number density of vacancies. In equilibrium, for  $N$  atoms per unit volume, there will be a production rate of

$$N_{vf} = N\nu_{f0} \exp \frac{-E_{v.f.}}{kT},$$

and a relaxation rate of neighboring atoms proportional to the number of vacancies per unit volume  $n_v$ , so that (Ryssel and Ruge, 1986)

$$Cn_v = N\nu_{f0} \exp \frac{-E_{v.f.}}{kT}.$$

The vacancy concentration in equilibrium is thus given by

$$\frac{n_v}{N} = \exp \frac{-E_{v.f.}}{kT},$$

as  $\nu_0/C$  is on the order of unity. The potential energy can be estimated from knowledge of elastic constants of the solid, or from more fundamental computations from known or realistically-assumed interatomic force laws. It turns out that for an energy of 1 eV, the room temperature vacancy concentration ratio is estimated to be just 1 in  $10^{17}$ , while for 2



eV, the concentration ratio is only 1 in  $10^{34}$ . Two electron-volts is the estimated vacancy potential energy in silicon. By raising the temperature, these concentrations can be significantly increased. At 1000 K, silicon would have vacancies on the order of 1 in  $10^{12}$  (Carter and Grant, 1976:107). If the vacancy potential energy in SiC were twice that of silicon, the vacancy ratio at 1000 K would be on the order of 1 in  $10^{32}$ . Thus, the formation and elimination of vacancies can be thermally manipulated but with much less effect in the more strongly bonded SiC. Reduction in vacancies by thermal treatment also depends on the mobility of these defects and the interstitial atoms. The vacancies must have a high probability to wander through the lattice and encounter excess atoms. The rate of vacancy migration by thermal means is given by a Boltzmann probability function similar to the one previously used for vacancy formation:

$$\frac{N_{vm}}{m} = \frac{N_{vmo}}{m} \exp \frac{-E_{v.m.}}{kT},$$

where  $E_{v.m.}$  is the migration energy. The rate of formation and migration is then merely the product of the rates:

$$\nu = \nu_o \exp \frac{(E_{v.f.} + E_{v.m.})}{kT}$$

This energy sum is known as the energy of self-diffusion. Theoretical calculations estimate this energy to be on the order of 1 eV for elemental semiconductors so that at room temperature, each vacancy only migrates once every  $10^4$  seconds. While at 1000K, this number drops to  $10^{-8}$  seconds. For SiC, the self-diffusion energy is not known. However, it is undoubtedly significantly higher than 1 eV. If a semiconductor is rapidly cooled, these vacancy concentrations can be locked-in, thus suggesting that the annealing should

be terminated with a relatively slow cool-down rate. For this study, the rate of cooling to room temperature was on the order of ten minutes and thus it is believed that the locking-in of vacancies was avoided.

During migration, vacancies may cluster together forming stable complexes. In radiation disordered semiconductors, divacancies are a favored configuration. These energies are also dependent on the charged state of the vacancy and are usually significantly smaller. Another possible configuration is the complexing of these vacancies with other defects such as the implanted atoms.

In silicon, the temperatures at which the different defects are annealed have been extensively studied. The formation and annealing temperatures for intrinsic defects for n-type silicon found by J. Corbett are illustrated in Fig. III-3 (Chadderton and Eisen,

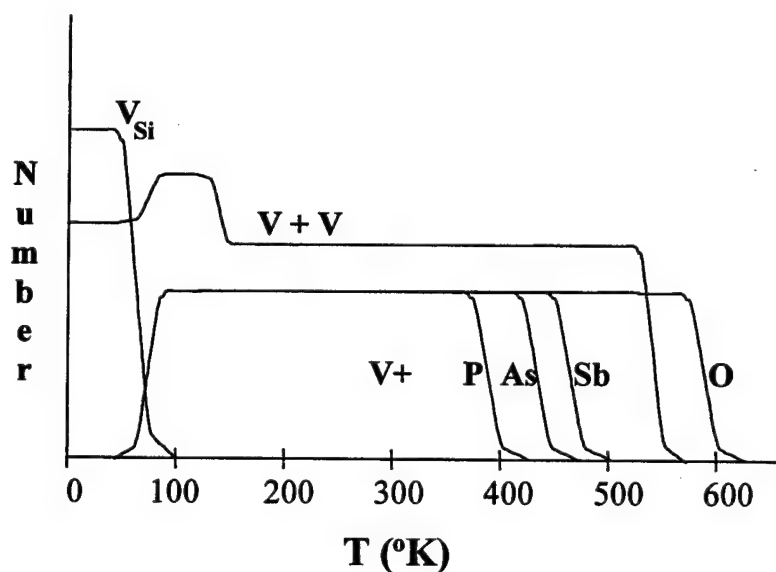


Figure III-3. Order of formation and loss of defects in n-type silicon.

1971:445). The first defect to be annealed is the silicon vacancy ( $V_{\text{si}}$ ) at 75 K. This coincides with the formation of both divacancies ( $V + V$ ) and vacancy-impurity pairs ( $V + P$ ,  $V + \text{As}$ ,  $V + \text{Sb}$ ,  $V + \text{O}$ ). At around 140 K, the divacancy effect is reversed, stabilizing out to 550 K, where it is fully annealed. The anneal temperature for the vacancy-impurity defects depends strongly on the impurity. The formation and annealing temperatures for the intrinsic defects in n-type SiC are not known. However, one can use the ordering in n-type silicon as a starting point. For example, it would be likely that the  $V_{\text{si}}-V_{\text{c}}$  defect would anneal at a higher temperature than either  $V_{\text{si}}$  or  $V_{\text{c}}$ . One could also speculate that the  $V_{\text{c}}$  defect would anneal at a lower temperature than  $V_{\text{si}}$  since the  $V_{\text{c}}$  defect in SiC would have a local environment similar to  $V_{\text{si}}$  in silicon while the  $V_{\text{si}}$  defect in SiC would have a local environment similar to  $V_{\text{c}}$  in diamond which requires a larger energy to mobilize than the  $V_{\text{si}}$  defect in silicon. Unfortunately, these types of correlations to the effects found in other similar materials is highly speculative at best and should only be used to suggest future material studies.

Defect levels are identified with multiple techniques and uniquely prepared samples to verify or eliminate any site assignment candidates. These techniques can be grouped as follows: luminescence, optical absorption, photoconductivity, acoustic paramagnetic resonance, Mossbauer spectroscopy, Hall effect, and junction techniques. This study employed luminescence, Hall effect, and junction techniques.

In the 1960's, the identification of radiation-induced defects was a major research effort while deep level impurities were hardly studied. The typical assumption was to assign the measured deep levels to the diffused impurity, usually at substitutional sites. In

the next decade, it became clear that this simplistic approach to deep level assignment had serious problems. It was observed that many deep levels in concentrations of similar order to those found in diffused impurity samples could be found in non-diffused samples merely by applying the same heat treatment used during the diffusion processes. Another problem is the formation of complexes and the formation of both acceptor and donor levels by a single impurity. By reading a portion of the volumes of articles on impurity and defect centers, it becomes clear that no two systems are exactly alike and no general prescription for quick identification is possible.

Researchers have learned that isotopic implants are powerful tools for identifying centers. By measuring small but observable shifts in the vibrational spectra, and the temporal shifts in the amplitudes of concentration-related measurements such as rate window peak heights in DLTS (Achtiger and Witthuhn, 1997), defect center assignments could be made. Even when the chemical impurity is associated to a level, a significant amount of research is still required to understand the atomic and electronic structural details. Cross-correlation of data is used to build a consistent model that explains the various observed characteristics of a center.

When a defect is formed in the lattice, the surrounding lattice will be distorted, changing the local environment. There are two ways for the lattice to relax: symmetry-preserving (breathing mode) and symmetry-breaking. In symmetry-preserving, the surrounding atoms can breathe either toward or away from the defect. If the atoms move toward the defect, stronger bonds are formed among the dangling hybrid-orbitals. This movement also weakens the back bonds. In the reverse case of moving away, the oppo-

site bond strength changes occur. Accurately predicting which symmetrical distortion will take place is still not possible, though calculations have been made with mixed results for other systems (Bar-Yam and Joannopoulos, 1984) (Scheffler, 1982) (Lindefelt, 1983) (Lindefelt and Zunger, 1984) (Baraff and Schluter, 1983) (Baraff and Schluter, 1984). Lattice relaxations that break the lattice symmetry have been associated with several cases. Two major causes are Jahn-Teller and pseudo-Jahn-Teller instability effects. Jahn-Teller instability is a localized system in an orbitally degenerate state that spontaneously distorts and lowers its symmetry until the final state is reached having no orbital degeneracy. The orbital degeneracy is replaced with orientational degeneracy. This is the case for the neutral vacancy in silicon for its ground state. The final state is an orbital singlet, with three possible orientations for the distortion. Symmetry-breaking distortions also take place without the initial undistorted state being orbital degenerate. For example, the ground state of substitutional nitrogen in diamond exists without undistorted orbital degeneracy but still undergoes a Jahn-Teller distortion.

As one can see, the complexity of predicting, modeling and identifying defects is greatly increased when researching deep level defects than when dealing with shallow level defects. Many different experimental techniques must be employed to sort through the possible candidates before a deep level defect can be definitively identified. This research focuses on both the formation of deep level defects in n-type 6H-SiC and the activation of implanted donor atoms in n-type 4H-SiC - both ion implanted at high temperatures.

## IV CHARACTERIZATION TECHNIQUES

### IV-1 Introduction

In this study, various electrical and optical characterization techniques were employed to measure the properties of both as-grown and ion implanted epitaxial 4H- and 6H-SiC polytypes. The results from these measurements were cross-correlated to construct a clearer understanding of donor activation; deep level trap formation and evolution; trapping mechanisms; and their impact on the electrical properties of the epitaxial material. For the electrical measurements, the sample devices were made by forming either p-n or Schottky junctions using epitaxial 4H- and 6H-SiC polytypes, respectively.

Electrical characterization techniques included several different deep level transient spectroscopies (DLTS), Hall effect measurements, current-voltage-temperature (I-V-T) and capacitance-voltage (C-V) measurements. The optical characterization technique used was cathodoluminescence (CL). These measurements were needed to understand the effects of high temperature implantations and annealing on the incorporation of dopants and formation and evolution of defects in the material.

The principal electrical characterization parameters measured or computed from measurements included resistivity ( $\sigma$ ); mobility ( $\mu$ ); free carrier density ( $n$ ); apparent sheet carrier concentration ( $n_s$ ); total impurity density ( $N_D - N_A$ ); donor energy level ( $E_D$ ); doping depth profile ( $N(x)$ ); deep state density ( $N_t$ ); deep state capture cross-section ( $\sigma_t$ ); deep state energy level ( $E_t$ ); anneal temperature ( $T_A$ ); and deep state concentration depth profile ( $N_t(x)$ ). Electrical properties of semiconductors are determined by the chemical composi-

tion of the crystal; its lattice defects such as chemical impurities; interstitials, vacancies, and antisites; and its crystal dimensions. Very small concentrations of defects or impurities can significantly affect the electrical properties of a semiconductor. Their electronic effects are determined by their site location, chemical identity, bonding in the crystal lattice, charge state, and interaction with other impurities and defects. Device performance is a direct consequence of the electrical properties of the materials. Therefore, measurements of these properties and subsequent association to defects and impurities are vital to producing high quality electronic devices. Electrical characterizations were accomplished chiefly through DLTS and Hall effect measurements. I-V-T and C-V techniques were also used to select the best functioning diodes for examination, to measure doping concentration profiles, and to characterize current mechanisms.

The cathodoluminescence (CL) studies were performed to examine implantation and annealing effects on radiative recombination centers and correlate the results of other measured effects, whenever possible. When electron-hole pairs recombine or when electrons or holes are trapped, conservation laws require that energy be conserved, possibly resulting in an optical emission. At room temperature, the probability is much higher that phonons will be generated instead of photons during trapping and recombination events. By lowering the temperature of the sample, the probability of photon generation can be increased. This can be understood by studying the quantum mechanical probability dependence on temperature for the occupation numbers of the normal modes (Blakemore, 1987:196-213). As the temperature is lowered, both phonon and Auger mechanisms will decrease in probability. This does not occur to the extent that the photon emission probabilities exceed those of lattice vibrational or collisional probabilities. It just means that

the probability of photon generation may be sufficiently large enough to permit optical detection.

Optical characterization parameters included cathodoluminescence and photoluminescence spectra recorded at various sample temperatures, CL beam intensities and CL beam energies. These spectra showed evidence of site activation and damage recovery in the ion implanted and annealed 4H-SiC epitaxial semiconductors.



## IV-2 Deep Level Transient Spectroscopy

If the concentration of a deep state impurity is so large that it determines the Fermi level position over a certain temperature range, then its activation energy and concentration can be computed from a temperature-dependent Hall effect measurement. However, when the concentration of deep level defects are less than about 10% of the compensated donor or acceptor concentration, Hall effect measurements can only measure the parameters associated with the shallower dopant and cannot be employed to characterize deep level defects. One must use a more sensitive technique such as Deep Level Transient Spectroscopy (DLTS). DLTS was developed in 1974 by D.V. Lang (Lang, 1974). Before 1974, deep states were detected by detrapping techniques like thermally stimulated current (TSC) and capacitance (TSCAP), or by directly recording the capacitance or current transients as a function of time. Since 1974, over 27 variations of DLTS have subsequently been developed for application in a variety of specific conditions. The fundamental concept of all these variations is the transient behavior of the filling and emptying of the defect sites either by thermal or optical stimulation. The methods used in this study were limited to constant-voltage DLTS (CV-DLTS), constant-capacitance DLTS (CC-DLTS), and double-correlated DLTS (DDLTS). Each of these techniques measure the transient capacitance or voltage with the diode sample in reverse bias (depletion). There are several advantages for using depletion region techniques:

- 1) the charge transients on deep states in the depletion region can be monitored by measuring the depletion capacitance or the diode current.

- 2) the measurements are very sensitive – ratio of values can be as low as  $(N_t/N_d) \sim 10^{-5}$ , where  $N_t$  is the trap concentration and  $N_d$  is the donor concentration.
- 3) trap response is determined by more than one process, so in depletion the capture process can be suppressed.
- 4) trap filling by majority carriers can be induced by lowering the reverse bias and readmitting electrons to the observation region.
- 5) by controlling the bias during trap filling and emptying, the spatial extent of the observation region can be controlled and depth profiling is possible.
- 6) by controlling the bias during trap filling and emptying, the electric field strength in the depletion region can be controlled which allows characterization of the trap's charge state.

In DLTS, the material being studied is fabricated into a junction device, either a Schottky or p-n junction diode. For the p-n diode, one side is heavily doped relative to the side being studied. This allows a depletion region to be formed mainly in the lightly doped side with an applied reverse bias. Uniform doping is preferred as this allows the depletion depth to vary proportionally to the square root of the applied voltage. This device design is known as a one-sided abrupt junction. A Schottky diode differs from a p-n diode by the replacement of the higher doped side with a rectifying metal contact. All calculations associated with DLTS apply to both types of diodes. To date, there is still no satisfactory theory for calculating the observed electronic properties of deep states and so indirect correlations with device processing are used to assign these levels to specific cen-

ters. DLTS is thus used, not only to measure their activation energy, effective capture cross-section, and relative concentration, but also to identify the most likely constituents forming the specific deep state.

Double-correlated deep level transient spectroscopy (DDLTS) is used to probe the depletion region. Probing the depletion region permits the development of a concentration profile of the deep level defects, and permits measuring the effect of the electric field on the trapping kinetics of the deep level defects. Constant capacitance deep level transient spectroscopy (CC-DLTS) is used to measure interface state densities and is used when the deep level density is not an order of magnitude lower than the dopant density. Deep state concentrations and properties are important for overall quality characterization, for understanding speed of response limits, and for establishing the influence of the defects and impurity centers in carrier recombination.

Figure IV-1 illustrates the device geometry for the tested 6H-SiC material. For this study, Schottky diodes were used for the 6H-SiC material. A single backside ohmic contact (aluminum) was made on the substrate side of the diodes. Schottky contacts were made by patterning a rectifying metal alloy dot array (nickel) onto the implanted epilayer.

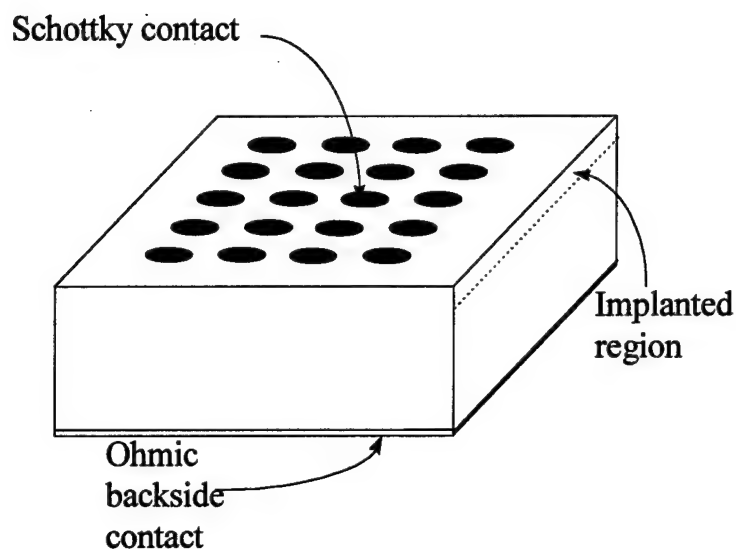


Figure IV-1. DLTS sample configuration where the Schottky contacts were formed on 6H-SiC material.

In DLTS measurements for a majority carrier trap, a diode is placed in reverse bias creating a depletion region. A slight forward bias is then applied to collapse the region and the traps in the former depletion region are filled as the Fermi level is raised above the trap energy level. Once the traps are filled, the reverse bias is reestablished, reforming the depletion region that now contains filled traps. This is illustrated in Figure IV-2. These traps then proceed to thermally emit the trapped carriers until they are again all empty. The nonzero electric field in the depletion region sweeps the emitted carriers away before they can be recaptured by the traps.

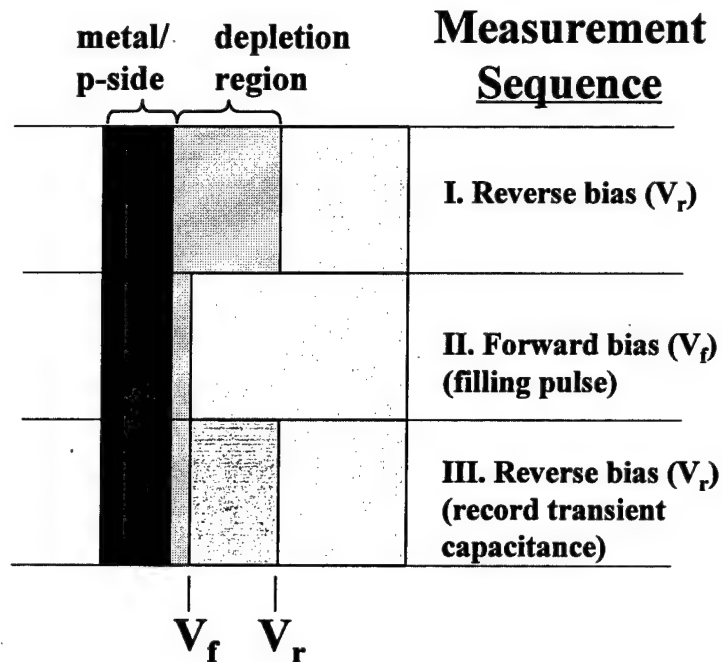


Figure IV-2. Sequence of a DLTS measurement.

The rates at which these traps are emptied are related to the trap energy level and capture cross-section, and the temperature of the sample via the solution to the rate equation of the filled traps. There are four processes that determine the dynamic electronic behavior of a deep state: capture and emission of holes, and capture and emission of electrons. If the total concentration of deep centers is  $N_t$  and  $n_t$  of these are occupied by electrons, then the electron capture rate per unoccupied state is

$$c_n = (\Delta n_t / \Delta t) / (N_t - n_t) = \sigma_n \langle v_n \rangle n,$$

where  $\sigma_n$  is the capture cross section for electrons,  $\langle v_n \rangle$  is the free electron rms (root-mean-square) thermal velocity, and  $n$  is the free carrier concentration. The delta quotient

term,  $(\Delta n_t / \Delta t)$ , is the rate of change of the occupied concentration ( $n_t$ ). A similar expression can be written for the capture rate of holes per occupied state,

$$c_p = \Delta(N_t - n_t) / (n_t \Delta t) = \sigma_p \langle v_p \rangle p.$$

The capture rate, per carrier, is related to the minority carrier lifetime through the recombination of electrons and holes at the deep state. Therefore, for p-type material, the lifetime of minority electrons is

$$\tau_n^{-1} = \Delta n_t / (n \Delta t),$$

and the non-radiative lifetime associated with deep state electron capture is

$$\tau_{nr}^{-1} = \sigma_n \langle v_n \rangle (N_t - n_t).$$

For low injection, the high capture rate of minority carriers (holes) ensures that the majority of states are empty. Therefore, in steady state,  $n_t = 0$  and the lifetime can be written

$$\tau_{nr}^{-1} = \sigma_n \langle v_n \rangle N_t.$$

This is how the capture cross-section and trap density control the lifetime.

Competing capture and emission processes determine the occupancy of the state. The net rate of change of electron occupancy is

$$dn_t/dt = (c_n + e_p)(N_t - n_t) - (c_p + e_n)n_t,$$

where  $e_n$  and  $e_p$  are the respective electron and hole emission rates (Blood and Orton, 1992).

Figure IV-3 illustrates these processes for n-type material. If  $N_t$  is small compared to the net doping concentration ( $N_d - N_a$ ),  $n$  and  $p$  can be assumed to be constant and the rate equation solution can be obtained for the appropriate initial and final conditions of the experiment. If  $N_t$  is comparable to ( $N_d - N_a$ ),  $n$  and  $p$  are time dependent and now we

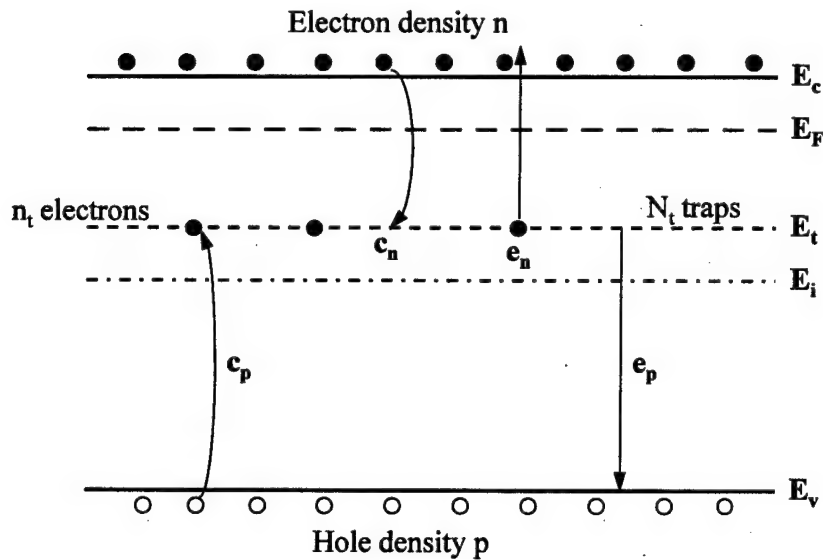


Figure IV-3. Emission and capture processes in n-type material

have three coupled differential equations. In thermal equilibrium, not only does  $dn_t/dt = 0$ , but the principle of detailed balance must also be satisfied where the rate of emission and capture of electrons must be equal, and likewise for holes.

This prevents the net transfer of electrons from one band to the other. From this one gets

$$e_n n_t = c_n (N_t - n_t) \quad \text{and} \quad e_p (N_t - n_t) = c_p n_t,$$

so that the thermal equilibrium occupancy of the trap is

$$n_t/N_t = c_n/(c_n + e_n) = e_p/(e_p + c_p).$$

Combined with the thermal equilibrium occupancy defined by the Fermi-Dirac distribution function for a deep state with energy  $E_t$ , empty state degeneracy  $g_0$ , and filled state degeneracy  $g_1$ , we get

$$e_n/c_n = (g_0/g_1)\exp[(E_t - E_F)/kT],$$

and for hole emission

$$e_p/c_p = (g_1/g_0)\exp[(E_F - E_t)/kT].$$

Since the ratio of degeneracies is about unity, when  $E_F$  is greater than  $E_t$ , the traps are filled and when  $E_F$  is less than  $E_t$ , the traps are empty. When  $E_F$  is equal to  $E_t$ , the traps are half-filled (or half-empty, like the glass of water). This Fermi level dependence is due to the free carrier concentration dependence on the location of the Fermi level.

Deep states may trap more than one electron. On the energy diagram this is represented as multiple trap energy levels,  $E_{t1}$ ,  $E_{t2}$ , etc. The state of the traps is determined by the position of the Fermi level. In non-degenerate semiconductors ( $n < N_c$ ),

$$n = N_c \exp[-(E_c - E_F)/kT],$$

$$\text{and } n_t = N_t \{1 + (g_0/g_1)\exp[(E_t - E_F)/kT]\}^{-1}.$$

Substituting into

$$e_n/c_n = (g_0/g_1)\exp[(E_t - E_F)/kT],$$



results in

$$e_n(T) = \sigma_n \langle v_n \rangle (g_0/g_1) N_c \exp[-(E_c - E_t)/kT].$$

Likewise, if  $p < N_v$ ,

$$e_p(T) = \sigma_p \langle v_p \rangle (g_1/g_0) N_v \exp[-(E_t - E_v)/kT].$$

These are the emission rates as functions of the capture cross sections ( $\sigma_n$  and  $\sigma_p$ ), and the trap energy level ( $E_t$ ). Since  $\langle v \rangle = (3kT/m^*)^{1/2}$  and  $N_c = 2M_c(2\pi m^*kT/h^2)^{3/2}$ , where  $M_c$  is the number of conduction band minima, we get a temperature dependent expression for  $e_n(T)$  of

$$e_n(T) = \gamma T^2 \sigma_{na} \exp(-E_{na}/kT),$$

where  $\gamma = 2(3)^{1/2} M_c (2\pi)^{3/2} k^2 m^* / h^3$ ,  $\sigma_{na} = (g_0/g_1) \sigma_\infty$  is the apparent cross section with  $\sigma_\infty$  being the high temperature limit of the cross section  $\sigma(T) = \sigma_\infty \exp(-\Delta E_\sigma/kT)$ , and  $E_{na}$  is the apparent trap energy with  $\Delta E_\sigma$  being the difference between the true trap level and the apparent trap level. A plot of  $\ln(e_n/T^2)$  versus  $1/kT$  yields a straight line with the absolute value of the slope equal to  $E_{na}$  and the y-intercept giving  $\sigma_{na}$ . The true values are not known, and so the apparent values are used to catalogue traps. This straight line can extend over several decades and is known as the "trap signature." Graphs that plot the natural log versus the exponent variable are known as Arrhenius plots (Blood and Orton, 1992).

By convention, the trap is labeled an "electron trap" if  $E_t > E_i$ , where  $E_i$  is the point where  $e_n = e_p$  given by

$$E_t = E_i + (kT/2) \ln \{ [\sigma_p \langle v_p \rangle (g_1/g_0)] / [\sigma_n \langle v_n \rangle (g_0/g_1)] \},$$

where  $E_i$  is the intrinsic Fermi level. If  $E_t < E_i$ , then the deep state is called a "hole trap."

To date, there are 26 different transient capacitance experiments for the study of deep states using the depletion region. The DLTS techniques employed in this research measured the depletion-capacitance transient signal as the diode sample is pulsed with a small forward bias then placed back into reverse bias. When placed back in reverse bias, the emitted carriers from the filled traps in the depletion region will be quickly swept out of the depletion region by the high electric field preventing recapture or recombination. The net space charge density of the depletion region increases, which causes a small dilation of the depletion region. For a large reverse bias where  $\lambda < x_d$ ,  $x_d$  being the depletion width and  $\lambda$  being the transition distance from the  $x_d$  to the position where  $E_F = E_t$ , the net space charge density during emission is

$$\rho(t) = e \{ N_d + N_t - n_t(t) \}.$$

Using the expression for capacitance for uniform material where  $(kT/e) \ll V$ ,

$$C = A(\epsilon \epsilon_0 N_d / 2)^{1/2} (V - kT/e)^{-1/2},$$

and replacing  $(eN_d)$  with  $\rho(t)$  gives

$$C(t) = C(\infty) \{ 1 - n_t(t) / (N_d + N_t) \}^{1/2},$$

where the steady state capacitance  $C(\infty) = A\{\epsilon\epsilon_0 e(N_d + N_t)/2\}^{1/2} V^{-1/2}$ . The square root term can be expanded when  $N_t, n_t \ll N_d$  giving

$$\Delta C(t)/C(\infty) = -n_t(t)/2N_d,$$

where  $\Delta C(t) = C(t) - C(\infty)$ . For the case of majority carrier trapping, the time constant is due almost entirely to the majority emission rate, ( $\tau^{-1} = e_n + c_n + e_p + c_p$ ), so that we get

$$\Delta C(t)/C(\infty) = -(N_t/2N_d)\exp(-e_n t) \quad (\text{for majority electron trap}).$$

This shows that the trap concentration can be determined by the initial transient capacitance value  $\Delta C(t=0)$  and the emission rate from the time constant of the capacitance transient  $\tau$ . This is true for a single trap level where the assumptions of 1) complete trap filling, 2) small "always filled" and "always empty" trap transition regions, and 3) the depletion approximation are valid (Blood and Orton, 1992).

To maintain these assumptions and use these equations, the DLTS transient capacitance measurement is restricted to small leakage currents. Since the leakage current is a function of temperature, this puts an upper limit on the sample temperature and thus an upper limit on the energy of the defect that can be detected. Due to the DLTS equipment properties, the temperature of the sample chamber is limited to 800 K. This temperature limit and the time restraints on making DLTS measurements limited the detection of traps to a trap energy of approximately 1.3 eV from either band edge. For SiC semiconductors, this leaves nearly 2/3 of the bandgap unprobed. To measure beyond this temperature limit, the development of an optical-assisted DLTS technique was started during this research. However, for this research, no data was obtained using optical-assisted DLTS.

Traditionally, boxcar-recording methods are employed that measured just two points of the transient capacitance or voltage signal, which are subsequently fit with a single exponential. This can lead to significant errors when there are multiple trap levels filling and emptying with similar time constants. For this research, the entire transient was recorded and used to characterize the trap. Computer software was employed that allowed up to three trap levels to be modeled to the transient signal.

Figure IV-4 illustrates the experimental setup for the DLTS variations performed in this research. The planned optical-assisted DLTS setup is also indicated.

To observe minority carrier traps, minority carrier injection is needed and this is accomplished either by using a p-n junction or by illumination. Minority carrier trap would cause a temporary increase in the space charge density of the depletion region and the initial capacitance would be higher than the steady state value. DLTS measurements were successfully made on the 6H-SiC samples with the majority carrier trap levels being detected and analyzed. Minority carrier trap levels were also detected due to the formation of junction-like structures within the depletion region created by the ion implantation/annealing process.

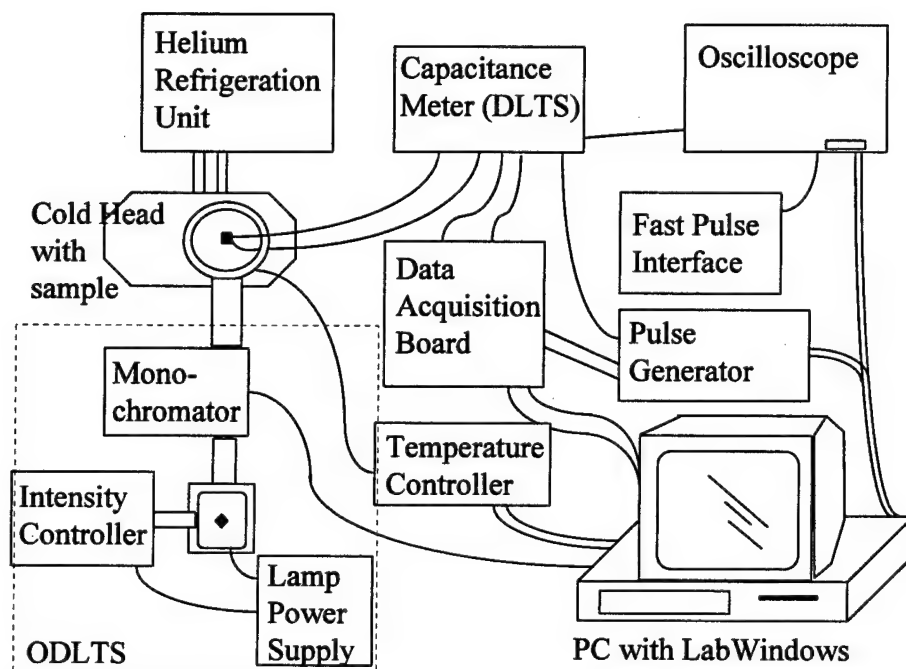


Figure IV-4. Deep level transient spectroscopy laboratory setup

### IV-3 I-V-T Measurements

Current-voltage (I-V) measurements over a temperature range can be used to assess the rectifying properties of a diode. The I-V measurements were made on every diode on each of the 46 test samples in this study. The I-V-T measurements were made on several selected diodes on each test sample and the best rectifying diodes were used for DLTS measurements.

Different resistivity effects dominate over different applied voltage ranges and those effective voltage ranges shift with temperature. For example at high forward voltages, series resistance will dominate while at lower forward voltages, other processes will dominate such as recombination, diffusion, and tunneling. The recorded I-V profiles (forward biases) were fit using the classical Sah-Noyce-Shockley (SNS) recombination-generation theory using the SNS equation

$$I = I_{\text{diff}} \exp(qV/A_1 kT) + I_{\text{rec}} \exp(qV/A_2 kT) + I_0 \exp(BV)$$

where  $A_1$ ,  $A_2$ , and  $B$  are the fitting parameters. The first term is the diffusion current, the second term is the recombination current, and the last term is the tunneling current. The factor  $A_1$  is the diffusion ideality factor. The factor  $A_2$  relates to recombination in the space charge region due to near midgap traps. The dominance of recombination or shunting behavior of a large portion of the diodes indicates a significant concentration of deep traps in these devices. By making I-V measurements over a range of temperatures, a recombination-activation Arrhenius plot can be made by plotting the log of the current at a

fixed voltage versus  $1/kT$ . The activation energy can then be obtained using the best linear fit to

$$I_{\text{rec}} \propto T^{5/2} \exp(-E_A/kT).$$

For near midgap traps, the activation energies should be about  $E_G/2$ .

Reverse voltage I-V curves over a temperature range were also generated to compare to the theoretical abrupt doping profile relationship

$$I_{\text{rev}} \propto V^{1/2}.$$

For wide bandgap material, the dominating current component should be thermally generated SCR. Deviations from this square-root dependence are due to perimeter and shunt reverse leakages. Again, an Arrhenius plot can be generated using the relationship

$$I_{\text{rev}} = C_1 \exp(-E_{A1}/kT) + C_2 \exp(-E_{A2}/kT).$$

The I-V-T results identifying any trap levels were correlated to the DLTS data. For DLTS, it is important to keep the leakage current relatively low. If the leakage current becomes too high, the approximation that the depletion region is free of carriers, and no significant free carrier capture is taking place during the transient capacitance or voltage measurement is invalid. Therefore, the DLTS is programmed to monitor the leakage current and stop the test if the preset 100  $\mu\text{A}$  limit is exceeded.

#### IV-4 Hall Effect

Free-carrier density and mobility are two important parameters for carrier transport devices such as field effect transistors. By measuring the Hall coefficient as a function of temperature and the resistivity using a van der Pauw geometry, the Hall mobility, free-carrier concentration, prevailing dopants ionization energies, total impurity density and compensation ratio values may be obtained.

For the 4H-SiC material, ohmic contacts were formed at the four corners on the surface of the epitaxial layer, using maximum separation (Figure IV-5). A low-energy nitrogen ion implantation was first required at these four corners to allow the formation of ohmic instead of rectifying contacts. This was accomplished by masking the rest of the surface prior to the low-energy ion implantation. This masking prevented the formation of a continuous highly doped cap layer. Such a cap layer would have permitted current flow between the contacts and prevented accurate Hall effect measurements.

After a subsequent 1400 °C anneal for 3 minutes, a thin highly doped layer ( $\sim 100$  Å) on the order of  $10^{18} \text{ cm}^{-3}$  was created, just at the corner contact areas. This was required because the low doping concentration of  $5 \times 10^{15} \text{ cm}^{-2}$  of the top epilayer was too low to allow significant tunneling required for ohmic contact formation on SiC. Ohmic contacts were made by the deposition of an appropriate metal or metal alloy, such as Al, Ti-Ni, or Al-Ti onto the samples followed by the appropriate high temperature annealing (e.g., 1000 °C for 5 min). The Hall effect system used pressure point contact wire to make electrical connections to the ohmic corner contacts as shown in Figure IV-5. From this configuration, both resistivity and Hall effect measurements were made. The Hall coefficient



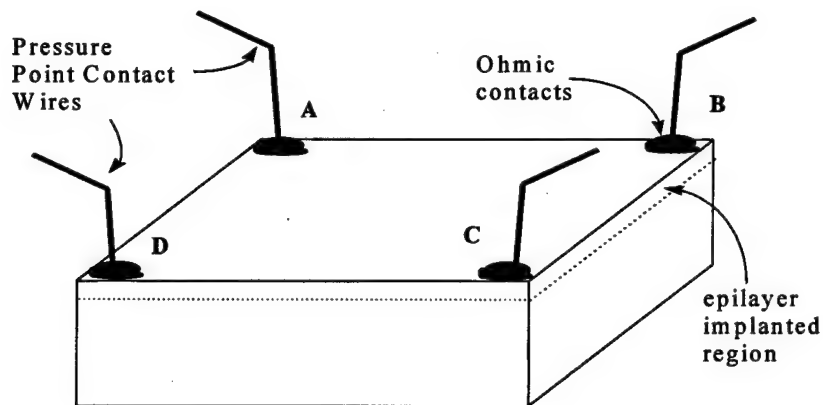


Figure IV-5. Hall sample configuration for 4H-SiC:N and :P samples

was measured over a temperature range of 77 to 700 K. The Hall effect scattering factor can be approximated, with the low field scattering factor taken as the ratio  $R_{H0}/R_{H\infty}$ , where 0 and  $\infty$  refer to the appropriate product  $\mu B_x$ , and is used in computing the free carrier density ( $n$  or  $p$ ), total impurity density ( $N_d + N_a$ ), dominant impurity energy level ( $E_d$  or  $E_a$ ), and compensation ratio ( $N_a/N_d$ ). The scattering factor should be different between  $n$ - and  $p$ -type material since the band structure is quite different between the valance and conduction levels.

The Hall coefficient is directly related to the free-carrier density by

$$R_H = -r/en \quad (\text{n-type}),$$

where  $r$  is the scattering factor that takes into account the distribution of energy of the free-carriers. This factor tends to be temperature and field (magnetic) dependent.

The drift mobility  $\mu$  is determined by the Hall effect measurement and resistivity,

$$\mu = \mu_H/r = R_H/r\rho,$$

where  $\rho$  is the resistivity and  $\mu_H$  is known as the Hall mobility. In the van der Pauw geometry,  $R_H$  is given as

$$R_H = W\Delta R_{BDAC}/B_x,$$

where  $W$  is the relative thickness of the lamella and  $\Delta R_{BDAC}$  is the change in the value  $R_{BDAC}$  due to an applied magnetic field  $B_x$ . The resistance term  $R_{BDAC}$  is the ratio  $V_{AC}/I_{BD}$ .  $V_{AC}$  is the voltage drop across the diagonal pair of contacts A and C, while  $I_{BD}$  is the applied current through the other diagonal pair of contacts B and D (see Fig. IV-5). Once  $R_H$  is measured, for n-type samples,  $n$  can be computed and the high temperature value, called the exhaustion value, will be equivalent to  $(N_d - N_a)$ . Using the linear slope over the temperature range from the natural log plot of  $n(T)$  versus  $1/T$ , the activation energy of the dominant donor can be obtained. This relationship is derived from the overall electrical neutrality equation; free-carrier density equation; and the donor atom electron density equation taking into account the proper degeneracy and band minima assumptions.

Resistivity obtained using the van der Pauw geometry is measured by passing a current through an adjacent contact pair (A and B) and measuring the induced voltage drop across the other contacts (C and D, see Fig. IV-5). The ratio  $V_{CD}/I_{AB}$  is then the resistance term  $R_{ABCD}$ . The resistivity is then calculated by

$$\rho = [\pi W/2(\ln 2)]\{R_{ABCD} + R_{BCDA}\}f\{R_{ABCD}/R_{BCDA}\}$$

where  $f$  is an asymmetry function dependent on the ratio  $Q = R_{ABCD}/R_{BCDA}$ . This function satisfies the transcendental equation

$$(Q - 1)/(Q + 1) = (f/\ln 2) \cosh^{-1}[0.5 \exp\{\ln 2/f\}].$$

This is easily programmable into an  $f(Q)$  table for use in the Hall effect software. In practice, averages are made using all the possible combinations of lead pairs. For square or disc samples, the resistance values should be equal. If the resistance values differ by more than a factor of 2, this indicates that the contacts are poor or that the sample has non-uniform doping. Variation of  $Q$  with temperature is also an indicator of the same effects. Sheet resistance can then be computed by merely dividing the resistivity by the sample thickness. Care was taken to use the best value for the sample thickness, taking into account such factors as band bending and inhomogeneities. Sheet resistance is of special importance for thin films where the film thickness is typically much smaller than the lateral dimensions of the sample. There is an error associated with measuring resistivity using surface finite contacts instead of side knife-edge contacts. This relative error is proportional to the squared ratio of the contact diameter to the sample diameter. This error, if not accounted for, gives a measured value less than the true value. This error was accounted for in this work. This error can be significantly reduced if the sample conduction area is patterned using a Greek cross mask during implantation. This study merely placed ohmic circular contacts as close to each corner as practical on the surface of the ion-implanted layers.

Since the mobility is determined by the various scattering mechanisms of the crystal and different mechanisms dominate over different temperature ranges, a value for the total impurity density ( $N_a + N_d$ ) can be obtained from measurements of the mobility. Ionized impurity scattering tends to dominate at low temperatures ( $\sim 4-50K$ ) so a measure of the mobility in this range will yield ( $N_a + N_d$ ). For deep dominant levels, the material

may become intrinsic before this exhaustion is reached. When combined with the exhaustion value ( $N_d - N_a$ ),  $N_a$  and  $N_d$  can be determined separately. By analyzing a wide range of data for n-SiC, an empirical relationship between  $\mu$  and  $(N_a + N_d)$  can be obtained at a specified single temperature. This information will allow a single temperature measurement of the mobility in estimating impurity content in SiC. Similar relationships have been determined for n-type GaAs and is believed to be reliable up to  $(N_d + N_a) = 10^{17} \text{ cm}^{-3}$  (Blood and Orton, 1992). Since annealing damage in SiC requires much higher temperatures, the reliability of this relationship for SiC may be considerably more limited.

#### IV-5 C-V-T Measurements

Capacitance-voltage measurements over a temperature range can provide information on the concentrations and characteristics of electrically active centers in the near surface regions of the Schottky diodes and in the lower doped layer of the one-sided p-n junction. Net doping density ( $N_D - N_A$ ) and depth profiling ( $N(x)$ ) can be obtained using C-V data, as well as the deep state concentrations ( $N_t$ ), when they are comparable to the net doping density.

The spatial distribution of traps can be obtained by measuring the amplitude of the capacitance transients at various pulse heights and reverse biases. Corrections are required to account for the non-abrupt depletion region edges, partial ionization of donor atoms, series capacitance, dependency of the emission rates on the electric field, and the incomplete trap filling in the modulated region. The existence of a transition region at the edge of the depletion region limits the spatial resolution to the order of the Debye length

$$L_D = (\epsilon\epsilon_0 kT/q^2 n)^{1/2}.$$

For uniformly doped material and when  $V \gg kT/e$ , the depletion capacitance behaves as if it were a parallel plate capacitor with capacitance

$$C = \epsilon\epsilon_0 A/x_d,$$

with  $x_d$  being the depletion width. When the doping is non-uniform, integration of the space charge density is required and we no longer have this simple relationship. Fortunately, there exists a similar effect in the change in capacitance with a change in applied voltage that depends on the local space charge density at the depletion edge ( $x_d$ ).

This relationship is given by

$$\Delta C / \Delta V_r = (\Delta C / \Delta x_d)(\Delta x_d / \Delta V_r) = -(\epsilon \epsilon_0 A / x_d^2)(\epsilon \epsilon_0 / x_d \rho(x_d)),$$

where  $\rho(x_d) = e\{N_d(x_d) - N_a(x_d)\}$ .

Ignoring compensation for the moment, so we have  $\rho(x_d) = e\{N_d(x_d)\}$ ,  $N_d(x_d)$  can be expressed as

$$N(x_d) = -(C^3 / \epsilon \epsilon_0 A^2) / (\Delta C / \Delta V_r) = -(2 / \epsilon \epsilon_0 A^2) / (\Delta C^2 / \Delta V_r),$$

which is consistent with the expression for uniform material. The slope from the plot of  $1/C^2$  versus  $V_r$ , is proportional to the doping profile while the intercept gives the built-in voltage ( $V_{bi}$ ).

The suitability of each diode for C-V testing was determined by I-V characterization - looking for small reverse current without abrupt discontinuities before breakdown; similar turn-on voltage; and low slope at high forward current showing low series resistance. The C-V profile was also analyzed to identify series capacitance. The programmed software does not account for the series capacitance and could result in invalid concentration and depletion width profile values. This is due to the series capacitance being and is equal to

$$C = \frac{1}{\sum \frac{1}{C_i}}$$

The program assumes a single capacitor model. If the series capacitance is of the same order of magnitude as the junction capacitance, the effect will be significant. This condition can occur when an additional depletion region is formed in the implanted layer at the

metal contact interface in the p-n junction diodes. At near zero bias, the depletion width at the metal contact interface will be on the order of the p-n junction depletion width. This will manifest itself as a reduced change in capacitance with reverse bias and reduced apparent depletion width modulation with voltage. This condition was observed in this study and severely complicated the analysis. Another serious complication was the C-V temperature dependence on the C-V measurement. As the temperature is increased, the space charge density is respectively increased and decreased with the emptying of majority and minority levels. The effect is a change in the depletion width with temperature. This means that when DDLTS is run, the region being characterized is shifting slightly as the sample temperature is changed. Pre-DDLTS C-V-T measurements are thus required to see how significant the shifts are and to determine the appropriate biases to use to maintain the depletion width throughout the temperature range. Figure IV-6 illustrates this shift in the depletion width as a function of temperature for a theoretical sample with shallow, but not fully ionized, donor levels. This space charge region deviation from the  $V^{1/2}$  dependence at the lower temperatures results in a deviation in the measured capacitance from the  $V^{-1/2}$  dependence. Figure IV-7 plots the capacitance using the approximate  $C \propto V^{-1/2}$  relation and using the deviated relationship between capacitance and bias caused by partial ionization of the donor atoms. Note that below room temperature, this deviation is significant. Therefore, C-V profiling was accomplished at room temperature and above to profile the junction region of the tested samples.

If the concentrations of deep states are significant compared to the doping level, the deep states can also affect the C-V profiling. Since the depletion width is due to band

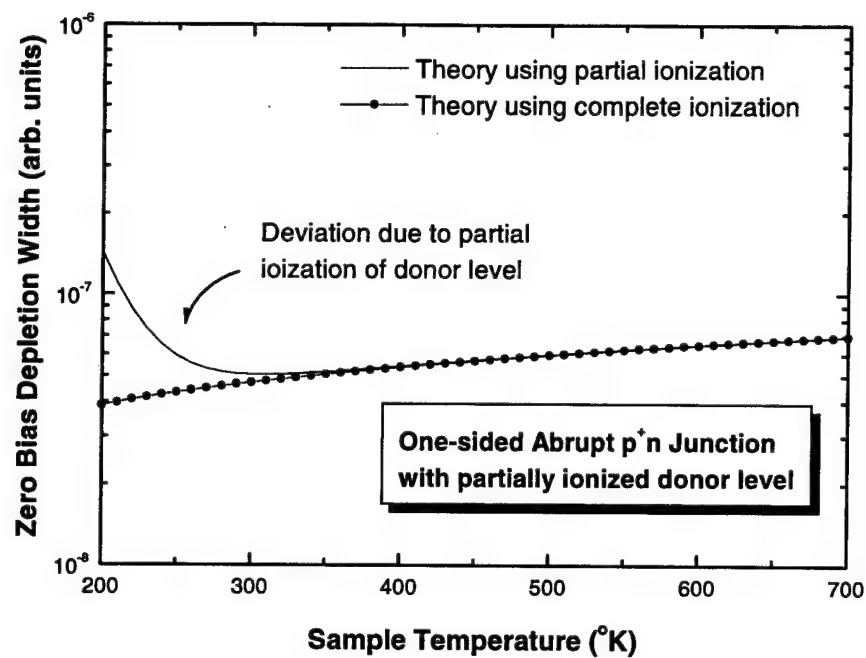


Figure IV-6. Shift in depletion width as a function of sample temperature.

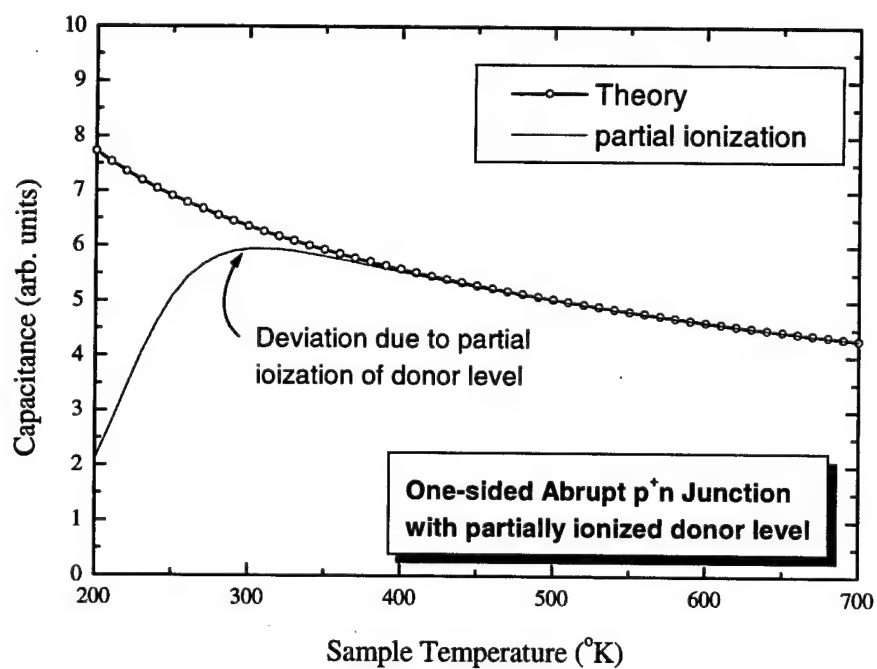


Figure IV-7. The effect of partial ionization of donor atoms on capacitance as a function of sample temperature.



bending, there is a point ( $x_1$ ) in the region where  $E_t = E_F$ , when  $(kT/e) \ll V$ . This is illustrated in figure IV-8. In the region between  $x_1$  and  $x_d$ , the space charge density is due to the doping concentration ( $eN_d$ ). From the barrier to  $x_1$ , this density is also due to the trap concentration ( $eN_d + eN_t$ ). The distance from  $x_1$  to  $x_d$  is known as the transition distance  $\lambda$ , given by

$$(x_d - x_1) = \lambda = \{(2\epsilon\epsilon_0/e^2N_d)(E_F - E_t)\}^{1/2},$$

for the usual condition of  $(kT/e) \ll V$ . When the bias is increased by a small amount  $\Delta V$ ,

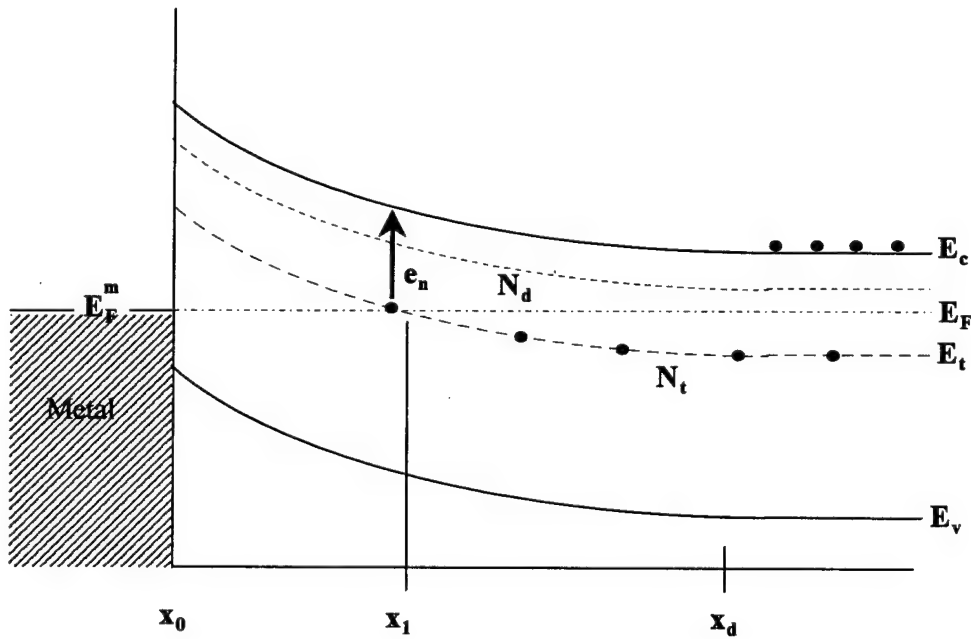


Figure IV-8. Schottky barrier energy band diagram (n-type) with a deep trap level.

the space charge due to the donors near  $x_d$  is increased by  $eN_d\Delta x_d$  and after a long time, compared to  $e_n^{-1}$ , we get an additional contribution of  $eN_t\Delta x_1$  from the traps near  $x_1$ . Decreasing the bias results in trap filling at the local capture rate  $c_n(x_1)$ . At  $x_1$ ,  $E_F = E_t$  so that  $c_n(x_1) = e_n$  and the response of the traps to a small oscillatory voltage of frequency  $\omega$  is

determined by the emission rate  $e_n$ . When  $e_n > \omega$ , the traps can respond to the oscillation and contribute to the fluctuating space charge and therefore the capacitance.

Depending on the relationship between the reverse bias and  $(E_F - E_t)$ , and the various frequencies and rates, different expressions for the capacitance and change in capacitance were employed. Raising the sample temperature allowed deeper traps to respond to the oscillation and thus be observed, and provide information about electrically active centers at the near surface region. C-V measurements required multiple traces to be recorded to reduce the level of background white noise. This limited the length of the traces to less than a few minutes at most to keep the recording time of a single measurement under a few hours. Normally, traces were kept to under a second to keep the temperature-dependent C-V measurements under twelve hours. Due to the exponential dependence of the capacitance to the trap energy, measuring trap levels greater than 1.3 eV would have resulted in a single C-V-T measurement series taking several weeks.

#### IV-6 Cathodoluminescence

There exists several techniques for generating radiative transitions in solid state materials, and most of these techniques have been developed as a means of investigating the properties of crystals. In this study, cathodoluminescence was chosen to investigate the effects of implantation and subsequent annealing on n-type 4H-SiC.

Cathodoluminescence (CL) is the technique of using an electron beam to irradiate the semiconductor sample to generate electron-hole pairs. When the resulting recombination or carrier trapping is radiative, a photon is generated. If the generated photons are not reabsorbed, a portion of the resulting luminescence can be detected and analyzed.

Cathodoluminescence can have the problem of charge build-up on the target material causing the electron beam to be deflected away from the target surface. When this occurs, the number of electrons excited across the bandgap in the semiconductor is dramatically reduced and the resulting luminescence is dramatically attenuated until no longer detectable. To eliminate charge build-up on the sample during a CL measurement, the target material must be electrically grounded. Even with this obstacle, CL is still a powerful technique and has several advantages over other luminescent techniques.

One significant advantage to cathodoluminescence is the ability to excite electrons with energies greater than the bandgap of the target material. This is critical for studying 4H-SiC with a bandgap greater than 3.2 eV. Another major advantage of cathodoluminescence over other luminescent techniques, such as photoluminescence, is the ability to control the depth of energy absorption. In CL, the beam energy can be decreased so that the energy is absorbed in the first few hundred Angstroms of the semiconductor or can be

increased so that the peak energy-absorption depth is much deeper. This is critical when examining samples having property variations with depth or when examining thin epitaxial layers. Both these conditions were the case in this research. Sample heating is another concern for this luminescent method. Only a small fraction of the beam energy is ultimately emitted from the sample as light. Most is converted to heat. This heat production requires that the sample also be thermally grounded to a 'cold finger' and tested under high vacuum. The sample is normally cooled to low temperatures (7 K to 160 K in this study) to control thermal quenching of the luminescent signal. Another reason for the high vacuum is to minimize losses in the excitation electron beam.

This luminescence method has its associated theories allowing for spectral analysis through varying such parameters as sample temperature, electron-beam energy, and electron-beam current. These theories will be discussed in the results section to explain the observed effects.

The peaks in the recorded CL spectra can be associated with transitions between energy levels. Radiative transitions include exciton recombination, shallow transitions, deep transitions, donor-acceptor transitions, and intraband transitions. Shown in Figure IV-9 is an energy band diagram illustrating the various radiative transitions. The transition labeled 'a' is a band-to-band transition. While other larger energy transitions are possible involving at least one additional particle (electron, phonon, or photon), the band-to-band transition is usually the largest energy transition observed by cathodoluminescence. In high quality material, it is also possible to detect transitions from other higher-

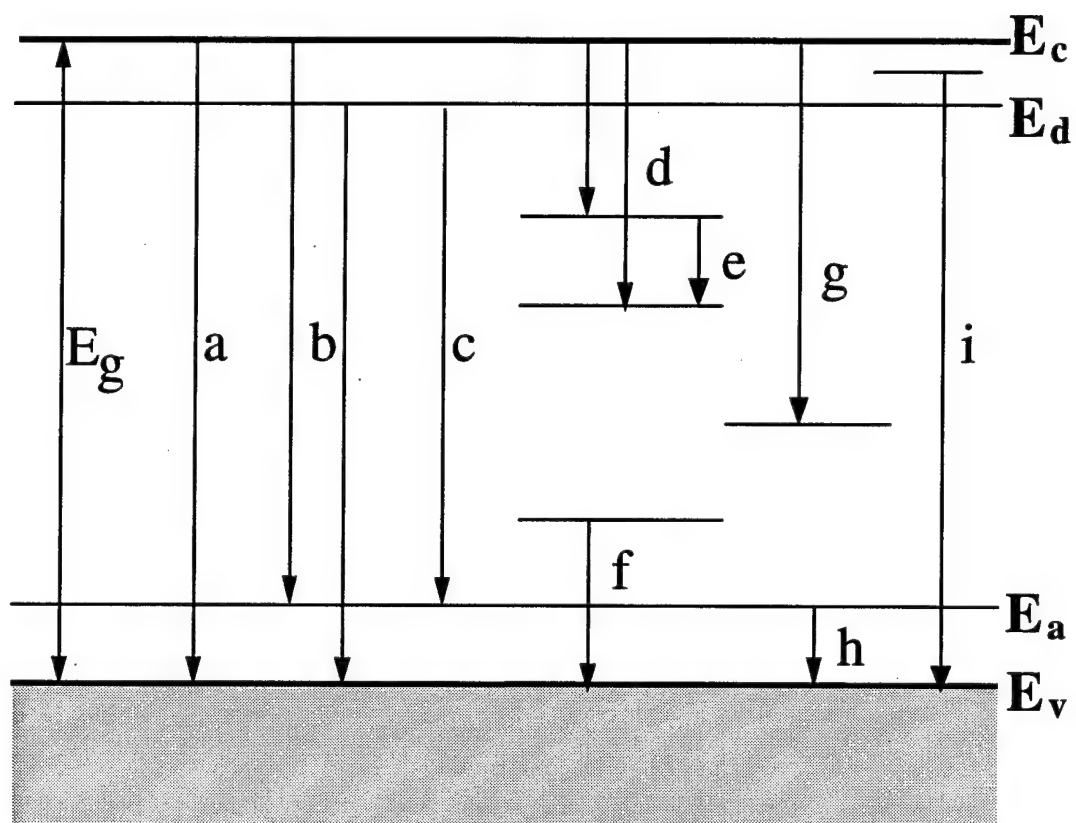


Figure IV-9. Various radiative transitions in semiconductors.

level conduction band minima. However, those spectral intensities are usually much smaller. This was the case in this study from the unimplanted 4H-SiC samples. The two transitions labeled 'b' are free-to-bound (FB) transitions, either from a donor level to the valence band or from the conduction band to an acceptor level. Transitions between a donor and acceptor level are called donor-acceptor (D-A) transitions and are labeled 'c' in the figure. Due to coulombic interaction between the bound electron at the donor site and bound hole at the acceptor site, and the fact that the distance between substitutional donor and acceptor atoms are discrete, these transitions form a series of predictably spaced spectral lines. Transitions 'd' through 'g' are related to deep levels and transition 'i' is related to exciton recombination which could either be free or bound to a center, such as a donor or an acceptor. The involvement of phonons and the unique pairing of energy levels in SiC due to inequivalent lattice sites make for a complex spectrum. Sample temperature dependence of the spectral lines, in terms of intensity, energy shifts, and peak broadening, is one technique for identifying their sources. Beam intensity can also be used to saturate the population of a level and drive the material into a shift in the transition probabilities, thus permitting the observation of additional transitions. Beam energy can also be adjusted to probe the sample. By observing changes in the intensities of the spectral peaks and knowing the doping profile, correlations can be made to help identify the sources of the luminescence. The intensities of the peaks are related to the occupation probabilities of these levels, momentum conservation, luminescent center densities, and relative transparency. The recorded spectral intensities are also affected by the spectral response of the detection system.

As shown in Figure IV-10, the spectral response of the detection system used in this study for a 1000 °C blackbody is not linear. The ratio of the theoretical blackbody curve to the recorded spectrum curve could be used to scale the recorded spectra to account for the nonlinear response of the detection system. Since other frequency dependencies could not be accurately modeled, this scaling was not done. For example, since the transparency of each emission is different, the resulting intensities may not accurately reflect the true recombination ratios. However, the effect of entrance and exit slit widths on spectral intensity were taken into account when the spectra of different samples were compared.

Spectral comparisons between samples can be used to further identify damage and impurity related levels. Impurities and defects can act as 'luminescent centers' where recombination can occur and so luminescent studies can provide information about these impurities and point defects. In addition, since there exists non-radiative processes for recombination, luminescence studies can provide a partial view of the mechanisms related to impurities and point defects. The laboratory setup for cathodoluminescence is shown in figure IV-11.

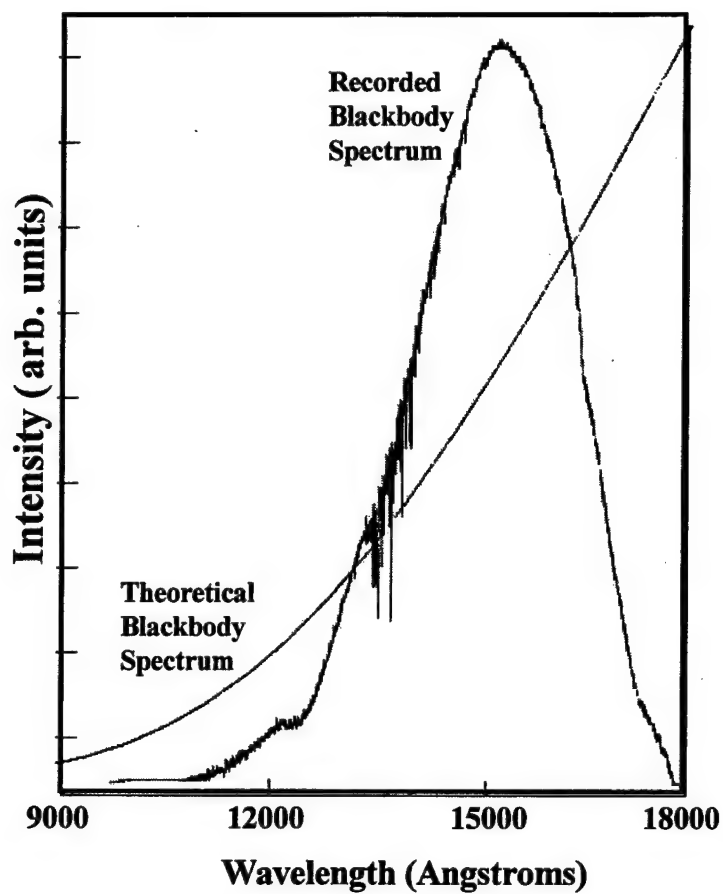


Figure IV-10. Spectrometer/Detector response curve using a 1000 °C blackbody source.



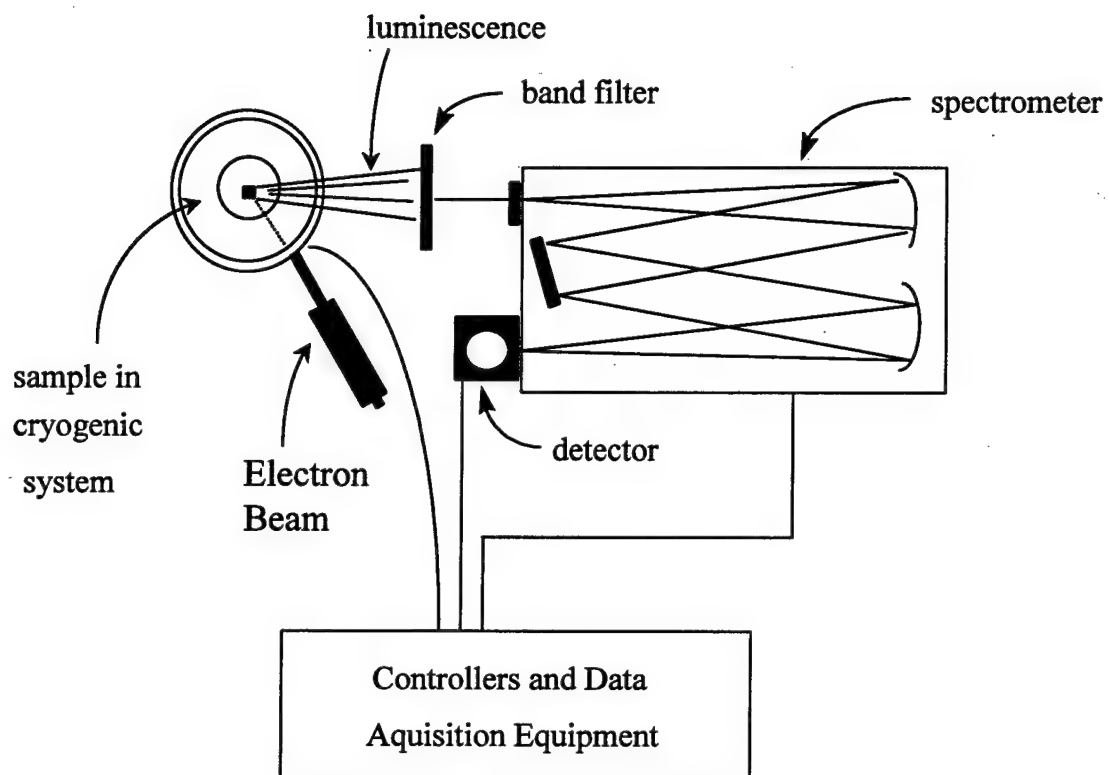


Figure IV-11. Cathodoluminescence Setup.

## **V EXPERIMENTAL SETUP**

### **V Experimental Setup**

Hall effect, cathodoluminescence (CL), and deep level transient spectroscopy (DLTS) measurements were performed on 6H-SiC and 4H-SiC test diodes. Each measurement technique required a different experimental setup and procedure. These setups include both the laboratory equipment layouts and the device designs.

#### **V-1 Devices**

The 6H-SiC specimens consisted of an n-type epitaxial layer grown on n-type bulk 6H-SiC material and were fabricated into Schottky diodes on which DLTS and electrical measurements were made. The 4H-SiC material consisted of an n-type epitaxial layer grown on p-type epitaxial 4H-SiC, which was, in-turn, grown on bulk 4H-SiC. The 4H-SiC specimens were fabricated into van der Pauw configured devices for Hall effect, and backside contacted for CL measurements. The ion-implanted n-type epitaxial surface layer was the investigated layer for both polytypes. Tables VI-1 and VI-10, in the Experiment and Results section, lists the implantation parameters for both the 6H- and 4H-SiC polytype test material, respectively.

##### **V-1-A 6H-SiC Schottky Diodes**

The 6H-SiC Schottky diodes used in this study were fabricated from a set of samples obtained from Dr. James Scofield of the Air Force Research Laboratory, Power and Propulsion Directorate, at Wright-Patterson AFB, Ohio. The samples were grown by the metal organic chemical vapor deposition (MOCVD) process, producing 6H polytype (0001) n-type conductivity epitaxy with net shallow impurity doping levels of  $1 \times 10^{16}$  to

$2 \times 10^{17} \text{ cm}^{-3}$  (measured at 23 °C). The substrate material was vicinal (0001) 6H-SiC polytype with n-type conductivity grown by the vapor transport process. The samples were cut into half-centimeter square pieces prior to implantation. The epitaxial layers were ion-implanted with Ar, Cr, or Mg ions to a concentration of  $2 \times 10^{12}$ ,  $5 \times 10^{12}$ , or  $2 \times 10^{14} \text{ cm}^{-2}$ . The implant energies were chosen to produce an implanted ion concentration peak at 2300 Angstroms from the surface. Table VI-1, in the Experiment and Results section, lists the implantation parameters for 6H-SiC polytype test devices.

For experiments requiring rectifying diodes, Schottky diodes were made by an ultra-violet photolithography processes and rf-sputtering to form 500  $\mu\text{m}$  diameter dot array patterns of Ti/Pt/Au. The forward slash (/) between elements denotes that the metals were deposited sequentially. The sample processing procedures are included in Appendix B.

Prior to the fabrication of the dot array, the specimen backside surfaces (bulk material) were rf-sputtered with 2000 to 3000 Å of nickel and then annealed at 1050 °C for 5 minutes in flowing  $\text{N}_2$  gas to convert the conductivity of the nickel contact from rectifying to ohmic.

Figures V-1 and V-2 illustrate the structure of the 6H-SiC test device. The metal contacts (both Schottky and ohmic) were made only after the epitaxial layer was ion-implanted and subsequently annealed. This device design meant that the ion implantations were made through the surface that would become the diode junction. Thereby, a significant concentration of interface defects would be formed that would contribute to an increase in the leakage current. This would prove to be an important limitation for

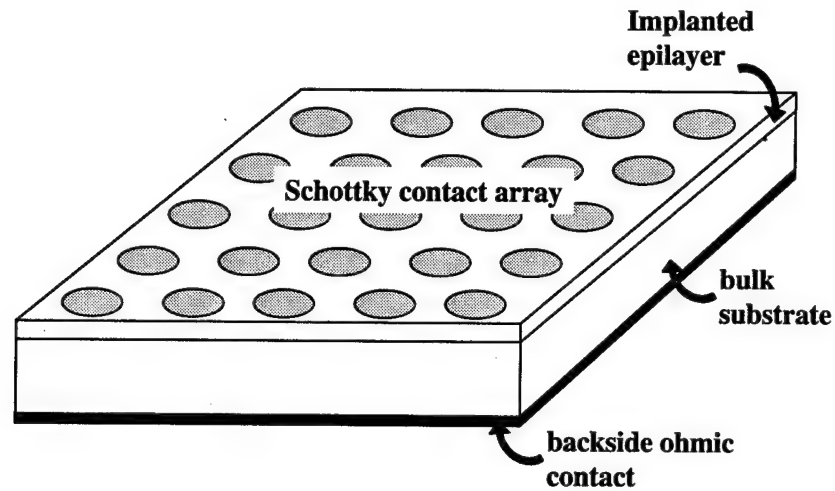


Figure V-1. 6H-SiC diode design used for electrical measurements.

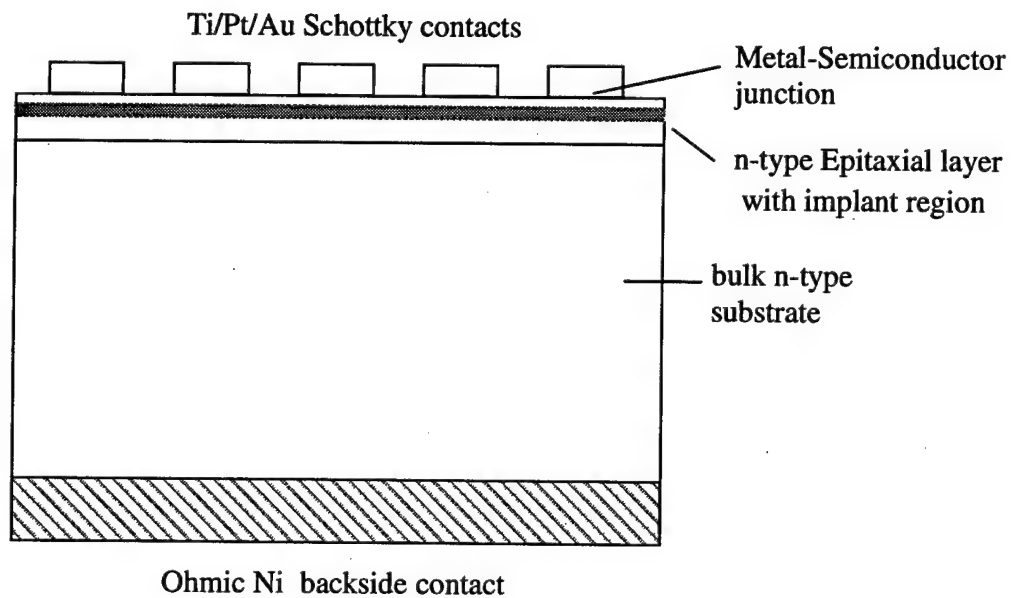


Figure V-2. Profile of the 6H-SiC diode design used for electrical measurements.

DLTS measurements where leakage currents must be kept low to satisfy the depletion approximation modeling criteria. This surface damage was also detectable by DDLTS.

Secondary-ion mass spectroscopy (SIMS) was performed on two of the ion-implanted 6H-SiC samples to confirm the predicted implant profile. Except for an extended tail, due to channeling effects, the sample profiles matched the calculations.

Figure V-3 illustrates the typical implantation profile for the samples used in this

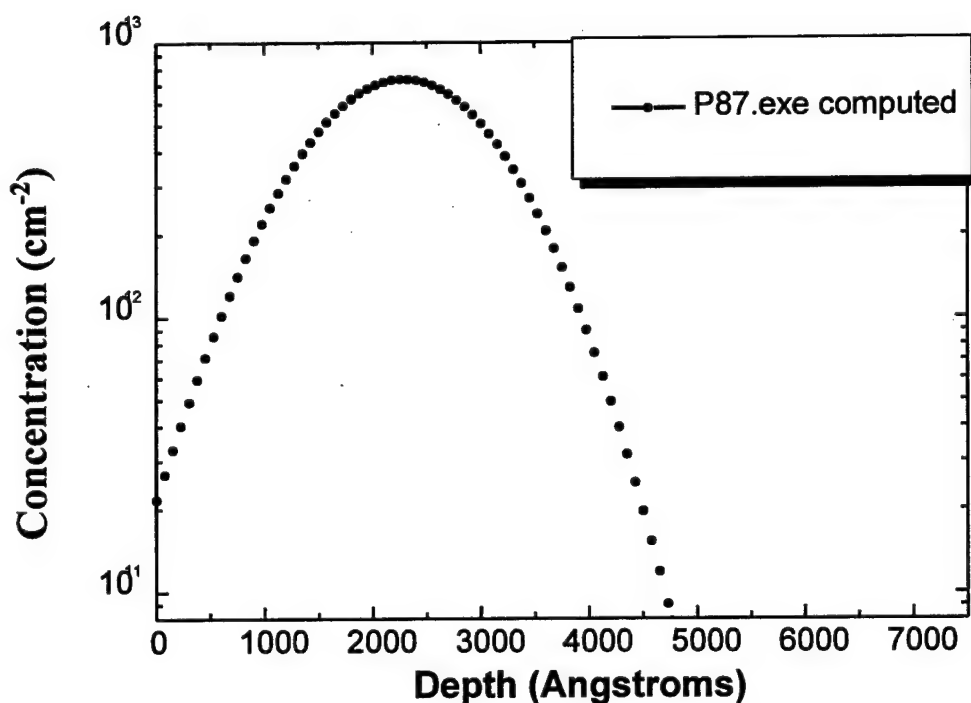


Figure V-3. Typical Implantation Concentration Profile for the 6H-SiC material used in this study.

study. Due to the number of samples (46) available for test, the annealing temperatures were limited to 1200, 1400 and 1600 °C. The reasons for choosing these temperatures were that the annealing temperatures needed to be higher than 1000 °C, where little or no

annealing effects occur, and lower than 2000 °C, where stoichiometric changes occur in the semiconductor. Additionally, two ion-implanted 6H-SiC samples were also annealed at 1800 °C - one implanted with Cr and the other with Mg. This anneal temperature proved to be too high and the samples were too leaky to run a complete DLTS measurement using standard contact diameters. Both 1800 °C annealed samples were reprocessed into MOS devices in an attempt to reduce the leakage current to acceptable levels. Unfortunately, this attempt did not yield useful results. Unimplanted samples were also analyzed and served as a baseline. The test matrix of donor concentrations and implant doses used in this study ensured that at least one subset of the fabricated 6H-SiC samples would have the proper donor to defect concentration ratio. This would permit a full DLTS analysis, and possibly permit an identification of the trap levels.

#### **V-1-B 4H-SiC p-n Diodes**

The 4H-SiC material was the second set of samples to be processed and tested. To avoid implanting through the device junction, the device design for the 4H-SiC material was changed from a Schottky device to a p-n junction device. This meant that all the contacts would have to be ohmic. This design change created its own set of problems, due to the difficulty in fashioning ohmic contacts on the lightly doped n-type 4H-SiC surface. By avoiding ion implanting through the junction, leakage currents problems that were experienced with the 6H-SiC Schottky diodes would be avoided.

Half-centimeter square 4H-SiC samples were cut from four n-type top epilayer 1.375" diameter wafers grown by CREE® of Durham, NC. Like the 6H-SiC samples, the 4H-SiC epilayers were grown by MOCVD, producing 4H polytype (0001) epilayers of 1.3

$\mu\text{m}$  thick. The top surface n-type conductivity epitaxy had a net donor concentration of  $5 \times 10^{15} \text{ cm}^{-3}$  (measured at  $23^\circ\text{C}$ ). The sub-epilayer was p-type and had a net acceptor concentration of  $1 \times 10^{18} \text{ cm}^{-3}$  (measured at  $23^\circ\text{C}$ ). The substrate material was vicinal (0001) 6H-SiC polytype with p-type conductivity grown by the vapor transport process and had a net acceptor concentration of  $1 \times 10^{18} \text{ cm}^{-3}$ . The growth parameters chosen (epilayer thickness and net dopant concentrations) resulted in placing the zero-bias depletion width  $0.7 \mu\text{m}$  from the p-n junction, allowing full depletion of the top epitaxial layer with a reverse bias of less than 5 volts. A one-sided abrupt junction depletion approximation was used to compute these values and select the design parameters.

Each wafer was examined under cross-polarizers to assess the uniformity and quality across the wafer. At the time of purchase, these wafers were of the highest available quality but still possessed a significant concentration of grain boundaries and variations especially near the edges. These flaws could be seen as changes in the both the intensity and polarization of the transmitted polarized light. Air Force Research Laboratory research scientists, also studying SiC, also viewed these wafers through cross-polarized light and commented that the wafers looked as good or better than the best material they were able to obtain.

Figure V-4 shows the use of ohmic contacts for both the backside contacts on the p-type substrate and the contact dot array on the top n-type epilayer. Ohmic contacts were readily formed on the p-type substrate using evaporated aluminum due to the high net acceptor concentration. However, since the net doping level of the top epilayer was only  $5 \times 10^{15} \text{ cm}^{-3}$ , ohmic contact formation was only accomplished after the material was ion-

implanted with low-energy 30 keV nitrogen ions to create a shallow implant layer. The material was then annealed at 1400 °C for three minutes in flowing argon gas to activate approximately 50 % of the low energy implanted ions.

Initially, a lower temperature of 1100 °C for one hour was first tried on several samples to activate the low energy implants. The duration time for this lower temperature

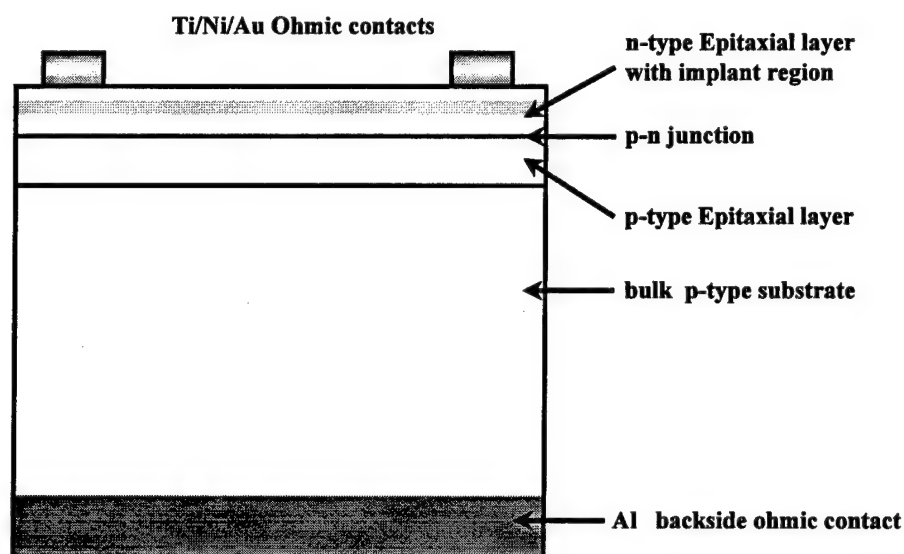


Figure V-4. 4H-SiC diode design used for electrical measurements.

was based on an exponential fit to two activation/duration value sets published on activating implanted nitrogen in 6H-SiC. The lower temperature was selected because it was the upper temperature limit for the department's tube furnace. This in-house anneal failed to sufficiently activate the implants and a subsequent 1400 °C anneal was performed at the NASA Lewis Research Center in Cleveland, Ohio. Numerous metals and metal alloys were deposited as possible ohmic contacts using various deposi-



tion/annealing processes until the best "formula" was found. The selection of contact candidates was based on a thorough literature search and the limitations of the in-house deposition systems. These systems consisted of a radio frequency (rf) sputterer and a resistive-heating evaporation system. The only reported success at creating ohmic contacts on SiC were on highly doped SiC. This suggests that the ohmic contacts being formed in these studies were tunneling contacts. Because of this, it was concluded that highly doped capping contact pads would be required before ohmic contacts would be formed on the low net donor concentration 4H-SiC epilayer samples.

Initially, Ni/Au contacts were tried. However, the Ni/Au contacts adhered poorly to the SiC surface. Titanium was then added as an initial binding layer (150 Å) for two reasons. First, titanium binds better than nickel to the surface of SiC, and second, titanium would react with the carbon in SiC, while the nickel reacted with the silicon to reduce the production of carbon stacks created when only nickel is deposited. The gold was used to serve as a capping layer to prevent oxidation of the nickel. It was also found that the gold reacted with the nickel, therefore, only a thin layer of gold was used. Ti/Ni/Au contacts were evaporated onto the n-type 4H-SiC surface and then annealed at 750 °C for 3 minutes. The 4H-SiC samples were fabricated with ohmic contacts at just the four corners to form the van der Pauw's contact pattern required for Hall effect measurements. All but the top surface corners were masked prior to the low-energy ion implantation. This prevented the formation of a continuous highly doped cap layer that would have created a near-surface conduction path between the ohmic contacts. Both the low- and high-energy implantations of the 4H-SiC specimens were done at IICO® Corporation, in Santa Clara, CA. While the nitrogen, phosphorus, and argon high-energy implantations were done at

500 °C, the nitrogen low-energy ion implantations that were implanted at 30 keV to a dose of  $5 \times 10^{15} \text{ cm}^{-2}$  were done at room temperature. The low-energy implantation produced an implantation profile peak 500 Å beneath the surface and a peak concentration of  $3 \times 10^{20} \text{ cm}^{-3}$ . This high peak concentration meant that only a small fraction of the nitrogen ions needed to be activated to create a high net donor concentrations at the surface corners. The surface damage created from the low-energy implant appeared to be adequately repaired by the 1100 °C anneal. Prior to implantation, the material was transparent with a slight greenish ting. After implantation, the implanted corner regions became dark and opaque. The repairing effect of the 1100 °C anneal treatment could be seen as these dark implanted corner areas returned nearly to their original appearance of slightly green and transparent. However, not all of the damage was eliminated through thermal annealing. After annealing, the unmasked corner regions still had a slightly different coloration than the masked region.

To create the main implantation layer for this study, the samples were ion-implanted at an elevated temperature of 500 °C with a single ion species of either Ar, Mg, or Cr at selected energies to produce an implant profile with a peak implant concentration at 2000 Å below the surface and peak implant concentration between  $1 \times 10^{16}$  to  $1 \times 10^{17} \text{ cm}^{-3}$ . The energies were selected after using a profiling program (called P87.exe; a Fortran® code) that calculates the projected range, peak concentration, straggling value, kurtosis and skewness values using LSS theory. Figure V-5 shows the predicted implantation profile for a typical implanted 4H-SiC sample.

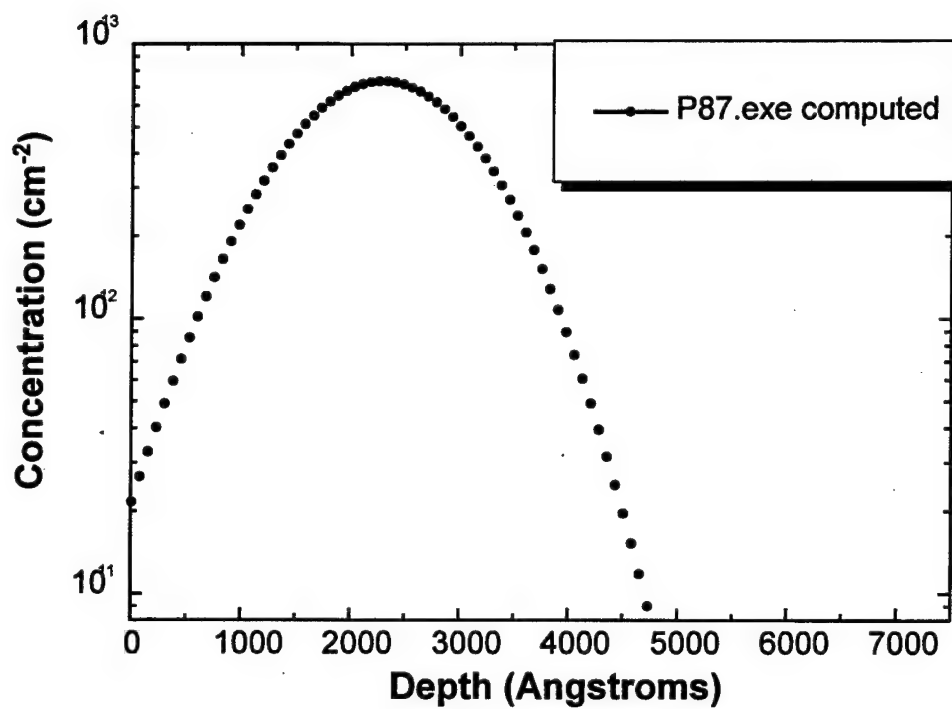


Figure V-5. Typical implanted ion concentration profile for the 4H-SiC material used in this research.

## V-2 DLTS and C-V Setup

The DLTS and C-V measurements used much of the same common equipment. The samples were mounted in an RMC coldhead, with the sample rested with its ohmic backside contacting the conducting plate while pressure point contacts were aligned to selected dots on the sample top surface. For DLTS and C-V measurements, the leads from

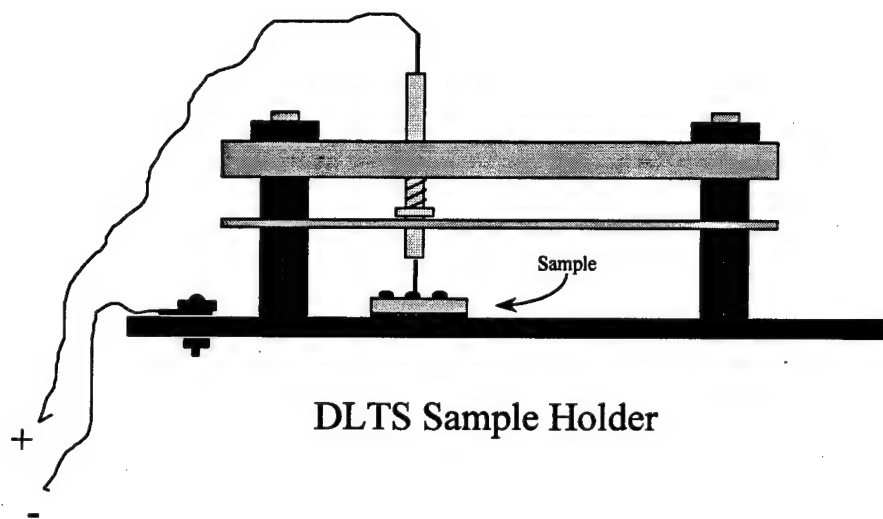


Figure V-6. Sample mount used in the cold head for DLTS, C-V, and I-V-T measurements.

the plate and point contacts ran to a SULA Technologies Deep Level Transient Spectrometer. The spectrometer was externally biased by a power supply and was synchronized and triggered through a pulse generator by way of a breakout board connect to the printer port of a personal computer. Figure V-6 shows the sample mount used for DLTS, I-V-T, and C-V measurements.

The LabWindows<sup>®</sup> software programs used to run the DLTS and C-V experiments were written by Dr. Johnstone and Dr. Scofield during their dissertation research. During

this research, I further modified most of the software programs to various degrees to increase the ease of operation, correct minor errors, and expand the software capabilities.

The temperature of the sample was controlled through a LabWindows® software program that controlled a Lakeshore 330 temperature controller. The temperature controller supplied the electrical heating while a helium gas cryogenic refrigeration system supplied the cooling. This setup allowed the sample temperature to be incremented 4 K over a from 50 to 750 K range. Due to carrier freeze-out and leakage current limits, DLTS and C-V tests were normally ran over a sample temperature range of 150 to 700 K. Figure V-7 illustrates the experimental layout for these two tests. Note the optical equipment included in the drawing. Optically assisted DLTS was being developed during this research, which included the writing of the software to automatically operate the optical equipment and perform the measurements. Several software validation runs were made to validate the LabWindows software written.

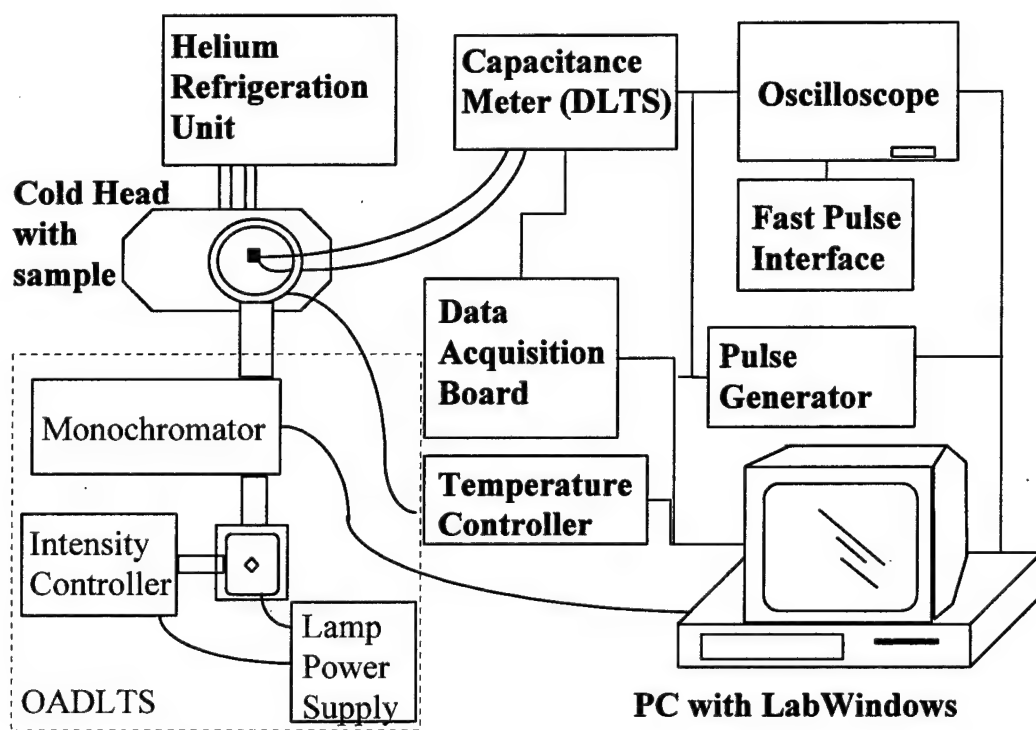


Figure V-7. Lab setup for DLTS and C-V measurements.

### **V-3 I-V-T Setup**

I-V-T measurements were also made with the samples mounted in the coldhead. However, the electrical leads were run through a Keithley relay box in order to match the input leads for the Keithley current-voltage measurement system. The current and voltage control and data recording was made using an IEEE interface to the personal computer. The temperature control and data recording was performed as for the C-V and DLTS measurements. The sample temperature was incremented by 4 K from 50 to 700 K. For all three measurements, multiple measurements were made to test the repeatability of the recorded data. These repeatability runs were done two ways – first by repeating the measurement, incrementing the sample temperature as before, and by incrementing the sample temperature in the reverse direction to observe any hysteresis. The sample temperature was stabilized to  $\pm 0.5$  K before taking a measurement.

#### **V-4 Hall Effect Setup**

The samples were prepared by forming ohmic contacts on the surface of the implanted epilayer. The contacts were placed in the corners without contacting the edges. The samples were mounted on the cold-finger using a sapphire slide to electrically isolate the sample from the cold-finger. Pressure contacts were made onto the ohmic contacts with the electrical connections tested before and after the cold-finger was mounted into the coldhead. The sample was then cooled to 77 K using liquid nitrogen. Pre-run Hall measurements were then made to establish the optimum current settings. Hall effect measurements were made up to 700 K using 10 K increments for the temperature range 77 to 300 K and using 20 K increments from 300 to 700. The Hall effect voltages and currents were made and recorded for each of the eight contact lead configurations. The Hall effect software was then run to compute the net sheet carrier concentration and mobility for each temperature. Multiple Hall effect measurements were made on the same sample to test the repeatability of the measurements and test for thermal or magnetic hysteresis. None were observed.



## V-5 Cathodoluminescence Setup

Prior to mounting on the cold finger, the 4H-SiC samples were cleaned using lab grade acetone and methanol to remove any organic surface films. The samples were then mounted to a cold finger using black wax and placed in a high-vacuum sample chamber. A  $10^{-7}$  torr high vacuum was then established and the sample cooled to 7 K. Measurements were also made at elevated temperatures up to 160 K. The sample temperature was stabilized to within  $\pm 0.5$  K before each run.

The tested sample was irradiated using an electron beam with a beam energy range of 5 to 10 keV and beam current range of 0.3  $\mu$ A to 2.4 A. A Faraday cup was used to measure the beam current and calibrate the current-voltage gauges. The electron beam was aligned and focused onto the sample surface and the resulting luminescence was collected and focused onto the entrance slit of the  $\frac{3}{4}$  meter spectrometer. The spectrometer and PMT were controlled by the personal computer using Spex<sup>®</sup> software. Optimization steps were taken which include defocusing the beam. This resulted in excellent signal-to-noise ratios. The collected light was detected using a nitrogen-cooled PMT with its output signal digitized and fed to a personal computer. The exit and entrance slits were optimized to collect the maximum amount of luminescence while maximizing the frequency resolution. With each CL run, the entire setup was systematically optimized to ensure that the sample was irradiated to the fullest extent possible, that the resulting luminescence was collected, aligned and collimated, and then focused into the entrance slit. The spectrometer was calibrated before and after the daily runs using multiple spectral lamps. CL tested samples were mounted side-by-side to enable intensity comparisons between samples. Multiple runs were made using different slit widths to collect both broadband

and high resolution data. The sample temperature, beam energy, and beam current were varied to investigate the luminescent centers. Repeatability runs were made to ensure that the data were reliable. This included removing examined samples and reexamining them days later. The data were recorded by the PC and analyzed using Origin<sup>®</sup> software.

## VI EXPERIMENTS AND RESULTS

### VI-1. Ar-, Cr-, and Mg-Implanted 6H-SiC

Deep Level Transient Spectroscopy (DLTS) measurements were made on 46 n-type epitaxial 6H-SiC samples. Of those, forty-two were ion implanted at high temperature ( $T_I = 475\text{ }^{\circ}\text{C}$ ), two were ion implanted at room temperature ( $T_I = 23\text{ }^{\circ}\text{C}$ ), and two were unimplanted (as-grown) – one unannealed and one annealed at  $T_A = 1400\text{ }^{\circ}\text{C}$ . Fifteen of the samples were implanted with magnesium, twelve of the samples were implanted with argon, and seventeen of the samples were implanted with chromium. Table VI-1 shows the sample properties and implantation parameters. Note that the annealing temperatures for the argon-implanted samples were 1200 and 1400  $^{\circ}\text{C}$ , while the magnesium- and chromium-implanted samples were annealed at  $T_A = 1200, 1400, 1600, \text{ and } 1800\text{ }^{\circ}\text{C}$  for 120 minutes in flowing argon gas.

The choice of anneal temperatures was based on 1) the number of samples available for each type of implant, 2) the availability of different temperature range annealing systems, and 3) the annealing results found in published research on SiC. Below  $T_A = 1000\text{ }^{\circ}\text{C}$ , activation of implanted ions in SiC is not detected and above 2000  $^{\circ}\text{C}$ , SiC does not remain stable (Kroko, 1966). The lower implantation energy of 195 keV was chosen for the magnesium implantations to create the same 2500 Å peak implantation depth as was produced in the argon and chromium 390 keV implantations.

The asterisks beside the implant energies in Table VI-1 indicate that the samples were implanted at room temperature ( $T_I = 23\text{ }^{\circ}\text{C}$ ). The room temperature implanted samples

<b>Implant Species</b>	<b>Implant Energy (keV)</b>	<b>Implant Dose (cm<sup>-2</sup>)</b>	<b>Doping Conc. (cm<sup>-3</sup>)</b>	<b>Anneal Temp (°C)</b>
Mg <sup>+</sup>	195	1x10 <sup>14</sup>	1x10 <sup>16</sup>	1200/1400
Mg <sup>+</sup>	195	1x10 <sup>14</sup>	7x10 <sup>16</sup>	1200/1400/1600/1800
Mg <sup>+</sup>	195	1x10 <sup>14</sup>	1x10 <sup>17</sup>	1200/1400
Mg <sup>+</sup>	195	5x10 <sup>12</sup>	1x10 <sup>16</sup>	1200/1400
Mg <sup>+</sup>	195	5x10 <sup>12</sup>	7x10 <sup>16</sup>	1200/1400
Mg <sup>+</sup>	195	5x10 <sup>12</sup>	1x10 <sup>17</sup>	1200/1400
Mg <sup>+</sup>	195*	2x10 <sup>14</sup>	7x10 <sup>16</sup>	1200
Ar <sup>+</sup>	390	2x10 <sup>14</sup>	1x10 <sup>16</sup>	1200/1400
Ar <sup>+</sup>	390	2x10 <sup>14</sup>	7x10 <sup>16</sup>	1200/1400
Ar <sup>+</sup>	390	2x10 <sup>14</sup>	1x10 <sup>17</sup>	1200/1400
Ar <sup>+</sup>	390	2x10 <sup>12</sup>	1x10 <sup>16</sup>	1200/1400
Ar <sup>+</sup>	390	2x10 <sup>12</sup>	7x10 <sup>16</sup>	1200/1400
Ar <sup>+</sup>	390	2x10 <sup>12</sup>	1x10 <sup>17</sup>	1200/1400
Cr <sup>+</sup>	390	2x10 <sup>14</sup>	1x10 <sup>16</sup>	1200/1400/1600
Cr <sup>+</sup>	390	2x10 <sup>14</sup>	7x10 <sup>16</sup>	1200/1400/1600
Cr <sup>+</sup>	390	2x10 <sup>14</sup>	1x10 <sup>17</sup>	1200/1400/1600
Cr <sup>+</sup>	390	5x10 <sup>12</sup>	1x10 <sup>16</sup>	1200/1400
Cr <sup>+</sup>	390	5x10 <sup>12</sup>	7x10 <sup>16</sup>	1200/1400/1800
Cr <sup>+</sup>	390	5x10 <sup>12</sup>	1x10 <sup>17</sup>	1200/1400
Cr <sup>+</sup>	390*	2x10 <sup>14</sup>	7x10 <sup>16</sup>	1200
unimplanted	---	---	7x10 <sup>16</sup>	----
unimplanted	---	---	7x10 <sup>16</sup>	1400

\* Sample was ion implanted at room temperature.

Table VI-1. List of n-type epitaxial 6H-SiC Schottky Diodes used in the DLTS Study. Note that all the ion implanted samples were implanted at 475 °C except for two, which were implanted at room temperature (23 °C).

were obtained from Dr. Scofield at the Air Force Research Laboratory, Wright-Patterson AFB, Ohio.

Secondary Ion Mass Spectrometry (SIMS) was accomplished on two ion-implanted 6H-SiC samples and confirmed that the calculated implant profile made by the program P87.exe was accurately estimated. The only exception was the failure of the profiling code (P87.exe) to accurately estimate the low concentration tail of the implanted ions extending into the material. This tail was most likely due to channeling effects, although the samples were ion implanted seven degrees off-axis to minimize channeling effects.

Following ion implantation and annealing, photolithography and metal deposition was accomplished to form an array of Schottky diodes on each sample from which Deep Level Transient Spectroscopy (DLTS) measurements were made. The backside of the samples were metallized with evaporated nickel and annealed at  $T_A = 1050\text{ }^{\circ}\text{C}$  for 5 minutes to form ohmic back side contacts. Details of the sample structures and fabrication processes can be found in chapter IV.

Current-voltage-temperature (I-V-T) and capacitance-voltage (C-V) measurements were made on the array of diodes on each prepared sample. The best rectifying diodes were chosen to make DLTS measurements. Current-voltage (I-V) measurements were made for each diode to determine the voltage limits as well as observe the effect of anneal temperature ( $T_A$ ) on the electrical properties of the diodes. Capacitance-voltage measurements were made to determine the voltage settings to use during DLTS measurements, measure the net donor concentration profile, and assess the quality of the diode junction.

DLTS analysis revealed several deep level defects in each of the implanted samples. No deep level defects were observed in the unimplanted-unannealed sample or in the un-

implanted-annealed sample to within the detectable energy range and concentration limits of the DLTS system. The DLTS system used in this study can detect concentration levels to five orders of magnitude below the net donor concentration level. Depending on the temperature/current limit of each sample and the capture cross-section of the defect, the DLTS system can detect trap energy levels as large as 800 meV to 1.3 eV. Increasing the anneal temperature produced varied effects on the deep level defects. Several deep level defects increased in concentration, several decreased, and some showed little effect from changes in the anneal temperature ( $T_A$ ). Electrical properties were also affected by changes in the anneal temperature. Changing the implantation temperature ( $T_I$ ) resulted in changes in both the formation of the deep level defects and the electrical properties of the diodes. Variation was also detected with changes in implantation dose and intrinsic net donor concentration.

## VI-1-A Electrical Properties

Temperature-dependent current-voltage measurements were performed over a temperature range of 100 to 700 K. Forward biased I-V-T measurements showed characteristic Sah-Noyce-Shockley (SNS) conduction. SNS recombination-generation theory identifies three current components – 1) diffusion across the barrier junction; 2) recombination in the depletion region; and 3) tunneling across the depletion region.

Figures VI-1 and VI-2 show typical I-V-T profiles for an ion-implanted sample in forward and reverse bias, respectively. The dominance of recombination or shunting behavior found in a large quantity of the tested diodes indicate the commonness of high concentrations of deep traps. The characteristic tunneling current can be seen as the dominant current component at the lower voltage levels.

Figure VI-3 shows typical C-V curves plotted as  $C^{-2}$  vs.  $V_{REV}$  for quality test diodes used in this research. A changing slope indicates a changing net donor concentration at the depletion region edge. A smaller slope corresponds to a larger net donor concentration. For most of the tested diodes with ion-implantation dose of  $\phi = 5 \times 10^{12} \text{ cm}^{-2}$ , the largest net donor concentrations tended to be near the diode junction (small  $V_{REV}$ ). However, for the higher doped samples ( $\phi = 1 \times 10^{14}$  and  $2 \times 10^{14} \text{ cm}^{-2}$ ), the net donor concentration peaked near a reverse bias of 3 volts. This is indicated by the shallower slope over the -2 to -4 volt range. The -3 volt reverse bias for the maximum net donor concentration corresponds quite well with the measured and predicted peak implantation concentration of 2500 Å. Most of the tested diodes produced C-V curves similar to the ones shown and fit well to the theoretical linear curve for a one-sided abrupt diode. The deviation from a

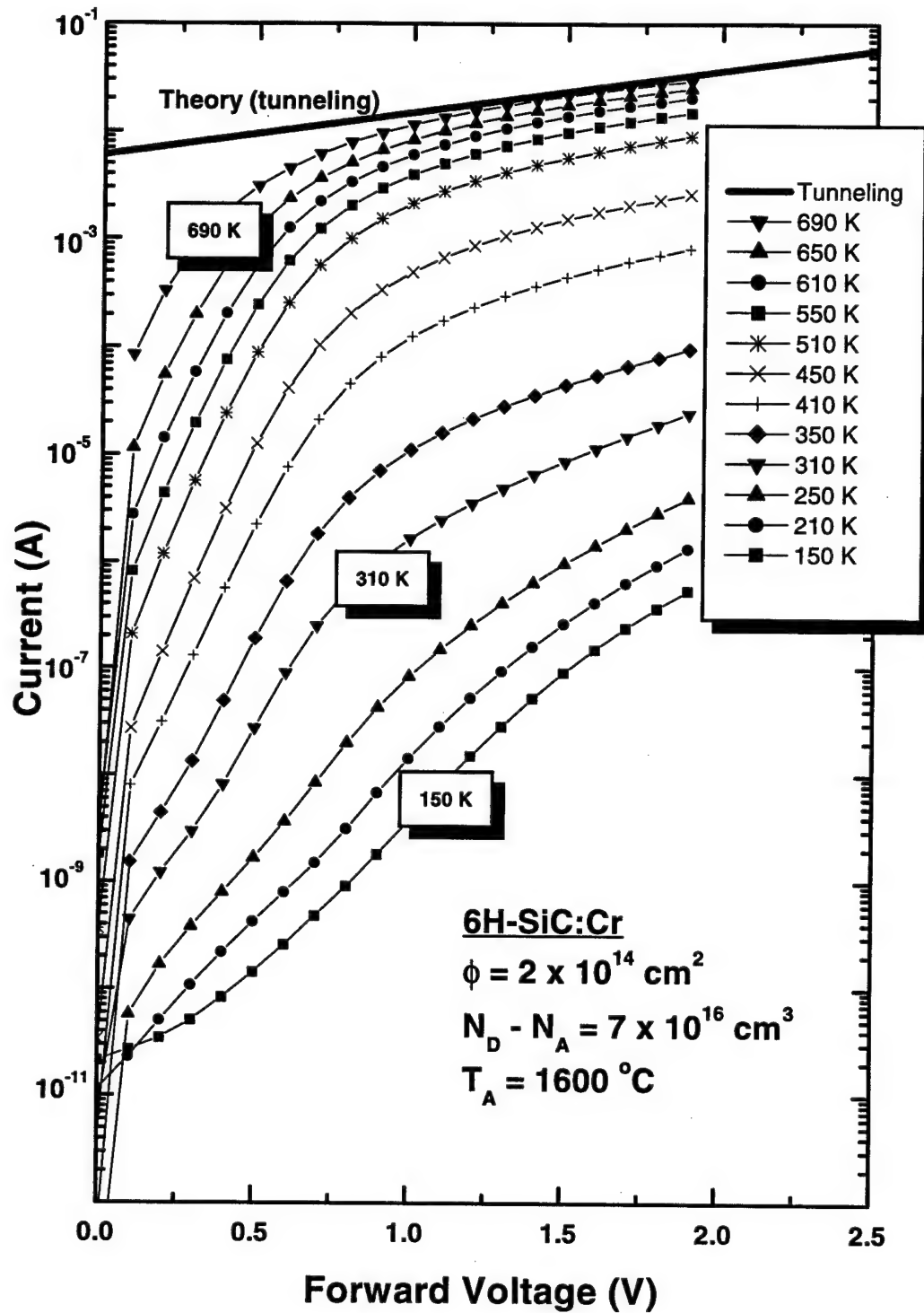


Figure VI-1. Typical forward-bias I-V-T curves for ion implanted 6H-SiC diodes chosen for DLTS measurements. The voltage range shown is where tunneling effects dominate the current. Most of the diodes used in this study had this "leaky" tunneling current. Above this voltage range, diffusion and recombination currents became the dominant current components. The theoretical tunneling current is plotted for reference.



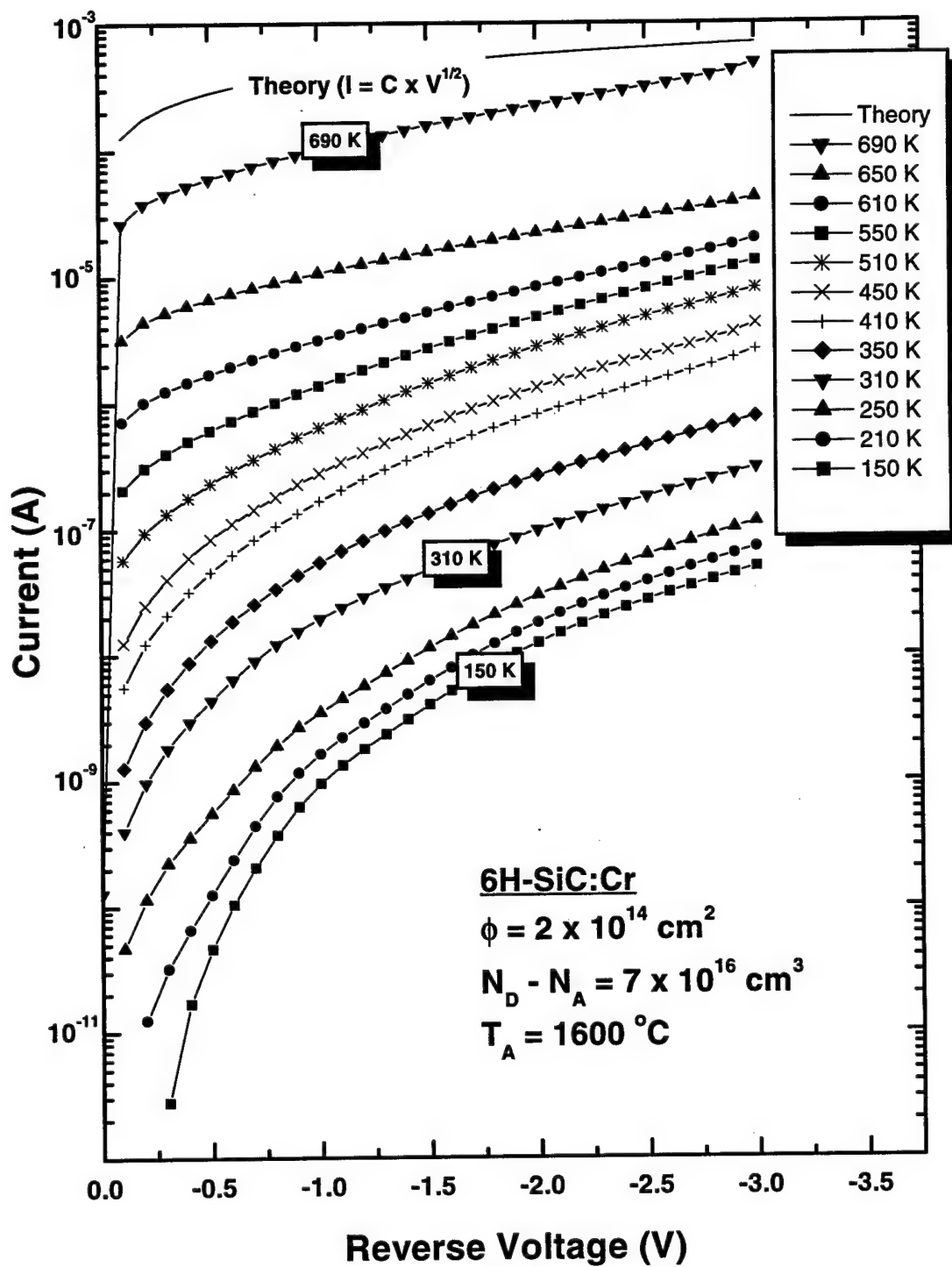


Figure VI-2. Typical reverse-bias I-V-T curves for ion-implanted 6H-SiC diodes chosen for DLTS measurements. The 6H-SiC Schottky diodes showed this consistent performance over the temperature range of 150 to 700 K. The theoretical  $V^{1/2}$  reverse-current dependency curve is plotted for reference.

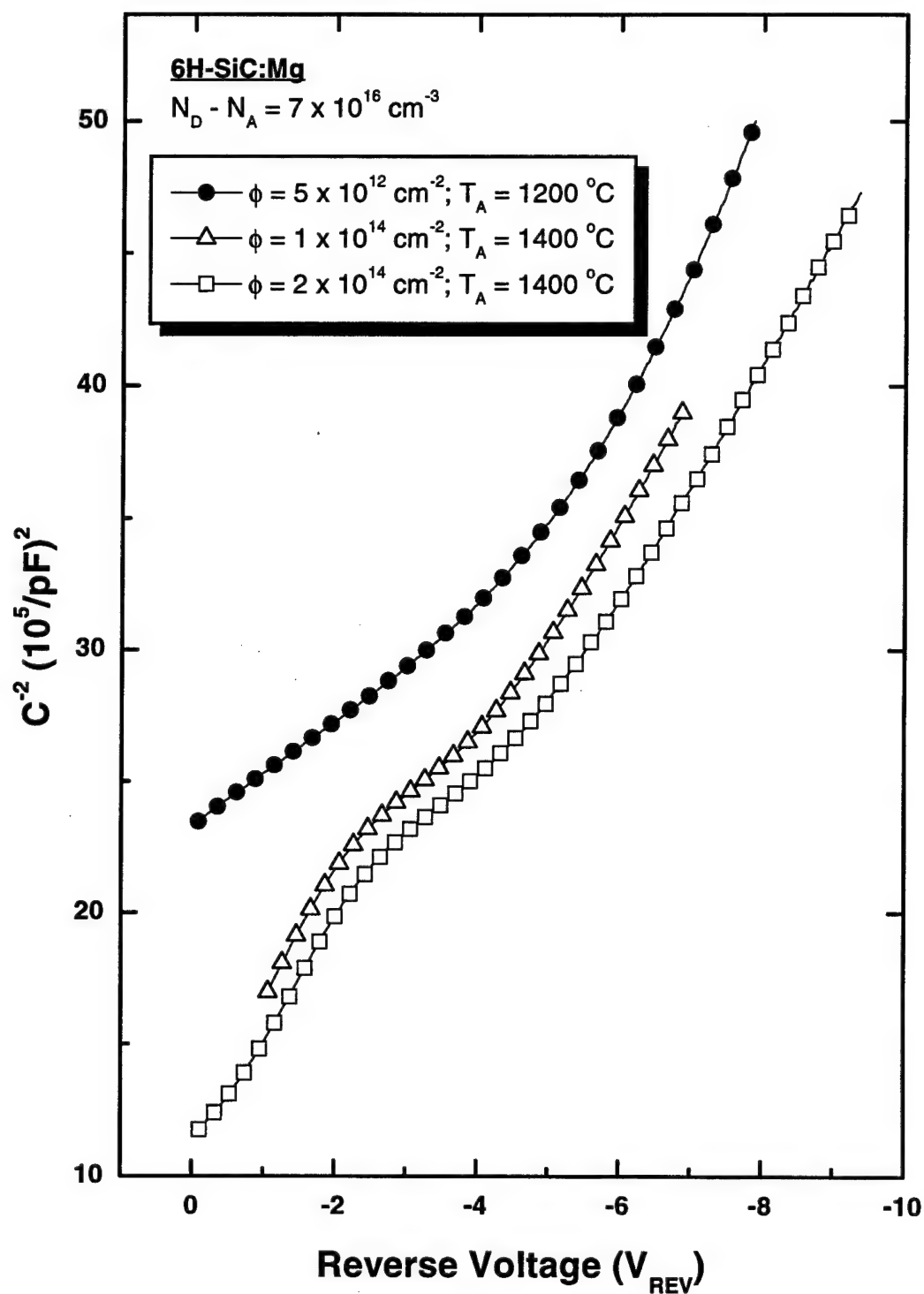


Figure VI-3. Typical C-V curve for the diodes used in this study (plotted  $1/C^2$  vs  $V_{\text{REV}}$ ). A changing slope indicates a changing net doping concentration. The reduced slope near  $V_{\text{REV}} = -3$  volts indicates a significant increase in the net doping concentration at the peak ion implantation depth (2500 Angstroms).

uniform concentration was important since the equations for DLTS were developed for a uniformly doped material and the use of the depletion approximation. It is from those assumptions that the capacitance-voltage function is derived. With non-uniform doping, we no longer have a linear  $C^{-2}$  vs.  $V_{REV}$  relationship. Instead, we must examine the rate of change of these variables ( $\Delta C^{-2}$  versus  $\Delta V_{REV}$ ). In this way, we can still determine the net donor concentration at the depletion edge.

The equation for the net donor concentration changes from

$$N_d = 2C^2 / ((V - kT/e) \epsilon \epsilon_0 A^2)$$

for uniform doping to

$$N_d(x_d) = -C^3 / (\epsilon \epsilon_0 A^2) * (\Delta C / \Delta V)^{-1}$$

for non-uniform doping.

In a DLTS measurement, the defect concentration is determined by knowing the net donor concentration at the depletion edge during the measurement,

$$N_t = 2(\Delta C)N_d / C(\infty),$$

where  $\Delta C$  is the change in capacitance during the measurement and  $C(\infty)$  is the steady state capacitance.

Figure VI-2 shows the reverse bias I-V-T for a typical test device (6H-SiC:Cr,  $T_A = 1600^\circ\text{C}$ ). If a generation center is dominant, the reverse current will approximate

$$I_{REV} = A[\exp(-E_a/kT)],$$

where  $E_a$  is the activation energy for the dominant center. Thus, the slope of a natural log plot of the reverse current vs.  $1/T$  for a fixed voltage will yield the activation energy.

Figure VI-4 shows the plot of the  $\ln(I)$  vs.  $1/T$  plot for  $V = -1.5$  V for the same sample shown in Fig. VI-2. Three distinct linear sections appear in the curve. The steepest linear section corresponds to a midgap center, at 1.5 eV. The next linear section gives a 250 meV deep generation center, and the shallowest linear section corresponds to a shallow 20 meV center. These values are based on the assumption of the dominant current being generation. The leakage current limit of the DLTS system prevented a confirmation measurement of the midgap level. However, trap levels near 250 meV were detected by DLTS in this sample. Significant reductions in the leakage current with increased annealing temperature were not observed either in the unimplanted or in the argon-implanted samples. This may be due to the high concentration of the 1.5 eV midgap level defect or to a high concentration of micropipes, which still plagues this material. Micropipes are screw-like dislocations that are formed during semiconductor growth, and have been attributed to premature breakdown in SiC (Neudeck, 1996). However, the leakage current in 6H-SiC:Cr was reduced significantly with increased anneal temperature. This suggests that chromium may be complexing with this near midgap level defect.

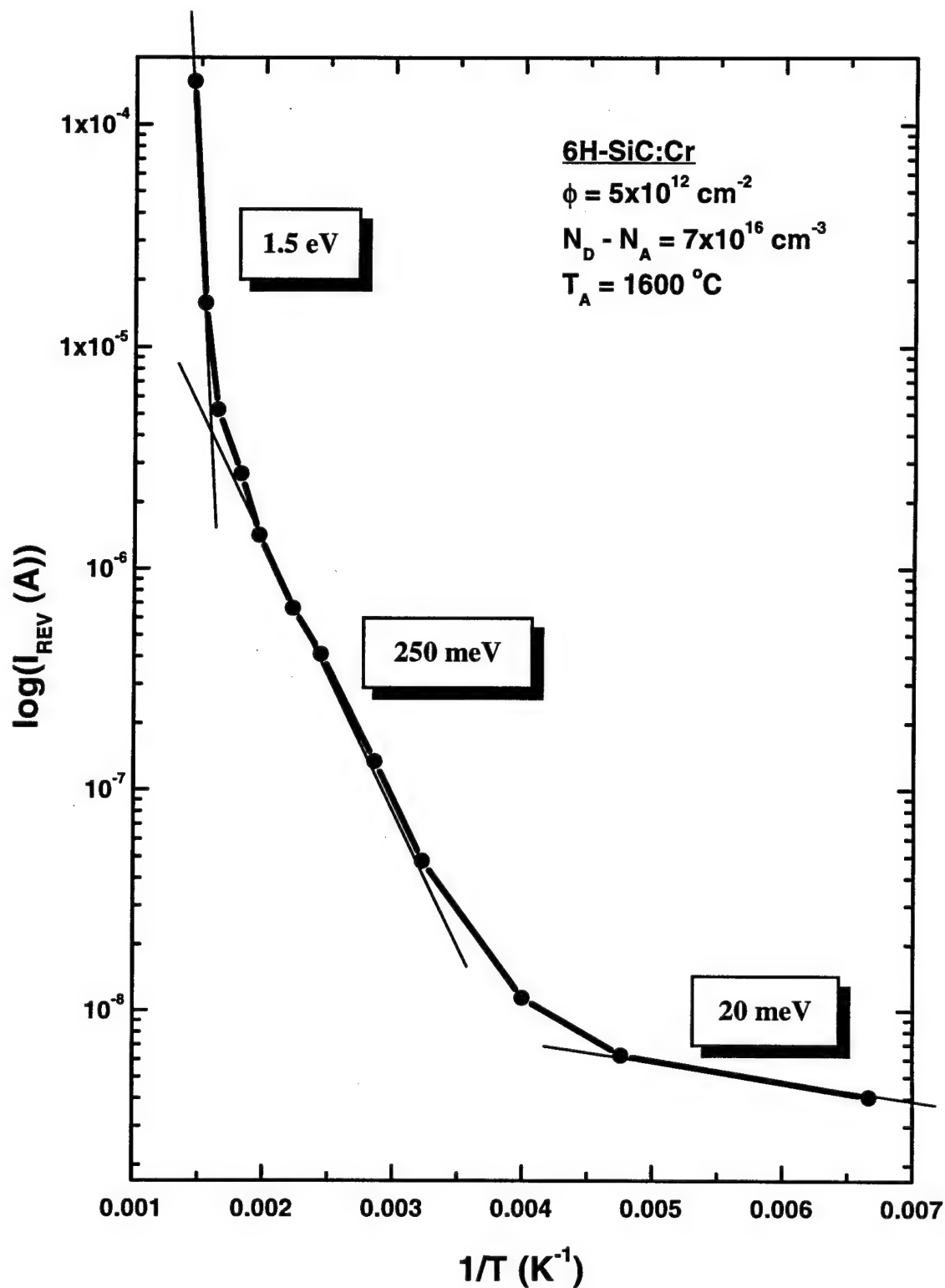


Figure VI-4. Arrhenius plot of Cr-implanted 6H-SiC Schottky diode showing three generation centers dominating the reverse current ( $V_{\text{REV}} = -1.5 \text{ V}$ ). The deeper level is at the midgap, the shallowest is near 20 meV, and the middle value is approximately 250 meV.

## VI-1-B Deep Level Transient Spectroscopy

DLTS measurements were made, from 100 to 700 K, using a computer controlled and triggered deep level transient spectrometer. Computer controlling allows automated incremental stepping through the temperature range and digital recording of the isothermal capacitance transients. To extract the trap parameters, post-test analysis employed both the modulating functions technique (Scofield, 1995) and curve fitting of the rate window curves. The modulating functions technique provides improved trap parameter characterization compared to Fourier transform or traditional analog methods. This is particularly important for defects in 6H-SiC where its polytypism often results in close energetic level pairs due to lattice site inequivalencies. Unfortunately, a coefficient error in the modulating functions based code was discovered late into the research that forced the use of curve fitting as the main characterization technique to obtain the trap parameters. However, the modulating functions routine was still used to identify trap levels. Manual curve fitting was also performed to augment the modulating functions technique, to gain an insight on the sensitivity of the rate window peaks to the trap parameters, and to increase the accuracy of the estimated trap parameters when the modulating functions software was limited by preset features such as the number of exponential terms that could be used to fit the transient capacitance traces.

The rate window plots shown for the high-temperature (475 °C) implanted samples used a rate window of  $\tau^{-1} = 402.4 \text{ s}^{-1}$  ( $\tau = [t_2 - t_1] / \ln[t_2/t_1]$ ). The room-temperature (23 °C) implanted samples used a rate window of  $\tau^{-1} = 511.7 \text{ s}^{-1}$ . The rate window is determined by the start and stop time of the recorded transient capacitance ( $t_1$  and  $t_2$ ). For  $\tau^{-1} = 402.4$

$s^{-1}$ ,  $t_1$  is 1 ms and  $t_2$  is 5 ms and for  $\tau^{-1} = 511.7 s^{-1}$ ,  $t_1$  is 0.5 ms and  $t_2$  is 5 ms. This difference in the starting time ( $t_1$ ) was accounted for during the analysis, and did not impact the ability to compare the DLTS and Arrhenius measurements. A rate window peak is formed when the emission rate of a deep level trap equals  $\tau^{-1}$ . This occurs at a specific sample temperature depending on two of the three trap parameters (trap energy ( $E_t$ ) and trap capture cross-section ( $\sigma_t$ )). The difference capacitance ( $C_2 - C_1$ ) or rate window plots have been normalized to the steady state capacitance ( $C_\infty$ ) which correlates to the net ionized donor concentration at each temperature. Unless otherwise indicated, the DLTS measurements shown were taken using constant-voltage deep level transient spectroscopy (CV-DLTS). This technique was sufficient for most of the diodes examined in this study. Constant-capacitance deep level transient spectroscopy (CC-DLTS) was used only when the concentration of the deep trap levels became greater than 20% of the net donor concentration. Double-correlated DLTS (DDLTS) was used to record the depth profile of the concentration of the deep level defects or when electric field effects were examined to determine the charge state of a trap. Deep level transient spectroscopy is a sensitive enough technique to be used for examining thin cross-sections of the depletion region.

Figures VI-5 and VI-6 show the main principles of a DLTS experiment. The first graph in Fig. VI-5 illustrates the cycling of the filling and reverse bias pulses. This bias cycling is done to collapse the depletion region (forward bias) to permit the trap defects in that region to trap carriers then reform the depletion region (reverse bias) to permit detrapping. The second graph in Fig. VI-5 shows the corresponding cycling of the measured diode capacitance transient as a function of time. Both the filling and emptying

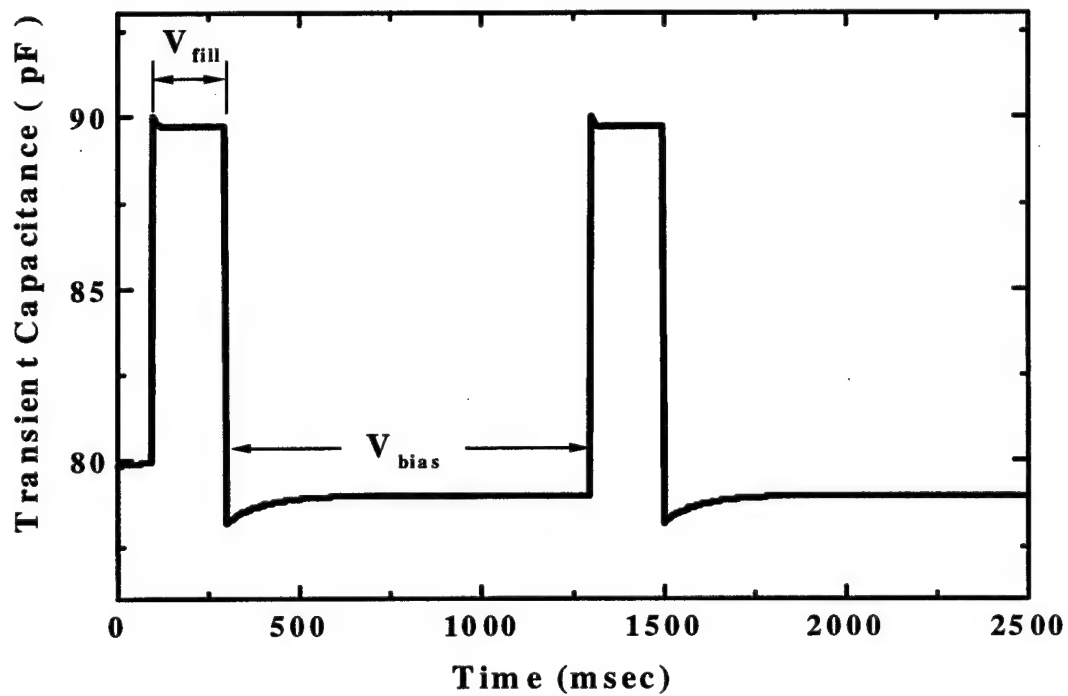
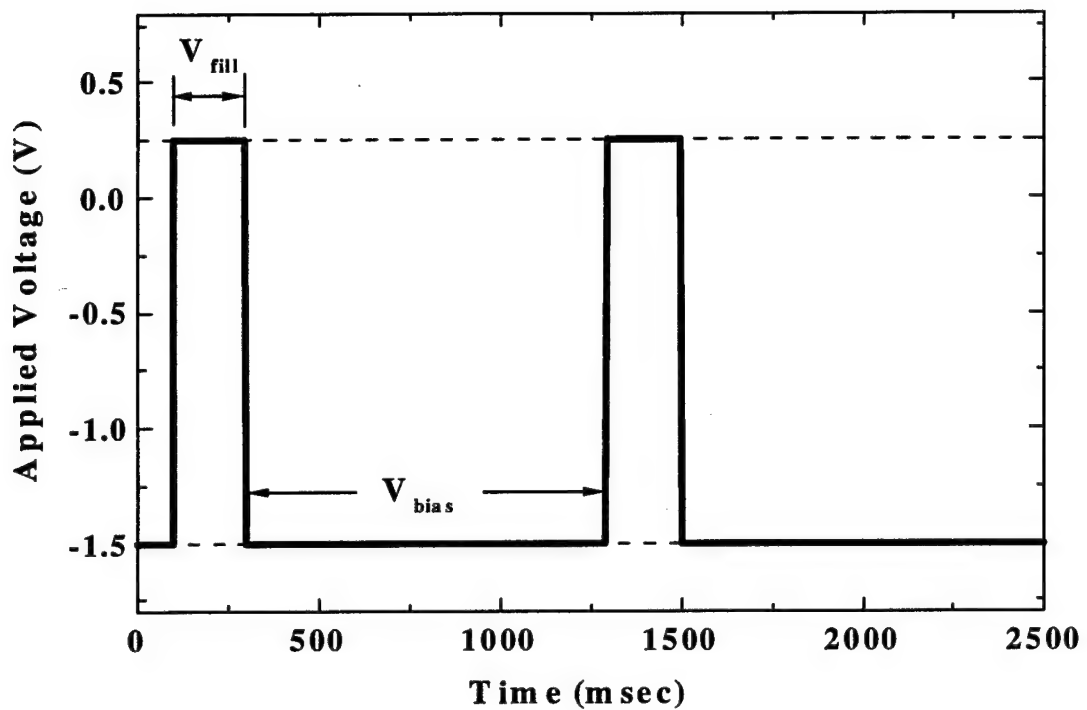


Figure VI-5. Principles of Deep Level Transient Spectroscopy - 1) Collapse and re-establishment of the depletion region using alternating filling and reverse biases, 2) Corresponding transient capacitance due to trapping and detrapping.



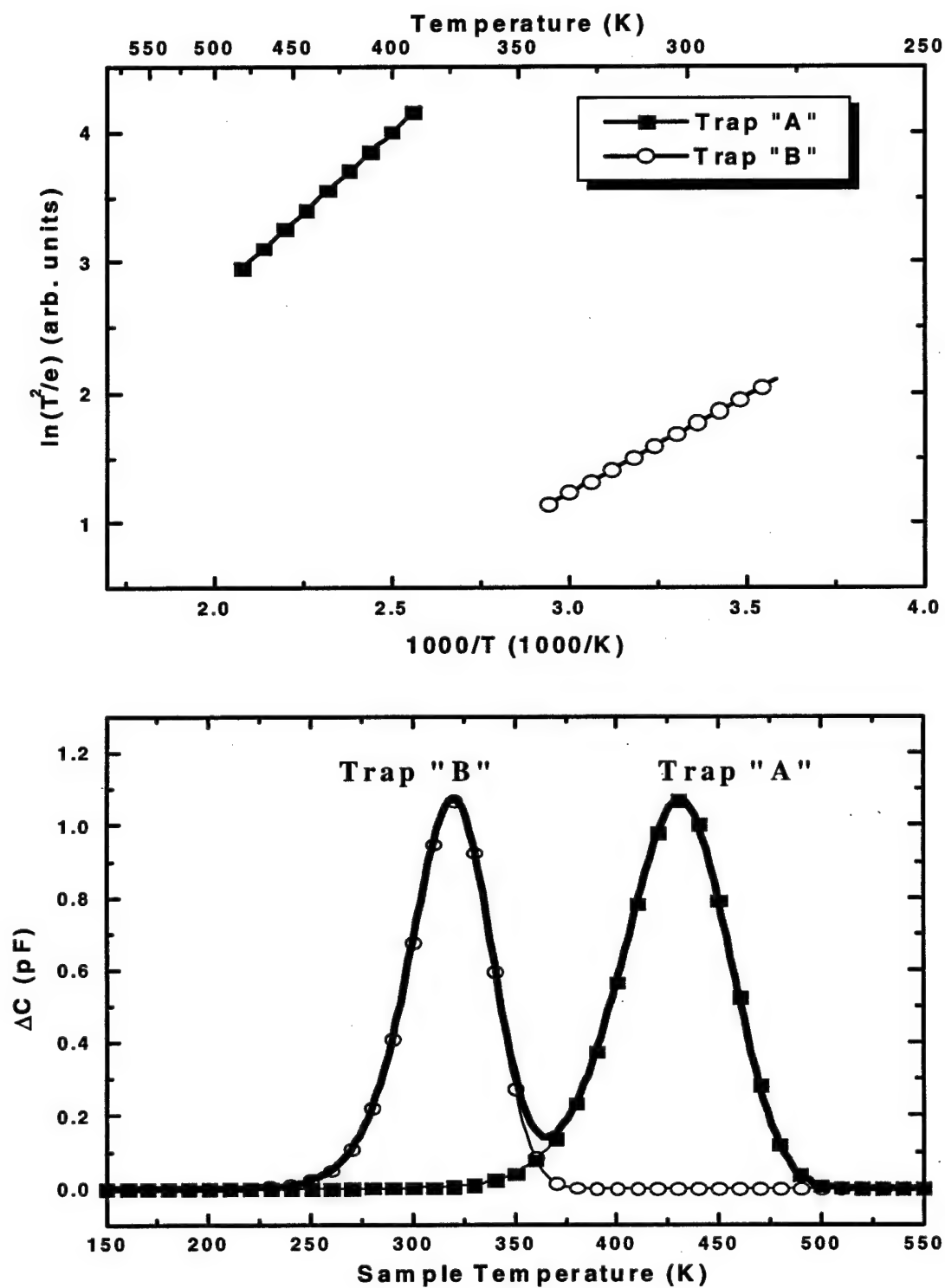


Figure VI-6. Principles of Deep Level Transient Spectroscopy - 3) Arrhenius plot showing the "trap signatures" of two deep levels and 4) Rate window plot showing two trap peaks.

pulse produce exponential curves. The first graph in Fig. VI-6 is an Arrhenius plot showing the response of two deep level defects as the temperature is lowered (the x-axis is in inverse temperature and the y-axis is in natural log of the time constant divided by  $T^2$  ( $\ln(\tau/T^2)$ )). As the temperature of the sample is lowered, the time constant of the trap level becomes larger. The second graph in Fig. VI-6 is a rate window plot showing the two rate window trap peaks. Each peak is located at the temperature where its trap time constant equals the reference time constant ( $\tau_{ref}$ ) or the inverse emission rate ( $e_n^{-1}$ ). Changing either the  $t_1$  or  $t_2$  times will result in a shift in the trap peak temperature position.

The change in the capacitance ( $\Delta C = C(t_1) - C(t_2)$ ) and the steady-state capacitance ( $C_\infty$ ) is used to determine the trap concentration ( $N_t$ ). The Arrhenius and rate window plots are used to determine the trap activation energy ( $E_t$ ) and the trap capture cross-section ( $\sigma_t$ ).

## VI-1-B-1 DLTS of 6H-SiC:Ar

Figure VI-7 shows the rate window plots (rate window =  $402.4 \text{ s}^{-1}$ ) from DLTS measurements of one unimplanted/unannealed and two Ar-implanted and annealed n-type 6H-SiC samples (implant dose =  $2 \times 10^{14} \text{ cm}^{-2}$ ,  $N_D - N_A = 7 \times 10^{16} \text{ cm}^{-3}$ ). The two 6H-SiC:Ar samples were ion implanted at  $475^\circ\text{C}$  and annealed at  $T_A = 1200$  and  $T_A = 1400^\circ\text{C}$  for 120 min, respectively. The DLTS response of the unimplanted/unannealed sample shows no deep level trap concentrations above the detectable level of approximately  $10^{11}$  to  $10^{12} \text{ cm}^{-3}$ . This was also true for the unimplanted/annealed ( $T_A = 1400^\circ\text{C}$ ) sample (not shown). The lack of any DLTS detectable trap levels in as-grown material is a good indication of the improved quality of epitaxial material over bulk 6H-SiC, which consistently possesses a high concentration of vanadium-related traps (Scofield, 1996) (Evwaraye *et al.*, 1994). Also, the lack of any DLTS detectable trap levels in the unimplanted/annealed sample indicates that the observed traps in the argon-implanted samples are created via ion implantation, and are not anneal-activated traps consisting of solely intrinsic defects. The rate window plot shown Fig. VI-7 for the  $1400^\circ\text{C}$  annealed 6H-SiC:Ar sample has been magnified by 20 to reveal its features.

Six dominant DLTS peaks at 216, 243, 270, 294, 316 and 339 K were observed from the  $1200^\circ\text{C}$  annealed 6H-SiC:Ar sample. These peaks appeared in pairs and were identified through the curve fitting of the rate window data using DLTS rate window peaks.

As shown in Fig. VI-7, the 339 K peak trap has an activation energy ( $E_t$ ) of 615 meV, capture cross-section ( $\sigma_t$ ) of  $1.0 \times 10^{-15} \text{ cm}^2$ , and a concentration ( $N_t$ ) of  $7.82 \times 10^{15} \text{ cm}^{-3}$ . A 615 meV trap with similar trap parameters was also reported by Pensl *et al.* in e-

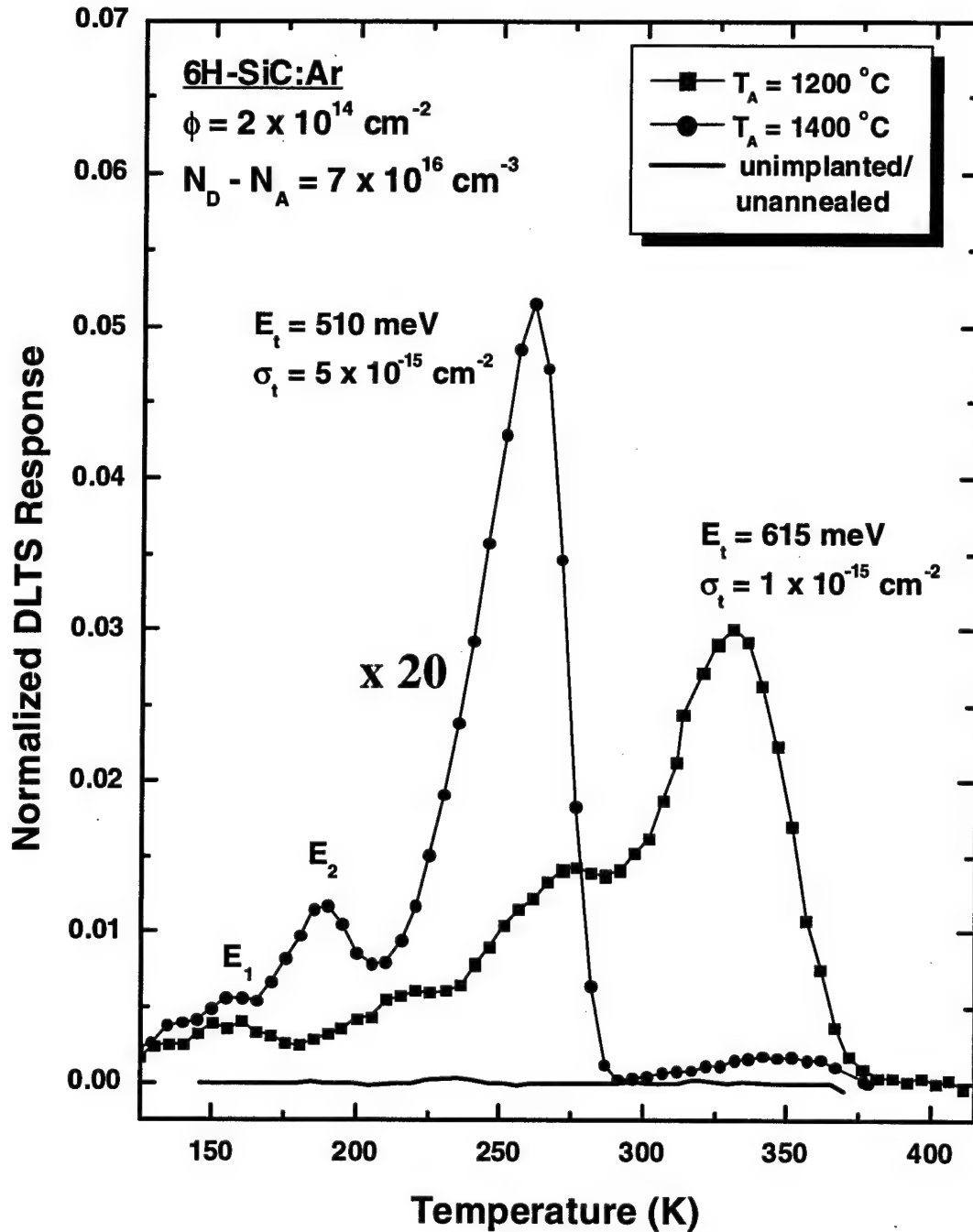


Figure VI-7. Rate window (CV-DLTS) plot of two 6H-SiC:Ar diodes annealed at 1200 and 1400 °C. Also shown is the CV-DLTS response of the unimplanted-unannealed 6H-SiC diode. The peaks labeled  $E_1$  and  $E_2$  correspond to traps similarly identified by Pensl. [Pensl and Choyke, 1993] The  $T_A = 1400^\circ \text{C}$  curve has been enlarge 20 times for clarity.

irradiated n-type LPE grown 6H-SiC films (Pensl and Choyke, 1993). Pensl attributed this peak to a double vacancy  $V_C-V_{Si}$  by correlating to the defect identified in a photoinduced electron spin resonance study by Vainer *et al.* (Vainer and Il'in, 1981). However, it has also been reported that carbon vacancies are annihilated between 100 and 300 °C, Si vacancies become mobile at around 750 °C, and divacancies are annihilated by 450 °C anneal in 3C-SiC (Itoh, 1989 and 1992). In addition, Kawasuso *et al.* showed that only one kind of vacancy-type defect is present in as-grown n-type 6H-SiC (Kawasuso, 1996), and theoretical positron lifetime calculations by Brouer *et al.* suggested that this is a Si vacancy (Brouer, 1996). Therefore, we believed that this 615 meV peak observed in this study is not due to a  $V_C$ -related defect. Furthermore, in this study, the concentration of this 615 meV majority electron trap is dramatically reduced by over 95 % when the annealing temperature is increased from 1200 to 1400 °C. Similar annealing behavior has been observed by Kawasuso *et al.* in n-type 6H-SiC with an observed defect disappearing at around 1400 °C. He attributed this 1400 °C annihilated trap to complexing of an impurity atom with  $V_{Si}$  (Kawasuso, 1996).

Figure VI-8 illustrated the composite effect of these six peaks in forming the rate window curve. Studies were made to understand the sensitivity of the trap parameters on fitting the rate window curves. The tolerances are  $\pm 5\%$  for the trap energy ( $E_t$ );  $\pm 50\%$  for the capture cross-section ( $\sigma_t$ ); and  $\pm 5\%$  for the trap concentration ( $N_t$ ). The 50 % uncertainty in the  $\sigma_t$  value is not significantly large. The uncertainties of the peak position and peak width values in the rate window plots depend on the uncertainty in the log of  $\sigma_t$  (and not  $\sigma_c$ ) in the same manner as they depend on the uncertainty of the  $E_t$  value.

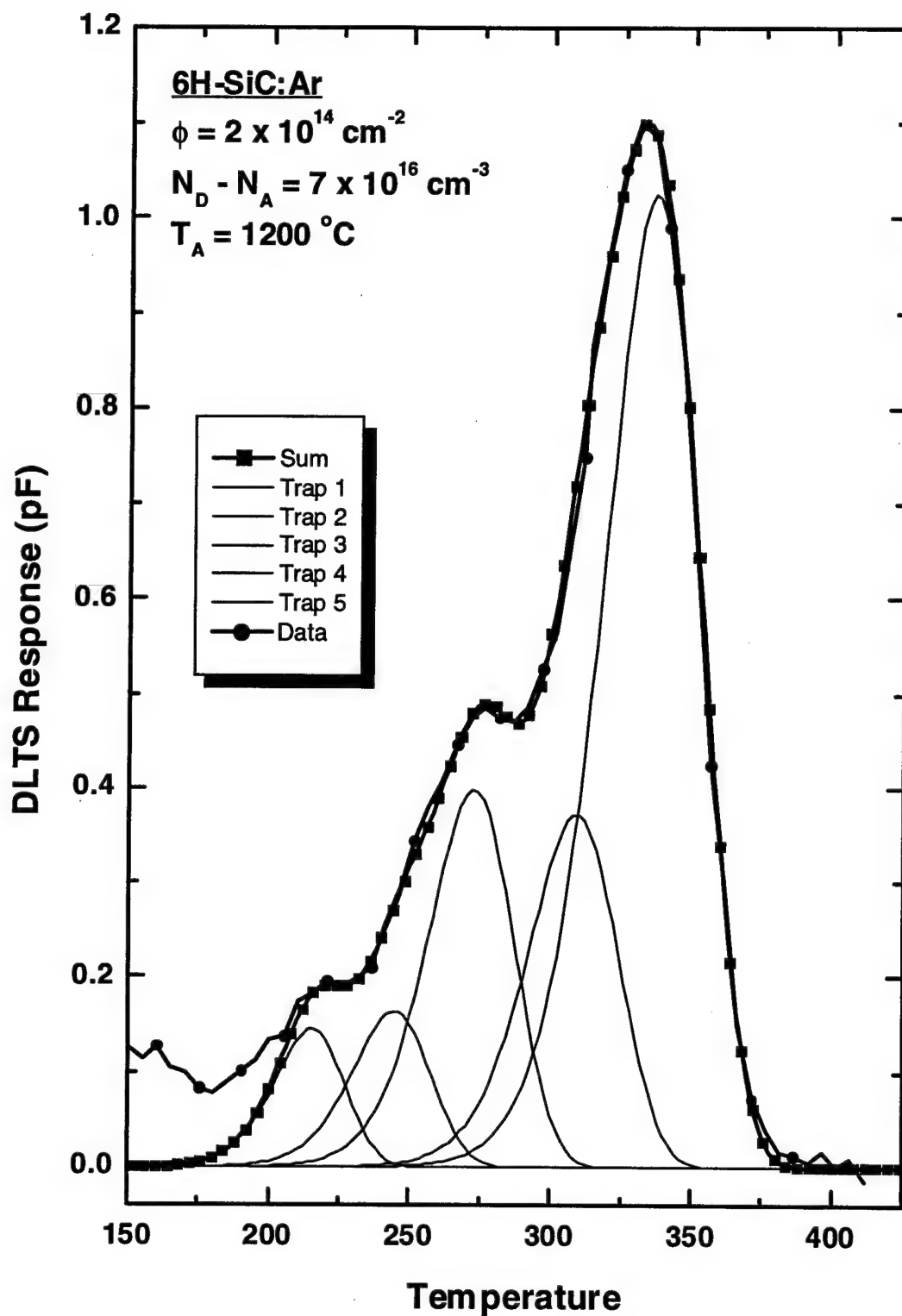


Figure VI-8. Composite curve fitting of rate window curve using DLTS rate window peaks for the sample 6H-SiC:Ar, annealed at 1200 °C.

The asymmetry of the rate window peak; the sensitivity of the peak's width and temperature position to both the trap energy and trap capture cross-section; the observed peak-pairing condition; and the observed isolated peaks formed in the variety of tested samples permitted this level of detailed curve-fitting. Published DLTS articles on both ion-implanted 6H- and 4H-SiC were used to compare the reasonableness of the fitting parameters.

Figure VI-9 illustrates the effect of increasing the ion implantation dose by 100 times on the concentration of this 615 meV electron trap. Shown are two rate window plots for the two 1200 °C annealed 6H-SiC:Ar samples ( $N_D - N_A = 7 \times 10^{16} \text{ cm}^{-3}$ ) with implantation doses of  $2 \times 10^{12}$  and  $2 \times 10^{14} \text{ cm}^{-2}$ , respectively. The concentration of the 615 meV trap increases dramatically while the concentrations of the remaining trap are reduced. It appears that this damage-related 615 meV electron trap is the most efficiently formed trap by a 500 °C argon-implant and subsequent high-temperature anneal of 1200 °C.

As seen in Fig. VI-9, the trap shoulder peak at 393 K is significantly reduced by an increase in the implantation dose for the 1200 °C annealed samples. Curve-fitting analysis revealed a trap energy of 645 meV for the 393 K peak with a capture cross-section of  $1.0 \times 10^{-16} \text{ cm}^2$ . Increasing the implantation dose results in increased damage to the lattice. If the damage becomes high enough, damage clusters can start to form, which can lower the observed concentration of the traps by forming clusters. This may be the case here. Another explanation may be that the damage-related trap responsible for the peak may be a complex forming a coupled trap pair. This pair may create a lower energy trap that may be annihilated with a higher anneal temperature. This same dose effect is also observed in the trap peaks at 246, 213, and 150 K.

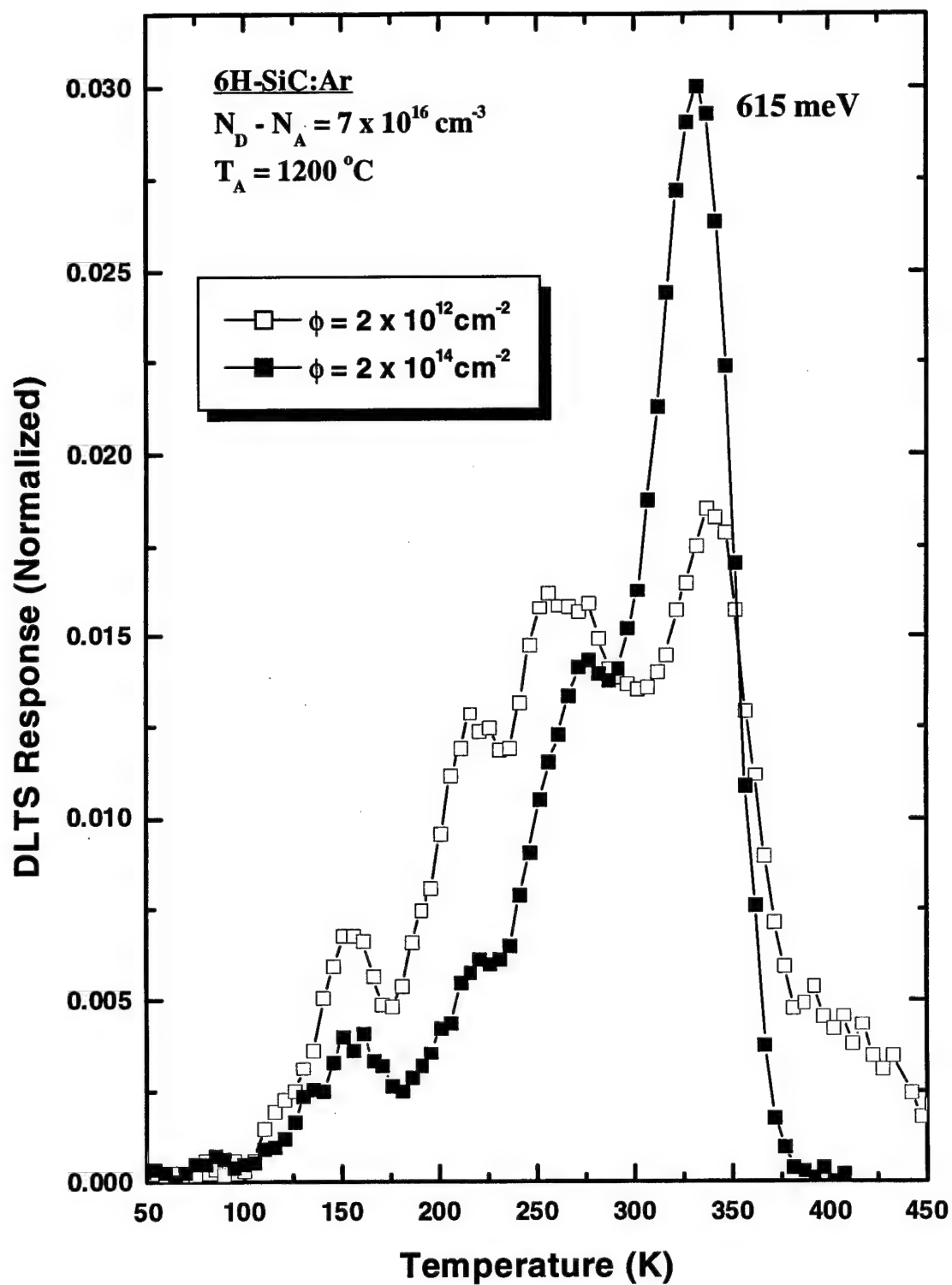


Figure VI-9. Two rate window plots illustrating the effect of implantation dose on the 615 meV trap peak in argon-implanted 6H-SiC. Note the change in peak heights as the ion implantation dose is increased by two orders of magnitude.



Curve-fitting analysis of the paired peak at 316 K resulted in trap parameters of  $E_t = 576$  meV,  $\sigma_t = 1 \times 10^{-15}$  cm<sup>2</sup>, and  $N_t = 3.85 \times 10^{15}$  cm<sup>-3</sup>. This peak trap behaves identically as the 615 meV peak trap with changes in annealing temperature, implantation dose, and donor concentration. The remaining four damage-related trap peaks also behave in pairs (294 and 270 K peaks, and 243 and 216 K peaks) to changes in anneal temperature, implantation dose, and donor concentration. This peak pairing is consistent with the inequivalent lattice site structure of silicon carbide. In the 6H polytype of SiC, the ratio of hexagonal to cubic sites is 2 to 1. The concentration ratios between peak pairs are near this 2:1 ratio. Pairing is also seen in the 4H-SiC luminescent spectra reported in this study. The computed trap parameters for these six trap peaks are summarized in the first section of Table VI-2. No published literature was found that reported on these observed peak traps. All the trap levels detected in the argon-implanted samples are attributed to damage-related defects since argon is an inert implant species.

Figure VI-10 shows the effect of the net donor concentration ( $N_D - N_A$ ) on the formation of the 615 meV electron trap. Shown are three rate window plots for the three 1200 °C annealed 6H-SiC:Ar samples ( $\phi = 2 \times 10^{12}$  cm<sup>-2</sup>) with net donor concentration of  $1 \times 10^{16}$ ,  $7 \times 10^{16}$ , and  $1 \times 10^{17}$  cm<sup>-3</sup>. The three DLTS curves that are shown in Fig. VI-10 have been normalized to the steady state capacitance of each diode. The steady state capacitance is proportional to the net donor concentration ( $N_D - N_A$ ). Therefore, if the normalized peak height is unchanged as the net donor concentration is changed, the concentration of the related trap is proportionally to the net donor concentration. This is exactly

$\phi = 2 \times 10^{14} \text{ cm}^{-2}, N_D = 7 \times 10^{16} \text{ cm}^{-3},$ $T_A = 1200^\circ \text{C}$			
Temp of Peak (K)	Trap Energy (meV)	Capture Cross-section (cm <sup>2</sup> )	Trap Conc. (cm <sup>-3</sup> )
339	615	$1 \times 10^{-15}$	$7.82 \times 10^{15}$
316	576	$1 \times 10^{-15}$	$3.85 \times 10^{15}$
294	470	$1 \times 10^{-16}$	$1.75 \times 10^{15}$
270	427	$1 \times 10^{-16}$	$3.35 \times 10^{15}$
243	383	$1 \times 10^{-16}$	$1.6 \times 10^{15}$
216	331	$9 \times 10^{-17}$	$1.4 \times 10^{15}$

$\phi = 2 \times 10^{12} \text{ cm}^{-2}, N_D = 7 \times 10^{16} \text{ cm}^{-3},$ $T_A = 1200^\circ \text{C}$			
Temp of Peak (K)	Trap Energy (meV)	Capture Cross-section (cm <sup>2</sup> )	Trap Conc. (cm <sup>-3</sup> )
393	645	$1 \times 10^{-16}$	$1.4 \times 10^{15}$
343	625	$1 \times 10^{-15}$	$4.3 \times 10^{15}$
318	574	$1 \times 10^{-15}$	$1.8 \times 10^{15}$
294	470	$1 \times 10^{-16}$	$1.75 \times 10^{15}$
271	430	$1 \times 10^{-16}$	$2.85 \times 10^{15}$
246	385	$1 \times 10^{-16}$	$2.6 \times 10^{15}$
213	331	$1 \times 10^{-16}$	$1.4 \times 10^{15}$

$\phi = 2 \times 10^{14} \text{ cm}^{-2}, N_D = 7 \times 10^{16} \text{ cm}^{-3},$ $T_A = 1400^\circ \text{C}$			
Temp of Peak (K)	Trap Energy (meV)	Capture Cross-section (cm <sup>2</sup> )	Trap Conc. (cm <sup>-3</sup> )
266	510	$5 \times 10^{-15}$	$1.68 \times 10^{14}$
250	476	$5 \times 10^{-15}$	$5.3 \times 10^{13}$
230	437	$5 \times 10^{-15}$	$2.0 \times 10^{13}$
211	392	$3 \times 10^{-15}$	$1.5 \times 10^{13}$
191	310	$3 \times 10^{-16}$	$3.7 \times 10^{13}$
162	260	$3 \times 10^{-16}$	$1.5 \times 10^{13}$

$\phi = 2 \times 10^{12} \text{ cm}^{-2}, N_D = 7 \times 10^{16} \text{ cm}^{-3},$ $T_A = 1400^\circ \text{C}$			
Temp of Peak (K)	Trap Energy (meV)	Capture Cross-section (cm <sup>2</sup> )	Trap Conc. (cm <sup>-3</sup> )
356	690	$5 \times 10^{-15}$	$2.3 \times 10^{15}$
323	624	$5 \times 10^{-15}$	$4.25 \times 10^{15}$
287	558	$5 \times 10^{-15}$	$5.0 \times 10^{15}$
263	503	$5 \times 10^{-15}$	$3.25 \times 10^{15}$
241	371	$1 \times 10^{-16}$	$3.65 \times 10^{15}$
219	326	$1 \times 10^{-16}$	$2.3 \times 10^{15}$
191	307	$3 \times 10^{-16}$	$7.0 \times 10^{15}$
158	262	$3 \times 10^{-16}$	$3.0 \times 10^{15}$

Table VI-2. Computed trap parameters for n-type 6H-SiC implanted with argon at 475 °C. The uncertainties are:  $\Delta E_t = \pm 0.05 \cdot E_t$ ;  $\Delta \sigma_t = \pm 0.50 \cdot \sigma_t$ ; and  $\Delta N_t = \pm 0.02 \cdot N_t$ .

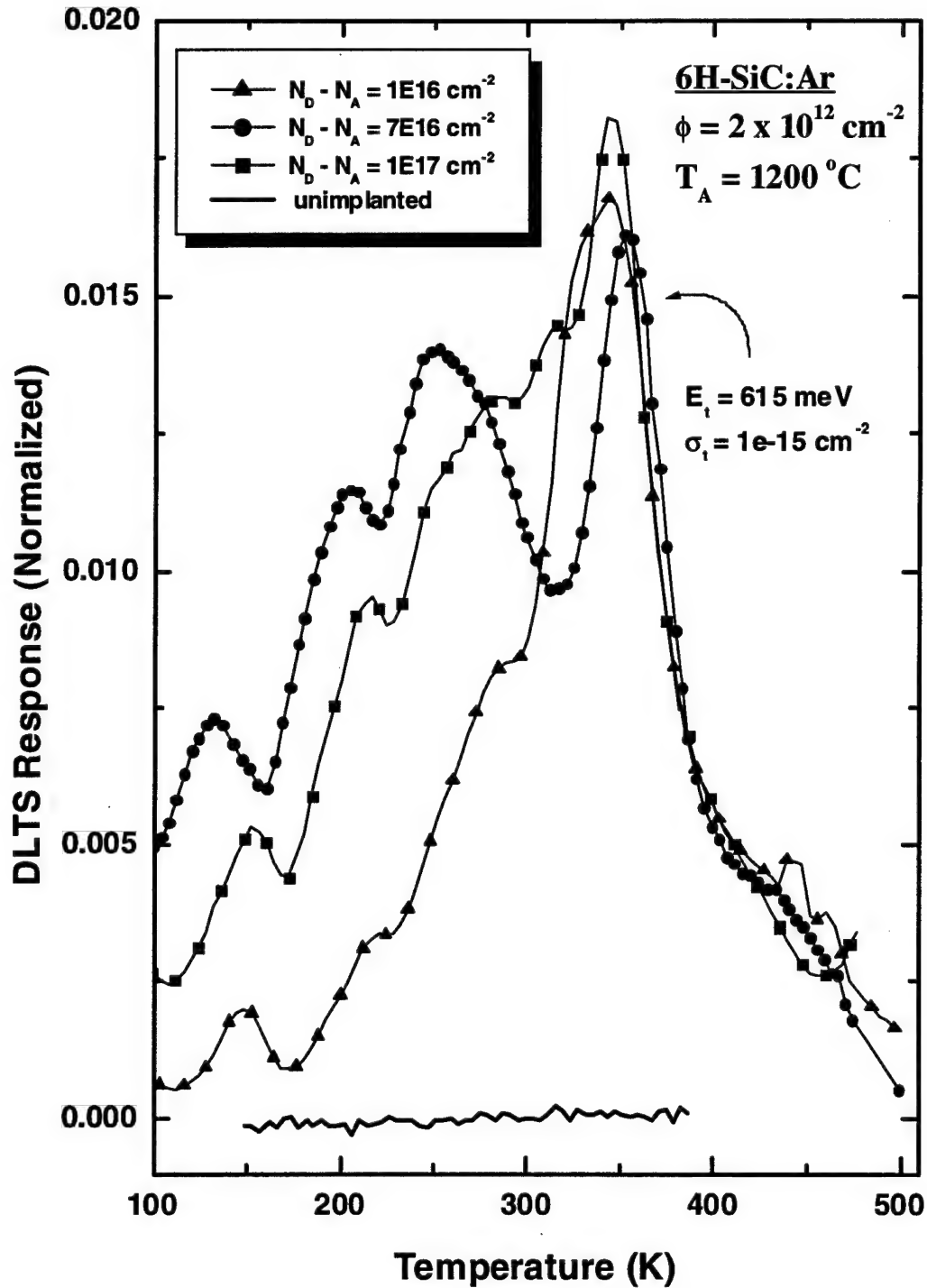


Figure VI-10. Donor concentration effect on the DLTS rate window plots. Shown are the normalized rate window plots for three n-type 6H-SiC:Ar diodes. The consistent peak height for the 615 meV trap indicates that the concentration of the trap is changing proportionally with the changing net donor concentration. This implies that one of the constituents of the 615 meV trap is substitutional nitrogen.

what is happening for the 615 meV trap. Nitrogen is used as the donor atom in the epitaxial growth process to form the donor levels in n-type 4H-SiC. Thus, substitutional nitrogen appears to be one of the constituents for this 615 meV trap. Since the concentration of the 615 meV peak is observed to proportionally increase with the net donor concentration (nitrogen) and the trap behavior correlates to reported trap behavior associated to a  $V_{Si}$ -related trap, this 615 meV trap may be a  $V_{Si}$ - $N_C$  complex.

The remaining damage-related trap concentrations increase dramatically when the net donor concentration is increased from  $1 \times 10^{16}$  to  $7 \times 10^{16} \text{ cm}^{-3}$ . This means that the concentrations of these traps are increasing faster than the increase in substitutional nitrogen. However, when the net donor concentration is further increased to  $1 \times 10^{17} \text{ cm}^{-3}$  the trend is reversed with their concentrations increasing slower than the increase in substitutional nitrogen. Apparently, the processes involved in the formation of these damage-related traps are sensitive to the concentration of substitutional nitrogen.

DDLTS (double-correlated DLTS) was also performed on these 6H-SiC:Ar samples in an attempt to determine the charge state of the trap levels and to examine the spatial distribution of traps. The results indicate that all the traps were neutrally charged and that the shallower energy level traps are concentrated more toward the surface of the epitaxial layer than the deeper energy level traps. In DDLTS, two transient measurements are made using two slightly different forward biases and a single reverse bias. This results in two depletion regions with slightly different widths. The two transients are differentiated and the resulting transient is analyzed as in normal DLTS. This permits the investigation of an isolated slice of the depletion region. By adjusting the reverse bias, the electric field in the investigated layer can be adjusted and charged traps will show a shift in their

trap energies. No shift was observed, leading to the conclusion that the observed traps were all charge neutral.

Increasing the anneal temperature to 1400 °C resulted in a significant change in the deep level transient spectra and subsequent rate window plots. Shown in figure VI-11 are the four rate window plots for the 1200 and 1400 °C annealed 6H-SiC:Ar samples for an implantation dose of  $2 \times 10^{14}$  and  $2 \times 10^{12}$  cm<sup>-2</sup>. The upper two curves have been shifted upward for clarity. Increasing an anneal temperature from 1200 to 1400 °C for higher implantation dose ( $\phi = 2 \times 10^{14}$  cm<sup>-2</sup>) samples (upper two curves) has the effect of decreasing all of the trap pair concentrations by approximately 20 times. Note that the rate window curve for the 1200 °C annealed sample has been magnified by a factor of 20 to show its features. This dramatic reduction indicates that the dissociation or annihilation temperature for these traps lie between 1200 and 1400 °C. While the concentrations of these six defect-related traps have been sufficiently reduced following a 1400 °C anneal, additional trap levels are observed in the 1400 °C annealed,  $2 \times 10^{14}$  cm<sup>-2</sup> dose sample, with the largest concentration trap peak occurring at 266 K. The computed trap parameters for all four samples shown are given in Table VI-2.

In the 1400 °C annealed sample with the higher implantation dose ( $2 \times 10^{14}$  cm<sup>-2</sup>), six different trap peaks are observed at 266, 250, 230, 211, 191, and 162 K. The 266 K peak trap has computed trap parameters of  $E_t = 510$  meV,  $\sigma_t = 5 \times 10^{-15}$  cm<sup>2</sup>, and  $N_t = 1.68 \times 10^{14}$  cm<sup>-3</sup>. Its associated pair trap at 250 K has trap parameters of  $E_t = 476$  meV,  $\sigma_t = 5 \times 10^{-15}$  cm<sup>2</sup>, and  $N_t = 5.3 \times 10^{13}$  cm<sup>-3</sup>. For a lower implantation dose, these trap peaks were not observed with the exception of the two peaks labeled  $E_1$  and  $E_2$ .

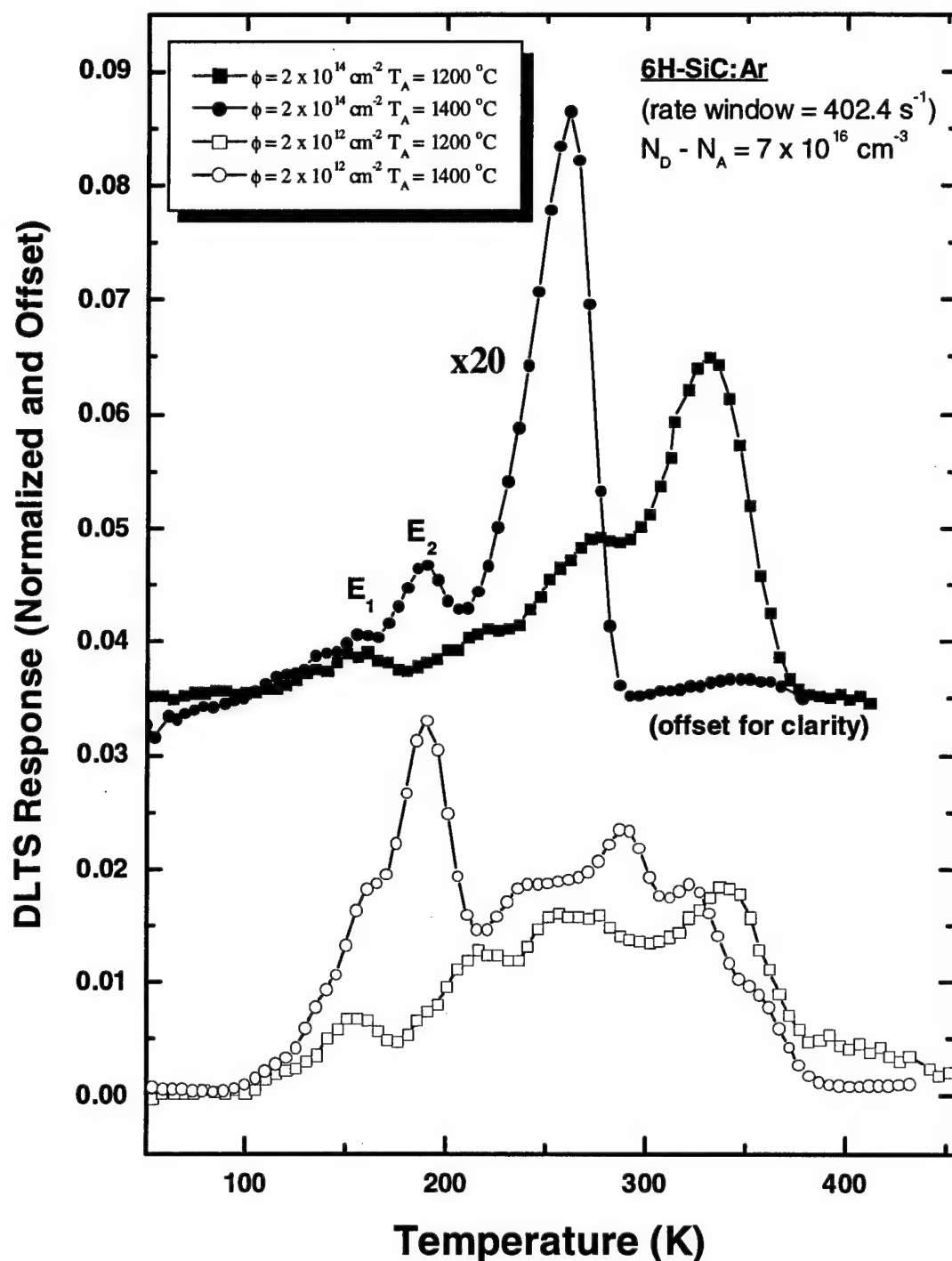


Figure VI-11. Rate window plots of argon-implanted n-type 6H-SiC at 475 °C. The two  $\phi = 2 \times 10^{14} \text{ cm}^{-2}$  curves have been offset for clarity. Also note that the  $\phi = 2 \times 10^{14} \text{ cm}^{-2}$ ,  $T_A = 1400^\circ\text{C}$  curve has been enlarged 20 times to show its features.

The two peaks labeled  $E_1$  and  $E_2$  at 162 and 191 K, respectively, in the 1400 °C annealed samples, were also reported by Pensl *et al.* in e-irradiated n-type LPE grown films (Pensl and Choyke, 1993). Curve fitting of the rate window curves resulted in trap parameters of  $E_t = 260$  meV,  $\sigma_t = 3 \times 10^{-16}$  cm<sup>2</sup>, and  $N_t = 1.5 \times 10^{13}$  cm<sup>-3</sup> for  $E_1$ , and  $E_t = 310$  meV,  $\sigma_t = 3 \times 10^{-16}$  cm<sup>2</sup>, and  $N_t = 3.7 \times 10^{13}$  cm<sup>-3</sup> for  $E_2$ . These values should only be used for comparison to other reported data because significant carrier freeze-out occurs in SiC below 200 K making the DLTS model assumptions invalid. Pensl and Choyke estimated the trap energy of the pair ( $E_1$  and  $E_2$ ) at 350 meV (Pensl and Choyke, 1993). The other measured traps found in this study for 6H-SiC:Ar have not been reported in the literature. As seen in the first 6H-SiC:Ar sample discussed, the traps also appear in pairs with similar capture cross-sections, near 2:1 concentration ratios, and trap energy differences of 40 to 50 meV. For both ion implantation doses, the two trap peaks ( $E_1$  and  $E_2$ ) are only detected after a 1400 °C anneal. Other than being damage-related, their identities are yet unknown.

When the anneal temperature is raised to 1400 °C, the lower implantation dose ( $2 \times 10^{12}$  cm<sup>-2</sup>) samples do not show the same dramatic reduction in trap concentrations as seen in the higher implantation dose samples. With the exception of the  $E_1$  and  $E_2$  trap peaks, the trap concentrations change only moderately. Only three of the observed trap peaks occur in both the 1200 and 1400 °C anneal samples at 343, 246, and 213 K. The other identified trap peaks in these samples are only observed in either the 1200 or 1400 °C anneal samples.

Several of the peaks seen in these argon-implanted samples were also observed in the Cr- and Mg-implanted samples, and were identified as damage-related as opposed to species-related.

The leakage current did not differ significantly between the 1200 and 1400 °C anneal samples. However, the leakage current was slightly reduced in the smaller implantation dose samples. This is indicated by the higher upper temperature limit of the DLTS data for the lower implantation dose samples ( $\phi = 2 \times 10^{12} \text{ cm}^{-2}$ ) as seen in Fig. VI-11. Due to the limits of the DLTS measurement system, any near midgap traps could not be directly detected and characterized by DLTS. However, the C-V measurements and I-V-T measurements do suggest a significant concentration of near midgap traps that may be the dominant mechanism for reverse bias current. The changing concentrations of the DLTS characterized traps had only a slight effect on the reverse current. A much stronger effect on the leakage current was raising the anneal temperature in the chromium- and magnesium-implanted samples.

To understand the variability of the measurements, repeatability tests were run - both using different diodes on the same sample and using the same diode. Shown in figure VI-12 is an Arrhenius plot for two different DLTS measurements from two diodes on the same sample (6H-SiC:Ar,  $\phi = 2 \times 10^{14} \text{ cm}^{-2}$ ,  $N_D - N_A = 7 \times 10^{16} \text{ cm}^{-3}$ ,  $T_A = 1200 \text{ °C}$ ). Note that both curves have nearly identical linear slope sections, and are located in the same position on the graph. These two combined features result in nearly identical trap energies and capture cross-sections. Repeatability tests using the same diode produced even closer overlying curves. This repeatability quality of the measurement permitted the level



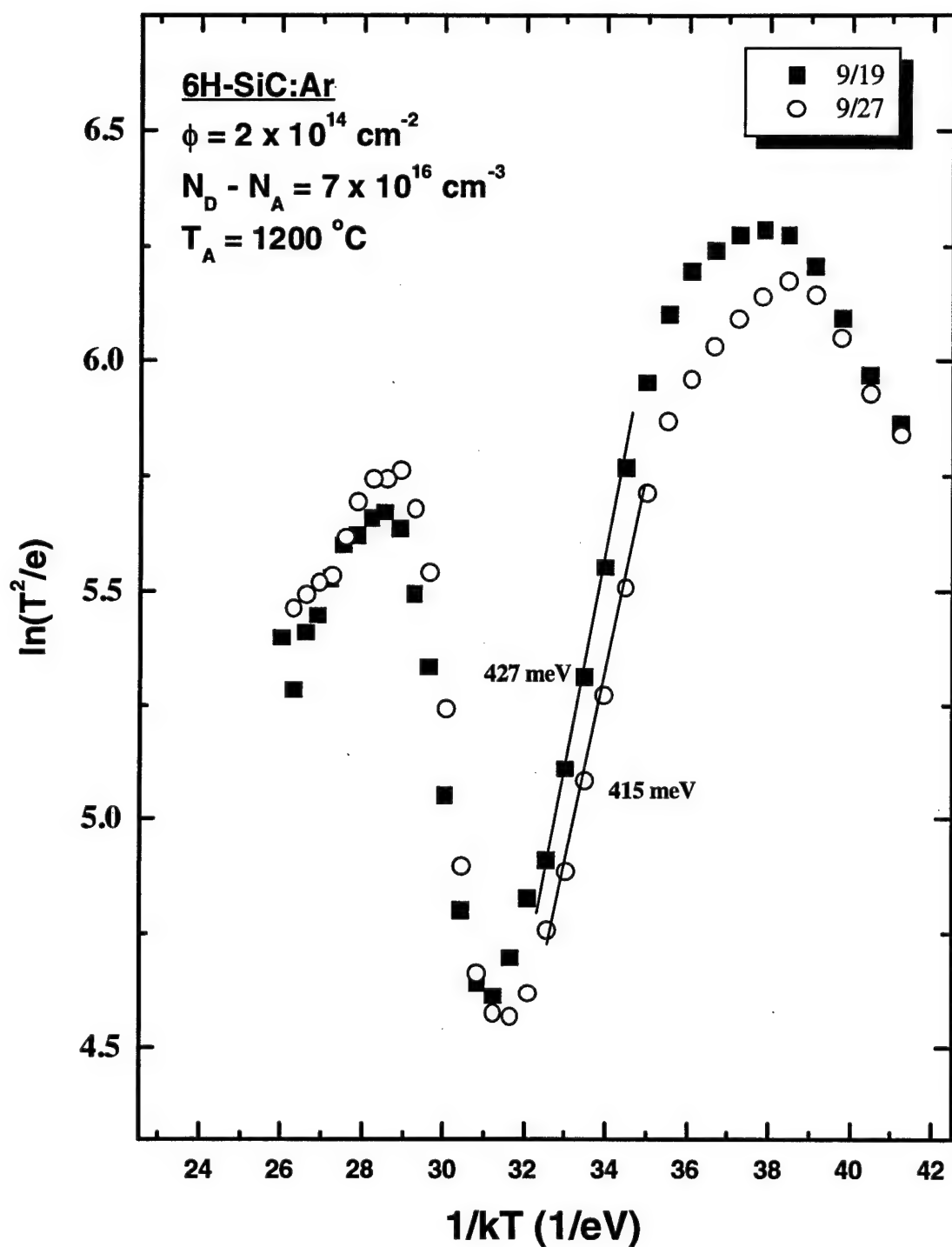


Figure VI-12. Two Arrhenius plots produced from DLTS data from two different diodes on a single 6H-SiC:Ar sample. The nearly overlapping linear sections illustrate the repeatability of the DLTS measurement. The slope of the linear section and position on the graph establishes the trap parameters  $E_t$  and  $\sigma_t$ . The legend indicates the date of measurements.

of analysis presented in the paper. The process of double-checking the test results was exercised throughout this research. Rechecking the test results also had the bonus effect of identifying laboratory equipment and setup problems. Shown in figure VI-13 is another example of an Arrhenius plot showing both distinct and nearly overlapping curves from different 6H-SiC:Ar samples. In this figure, just the linear slope sections of the Arrhenius curves are plotted for the strongest trap peaks for three high temperature (475 °C) Ar-implanted samples. The  $E_1$  and  $E_2$  traps that were detected in two different samples had nearly overlapping Arrhenius "trap signatures." The major trap peak pairs characterized earlier are also plotted in this Arrhenius space to illustrate their distinctness.

Reverse engineering of the trap peaks was initially done to gain insight into the sensitivity of the trap parameters on the rate window plot curves. This was done by modeling the deep level transient spectroscopy technique using Origin™ 5.0 scientific/engineering software that permitted the DLTS equations to be coded to generate the transient capacitance curves, the Arrhenius fits, and the rate window plots. The trap parameters were then used to generate rate window traces that fit the recorded data. Data reported in published SiC articles were used to validate the model (Scofield, 1996) (Suttrup, 1992). This process revealed a significant disagreement between the modulating function software results and the published data when the published fundamental coefficients for 6H-SiC were used. In Appendix C, a detailed explanation is given of this uncovered error in the coefficient  $\gamma$  used in the Modulating Function software (Arrhen6.bas). Adjusting this coefficient to a value based on published fundamental measurements of 6H-SiC resulted

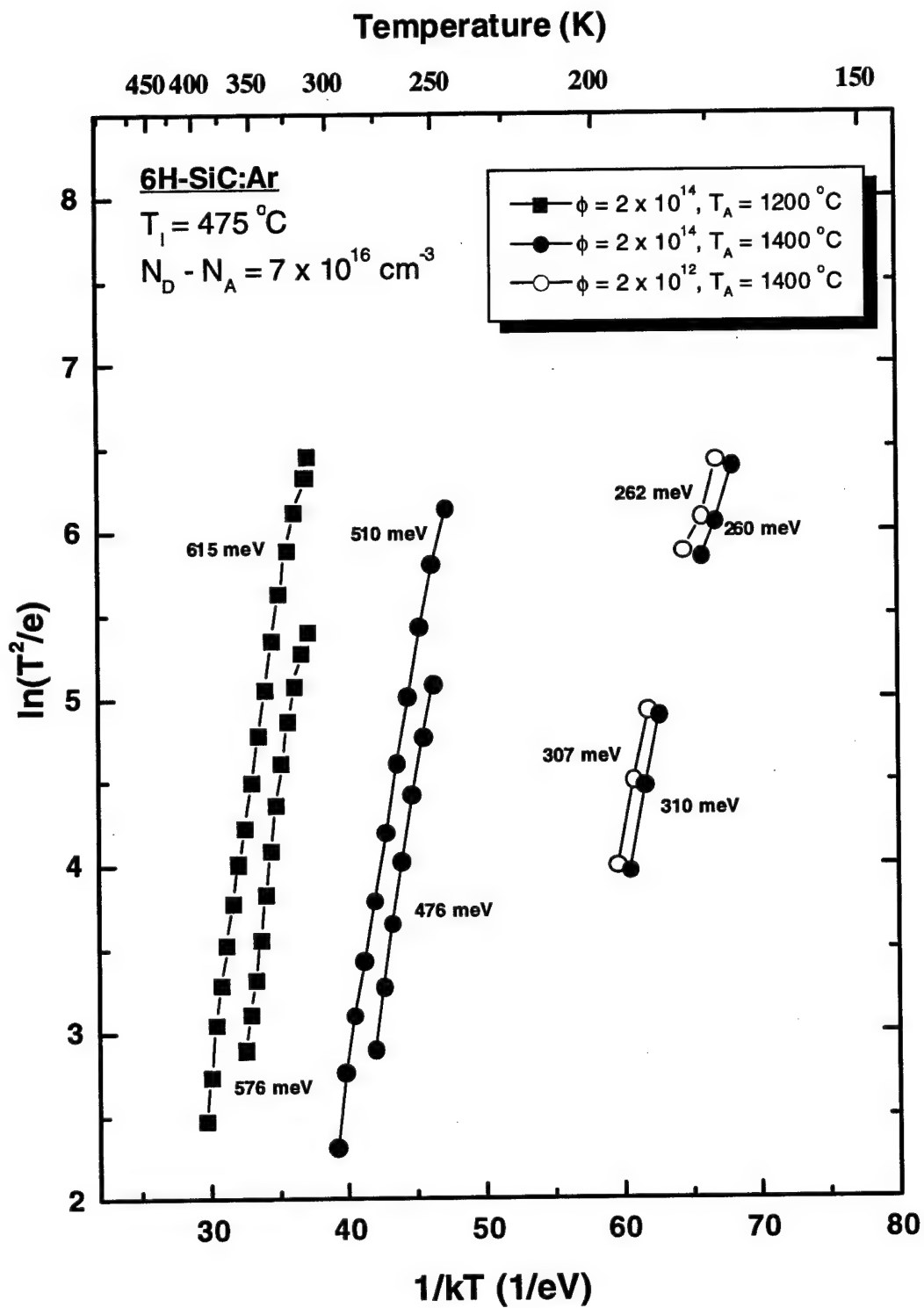


Figure VI-13. Arrhenius plot of the strongest trap peaks for three high temperature ( $475^\circ\text{C}$ ) implanted 6H-SiC:Ar samples. Note the pair of trap levels (615 & 576 meV and 510 & 476 meV) and the near overlapping of the 262 and 260 meV curves as well as the 307 and 310 meV curves.

in a shift in the computed trap parameters. With this fix in hand, the test results were re-evaluated and are reported in this dissertation.

The ion-implanted samples with the net donor concentration of  $7 \times 10^{16} \text{ cm}^{-2}$  formed the backbone of this analysis since they consistently produced the higher quality test diodes (repeatability, lowest leakage current, largest sample set across the three implant species).

#### **VI-1-B-2 DLTS of 6H-SiC:Cr**

When the implantation species was switched to chromium, the formation and evolution of the trap levels changed substantially. Figure VI-14 shows the DLTS rate window responses for three high temperature (500 °C) Cr-implanted samples annealed at three different temperatures (1200, 1400, and 1600 °C). The Cr-implanted samples annealed to  $T_A = 1800 \text{ °C}$  had a reverse leakage current that was too high to make reliable DLTS measurements above 300 K. Also included in Fig. VI-14, is the DLTS rate window response for the unimplanted-annealed ( $T_A = 1400 \text{ °C}$ ) sample showing no detectable majority carrier defect levels. For the three 6H-SiC:Cr samples, the ion implantation dose was  $2 \times 10^{14} \text{ cm}^{-2}$ . The net donor concentration was  $7 \times 10^{16} \text{ cm}^{-3}$  for all four samples. From the 6H-SiC:Cr sample annealed at 1200 °C, the rate window plot showed two additional trap peaks at 376 and 400 K not seen in the argon-implanted samples. Their absence from the 6H-SiC:Ar DLTS measurements suggests that these two traps are Cr-related defects. In addition, the damage-related peaks observed in the 6H-SiC:Ar samples are also detected at 216, 243, 270, 294, 316, and 339 K. The two peaks occurring at 376 and 400 K had trap parameters of  $E_t = 683 \text{ meV}$ ,  $\sigma_t = 1 \times 10^{-15} \text{ cm}^2$ , and

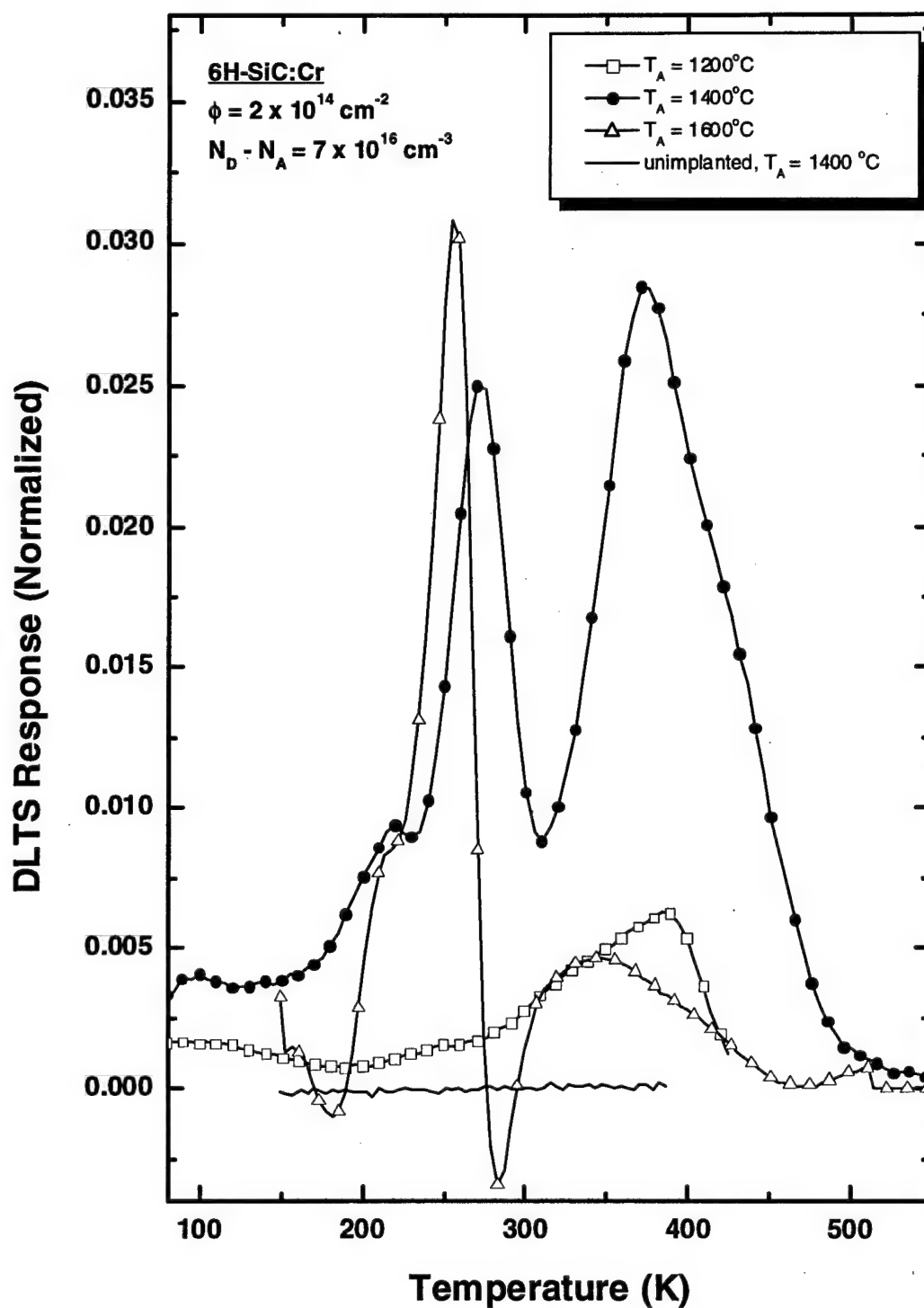


Figure VI-14. Rate window plots of three high temperature (475 °C) implanted 6H-SiC:Cr samples annealed at 1200, 1400, and 1600 °C. Also shown is the rate window plot of the unimplanted 6H-SiC sample annealed at 1400 °C.

$N_t = 1.17 \times 10^{15} \text{ cm}^{-3}$ , and  $E_t = 732 \text{ meV}$ ,  $\sigma_t = 1 \times 10^{-15} \text{ cm}^2$ , and  $N_t = 8.24 \times 10^{14} \text{ cm}^{-3}$ , respectively. Raising the anneal temperature to  $1400^\circ\text{C}$  caused both the damage-related (peak observed from both 6H-SiC:Ar and 6H-SiC:Cr samples) and Cr-related (peaks observed from only 6H-SiC:Cr samples) trap concentrations to dramatically increase. In addition, the leakage current was sufficiently reduced, allowing the DLTS upper temperature limit to go from 430 K to 550 K. The increase in the concentrations of the damage-related traps by increasing the anneal temperature in 6H-SiC:Cr is counter to the effect seen in 6H-SiC:Ar. This may be due to the competing role chromium has with these damage-related traps. During the annealing process, each defect has two rates – a rate of formation and a rate of annihilation. The addition of chromium appears to lower the rate of annihilation for these damage-related defects when the anneal temperature is raised to  $1400^\circ\text{C}$  and thus their concentrations become higher. Another possibility is the presence of damage clusters from which the defects diffuse during annealing. When chromium is implanted, the diffusion rates for the constituents of the damage-related defects may be raised thereby producing additional isolated damage-related traps. Which mechanism is operating here cannot be determined solely from these measurements. The reduced leakage current may be due to chromium atoms forming complexes with the near midgap defects, resulting in a different defect with a energy level further from the midgap and thereby less effective as a generation center. This reduced leakage current effect is not observed in the argon-implanted samples.

The  $1400^\circ\text{C}$  annealed 6H-SiC:Cr (dose =  $2 \times 10^{14} \text{ cm}^{-2}$ ) sample developed two additional trap levels. The first produced a rate window shoulder peak at 426 K and had trap

parameters of  $E_t = 787$  meV,  $\sigma_t = 1 \times 10^{-15}$  cm<sup>2</sup>, and  $N_t = 2.2 \times 10^{15}$  cm<sup>-3</sup>. The other formed its additional shoulder peak at 451 K and had trap parameters of  $E_t = 840$  meV,  $\sigma_t = 1 \times 10^{-15}$  cm<sup>2</sup>, and  $N_t = 2.9 \times 10^{15}$  cm<sup>-3</sup>. Although hard to distinguish in the rate window curve, these two shoulder peaks were resolved through curve fitting. These additional defects are attributed to chromium-related by comparing DLTS data of the argon-implanted samples and the magnesium-implanted samples, which will be shown later.

When the anneal temperature was further raised to 1600 °C, the rate window plot showed a dramatic reduction in the concentrations of the damage-related trap levels at 345 and 317 K and chromium-related trap levels at 451, 426, 400, and 376 K. However, the concentration of the damage-related trap with its peak at 269 K is increased dramatically. The formation of what appears to be a minority carrier trap peak near 280 K is masking the true concentration of the 294 K peak that is paired with the 269 K peak. Minority carrier traps should not be detected by DLTS when using a Schottky diode because there should not be any significant minority carrier injection. However, this negative trap peak may be due to the creation of a highly resistive region due to the formation of near midgap defects or a p-n junction due to diffusion of donor or acceptor defects. Such a formation would then permit the detection of minority trap levels in a Schottky diode test sample. The detection of minority carrier traps in non-illuminated Schottky diodes have been reported by others and have been attributed to the formation of a "high barrier" Schottky contact due to the super-positioning of the depletion region and grain boundaries (Hassler, 1993).

No other new trap peaks were detected in the 1600 °C annealed sample. The trend reversal of the reduction of the reverse leakage current with increasing anneal temperature observed in the 1800 °C anneal 6H-SiC:Cr sample suggests that a critical temperature exists in the 1600 to 1800 °C range where an increase in the concentration of near midgap generation centers occurs. Whether these are the same centers responsible for the leakage current in the 1200 °C anneal samples is unknown.

Shown in figure VI-15 are the rate window plots for four 6H-SiC:Cr samples, with the  $\phi = 2 \times 10^{14} \text{ cm}^{-2}$  curves offset for clarity. Note that the concentration of the trap forming the 368 K peak decreases with increasing anneal temperature in the lower implantation dose sample ( $5 \times 10^{12} \text{ cm}^{-2}$ ) but increases with increasing anneal temperature in the higher implantation dose sample ( $2 \times 10^{14} \text{ cm}^{-2}$ ). This may be due to the interaction of the chromium with other defects including the near midgap defects. Also, note that the higher dose, higher anneal temperature sample has the smallest leakage current as indicated by its higher temperature to which DLTS measurements were made. Comparing the 1400 °C annealed samples (curves with circle symbols,  $-\bullet- -\circ-$ ), one can see that the 292 and 269 K peaks decrease with increasing implantation dose. This indicates that the implanted chromium is either competing with the formation of these defects or aided the diffusion of these defects from cluster sites. Tables VI-3 and VI-4 give the associated computed trap levels for these 6H-SiC:Cr samples annealed at 1200 and 1400 °C, respectively.

The effect of the implantation temperature on the formation/evolution of trap levels is illustrated in figure VI-16. Shown are two 475 °C implanted samples (6H-SiC:Ar, 6H-



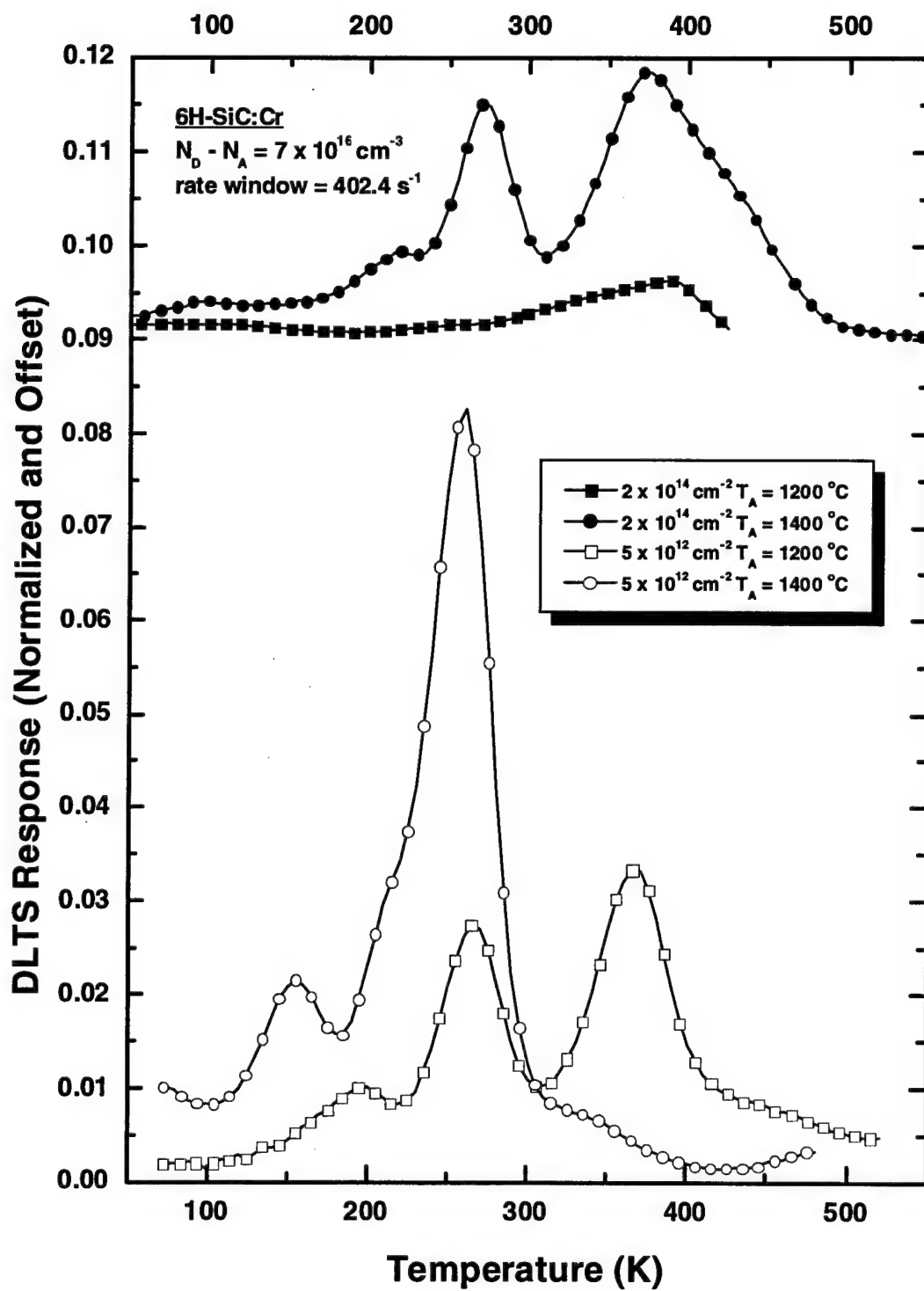


Figure VI-15. Rate Window curves for four high temperature ( $475^\circ \text{C}$ ) implanted 6H-SiC:Cr samples. The upper two curves have been shifted upward for clarity. Note the effect of anneal temperature ( $T_A$ ) and implantation dose on the trap peaks.

$\phi = 2 \times 10^{14} \text{ cm}^{-2}, N_D - N_A = 7 \times 10^{16} \text{ cm}^{-3}, T_A = 1200 \text{ }^\circ\text{C}$			
Temp of Peak (K)	Trap Energy (meV)	Capture Cross-section ( $\text{cm}^2$ )	Trap Conc. ( $\text{cm}^{-3}$ )
400	732	$1 \times 10^{-15}$	$1.17 \times 10^{15}$
376	683	$1 \times 10^{-15}$	$8.24 \times 10^{14}$
345	624	$1 \times 10^{-15}$	$7.39 \times 10^{14}$
317	575	$1 \times 10^{-15}$	$4.87 \times 10^{14}$
294	469	$1 \times 10^{-16}$	$3.17 \times 10^{14}$
269	427	$1 \times 10^{-16}$	$2.49 \times 10^{14}$
244	381	$1 \times 10^{-16}$	$2.83 \times 10^{14}$
215	332	$1 \times 10^{-16}$	$1.81 \times 10^{14}$

$\phi = 5 \times 10^{12} \text{ cm}^{-2}, N_D - N_A = 7 \times 10^{16} \text{ cm}^{-3}, T_A = 1200 \text{ }^\circ\text{C}$			
Temp of Peak (K)	Trap Energy (meV)	Capture Cross-section ( $\text{cm}^2$ )	Trap Conc. ( $\text{cm}^{-3}$ )
451	840	$1 \times 10^{-15}$	$2.2 \times 10^{15}$
427	790	$1 \times 10^{-15}$	$1.1 \times 10^{15}$
400	740	$1 \times 10^{-15}$	$2.6 \times 10^{15}$
368	675	$1 \times 10^{-15}$	$9.9 \times 10^{15}$
339	615	$1 \times 10^{-15}$	$1.9 \times 10^{15}$
318	575	$1 \times 10^{-15}$	$1.3 \times 10^{15}$
295	470	$1 \times 10^{-16}$	$1.98 \times 10^{15}$
269	426	$1 \times 10^{-16}$	$7.35 \times 10^{15}$
245	385	$1 \times 10^{-16}$	$3.2 \times 10^{15}$
215	330	$1 \times 10^{-16}$	$1.65 \times 10^{15}$
191	315	$3 \times 10^{-16}$	$2.2 \times 10^{15}$
162	260	$3 \times 10^{-16}$	$7.0 \times 10^{14}$

Table VI-3. Computed trap parameters for high temperature (475 °C) implanted 6H-SiC:Cr annealed at 1200 °C. The uncertainties are:  $\Delta E_t = \pm 0.05 \cdot E_t$ ,  $\Delta \sigma_t = \pm 0.50 \cdot \sigma_t$ , and  $\Delta N_t = \pm 0.02 \cdot N_t$ .

$\phi = 2 \times 10^{14} \text{ cm}^{-2}, N_D - N_A = 7 \times 10^{16} \text{ cm}^{-3}, T_A = 1400 \text{ }^\circ\text{C}$			
Temp of Peak (K)	Trap Energy (meV)	Capture Cross-section ( $\text{cm}^2$ )	Trap Conc. ( $\text{cm}^{-3}$ )
451	840	$1 \times 10^{-15}$	$2.9 \times 10^{15}$
426	785	$1 \times 10^{-15}$	$2.2 \times 10^{15}$
400	737	$1 \times 10^{-15}$	$5.25 \times 10^{15}$
366	673	$1 \times 10^{-15}$	$7.0 \times 10^{15}$
337	615	$1 \times 10^{-15}$	$1.6 \times 10^{15}$
317	575	$1 \times 10^{-15}$	$1.2 \times 10^{15}$
292	470	$1 \times 10^{-16}$	$1.5 \times 10^{15}$
269	432	$1 \times 10^{-16}$	$6.95 \times 10^{15}$
247	383	$1 \times 10^{-16}$	$2.0 \times 10^{15}$
213	332	$1 \times 10^{-16}$	$2.30 \times 10^{15}$

$\phi = 5 \times 10^{12} \text{ cm}^{-2}, N_D - N_A = 7 \times 10^{16} \text{ cm}^{-3}, T_A = 1400 \text{ }^\circ\text{C}$			
Temp of Peak (K)	Trap Energy (meV)	Capture Cross-section ( $\text{cm}^2$ )	Trap Conc. ( $\text{cm}^{-3}$ )
448	841	$1 \times 10^{-15}$	$6.0 \times 10^{14}$
424	790	$1 \times 10^{-15}$	$6.0 \times 10^{13}$
405	740	$9 \times 10^{-16}$	$3.0 \times 10^{14}$
373	674	$8 \times 10^{-16}$	$9.0 \times 10^{14}$
340	621	$1 \times 10^{-15}$	$1.75 \times 10^{15}$
318	575	$1 \times 10^{-15}$	$1.25 \times 10^{15}$
294	470	$1 \times 10^{-16}$	$2.75 \times 10^{15}$
268	423	$1 \times 10^{-16}$	$2.2 \times 10^{16}$
245	385	$1 \times 10^{-16}$	$1.35 \times 10^{16}$
213	330	$1 \times 10^{-16}$	$6.95 \times 10^{15}$
194	308	$3 \times 10^{-16}$	$3.5 \times 10^{15}$
164	265	$3 \times 10^{-16}$	$4.6 \times 10^{15}$

Table VI-4. Computed trap parameters for high temperature (475 °C) implanted 6H-SiC:Cr annealed at 1400 °C. The uncertainties are:  $\Delta E_t = \pm 0.05 \cdot E_t$ ,  $\Delta \sigma_t = \pm 0.50 \cdot \sigma_t$ , and  $\Delta N_t = \pm 0.02 \cdot N_t$ .

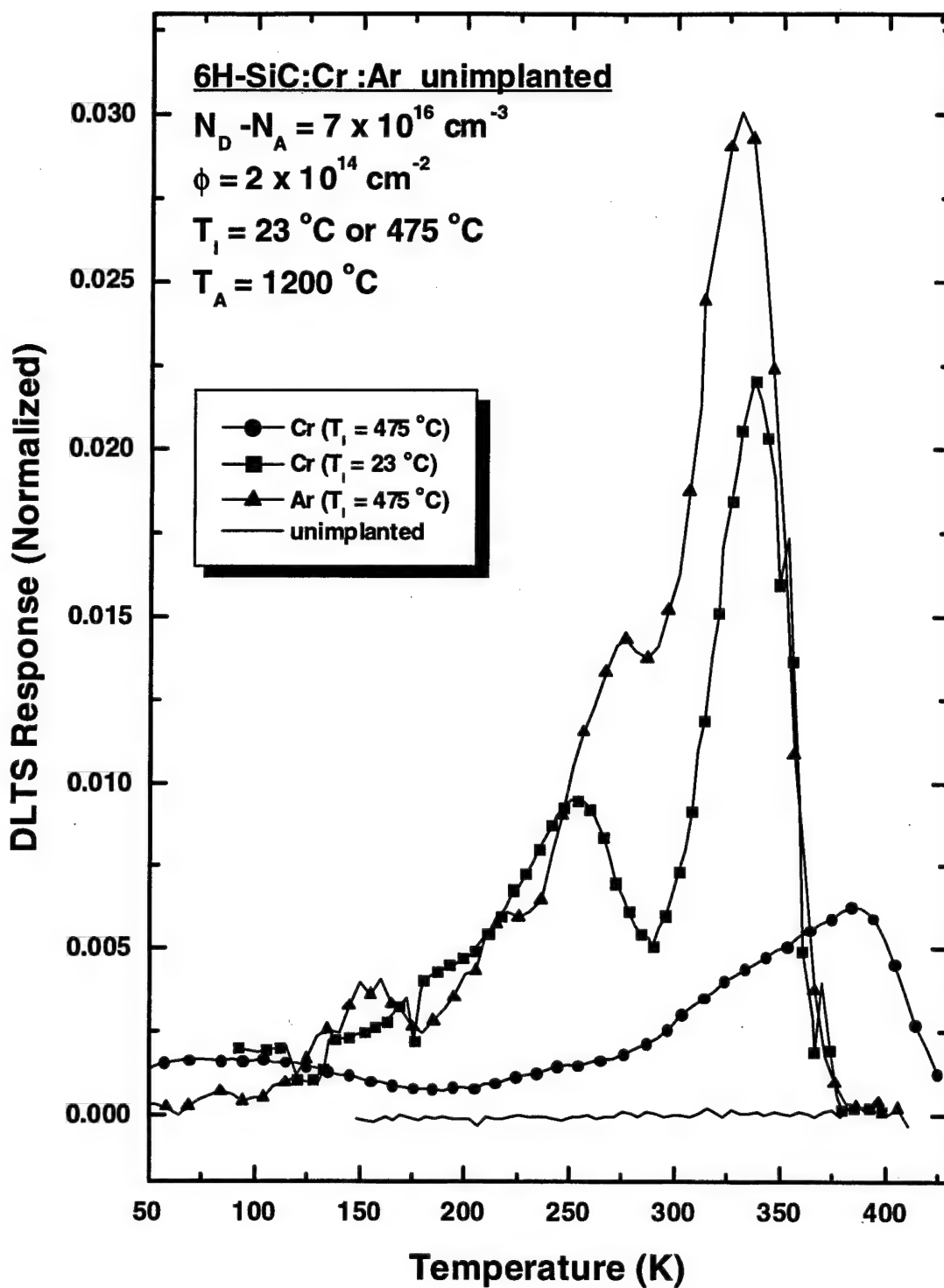


Figure VI-16. Rate window plots for room temperature ( $23^\circ\text{C}$ ) and  $475^\circ\text{C}$  implanted 6H-SiC:Cr annealed at  $1200^\circ\text{C}$  illustrating the effect of implantation temperature on the formation/evolution of damage- and chromium-related traps. Also shown are the rate window plots for unimplanted 6H-SiC and high temperature ( $475^\circ\text{C}$ ) implanted 6H-SiC:Ar.

SiC:Cr), one room temperature implanted sample (6H-SiC:Cr (RT)), and one unimplanted sample ( $T_A = 1400^\circ\text{C}$ ). The ion-implanted samples were annealed at  $1200^\circ\text{C}$  and had an implantation dose of  $2 \times 10^{14} \text{ cm}^{-2}$ , and all the samples had a net donor concentration of  $7 \times 10^{16} \text{ cm}^{-3}$ . The most notable effect shown is the dramatic reduction in the concentration of the 615 meV damage-related trap (peak at 339 K) in 6H-SiC:Cr as the implantation temperature is raised from room temperature to  $475^\circ\text{C}$ . Note the high concentration of the 615 meV damage-related trap level (at 339 K) in the room-temperature implanted 6H-SiC:Cr sample and hot temperature implanted 6H-SiC:Ar. This dramatic reduction in concentration also occurred for the other damage-related defects in 6H-SiC:Cr. During ion implantation, damage-related and species-related defects are being formed and possibly partially annihilated. The rates of both formation and annihilation are implantation temperature dependent. This dependency controls the net concentration of the various traps. However, this dependency on implantation temperature varies for each trap and is not a linear relationship. There exist critical temperatures for each defect where the formation and annihilation rates can make a dramatic change. At least one of these critical temperatures exists for the 615 meV damage-related trap and other damage-related traps in ion-implanted 6H-SiC:Cr between room temperature and  $475^\circ\text{C}$  (admittedly a wide range). Testing this effect at other implantation temperatures could narrow the uncertainty of these critical implantation temperature and perhaps identify other critical temperatures for the trap levels. This includes ion implantation at temperatures lower than room temperature, as well. Studies in low-temperature boron-implanted diamond have produced the highest activation of boron to date (Fontaine,

1996). Low-temperature ion implantation in SiC could also prove to be an effective method for ion activation.

In addition to the dramatic reduction in the concentration of the damage-related traps by a "hot" implantation, the 475 °C ion implantation appears to enhance the formation of the Cr-related defects. This is evident by the dramatic increase in concentration of the 732 and 683 meV (400 and 376 K, respectively) Cr-related peaks following a "hot" implantation. At this elevated implantation temperature, at least one of the constituents for these traps is becoming mobile and has a sufficiently high probability of forming the Cr-related defects. This increased probability may be due to either reduced competition for the mobile constituent or increased concentration of the mobile constituent.

The increased implantation temperature in 6H-SiC:Cr also had the effect of reduced the reverse leakage current. This is illustrated in Fig. VI-16 by the increase in the upper temperature limit to which the DLTS measurement was made when the implantation temperature was raised to 475 °C. The elevated implantation temperature may be reducing the concentration of defect traps that are participating in conducting current.

Double-correlated DLTS (DDLTS) measurements were also made on the chromium-implanted samples and indicate a depth dependence for many of the trap concentrations. Figure VI-17 shows the overlay of five DDLTS rate window plots recorded for five different regions of the implanted semiconductor. The plots are labeled A through E and correspond to the regions labeled in the upper left inset drawing. Region A is closest to the metal-semiconductor interface and region E is the deepest. Also plotted is a composite of the five traces as well as the CV-DLTS rate window plot for the same sample. As the implanted atoms travel into the semiconductor, they interact with the material and

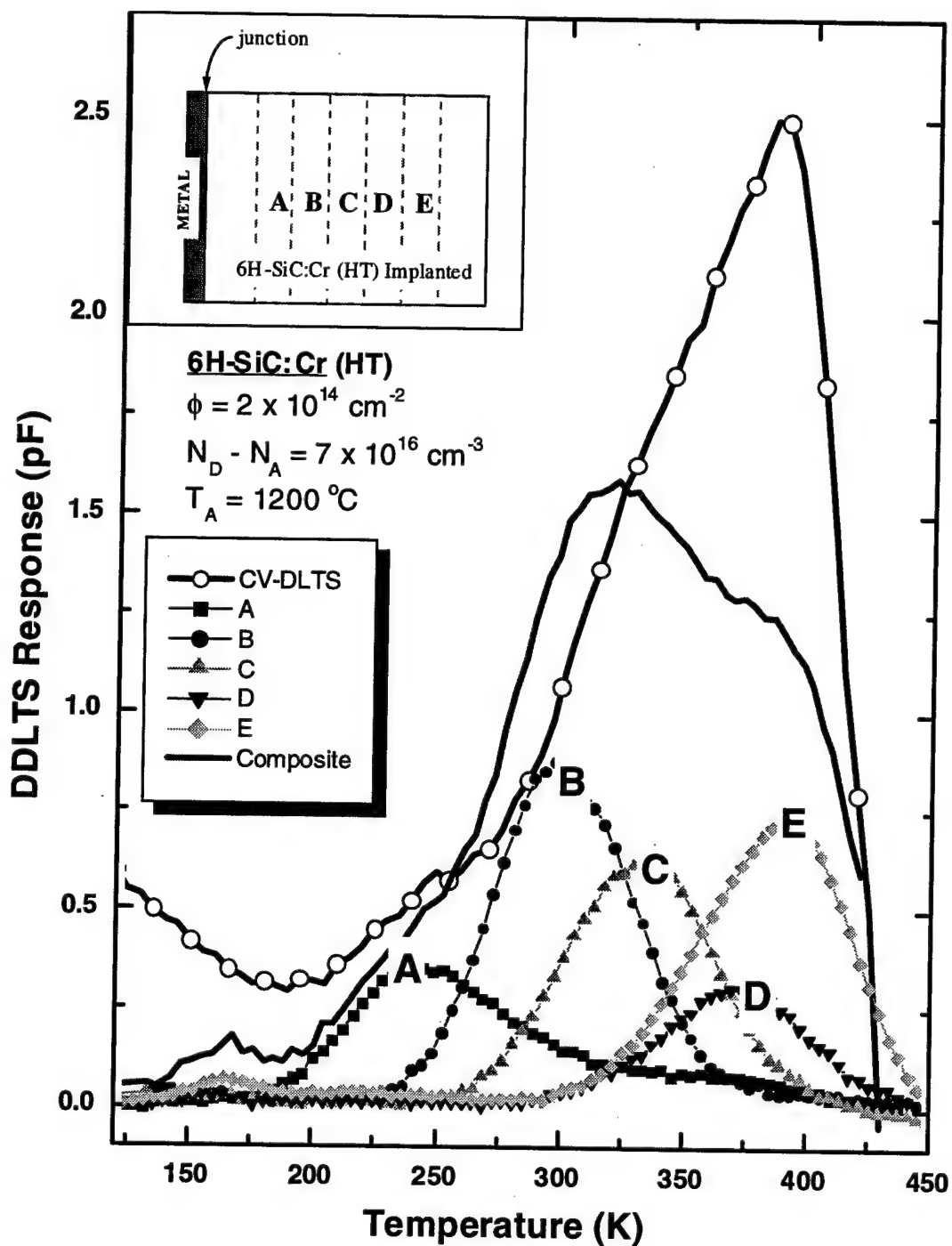


Figure VI-17. Double-correlated DLTS (DDLTS) rate window plots for five different areas from a high temperature (HT) implanted 1200 °C annealed 6H-SiC:Cr sample. The plot illustrates the depth dependence of the trap concentrations. The upper left inset shows the relative locations of the regions measured.

lose their energy. How the implanted atoms interact is energy dependent and thus depth dependent. This causes the distribution of the different defects to be depth dependent. With annealing, some of these defects become mobile and evolve – being annihilated or forming complexes. Diffusion takes place to various degrees depending on the type of defect of the surrounding environment. These events combine to produce a depth-dependence as indicated by the DDLTS measurement. Another factor to consider is that the peak damage depth will not be at the same depth as the implanted species peak concentration. In fact, the DDLTS measurement indicates that the Cr atoms are distributed deeper than the damage-related defects.

Figure VI-18 shows the effect of the anneal temperature on the concentration of observed damage-related and chromium-related traps in high temperature (475 °C) high implantation dose ( $\phi = 2 \times 10^{14} \text{ cm}^{-2}$ ) chromium-implanted n-type 6H-SiC. Most of the observed traps had a peak concentration following a 1400 °C anneal. The only exception is the 427 meV damage-related trap. The 427 meV trap concentration increases about 700 % with an increase in anneal temperature from 1200 to 1400 °C and increases about 60 % with an increase in anneal temperature from 1400 to 1600 °C. The 381/332 meV trap pair concentration doubles going from  $T_A = 1200 \text{ °C}$  to  $T_A = 1400 \text{ °C}$ , then remains about constant following a 1600 °C anneal. In the lower implantation dose ( $\phi = 5 \times 10^{12} \text{ cm}^{-2}$ ) 6H-SiC:Cr samples, the trap concentrations decrease or remain steady for all the traps as the anneal temperature increases from 1200 to 1400 °C except for the 381/332 meV trap pair which increases by about 350%. This is shown in figure VI-19. This difference in anneal temperature behavior between the 6H-SiC:Cr samples having different



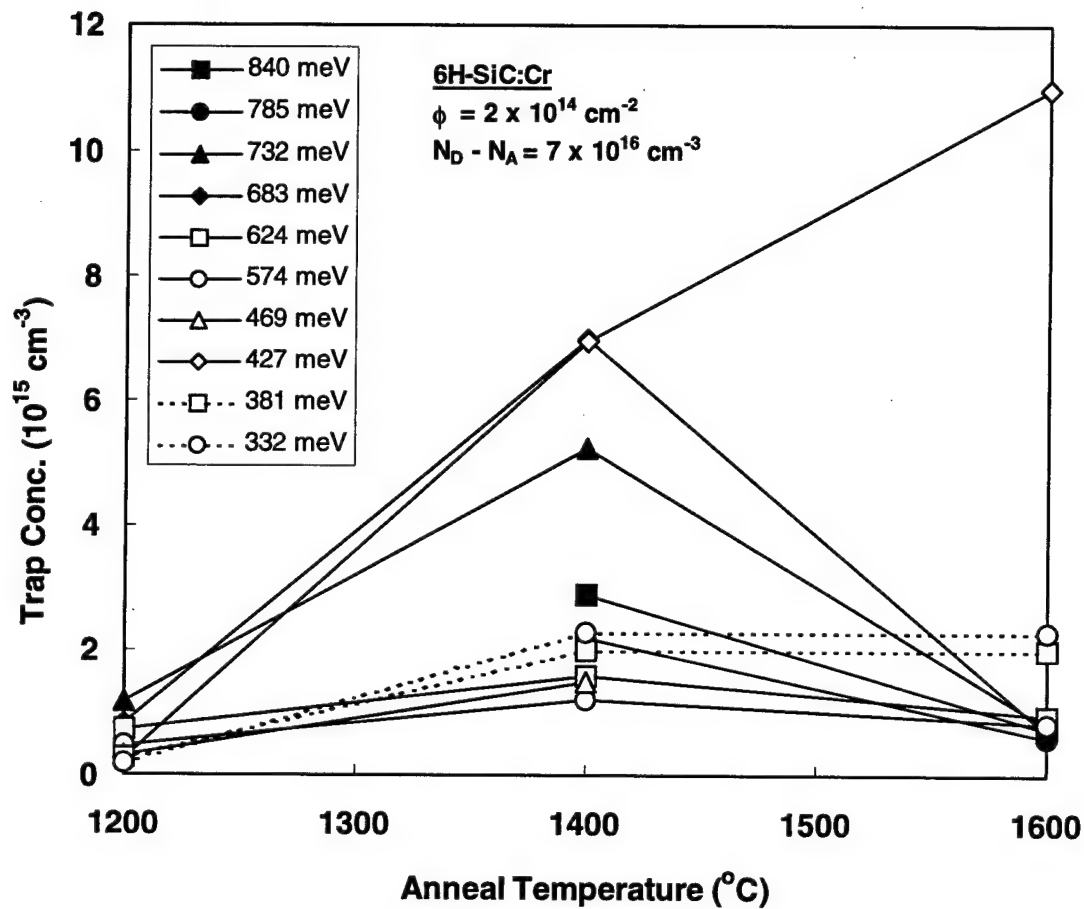


Figure VI-18. Graph of trap concentration as a function of anneal temperature from high temperature (475 °C) implanted ( $\phi = 2 \times 10^{14} \text{ cm}^{-2}$ ) 6H-SiC:Cr. Most of the trap levels had peak concentrations following a 1400 °C anneal. The only exception was the 427 meV damage-related trap.

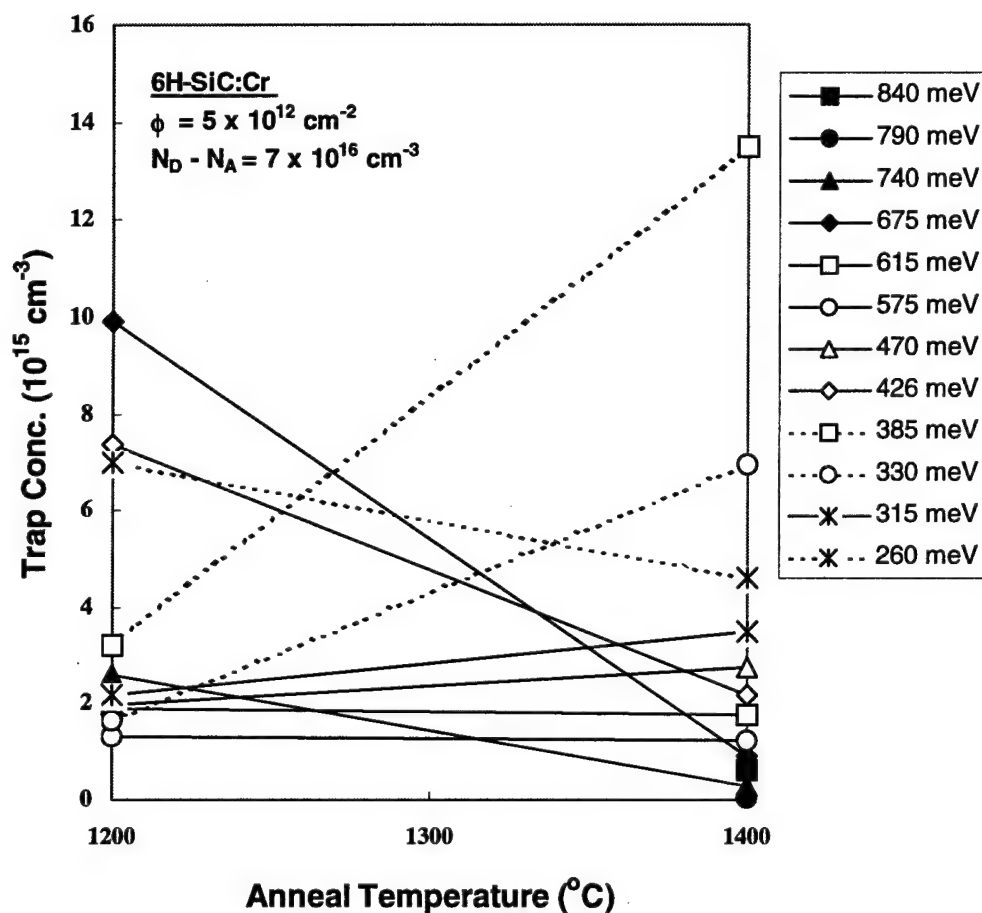


Figure VI-19. Graph of trap concentration as a function of anneal temperature from high temperature (475 °C) implanted ( $\phi = 5 \times 10^{12} \text{ cm}^{-2}$ ) 6H-SiC:Cr. Most of the trap level concentrations decreased or remained constant following a 1400 °C anneal. The only exceptions were the two damage-related trap pair (381 and 332 meV) which increased by approximately 350 %.

chromium implantation doses suggests that the implanted chromium or subsequent damage is interfering with the formation of the 624/575 meV and 469/427 meV damage-related traps pairs. This is possible since the formation of defects is dependent on the crystal environment including the presence of other defects.

There also exists an implantation dose dependency of the anneal temperature behavior of the chromium-related trap pair concentrations. This suggests that the implanted chromium is being affected by other defects and that the implantation dose must be sufficiently high (greater than some threshold level) to permit the formation of the 840/785 meV and 732/683 meV chromium-related trap pairs with a 1400 °C anneal. When the 6H-SiC:Cr is heavily ion-implanted, where there is a higher concentration of both chromium and damage, the Cr-related sites are well formed following a 1400 °C anneal. However, when the 6H-SiC:Cr is lightly ion-implanted, where there is a lower concentration of both chromium and damage, the Cr-related sites are well formed following a 1200 °C anneal but are nearly completely annihilated with a 1400 °C anneal. Reducing the concentration of the other defects may significantly improve the activation of the implanted chromium. This could possibly be accomplished by elevating the ion implantation temperature above 475 °C.

### VI-1-B-3 DLTS of 6H-SiC:Mg

The DLTS investigation of high-temperature implanted 6H-SiC continued with magnesium-implanted (195 keV at 475 °C) 6H-SiC. The 195 keV implantation formed a 2500 Å peak implantation depth profile. The DLTS and electrical measurements of the 6H-SiC:Mg samples revealed the dramatic effects of anneal temperature, implantation temperature, implantation dose, and net donor concentration on the formation and evolution of both damage-related and magnesium-related trap levels.

The anneal temperature effect is illustrated in figure VI-20 which shows the CV-DLTS rate window plots of three magnesium-implanted n-type 6H-SiC samples ( $\phi = 1 \times 10^{14} \text{ cm}^{-2}$ ,  $N_D - N_A = 1 \times 10^{16} \text{ cm}^{-3}$ ) annealed at 1200, 1400, and 1600 °C as well as an unimplanted sample ( $T_A = 1400 \text{ °C}$ ). Three well-defined majority carrier electron trap peaks were formed at 216, 343, and 525 K after a 1200 °C anneal. The 216 K peak has a strong asymmetrical shape indicating the presence of at least two trap levels. The activation energies of the 216 K peaks are 293 and 250 meV, with identical capture cross-sections of  $1 \times 10^{-17} \text{ cm}^2$ . The trap peak at 343 K also consists of two trap levels, has activation energies of 560 and 618 meV, and identical capture cross-section of  $1 \times 10^{-16} \text{ cm}^2$ . The formation of a negative rate window peak at 470 K prevented a proper estimation of the trap parameters and peak position of the higher temperature positive peak near 525 K using only this sample. The formation of a negative peak, which represents minority carrier trapping, was also observed in chromium-implanted 6H-SiC samples. When using a Schottky junction device to make DLTS measurements, minority carrier trap detection is not expected since there should not be sufficient minority carrier

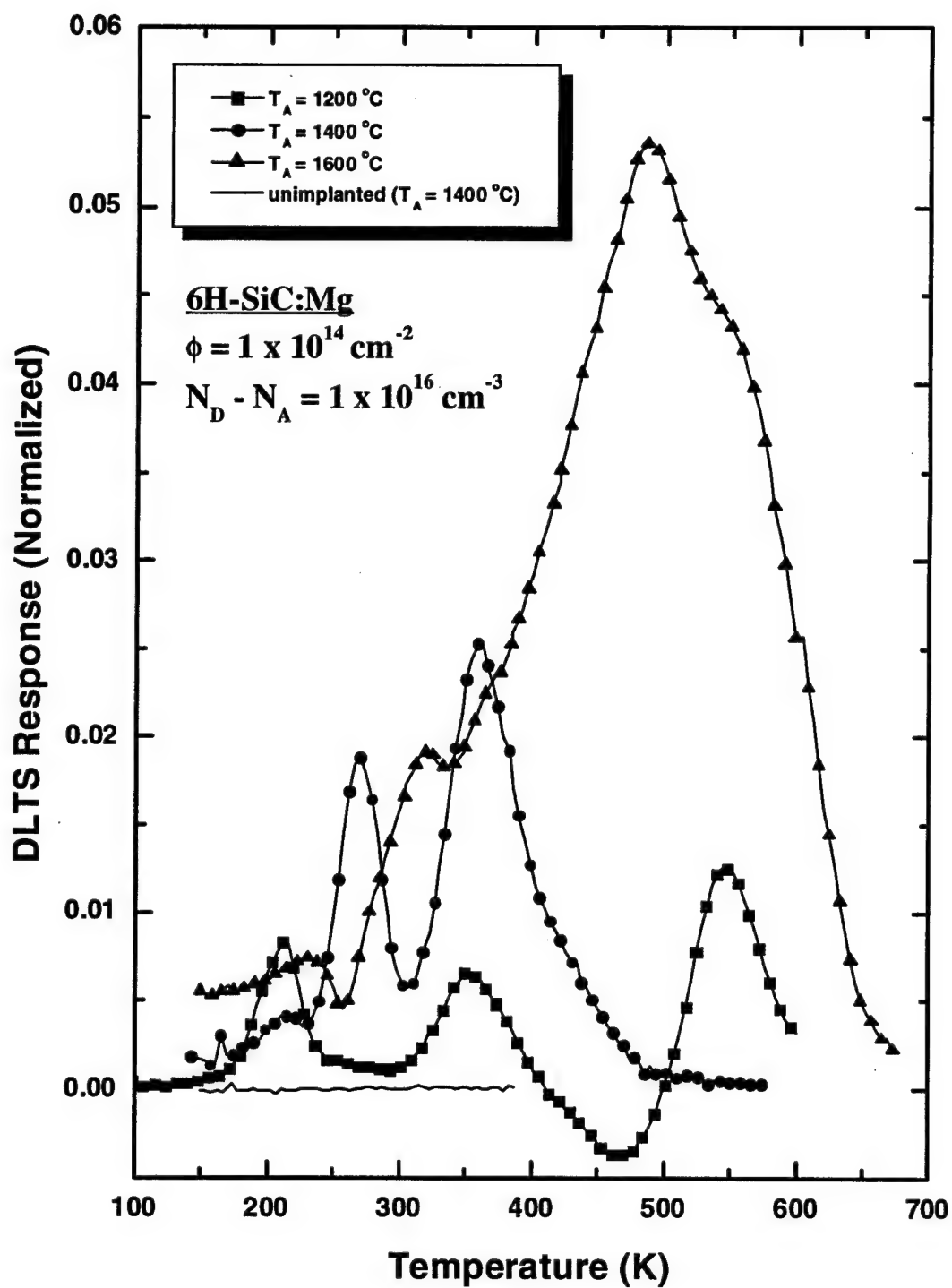


Figure VI-20. Rate window plots of three high temperature (475 °C) 6H-SiC:Mg samples annealed at 1200, 1400, and 1600 °C. Also shown is the rate window plots of the 1400 °C annealed unimplanted 6H-SiC sample.

injection into the depletion region to allow sufficient capture during the filling cycle of the measurement. However, this condition is not unheard of and has been explained by the formation of p-n junction regions within the semiconductor by either donor or acceptor defect diffusion or the formation of "high barrier" grain boundaries (Hassler, 1993). By examining other samples, it was determined that this apparent 525 K majority trap has its true peak at 488 K, has an activation energy of 896 meV, and capture cross-section of  $6 \times 10^{-16} \text{ cm}^2$ . It too has an associated trap pair with trap parameters of  $E_t = 968 \text{ meV}$  and  $\sigma_t = 6 \times 10^{-16} \text{ cm}^2$ . The peak heights would also be significantly higher without the competing effect of the negative peak. For the most part, the magnesium-implanted samples had the best rectification of the three types of ion-implanted samples as indicated by the highest temperature limit that CV-DLTS measurements were taken.

When the anneal temperature was raised to 1400 °C, the minority carrier trap peak is annihilated. Also, there is a dramatic reduction in the concentration of the 896/968 meV trap pair. The concentration of the 293/250 meV trap level pair also decreases. However, a new peak is formed at 250 K and the concentration of the peak pair at 343 K dramatically increases. The 250 K peak level has an activation energy of 363 meV and capture cross-section of  $1 \times 10^{-17} \text{ cm}^2$ . No associated peak was observed with this trap level. The leakage current was not affected with this change in anneal temperature. This indicates that the 1400 °C anneal did not sufficiently annihilate the traps involved in the reverse bias current.

Increasing the anneal temperature to 1600 °C caused several changes to the sample. First, the high-temperature measurement-limit is increased to nearly 700 K. This indicates that between 1400 °C and 1600 °C, a disassociation or annihilation temperature exists for at least one of the defects responsible for the shunting behavior of these test diodes. Second, the concentration of the 896 meV trap level increased more than two orders of magnitude indicating that at least one of its constituents is made mobile at a temperature between 1400 and 1600 °C. Third, the concentration of another electron-trap level that is over 1 eV deep (1107 meV) showing up in the rate window plot at 579 K is dramatically increased. Fourth, the concentrations of the 363 and 560 meV trap levels are decreased – the 560 meV trap level only slightly and the 363 meV trap level to about ¼. In addition to these major changes, another trap level peak pair is clearly formed at 298 K. These trap levels have activation energies of 474 and 424 meV and identical capture cross-section of  $1 \times 10^{-16} \text{ cm}^2$ . The 293/250 meV trap level pair concentrations begin to reverse its trend – increasing to near  $T_A = 1200 \text{ °C}$  levels.

By comparing these trap peaks to those seen and analyzed in 6H-SiC:Ar and 6H-SiC:Cr, associations to either Mg-related or damage-related defects can be put forth. The trap pair forming the 216 K peak is believed to be damage-related as similar trap levels are observed in both 6H-SiC:Ar and 6H-SiC:Cr. Their peak position, however, is too high to be assigned to the  $E_1/E_2$  Pensl levels. The peak pair forming the 343 K peak is seen in all of the implanted samples and is associated to a damage-related defect. Another damage-related trap level pair is forming the rate window peak at 298 K. Again, this trap level pair is detected in each of the three types of implants. The trap level pairs forming the 488 K peak and the 579 K peak appear to be Mg-related. The 488 K peak is

not observed in the 6H-SiC:Cr and there is no indication of the start of the 579 K peak in the 6H-SiC:Cr rate window plots measured up to 550 K. Both Mg-related traps are activated by a 1600 °C anneal. Another trap level pair is also detected at 679 and 760 meV with identical capture cross-section of  $1 \times 10^{-16} \text{ cm}^2$  forming the low temperature side of the broad 488 K peak as seen in Fig. VI-20. This trap pair is believed to be Mg-related as it is only observed in the Mg-implanted samples and has the anneal temperature behavior as the other Mg-related defects.

The lighter element magnesium ( $Z = 10$ ,  $A = 24.3$ ) should produce a different distribution in the concentrations of the various types of damage-related defects than the distribution produced by the heavier atoms of chromium ( $Z = 24$ ,  $A = 52.0$ ) and argon ( $Z = 18$ ,  $A = 40.0$ ). These distribution differences are in terms of both the magnitude and ratio of the trap concentrations, as well as their one-dimensional spatial distribution along the c-axis within the implantation region. Magnesium has about twice the mass of carbon ( $Z = 6$ ,  $A = 12.0$ ) and nearly the same mass as silicon ( $Z = 14$ ,  $A = 28.1$ ). Chromium is more than twice the mass of magnesium and about 1/3 more massive than argon. Therefore, it is quite expected that the anneal temperature effect seen in 6H-SiC:Mg should be considerably different from the effect seen in 6H-SiC:Ar and 6H-SiC:Cr implanted with the heavy elements of argon and chromium. Also, since the diffusion of these implanted atoms in the crystal depends on both their electrical and physical properties, there should also be a significant difference in the diffusion of the implanted ions both during the high temperature implantation and subsequent annealing.

Altering the implantation dose in 6H-SiC:Mg caused significant changes to the formation and evolution of the trap level concentrations. Shown in figure VI-21 are four CV-



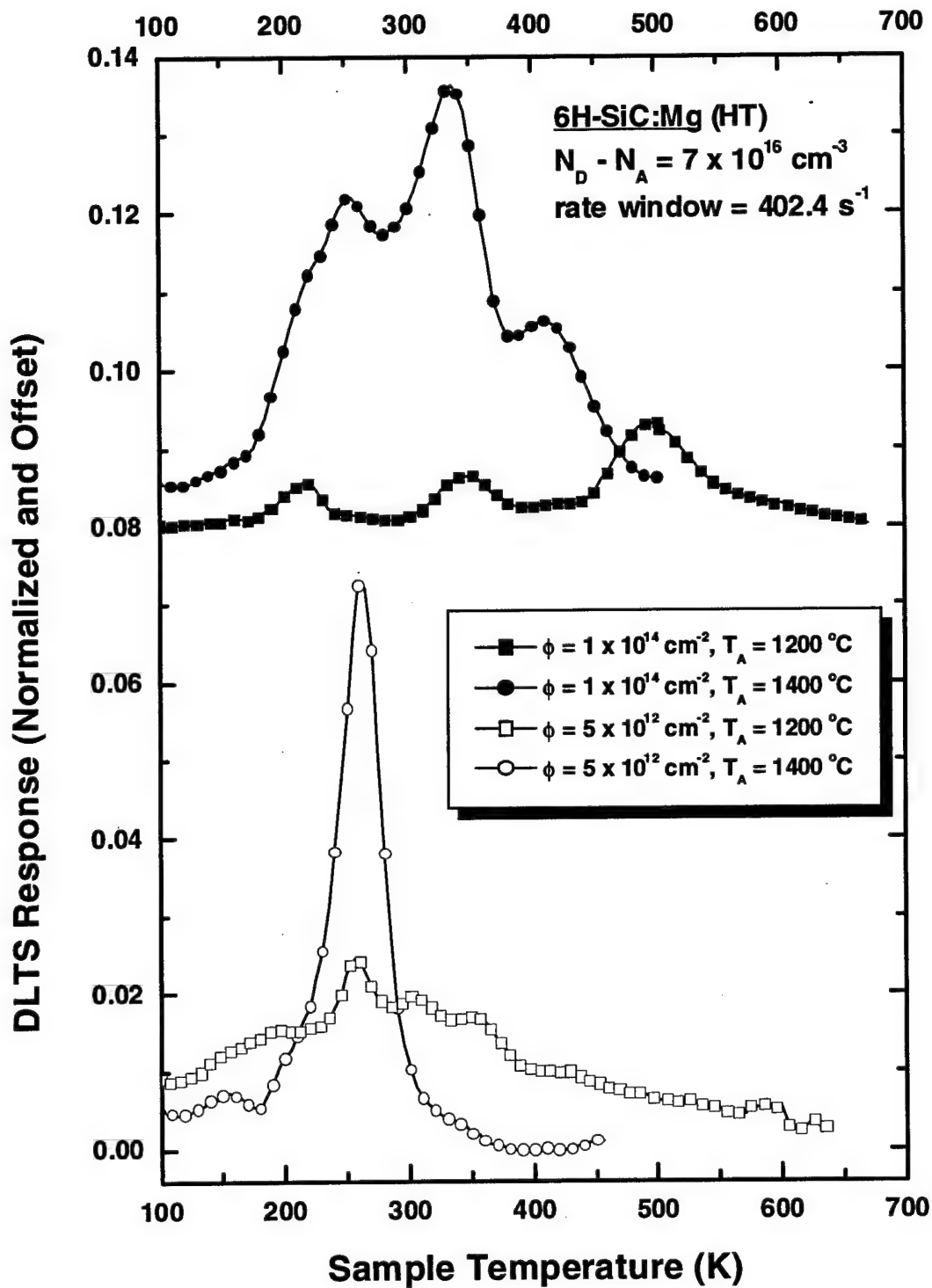


Figure VI-21. Rate Window curves for four high temperature ( $475 \text{ }^\circ\text{C}$ ) implanted 6H-SiC:Mg samples. The upper two curves have been shifted upward for clarity. Note the effect of anneal temperature ( $T_A$ ) and implantation dose on the trap peaks.

DLTS rate window plots showing the effect of increasing the anneal temperature from 1200 to 1400 °C for n-type 6H-SiC:Mg implanted at two different doses –  $5 \times 10^{12}$  and  $1 \times 10^{14} \text{ cm}^{-2}$ . The upper two curves have been shifted upward for clarity. In the lower implantation dose samples (lower two curves), the concentration of the 250 K peak trap dramatically increased following a 1400 °C anneal. This electron trap level has a computed activation energy of 363 meV and capture cross-section of  $1 \times 10^{-17} \text{ cm}^2$ . All other trap concentrations were significantly reduced following a raise in the anneal temperature to 1400 °C. Notice also the indication of the dramatic increase in the leakage current with increased anneal temperature by the reduction in the DLTS upper temperature limit from 630 K to just 450 K. This was the largest change in leakage current of all 6H-SiC:Mg samples tested due to changing the anneal temperature from 1200 to 1400 °C.

When the implantation dose is increased 20 times to  $1 \times 10^{14} \text{ cm}^{-2}$ , the results are quite different. For this case, the 1200 °C anneal sample shows the same triple peak profile as seen in Fig. VI-21 in the lower donor concentration ( $N_D - N_A = 1 \times 10^{16} \text{ cm}^{-3}$ ) samples but without the minority trap negative peak. Increasing the anneal temperature to 1400 °C results in the significant increase in several trap level concentrations with the exception of the 896/968 meV trap level pair. Consistent between both dose sets of curves is the increase in the leakage current when the anneal temperature is raised from 1200 to 1400 °C. This indicates that, in the higher donor concentration samples ( $7 \times 10^{16} \text{ cm}^{-3}$ ), there is an activation temperature between 1200 and 1400 °C for one of the defects responsible for the shunting behavior.

The 363 meV trap level observed in the 1400 °C annealed low-dose sample has the same anneal temperature behavior as the 385 meV trap level observed in low-dose 6H-

SiC:Cr sample (see Fig. VI-15). If they are the same trap, the trap cannot be species-related. There also exists a damage-related peak in the Ar-implanted samples near 250 K. However, this trap is a much deeper trap (510 meV) and does not appear to increase in trap concentration following an increase in the anneal temperature from 1200 to 1400 °C. Why this 363 meV trap level is not seen in the 6H-SiC:Ar samples is not clear.

In the higher-dose samples ( $1 \times 10^{14} \text{ cm}^{-2}$ ), the majority of the trap levels increase in concentration with anneal temperature and are the same damage-related traps observed in either the 6H-SiC:Ar or 6H-SiC:Cr samples, or both. The only exceptions are that the 679 meV trap level increases in concentration with increasing anneal temperature, the 896 meV trap level decreases in concentration with  $T_A$  going from 1200 to 1400 °C and then increases in concentration when  $T_A$  is raised to 1600 °C, and the 1107 meV trap level can be seen only in the  $T_A = 1600 \text{ °C}$  sample (Fig. VI-20). These deeper trap levels are considered to be magnesium-related as they are not evident in the 6H-SiC:Cr that were also tested over the higher DLTS temperature range.

Shown in tables VI-5 and VI-6 are the computed trap parameters for the observed trap levels in the 6H-SiC:Mg samples. The four samples listed in the tables are the same four samples used in CV-DLTS rate window plots shown in Fig. VI-21. The traps found in the magnesium-implanted samples also show the trend of trap pairing found in the other implanted samples.

Shown in figure VI-22 are two rate window plots for two high temperature (475 °C) implanted 6H-SiC:Mg ( $N_D - N_A = 1 \times 10^{16}$  and  $7 \times 10^{16} \text{ cm}^{-3}$ ) samples. The DLTS responses have been normalized to the steady state capacitance, which corresponds to the

$\phi = 1 \times 10^{14} \text{ cm}^{-2}, N_D - N_A = 7 \times 10^{16} \text{ cm}^{-3}, T_A = 1200 \text{ }^\circ\text{C}$			
Temp of Peak (K)	Trap Energy (meV)	Capture Cross-section (cm <sup>2</sup> )	Trap Conc. (cm <sup>-3</sup> )
579	1107	1.00E-15	$3.6 \times 10^{13}$
525	968	6.00E-16	$6.98 \times 10^{13}$
488	896	6.00E-16	$1.19 \times 10^{14}$
416	938	1.00E-13	$2.68 \times 10^{13}$
377	691	1.00E-15	$2.47 \times 10^{13}$
343	560	1.00E-16	$7.35 \times 10^{13}$
298	477	1.00E-16	$6 \times 10^{12}$
255	401	1.00E-16	$1.8 \times 10^{13}$
216	293	1.00E-17	$6.85 \times 10^{13}$
186	250	1.00E-17	$1.2 \times 10^{13}$

$\phi = 5 \times 10^{12} \text{ cm}^{-2}, N_D - N_A = 7 \times 10^{16} \text{ cm}^{-3}, T_A = 1200 \text{ }^\circ\text{C}$			
Temp of Peak (K)	Trap Energy (meV)	Capture Cross-section (cm <sup>2</sup> )	Trap Conc. (cm <sup>-3</sup> )
581	880	1.00E-17	2.40E+13
514	952	6.00E-16	2.50E+13
464	848	6.00E-16	3.50E+13
421	695	1.00E-16	4.50E+13
373	618	1.00E-16	5.90E+13
347	565	1.00E-16	6.20E+13
304	368	1.00E-18	1.03E+14
263	363	1.00E-17	9.70E+13
228	310	1.00E-17	6.90E+13
202	269	1.00E-17	6.80E+13

Table VI-5. Computed trap parameters for high temperature (475 °C) implanted 6H-SiC:Mg and annealed at 1200 °C. The uncertainties are:  $\Delta E_t = \pm 0.05 \cdot E_t$ ,  $\Delta \sigma_t = \pm 0.50 \cdot \sigma_t$ , and  $\Delta N_t = \pm 0.02 \cdot N_t$ .

$\phi = 1 \times 10^{14} \text{ cm}^{-2}, N_D = 7 \times 10^{16} \text{ cm}^{-3}, T_A = 1400 \text{ }^{\circ}\text{C}$			
Temp of Peak (K)	Trap Energy (meV)	Capture Cross-section (cm <sup>2</sup> )	Trap Conc. (cm <sup>-3</sup> )
446	740	1.00E-16	5.00E+13
412	679	1.00E-16	9.00E+13
372	681	1.00E-15	8.70E+13
340	619	1.00E-15	2.40E+14
320	577	1.00E-15	1.00E+14
298	474	1.00E-16	1.50E+14
269	424	1.00E-16	1.70E+14
244	383	1.00E-16	1.80E+14
218	293	1.00E-17	1.60E+14
188	250	1.00E-17	8.00E+13

$\phi = 5 \times 10^{12} \text{ cm}^{-2}, N_D = 7 \times 10^{16} \text{ cm}^{-3}, T_A = 1400 \text{ }^{\circ}\text{C}$			
Temp of Peak (K)	Trap Energy (meV)	Capture Cross-section (cm <sup>2</sup> )	Trap Conc. (cm <sup>-3</sup> )
346	565	1.00E-16	1.00E+13
304	368	1.00E-18	4.00E+13
264	363	1.00E-17	5.50E+14
229	310	1.00E-17	7.00E+13
203	269	1.00E-17	5.00E+13

Table VI-6. Computed trap parameters for high temperature (475 °C) implanted 6H-SiC:Mg and annealed at 1400 °C. The uncertainties are:  $\Delta E_t = \pm 0.05 * E_t$ ,  $\Delta \sigma_t = \pm 0.50 * \sigma_t$ , and  $\Delta N_t = \pm 0.02 * N_t$ .

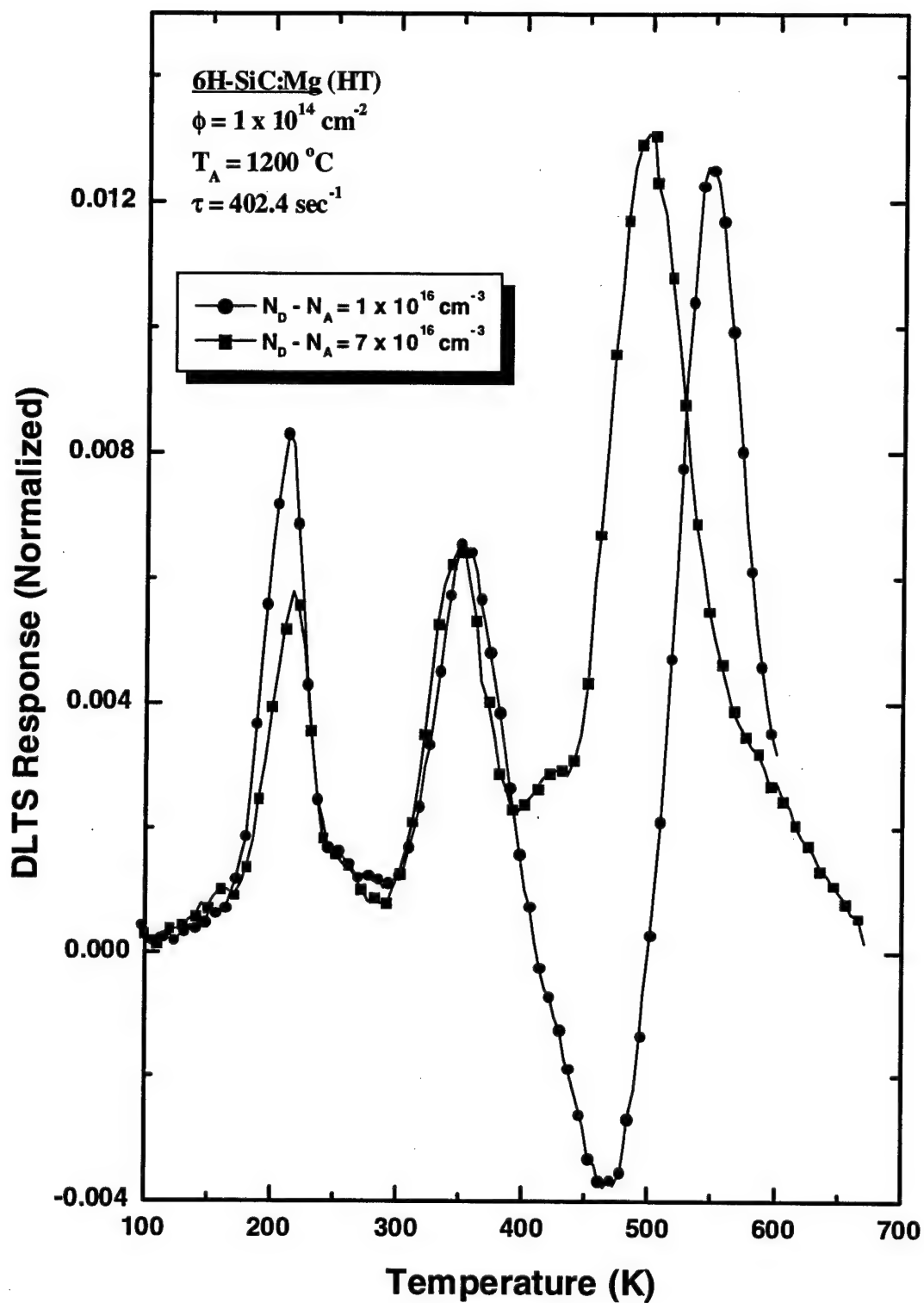


Figure VI-22. Two rate window plots for two high temperature (HT) implanted 6H-SiC:Mg samples having different net donor concentrations. The lower net donor concentration sample formed a minority carrier trap peak (near 460 K), which distorts the position of the majority carrier trap peak near 500 K.

net donor concentration. The 343 K peak appears in both curves and has the same height. This strongly suggests that the related trap level is a complex with substitutional nitrogen. By comparing this peak to the DLTS results for the 6H-SiC:Cr samples, it appears that this is the same 615 meV peak that has been identified as a  $V_{\text{Si}} - \text{N}$  complex.

Figure VI-22 also gives a clear illustration of the effect of the donor concentration on the formation of the minority carrier trap peak and how its presence is obscuring the actual position and shape of the majority carrier trap peak. When the donor concentration is raised to  $7 \times 10^{16} \text{ cm}^{-3}$ , the p-n-like junction structures are not formed. By referring back to Fig. VI-21, it is apparent that these structures are annihilated at an anneal temperature in the range of 1200 to 1400 °C. The fact that raising the donor concentration also eliminates their presence agrees with the idea that these p-n-like structures may be formed by the diffusion and concentration of acceptors in the n-type material. The higher donor concentrations found in the  $N_{\text{D}} - N_{\text{A}} = 7 \times 10^{16} \text{ cm}^{-3}$  samples are more able to compensate for the relatively constant concentration of acceptors that are created during ion implantation and annealing. This means that the p-type regions in the material cannot be formed. It should be noted that other negative trap peaks may exist that are not high enough in concentration to be detected by DLTS.

The dependence of the formation and evolution of trap levels in 6H-SiC:Mg on ion-implantation temperature is displayed in figure VI-23. In the figure, are the CV-DLTS rate window plots from two 6H-SiC:Mg, one 6H-SiC:Ar, and one unimplanted 6H-SiC samples. One of the 6H-SiC:Mg samples was ion implanted at room temperature (23 °C) while the other 6H-SiC:Mg was ion-implanted at 475 °C (HT). The 6H-SiC:Ar sample was also ion implanted at 475 °C. The donor concentration of all four samples is  $7 \times 10^{16}$

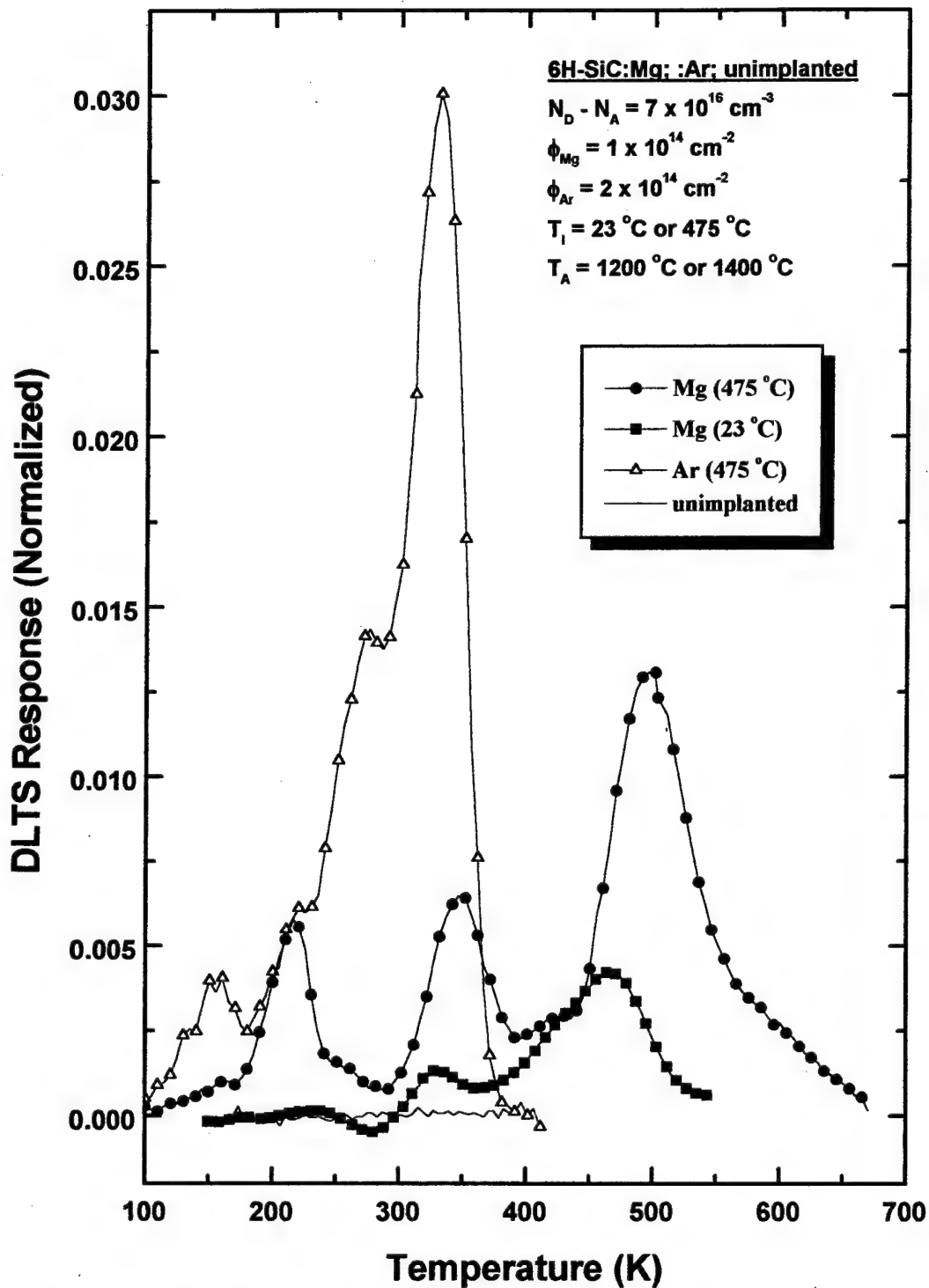


Figure VI-23. Rate window plots showing the effect of ion implantation temperature on the formation and evolution of trap levels in magnesium-implanted n-type 6H-SiC. Compare this figure to figure VI-16 to witness the difference of room temperature ion implantation between Cr- and Mg-implantation.



cm<sup>-3</sup>. The implantation dose is  $1 \times 10^{14}$  cm<sup>-2</sup> for the 6H-SiC:Mg ion-implanted samples and  $2 \times 10^{14}$  cm<sup>-2</sup> for the 6H-SiC:Ar sample. The implanted samples were annealed at 1200 °C while the unimplanted sample was annealed at 1400 °C.

The lower implantation temperature had the effects of reducing the formation of the trap peak pairs at 200, 343, and 488 K. The leakage current was significantly larger in the room temperature ion-implanted 6H-SiC:Mg. Ion implanting at 475 °C improved the performance of the diode, permitting DLTS measurements up to 675 K. Without raising the implantation temperature, the tested diode would leak too severely to allow testing beyond 540 K. Room temperature ion-implantation also permitted the formation of a negative trap peak (near 280 K). These changes indicate that elevating the ion-implantation temperature did have a significant impact on the formation and evolution of some of the defect levels and damage structures in this material. Unlike the chromium-implanted samples, the magnesium-implanted samples did not produce the dominating damage-related peak concentrations similar to the high temperature argon-implanted samples (Fig. VI-16). This is not surprising considering that the chromium ion is nearly equal in mass to the argon ion and the magnesium ion is much lighter than the argon ion. This mass difference should have a considerable effect on both the concentration and distribution of the various types of damage.

Double-correlated DLTS measurements were also made on the magnesium-implanted samples to observe the depth dependence and to measure the charge state of the various defects. All the measured defects indicated a neutral charge state because their trap parameters were unchanged when the E-field was dramatically increased. By adjusting the filling and reverse biases, a fixed layer of the implanted region can be analyzed under

various E-field strengths. A charged trap will be influenced by the E-field and its computed trap parameters will shift. An analysis of the rate of change of the trap's activation energy will reveal whether the charged state is single, double, or triple. DDLTS measurements also revealed the depth profile of the various defects in the implantation region.

Illustrated in figure VI-24 is the depth variation of the concentration of the 293/450, 474/424, and 679/740 trap pairs found in a 1400 °C annealed 6H-SiC:Mg ( $\phi = 1 \times 10^{14} \text{ cm}^{-2}$ ,  $N_D - N_A = 7 \times 10^{16} \text{ cm}^{-3}$ ) sample. In the rate window plot, the 293/450 and 679/740 trap pairs show no change in concentration going from 2000 to 2500 Å (peak implantation depth). However, the 474/424 meV trap pair shows that its concentration is higher nearer the peak implantation depth.

Figure VI-25 illustrates the change in trap concentrations as the region beyond the peak implantation depth is probed. Note that the damage-related trap concentrations remain fairly constant while the Mg-related trap concentrations are significantly reduced in the deeper region. This indicates that the implanted Mg ions are more concentrated around the implantation peak than the damage-related defects, which are more uniformly distributed. The fact that the peak concentrations of the Mg-related traps are shallower than a significant concentration of damage-related traps suggests a slight diffusion of the magnesium atoms toward the surface after their initial implantation.

Figure VI-26 shows the effect of the anneal temperature on the concentration of observed damage-related and magnesium-related traps in high temperature (475 °C) magnesium-implanted ( $\phi = 1 \times 10^{14} \text{ cm}^{-2}$ ) n-type 6H-SiC. A clear distinction can be seen between the anneal temperature behavior of the damage- and magnesium-related trap

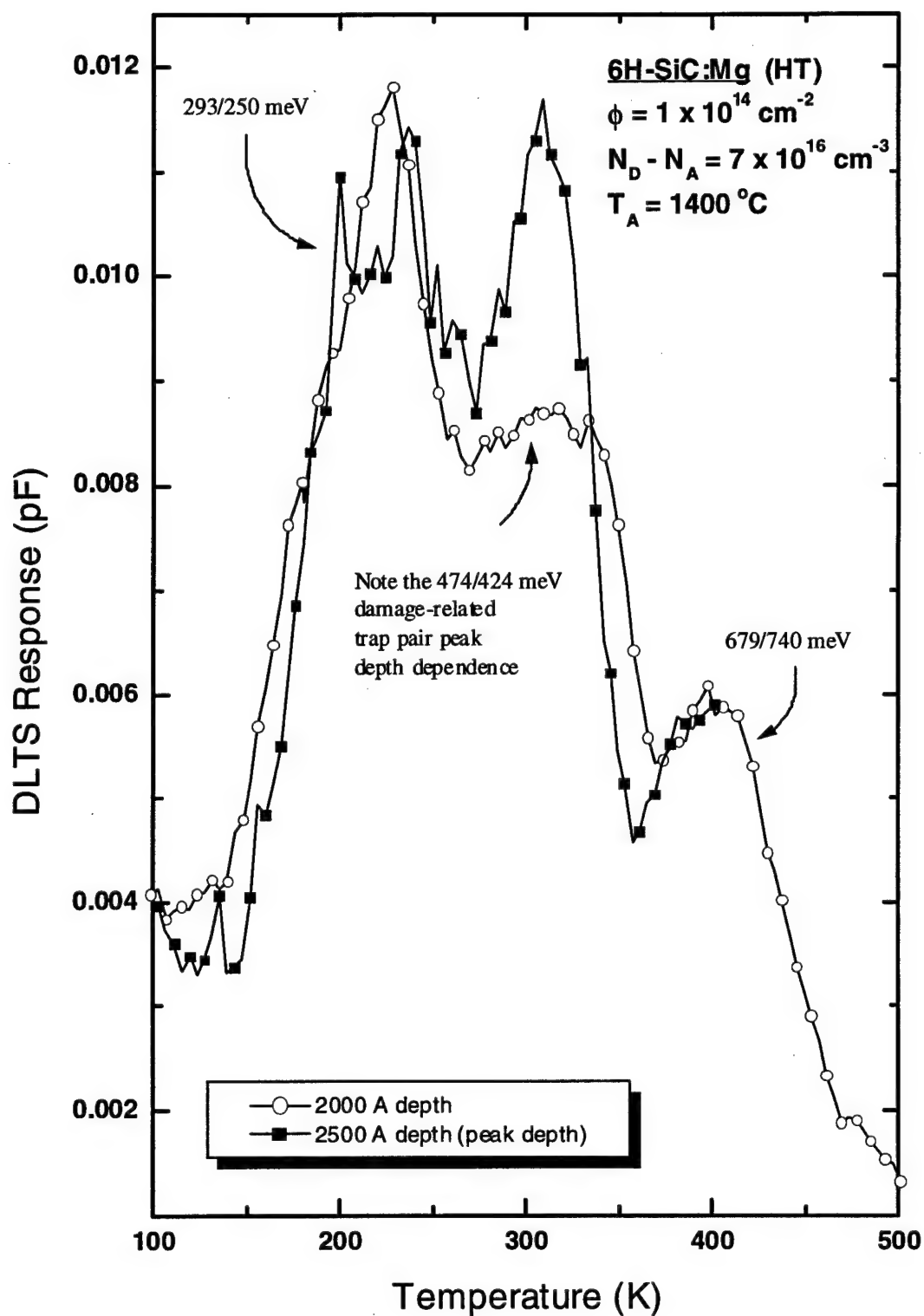


Figure VI-24. Rate window plot from Double-correlated DLTS (DDLTS) measurements showing the trap concentration depth dependence. The 474/424 meV trap pair concentrations increase significantly in the region of the ion implantation peak.

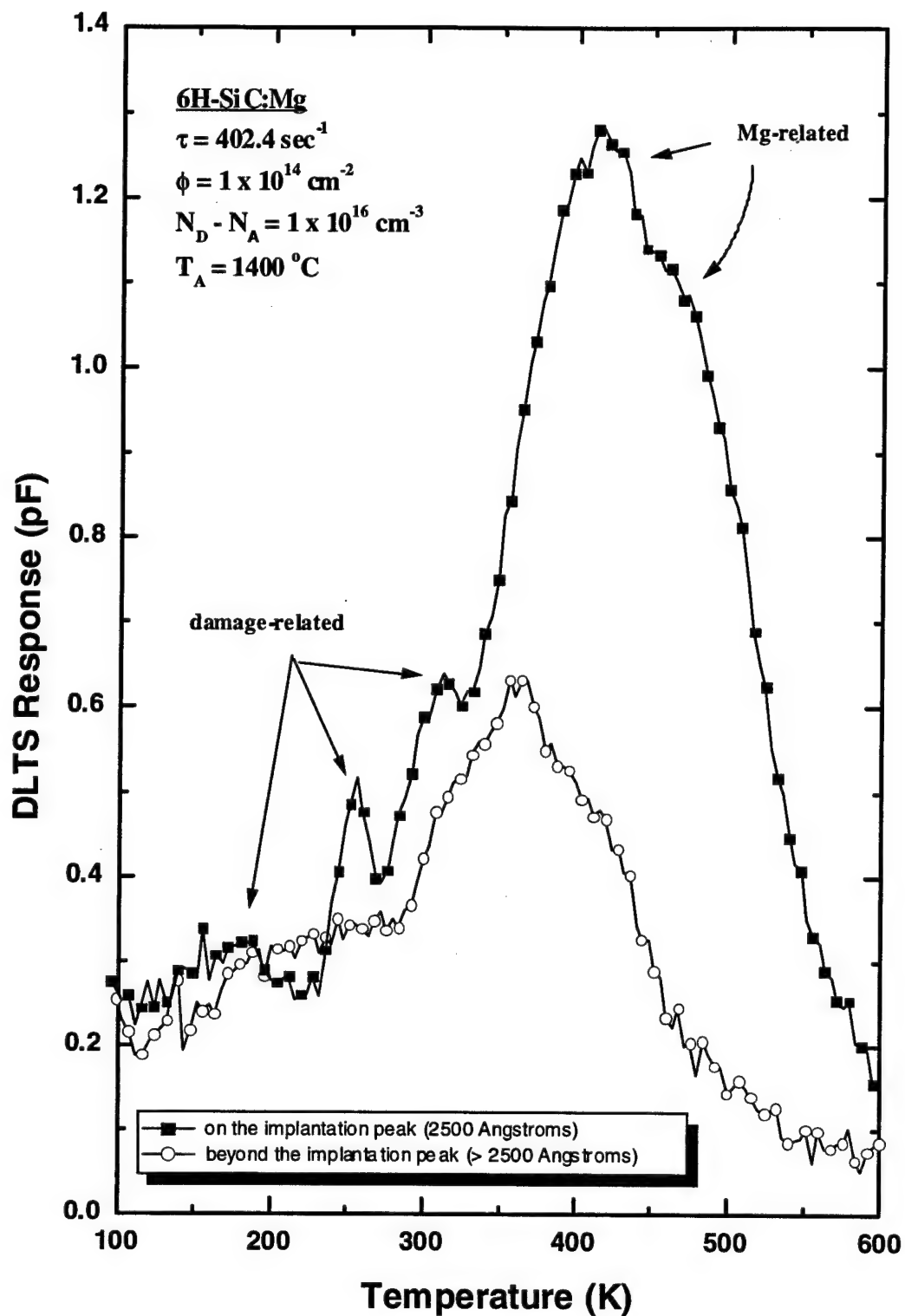


Figure VI-25. Rate Window plot from double-correlated DLTS (DDLTS) measurements showing the trap concentration depth dependence. Note the dramatic decrease in concentration of the Mg-related traps when probing beyond the implantation peak of 2500 Angstroms.

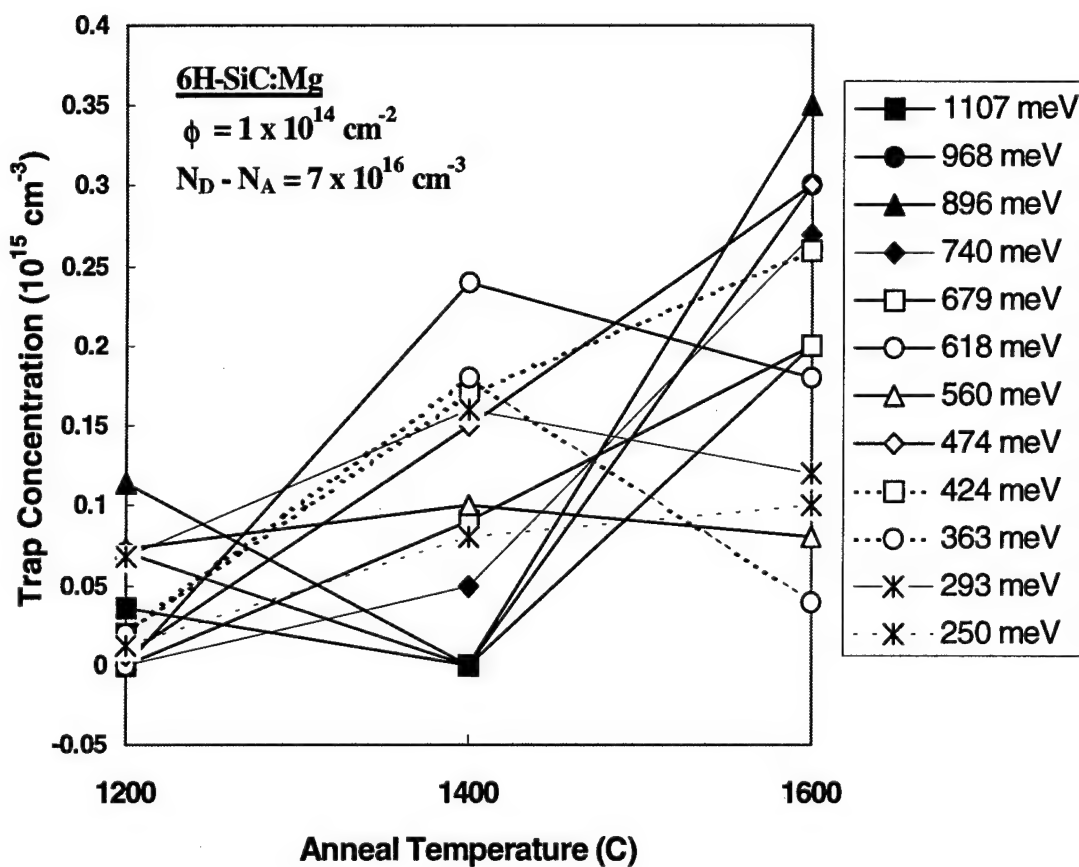


Figure VI-26. Graph of trap concentrations as a function of anneal temperature from the heavier implanted ( $1 \times 10^{14} \text{ cm}^{-2}$ ) 6H:SiC:Mg ( $T_1 = 475^\circ\text{C}$ ). Most of the damage-related trap concentrations increased in concentration following a  $1400^\circ\text{C}$  anneal followed by a slight changes with a  $1600^\circ\text{C}$  anneal. The Mg-related trap concentrations initially decreased when the anneal temperature was raised to  $1400^\circ\text{C}$  then dramatically increased following a  $1600^\circ\text{C}$  anneal.

concentrations. Most of the observed damage-related trap concentrations increased following a 1400 °C anneal while most of the Mg-related trap concentrations decreased. The only exception was the 474/424 meV damage-related trap pair, which continued to increase in concentration going from 1400 to 1600 °C. In the lower dose ion-implanted samples, the concentration of all detectable trap levels decreased when the anneal temperature was raised from 1200 to 1400 °C. No 1600 °C annealed 6H-SiC:Mg samples were available to for test having the lower dose ( $\phi = 5 \times 10^{12} \text{ cm}^{-2}$ ). The dominant damage-related defect seen in the lower dose samples indicates that the defect is the easiest to form via implantation/annealing, and that high implantation doses and high anneal temperatures are required to create a significant concentration of Mg-related defect levels. Since higher anneal temperatures improve both the rectification and generation of the Mg-related defect levels, it may be possible that one of the generation centers in 6H-SiC:Mg is Mg interstitial.

### VI-1-C Summary

DLTS measurements on n-type 6H-SiC samples that were unimplanted or implanted with argon, chromium, or magnesium have revealed the formation and evolution of both damage-related and species-related trap levels. These trap levels appear to form in pairs due to the inequivalent lattice sites that exist in 6H-SiC, a polytype semiconductor. The concentrations of the defect centers are sensitive to both implantation temperature and anneal temperature, and exhibit a depth dependence. Table VI-7 summarizing the observed trap levels in these studied samples. The assignment of the defects to either damage or implant species was based on the behavior of the defect to implantation and anneal parameters. Three trap levels were found in published reports. They were the two Pensl-reported  $E_1$  and  $E_2$  trap levels (Pensl and Choyke, 1993) and the 615 meV trap level (Pensl and Choyke, 1993) (Kawasuso, 1996) that is being assigned here to a  $V_{si}$ -N complex.

The DLTS study of Ar-implanted n-type 6H-SiC revealed two dominant implantation damage-related majority carrier trap pair levels at 510/476 and 615/576 meV. The 615/576 meV levels are believed to be due to a Si vacancy-N complex based on anneal temperature and donor concentration behavior. Near surface damage-related trap levels were detected by double-correlated DLTS. DDLTS also detected a slight diffusion of magnesium. Cr- and Mg-implanted samples showed many of the same damage-related trap pair levels as those measured in the 6H-SiC:Ar samples. It is interesting to note that there were no damage-related trap levels observed in both 6H-SiC:Ar and 6H-SiC:Mg that were not also observed in 6H-SiC:Cr. However, damage-related trap levels were observed in both 6H-SiC:Ar and 6H-SiC:Cr that were not detected from 6H-SiC:Mg samples.

Trap Label	Energy (meV)	cross-section (cm <sup>2</sup> )	Association	implanted samples	Temp of peak (K) ( $\tau = 402.4 \text{ sec}^{-1}$ )
A	510/476	$5 \times 10^{-15}$	damage	Ar	266/250
B	615/576	$1 \times 10^{-15}$	V <sub>si</sub> -N complex	Ar, Cr, Mg	316/339
C	470/427	$1 \times 10^{-16}$	damage	Ar, Cr, Mg	292/269
D	383/332	$1 \times 10^{-16}$	damage	Ar, Cr	247/213
E <sub>1</sub> /E <sub>2</sub>	310/260	$3 \times 10^{-16}$	damage	Ar, Cr	191/162
F	690/645	$1 \times 10^{-16}$	damage	Ar	356/393
G	683/732	$1 \times 10^{-15}$	Cr	Cr	376/400
H	785/840	$1 \times 10^{-15}$	Cr	Cr	426/451
I	293/250	$1 \times 10^{-17}$	damage	Mg	218/188
J	897/968	$6 \times 10^{-16}$	Mg	Mg	488/525
K	363	$1 \times 10^{-17}$	Mg or trap "D"	Mg, possibly Ar, Cr	250
L	1107	$1 \times 10^{-15}$	Mg	Mg	579
M	679/760	$1 \times 10^{-16}$	Mg	Mg	412/446

Table VI-7. Dominant trap levels detected in DLTS measurements of n-type 6H-SiC implanted at 475 °C with either argon, chromium, or magnesium.



Two different negative rate window peaks were observed in the 1600 °C annealed Cr-implanted sample and in the 1200 °C annealed Mg-implanted sample. No minority carrier trap levels were detected in the argon-implanted samples. The negative peak in the 6H-SiC:Mg was absent following a 1400 °C anneal. This indicates that at least two types of p-n-like junction structures are being created by implantation/annealing. It also suggests that implanted Cr- and Mg-related defects may be involved in the formation of these structures.

Annealing at 1600 °C appears to activate Mg-related trap levels more effectively than Cr-related trap levels. In fact, raising the anneal temperature up to 1600 °C actually diminishes the activation of the Cr-related trap levels. In both the Cr- and Mg-implanted samples, increasing the anneal temperature to 1600 °C improved the electrical quality of the test diode allowing higher temperature DLTS measurements. This effect was reversed for the Cr- and Mg-implanted samples when the annealed temperature was raised to 1800 °C. These effects place a major constraint on using thermal annealing to activate these implanted ion species.

Increasing the implantation temperature from room temperature to 475 °C had the greatest effect on the reduction of damage-related defects in 6H-SiC:Cr. 6H-SiC:Mg samples showed an implantation temperature effect to a lesser degree. The elevated implantation temperature also generated a higher concentration of Cr-related and Mg-related deep level traps that thermal annealing up to 1600 °C failed to reduce below detectable levels. Ion-implanted samples of both species showed reduced leakage current with the higher implantation temperature. Ion-implantation temperature studies using both higher

and lower implantation temperatures should be conducted to see the extent of these effects.

The ideal end state of ion implantation and thermal annealing is the complete activation of the implanted ion species and the total repair the implantation-induced damage of the crystal lattice. In the case of ion-implanted magnesium and chromium, this would mean the activation of the Mg and Cr atoms without degrading the quality of the crystal as evident by its electrical behavior and lack of detectable deep level defects (both damage- and species-related). This studied showed how ion implantation at an elevated temperature (475 °C) produced both damage-related and species-related deep levels that varied greatly in their response to thermal treatment. Elevating the implantation temperature appears to aid in reducing the concentration of some types of damage-related defects. However, not all defect types are responding to this treatment, even following a 1600 °C anneal.

Increasing the dose 20 to 40 times did not produce a proportional increase in the defect level concentrations. Cluster formation is a strong possibility at these dose levels and it may be wise to study the effect of varying the dose level over a much wider range, including much lower dose levels. Material quality improvements are still needed to fabricate test devices with better electrical performance before more detailed studies can be accomplished.

The uncertainties associated with the computed trap parameters are chiefly due to three error sources – error of the DLTS model, errors in the test measurements, and errors in the curve-fitting process. The DLTS model error is due chiefly to the error associated with the depletion approximation and the failure to model the narrow transition regions at

the leading and trailing edges of the depletion region. This error would be consistently repeated between samples and would tend to shift only the trap energy and trap concentration parameter values in a consistent manner. This could be as much as a 10 % shift in the trap energies and a 20 % shift in the trap concentrations. The change in the capture cross-section value would be insignificant. The errors in the test measurements were minimized through periodic electrical measurement checks and calibrations. It is believed that this error is small relative to the other two error sources. Curve-fitting errors are estimated to be near  $\pm 5$  % of the computed values of the three trap parameters ( $E_t$ ,  $\log(\sigma_t)$ , and  $N_t$ ). This estimate is based on detailed analysis of the sensitivity of the curve-fit to changes in the trap parameters.

## VI-2 N- and P-Implanted n-type 4H-SiC

Hall effect and cathodoluminescence (CL) measurements were made on 29 epitaxial MOCVD grown (0001) n-type 4H-SiC samples. The majority of the test diodes were nitrogen-, phosphorus-, and argon-implanted n-type ( $N_D - N_A = 5 \times 10^{15} \text{ cm}^{-3}$ ) samples. The ion implantations were performed at an elevated sample temperature of 500 °C and were annealed at temperatures of 1400, 1600, or 1800 °C. Unimplanted n-type 4H-SiC samples were also examined, with one unimplanted sample being annealed at 1800 °C. These temperatures were chosen based on published studies on ion-implanted SiC polytypes (Kroko, 1966; Campbell, 1973; Ahmed, 1995) and the limit in the number of samples available for test. Activation of ion-implanted atoms are not observed with a thermal anneal below 1200 °C. Above 2000 °C, the silicon carbide semiconductor becomes unstable.

The purposes for making Hall effect and cathodoluminescence measurements of N- and P-implanted and annealed n-type epitaxial 4H-SiC samples were to assess the activation of these donor ions and evaluate the level of damage recovery. The n-type epitaxial 4H-SiC samples were ion-implanted with  $N^+$ ,  $P^+$ , or  $Ar^+$  at 130, 215, and 310 keV, respectively, to create a peak implantation depth of 2000 Å. The selected implantation doses ranged from  $\phi = 1 \times 10^{13}$  to  $\phi = 1 \times 10^{14} \text{ cm}^{-2}$  for each of the three implant species to create a peak implantation concentration, ranging from  $2 \times 10^{17}$  to  $1 \times 10^{19} \text{ cm}^{-3}$ . The implantation and anneal parameters and measurement techniques used for the tested samples are listed in Table VI-8.

<b>Implant Species</b>	<b>Implant Energy (keV)</b>	<b>Implant Dose (cm<sup>-2</sup>)</b>	<b>Dopant Conc. (cm<sup>-3</sup>)</b>	<b>Anneal Temperature (°C)</b>	<b>Measurement Technique</b>
N <sup>+</sup>	130	1x10 <sup>13</sup>	5x10 <sup>15</sup>	1400/1600/1800	CL
N <sup>+</sup>	130	3x10 <sup>13</sup>	5x10 <sup>15</sup>	1400/1600/1800	CL, Hall
N <sup>+</sup>	130	1x10 <sup>14</sup>	5x10 <sup>15</sup>	1400/1600/1800	CL
P <sup>+</sup>	215	1x10 <sup>13</sup>	5x10 <sup>15</sup>	1400/1600/1800	CL
P <sup>+</sup>	215	3x10 <sup>13</sup>	5x10 <sup>15</sup>	1400/1600/1800	CL, Hall
P <sup>+</sup>	215	1x10 <sup>14</sup>	5x10 <sup>15</sup>	1400/1600/1800	CL
Ar <sup>+</sup>	310	1x10 <sup>13</sup>	5x10 <sup>15</sup>	1400/1600/1800	CL
Ar <sup>+</sup>	310	3x10 <sup>13</sup>	5x10 <sup>15</sup>	1400/1600/1800	CL
Ar <sup>+</sup>	310	1x10 <sup>14</sup>	5x10 <sup>15</sup>	1400/1600/1800	CL
un	--	--	5x10 <sup>15</sup>	unannealed/1800	CL

Table VI-8. List of n-type epitaxial 6H-SiC p-n diodes used in the Hall effect (Hall) and cathodoluminescence (CL) studies. Ion implantations were made at 500 °C.

## VI-2-A Cathodoluminescence Measurements

Before cathodoluminescence measurements could be made, backside ohmic contacts were formed on the p-type substrate (backside) side of the 4H-SiC samples. The samples consisted of bulk p-type material on which an epitaxial p-type layer was grown, followed by an epitaxial n-type layer. The ion implantations were done into the n-type epilayer. The ohmic contacts were formed by evaporative deposition of aluminum. Ohmic contacts on the backside of the samples were required since, the sample must be grounded to "bleed off" any built-up charges created by the excitation electron-beam in cathodoluminescence. Without grounding, the electron-beam would be deflected by the repulsive surface charge. Good thermal contacts were also required to ensure that the sample temperature was controlled and accurately measured. The energy, current, and focus of the excitation electron-beam was controlled and monitored to ensure repeatability between measurements. Multiple samples were examined during each CL measurement session by placing multiple samples on the "cold finger" sample holder and making multiple measurements. Using an electron-beam penetration-range model based on a modification of the Bethe formula by C. Feldman (Feldman, 1968), the penetration depth of 10 keV electrons was calculated to be approximately 1.3  $\mu\text{m}$  in SiC - the thickness of the top epilayer. By controlling the beam energy, excitation could be limited to just the ion-implanted epilayer (top layer).

In figure VI-27, the CL spectra are shown for the nitrogen-, phosphorus-, and argon-implanted ( $\phi = 3 \times 10^{13} \text{ cm}^{-2}$ ) 4H-SiC samples annealed at 1600 °C. Also shown are the CL spectra for two unimplanted samples – one unannealed and one annealed at 1800 °C.

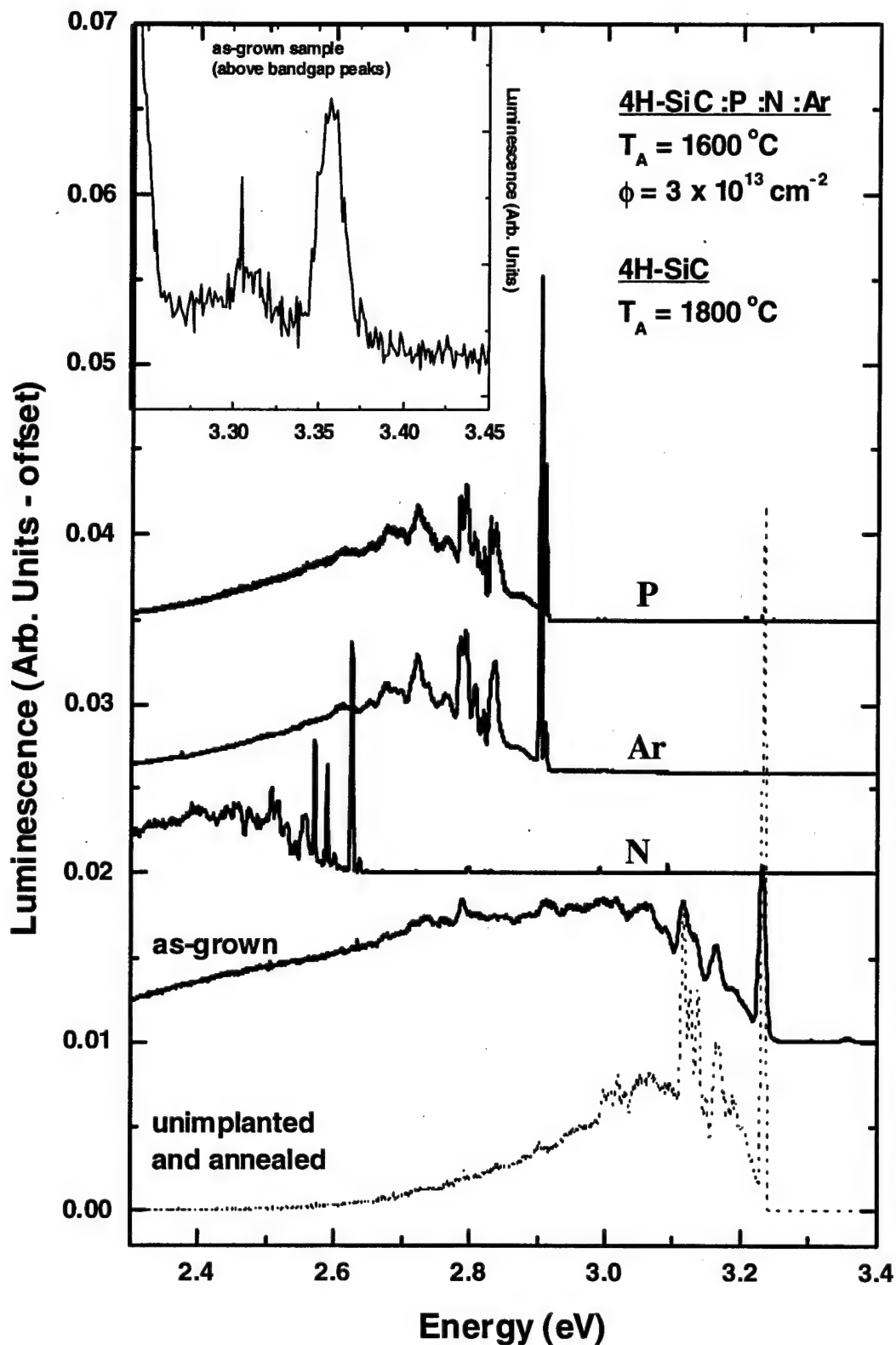


Figure VI-27. Cathodoluminescence spectra of as-grown, unimplanted/annealed ( $T_A = 1800\text{ }^{\circ}\text{C}$ ), and ion implanted/annealed ( $T_A = 1600\text{ }^{\circ}\text{C}$ ) epitaxial n-type 4H-SiC. Inset shows the above bandgap peaks observed from the as-grown samples. The spectra have been offset for clarity.

These spectra were recorded at 7 K using a  $\frac{3}{4}$  meter spectrometer with a 1200 lines/mm grating, 400 mm entrance and exit slits, and a liquid nitrogen cooled photomultiplier tube (PMT). This cathodoluminescence setup gives a spectral resolution of 3.2 meV at 3.0 eV. For the shown spectra, the beam energy was set to 7 keV with a predicted penetration depth of 0.7  $\mu\text{m}$  (7000 Å). Each spectrum will be discussed in detail in the following sections.

The inset in figure VI-27 is an enlargement of the above bandgap CL spectra ( $E_g = 3.256$  eV at 7 K) from the as-grown (unannealed) n-type 4H-SiC sample. Clearly shown in the inset are two luminescence peaks at 3.36 and 3.31 eV. This above-bandgap peak pair may be associated with transitions from a higher-level conduction band minimum. A similarly reported observation was made by Kaczer *et al.* from BEEM (Ballistic Energy Electron Microscopy) measurements of 4H-SiC (Kaczer, 1998). This cathodoluminescence observation is only the second reported observation of the higher conduction band minimum in 4H-SiC. Energy band calculations predict the existence of a higher conduction band minimum in 4H-SiC (Nilsson, 1996). This is another example of the effect of polytypism on the electrical/optical properties of silicon carbide. In 6H-SiC, energy band calculations predict an overlap of the next highest conduction band minimum with the lower conduction-band minimum. The BEEM measurements placed the higher conduction band minimum in 4H-SiC at 130 meV above the lower conduction-band minimum. That value agrees well with this study's CL measurements which places the higher conduction band minimum in 4H-SiC at 120 meV above the lower conduction-band minimum. The difference in values is well within measurement error and the varia-



tion between the two measurement techniques (enthalpy differences). This above-bandgap peak pair is not observed in any of the other tested samples and thus indicates the level of material quality required for such an observation.

Also seen in the as-grown samples is the near-bandgap N-associated zero-phonon lines (ZPL) at 3.23 eV and associated phonon replica lines. This spectrum is due to the recombination of an exciton bound to substitutional neutral nitrogen. These lines occur in pairs due to the hexagonal- and cubic-like inequivalent lattice sites that exist in the silicon carbide polytype 4H. The ratio of hexagonal to cubic sites is 1:1 with the hexagonal site producing the higher energy peaks in each pair. This is better illustrated in figure VI-28 showing the CL spectrum of the 1800 °C annealed unimplanted sample. The energy spacing between paired spectral lines is approximately 11 meV. The dissociation energies of the exciton bound to the neutral nitrogen are approximately 9 and 20 meV for the hexagonal and cubic sites, respectively. The higher binding energy at cubic sites results in a more localized exciton and significantly increases the probability of recombination without momentum-conserving phonons. This is evident by the intensity of the 3.234 eV cubic-site ZPL ( $Q_0$ ) and near lack of the 3.245 meV hexagonal-site ZPL ( $P_0$ ). The P-series denotes recombinations of excitons bound to neutral nitrogen substituting at hexagonal sites while the Q-series denotes recombinations of exciton bound to neutral nitrogen substituting at cubic sites. The subscripts identify the energies of the phonons involved in the recombinations. By measuring the energy spacing of the ZPL pair and the associated phonon-replica lines, phonon energies were calculated to be 37, 68, 95, and 108 meV. Figure VI-29 is a comparison of these calculated values to the SiC phonon dispersion curves (c-axis) developed by Feldman showing relatively excellent agreement.

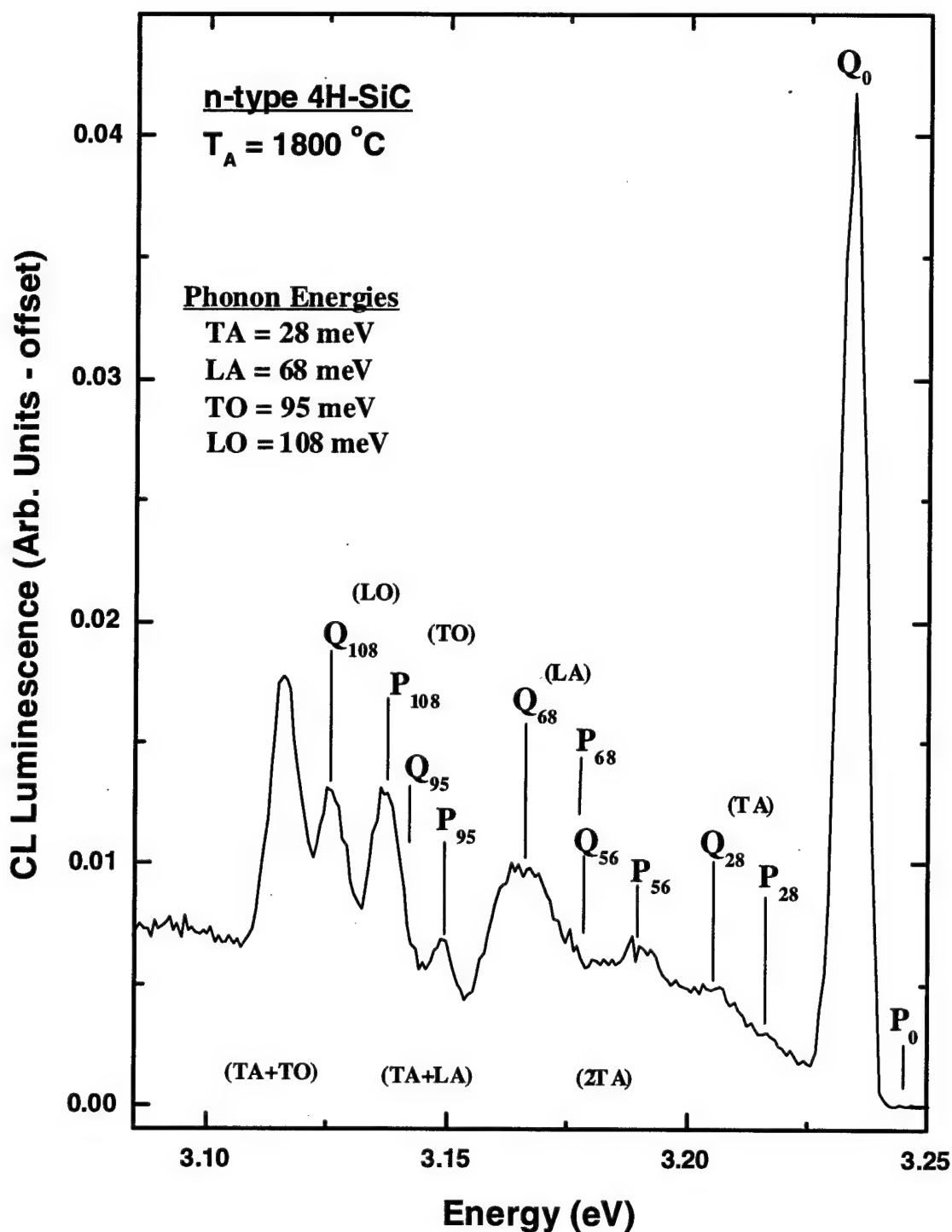


Figure VI-28. Cathodoluminescence spectra of n-type 4H-SiC epilayer annealed at  $T_A = 1800\text{ }^{\circ}\text{C}$ . The first ten phonon replicas are labeled. The P-series denotes hexagonal sites and the Q-series denotes cubic sites with the subscripts denoting the phonon energies in meV involved in the recombinations. The cubic-site zero phonon line (ZPL) dominates the spectrum due to a higher recombination probability for the tighter bond exciton.

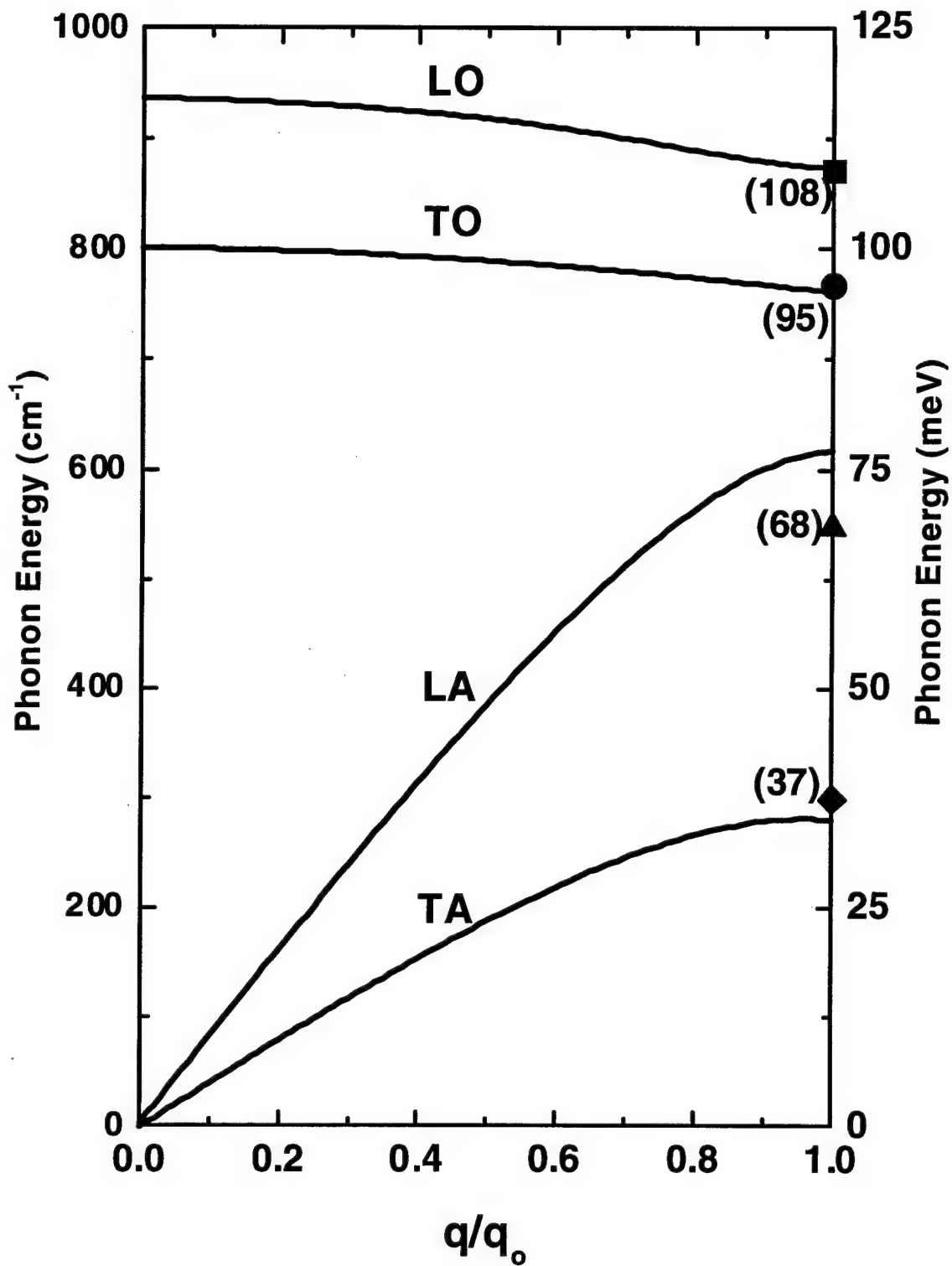


Figure VI-29. Shown are the calculated phonon energies of 37, 68, 95 and 108 meV (shown along the right hand side of the graph) from cathodoluminescence measurements of n-type 4H-SiC. The curves shown are those reported by Feldman for the phonon energies for SiC along the c-axis. (Feldman, 1968)

Feldman's curves are generated from a collection of phonon measurements made from 3C-, 4H-, 6H-, and 15R-SiC (Feldman, 1968).

Shown in figure VI-30 are the detailed CL spectra of the two unimplanted samples. When the unimplanted sample was annealed to 1800 °C (the highest anneal temperature used in this study), the above-bandgap peak pair is no longer observed, indicating a change in the material sufficient to either significantly reduce the probability of these radiative transitions or generate absorption centers for these optical energies. However, the annealing did dramatically increase the cubic-site ZPL intensity and the intensities of the single-phonon replica lines while reducing the intensities of the multiple-phonon replica lines. This indicates that the 1800 °C anneal has altered the local environment of the residual substitutional nitrogen to significantly increase the probability of zero- and single-phonon radiative recombination of bound-electrons at substitutional nitrogen sites while reducing the probability of multi-phonon radiative recombination. Another possibility for the observed spectral-intensity change is that the 1800 °C anneal may have effectively reduced the concentration of other defects that were participants in alternative non-radiative relaxation processes.

Beam-parameter and sample-temperature CL studies were also accomplished to gain insight into the depth dependencies and nature of the observed spectra lines. In figure VI-31, sample temperature-dependent CL spectra are shown for the unimplanted-annealed ( $T_A = 1800$  °C) sample. The beam energy was kept constant at 7 keV as the sample temperature was raised from 6 to 35 K. Each spectral line, associated with the near-bandgap bound-exciton recombination, is proportionally quenched, without any significant line broadening or shifting of the peak energies. As the intensity of the lines are

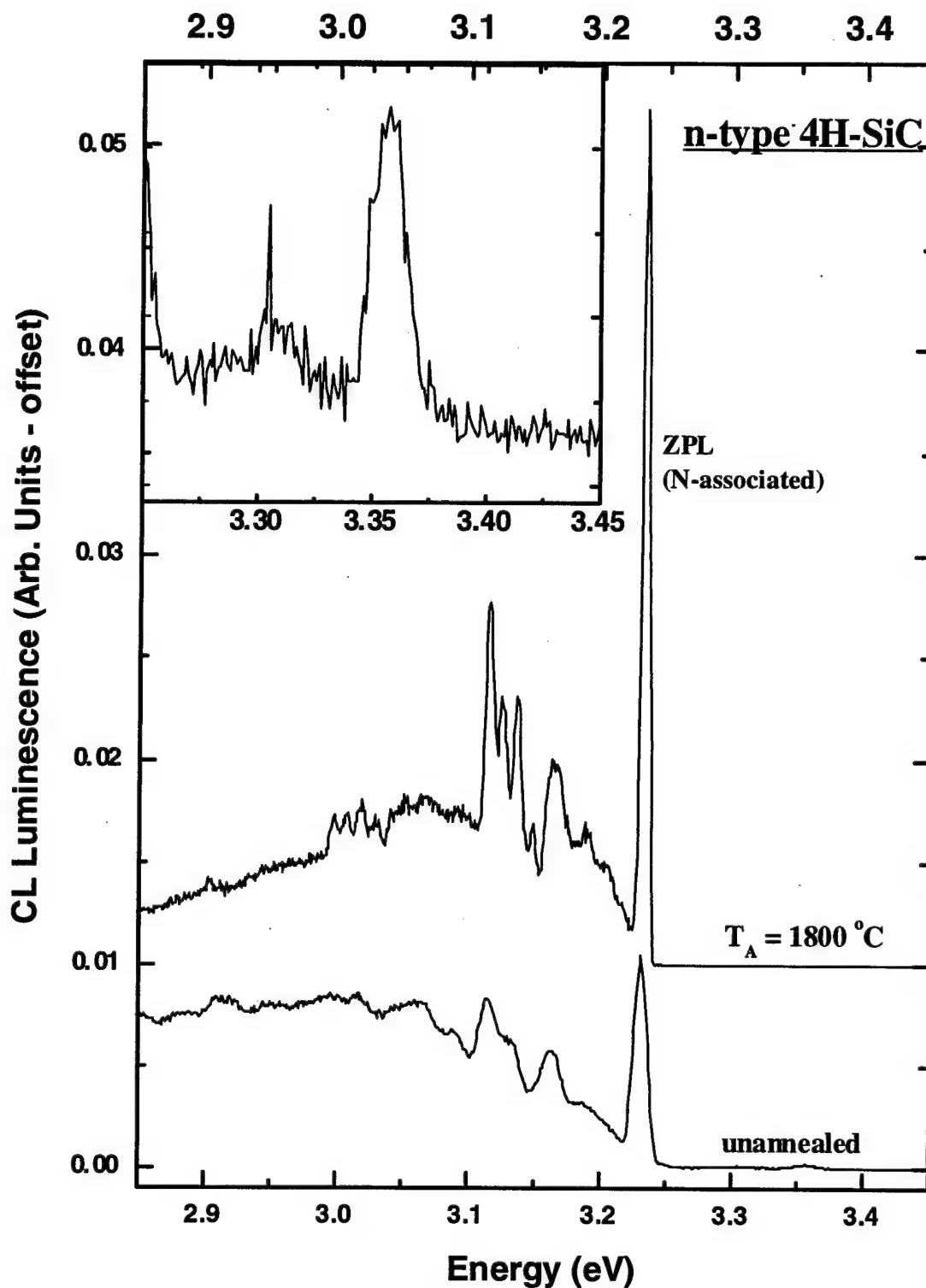


Figure VI-30. Cathodoluminescence spectra of n-type 4H-SiC epilayer - unannealed and annealed at  $T_A = 1800^\circ\text{C}$ . Note the effect of annealing on the N-associated zero-phonon line pair and associated phonon-replica line pairs. Spectrum of annealed sample is offset for clarity. Inset shows the above bandgap peaks observed only from the unannealed (as-grown) sample.

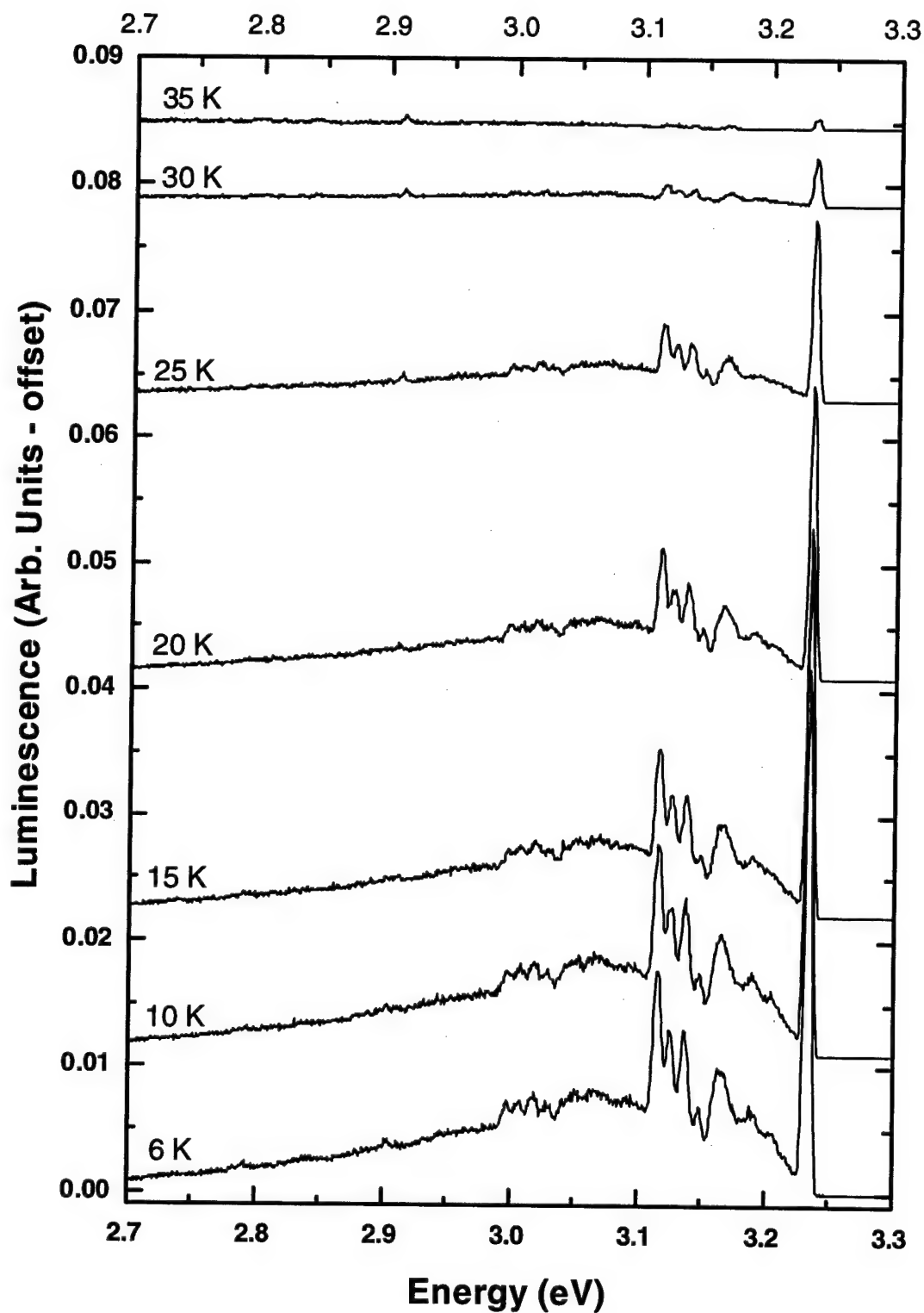


Figure VI-31. Sample temperature dependent cathodoluminescence spectra of unimplanted 4H-SiC annealed at 1800 °C. Spectra are offset for clarity. Note proportional intensity reduction of ZPLs and associated phonon replica lines.

reduced with increasing temperature, an additional line become apparent at 2.91 eV. The intensity of the 2.91 eV line does not reduce significantly with increasing sample temperature and is therefore associated with a different defect site. This 2.91 eV line is also observed in P- and Ar-implanted samples and is believed to be damage-related.

No other cathodoluminescence peaks are generated by merely annealing the unimplanted 4H-SiC sample. Any defect centers generated solely by annealing are either non-radiative in the detectable CL range of 1.4 - 3.45 eV or too low in concentration to be detected by cathodoluminescence techniques. Therefore, the CL peaks generated in the ion-implanted and annealed samples are related to ion implantation effects.

### VI-2-A-1 CL Measurements of 4H-SiC:N

Shown in figure VI-32 are the CL spectra for three high-temperature (500 °C) N-implanted ( $\phi = 3 \times 10^{13} \text{ cm}^{-2}$ ) n-type 4H-SiC samples annealed at 1400, 1600, and 1800 °C. The N-associated near-bandgap ZPLs (3.23 eV) and associated phonon replica lines are not detected in the nitrogen-implanted and annealed samples. From the sample annealed at 1400 °C, a zero-phonon line pair of a new free-to-bound spectra is detected at approximately 2.637 and 2.626 eV with the lower energy peak being an order of magnitude more intense than the higher energy peak. The identities of the site constituents are unknown. However, this spectrum is not detected in the unimplanted, Ar-implanted or P-implanted 4H-SiC samples. These two conditions suggest that the ion-implanted nitrogen is not being annealed to form isolated substitutional nitrogen but, instead, is complexing with at least one other defect to form a radiative defect center. Additional peak pairs in Fig. VI-32 at lower energies are the associated phonon-replica spectra lines. The spacing of these lines is identical to the spacing of the phonon-replica lines related to the N-associated near-bandgap peak pair reported earlier for the unimplanted samples. This equivalent spacing is expected as the phonon energies are determined by the host crystal-line structure.

When the N-implanted sample was annealed at  $T_A = 1600 \text{ °C}$ , the same CL spectral lines were produced with two differences. One difference was that the higher energy peak of the ZPL pair becomes an order of magnitude more intense than the lower energy peak. It appears that there is an inequivalent-site dependence on the formation and evolution of this defect with anneal temperature. This switch in relative intensity is also



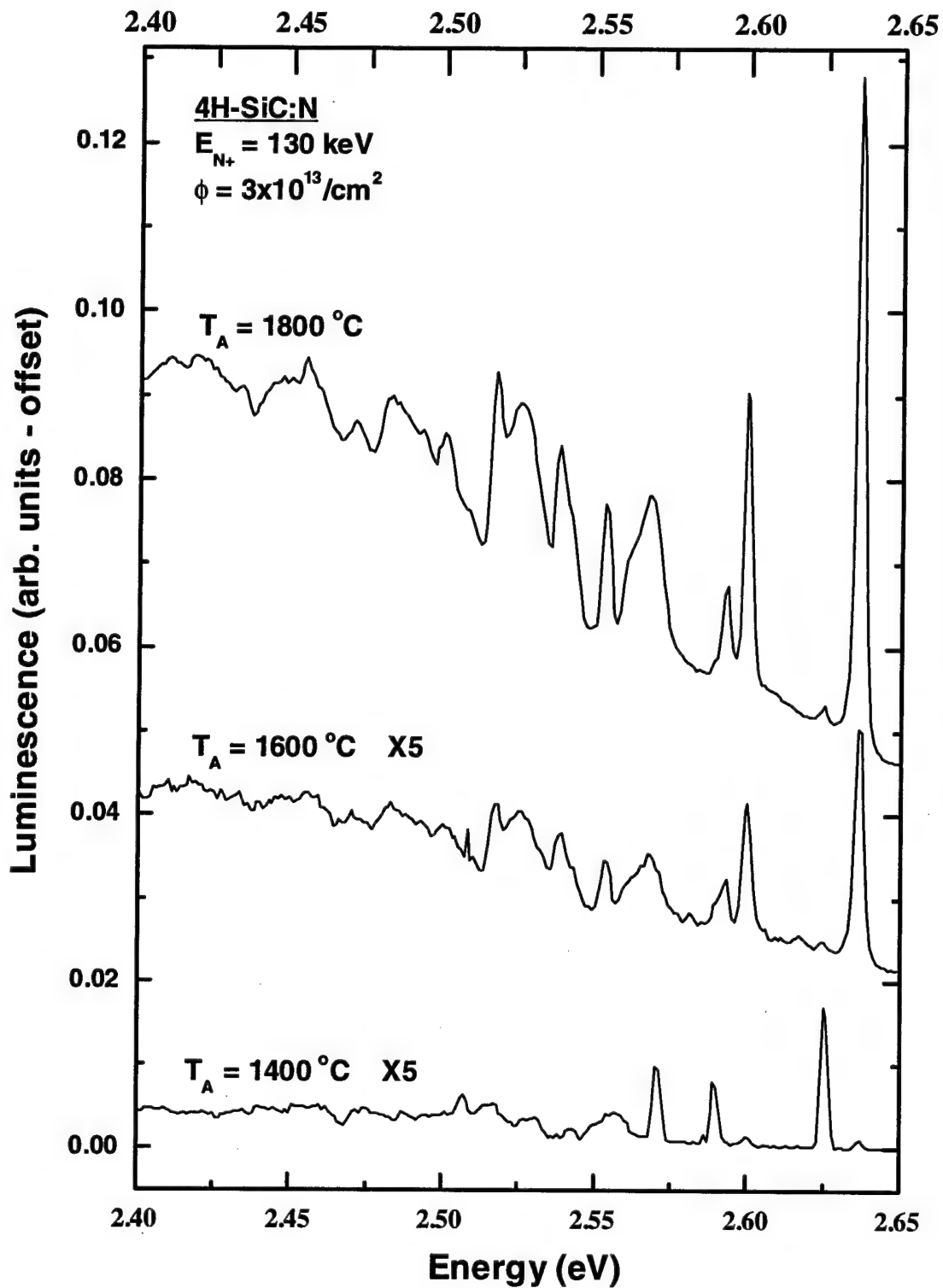


Figure VI-32 CL spectra of N-implanted ( $500^\circ\text{C}$ ) n-type 4H-SiC annealed at 1400, 1600, and  $1800^\circ\text{C}$ . Note the dramatic increase in intensity of peaks following an  $1800^\circ\text{C}$  anneal.

seen in the associated phonon-replica peak pairs. This mirroring behavior in the phonon replica lines aided in calculating the phonon energies since each replica line could then be associated to the appropriate inequivalent lattice site. Another difference was the increase in the intensity of the broad spectra centered at 2.42 eV. The spectrum produced in this energy region is believed to be the multi-phonon replica lines of the 2.637 and 2.626 eV ZPL pair. However, this broad peak also corresponds to a previously reported deep donor-acceptor (DAP) spectra associated with nitrogen and a deep level acceptor-type defect (Scofield, 1996).

Following a thermal anneal of  $T_A = 1800$  °C, the CL spectra again remain the same with the exception of an increase in intensity by more than an order of magnitude. The ratio of intensity between the paired lines remains the same as observed in the  $T_A = 1600$  °C sample. The intensity of the CL spectrum near 2.42 eV increases and the distinctive peaks that develop correspond to multi-phonon replica locations. If this broad peak was due to DAP recombination, associated distant DAP peaks would also be present. However, none are detected. It is quite interesting that there is no CL evidence that the substitutional nitrogen site is being restored, even following an anneal of 1800 °C. The radiative transition associated with the relaxation of a bound electron at a substitutional nitrogen site and observed in unimplanted n-type 4H-SiC may be prevented by non-radiative relaxations that include relaxations involving this nitrogen-related complex. Apparently, there exists a large number of ion-implantation damage-related defects that are not repaired by these high-temperature anneals.

The temperature dependence of the CL spectrum of the N-implanted samples was examined to gain an insight into the nature of the created defect. In figure VI-33, the CL

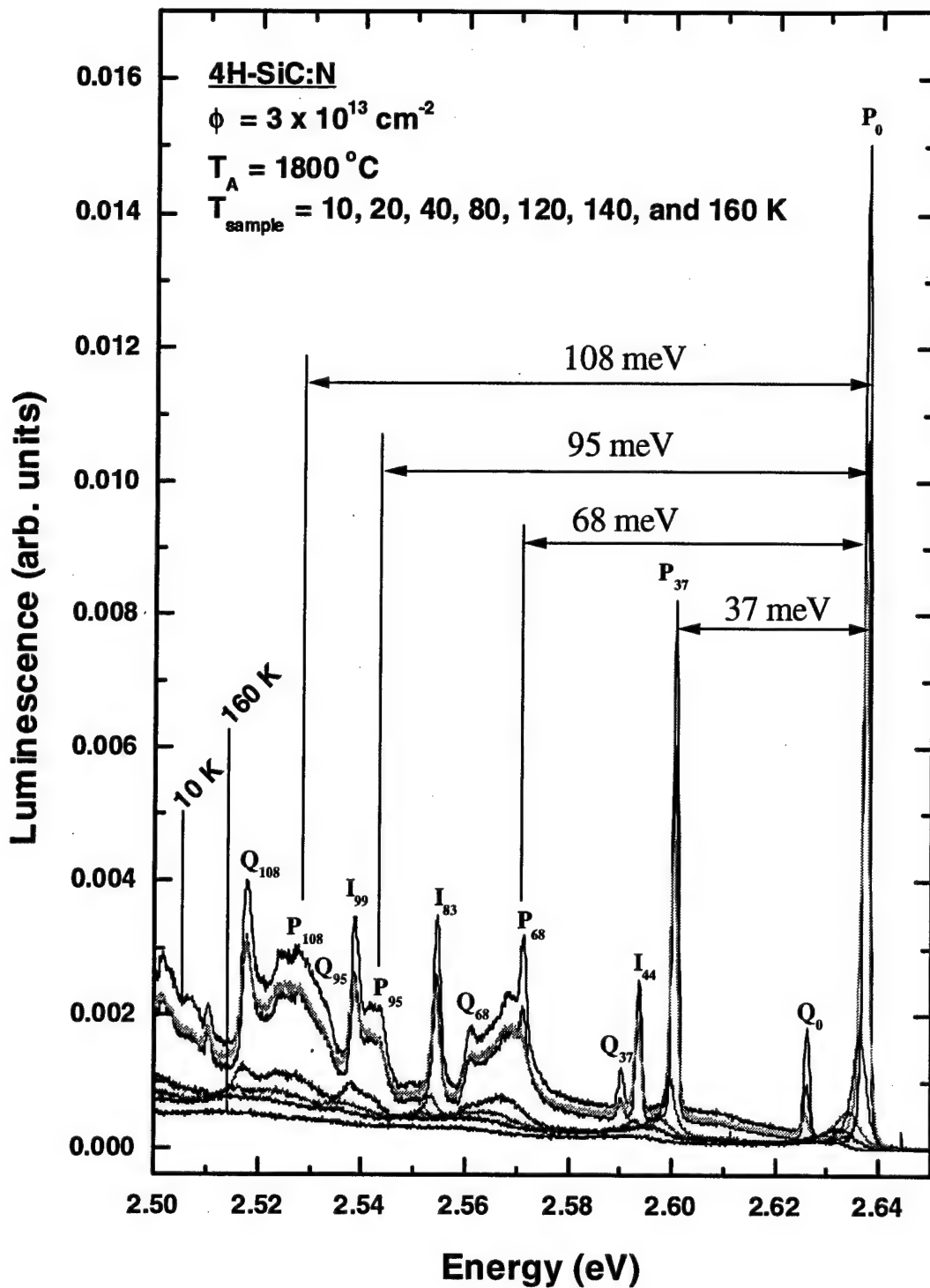


Figure VI-33. Sample temperature dependent cathodoluminescence spectra of 4H-SiC:N sample annealed at  $1800^\circ\text{C}$ , showing the shifting of the peaks to lower energy with increasing sample temperature. Also shown are the phonon replica corresponding to previously calculated values. Note that, unlike the exciton peaks, these peaks are not as quickly thermally quenched indicating a free-to-bound transition.

spectrum is shown for the 1800 °C annealed 4H-SiC:N ( $\phi = 3 \times 10^{13} \text{ cm}^{-2}$ ) sample at sample temperatures from 10 to 160 K. The hexagonal- and cubic-site related peaks are labeled P and Q, respectively, along with the associated phonon replica lines. Shown are the previously computed phonon energies matching the spacing of the P-series peaks. Two significant differences exist between these spectra lines and the previously shown CL spectrum lines for the unimplanted samples. First, the thermal quenching of the lines from the 4H-SiC:N samples is not as rapid. In the unimplanted samples, the CL lines were fully quenched by  $T_{\text{sample}} = 40 \text{ K}$ . In the N-implanted samples, the CL lines are still detectable to a sample temperature of  $T_{\text{sample}} = 160 \text{ K}$ . This suggests that the CL spectrum of the 4H-SiC samples are not due to excitons. Excitons are weakly bound and tend to exist only at low temperatures. The second major difference is the shift of the CL spectrum lines to lower energies with increasing sample temperature. This shift correlates well with the bandgap dependence on temperature. At temperatures below the Debye temperature of the semiconductor ( $\sim 311 \text{ K}$  for SiC) (Pankove, 1971), the bandgap varies proportionately to the square of the temperature.

Shown in figure VI-34 is the peak position of the 2.6376 eV peak plotted versus sample temperature. This rate of change with sample temperature suggests that these ZPL peak pair lines are due to free-to-bound (F-B) transitions. The two possible F-B transitions are a donor-like defect to valance band transition or a conduction band to an acceptor-like defect transition. Which transition is actually occurring cannot be determined solely by the CL spectra.

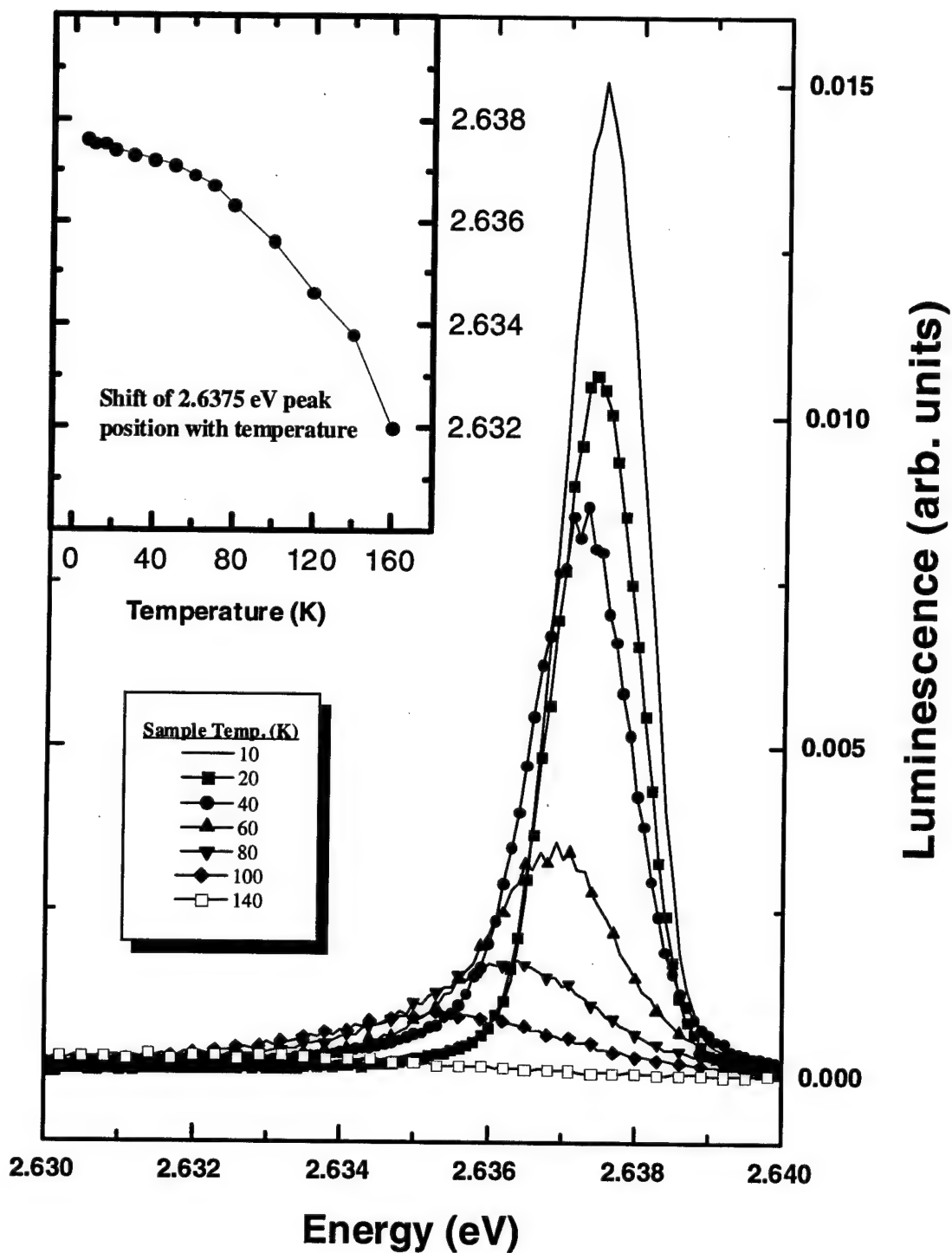


Figure VI-34. Shift of the 2.6376 eV (at 6.5 K) ZPL in 4H-SiC:N ( $T_A = 1800^\circ\text{C}$ ) with sample temperature. Inset shows the square dependence of the peak position with temperature which corresponds to the square dependence of the bandgap with temperature. This indicates that the transition is band-related.

Shown in figure VI-35 is the depth-dependent CL spectra of the 4H-SiC:N sample ( $T_A = 1600^\circ\text{C}$ ) for 5, 6, 8, and 10 keV electron beam energies. The corresponding calculated penetration depths for the four beam energies are 0.4, 0.5, 0.9, and 1.3  $\mu\text{m}$ , respectively. The peak implantation depth for the ion-implanted nitrogen is 0.2  $\mu\text{m}$ . Due to limitations of the electron-beam gun, beam energies were not controllable below 5 keV and so depth variations could only be examined in the implantation tail region. No new spectra lines were detected as the beam energy was stepped through the four values. The only depth dependent change was a slight increase in the intensity ratio of the multi-phonon replica lines and the ZPLs. This disproportional increase in the multi-phonon spectra intensity is understandable since increasing the electron-beam energy results in additional energy being deposited in the epilayer, thereby locally heating the sample and increasing the probability of multi-phonon transitions. If the electron-beam penetration depth estimate is accurate, electron-hole pair production should also be occurring in the deeper undisturbed n-type material including the formation of nitrogen bound excitons. The lack of the previously observed 3.23 eV ZPLs in the 4H-SiC:N CL spectra must be due to re-absorption. The damage closer to the surface is re-absorbing these photons making the material opaque at these energies.

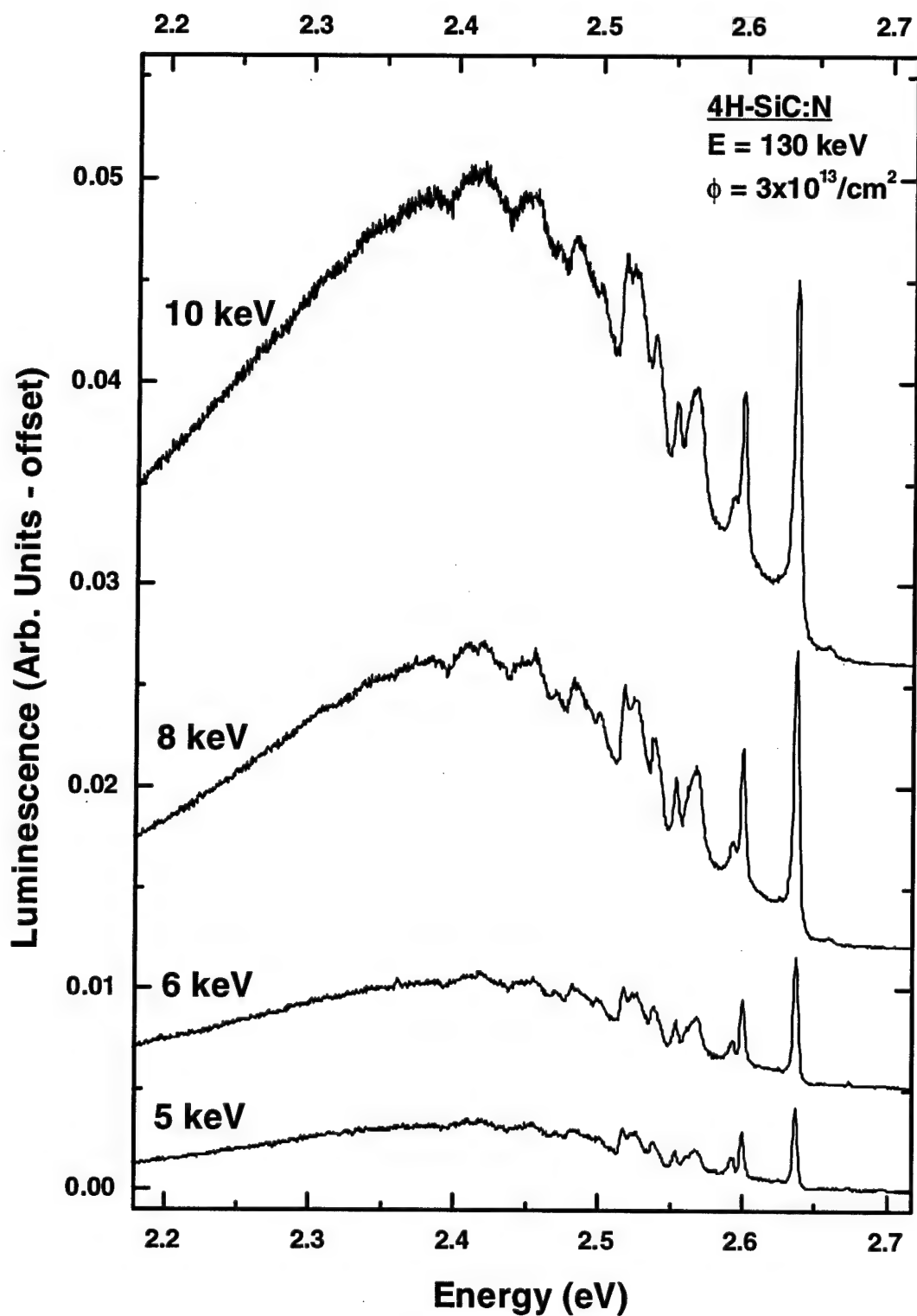


Figure VI-35. Cathodoluminescence spectrum of 2.63 eV ZPL pair and associated phonon-replica for 4H-SiC:N ( $\phi = 3 \times 10^{13} \text{ cm}^{-2}$ ,  $T_A = 1600 \text{ }^\circ\text{C}$ ) at four different electron beam energies (5, 6, 8, and 10 keV).

## VI-2-A-2 CL Measurements of 4H-SiC:P

Shown in figure VI-36 is the CL spectra for three P-implanted ( $\phi = 3 \times 10^{13} \text{ cm}^{-2}$ ) samples annealed at 1400, 1600, and 1800 °C. The CL spectra of the N-associated ZPLs for the 1600 °C annealed 4H-SiC:P sample is shown in the inset. Unlike the nitrogen-implanted samples, the phosphorus-implanted samples did show evidence of the near-bandgap ZPLs (3.23 eV) related to isolated substitutional nitrogen. However, the CL signal was drastically diminished from the intensity measured for the unimplanted samples. This indicates either less complexing of the residual substitutional nitrogen or less scattering sites are produced in phosphorus-implanted 4H-SiC than in nitrogen-implanted 4H-SiC. The CL spectra developed by the P-implanted samples also contained a ZPL pair at 2.91 eV and associated phonon replica lines. Again, the ZPLs are accompanied by an associated phonon replica spectrum with the same line spacing as measured in the CL spectra from 4H-SiC:N and unimplanted 4H-SiC. This is better illustrated in figure VI-37 showing the same three CL spectra expanded about the 2.91 eV ZPLs and phonon replica lines. The inset in this figure shows how the anneal temperature is affecting the intensity of the zero-phonon lines. With a 1400 °C anneal, the lower energy peak is about twice as intense as the higher energy peak. Following a 1600 °C anneal, the ratio is reversed with the higher energy peak nearly three times more intense than the lower energy peak. The 1800 °C anneal resulted in still another reversal in intensity between the two peaks. The amplitudes of these peaks are also comparable between samples since the ca



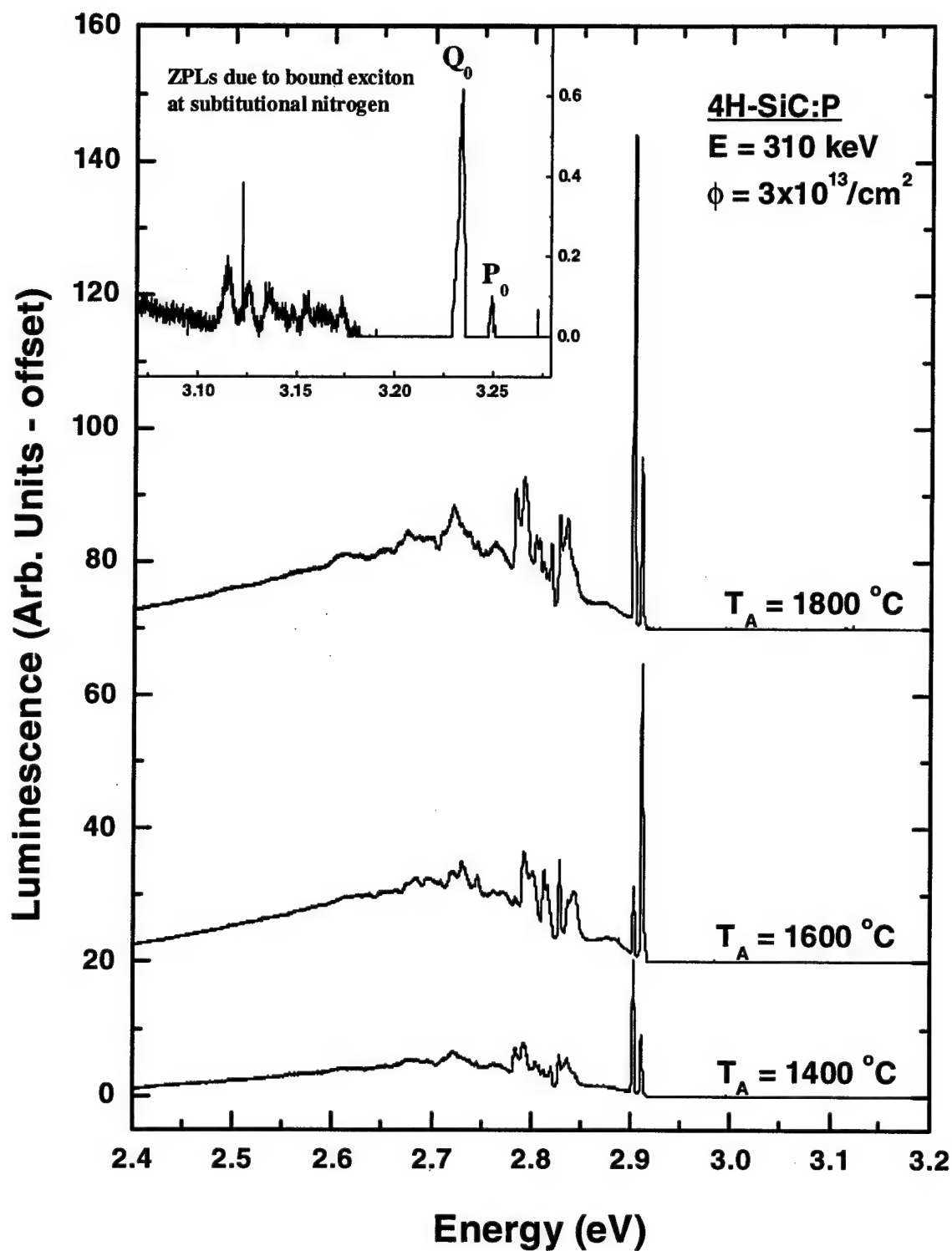


Figure VI-36. Cathodoluminescence spectra for the high temperature (500 °C) P-implanted ( $\phi = 3 \times 10^{13} \text{ cm}^{-2}$ ) n-type epitaxial 4H-SiC samples annealed at 1400, 1600, and 1800 °C. The inset shows the presence of the ZPLs detected in the unimplanted samples and related to the exciton bound to at substitutional nitrogen. The curves are offset for clarity.

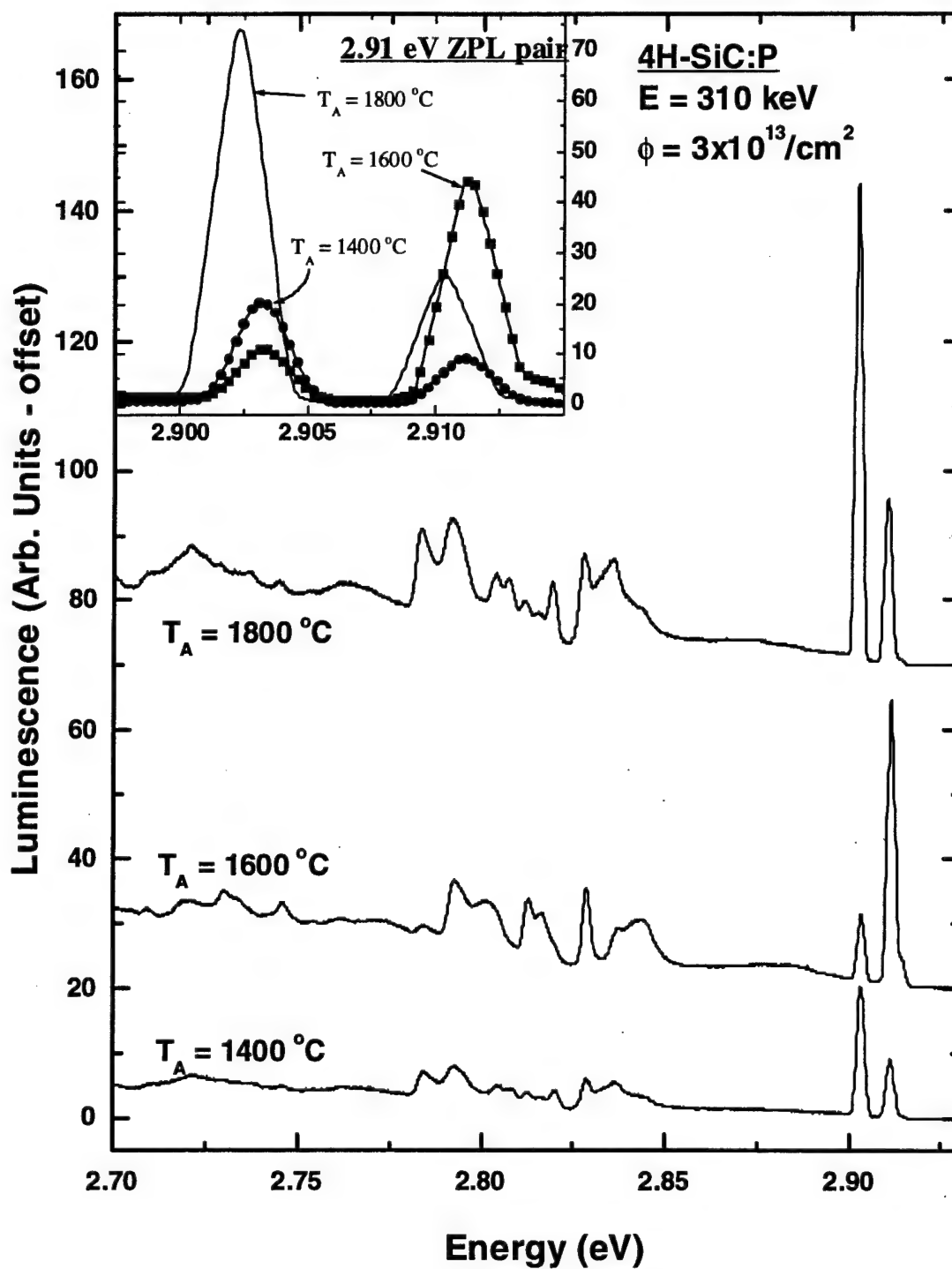


Figure VI-37. Cathodoluminescence spectra for 4H-SiC:P ( $\phi = 3 \times 10^{13} \text{ cm}^{-2}$ ) annealed at 1400, 1600, and 1800 °C. Spectra are offset for clarity. The inset shows the ZPLs dependence on anneal temperature. Note the slight shifting in the ZPL peaks and the changes in intensity with anneal temperature. Curves have been offset for clarity.

thodoluminescence measurements were accomplished during the same CL session. This CL session included a repeat measurement of the first CL run to ensure that the measurements were repeatable, including intensity. Comparing the intensities between samples reveals that a 1400 °C anneal minimizes the lower energy peak while maximizing the higher energy peak. However, high temperature implantation and annealing up to 1800 °C failed to significantly repair the damage associated with this spectrum. For comparison, the CL spectra for the P- and Ar-implanted ( $\phi = 3 \times 10^{13} \text{ cm}^{-2}$ ) samples annealed at 1400 °C are shown in figure VI-38. An electron-beam energy of 10 keV was used to generate these spectra, thus representing the deepest probing measurements. The appearance of the same ZPL pair and associated replica spectrum for the Ar-implanted sample suggests a damage-related radiative center. In addition, since phosphorus is not present in the Ar-implanted sample, phosphorus is not one of the constituents of this radiative center. The only differences between the CL spectra of the 4H-SiC:P and 4H-SiC:Ar samples were the relative intensities between paired peaks and the lack of the N-associated ZPLs in the Ar-implanted samples. Apparently, the argon implantation has generated much greater damage than the phosphorus implantation. This is understandable considering that a higher implant energy (310 versus 215 keV) was used to implant the argon ions. The different ion implantation energies were chosen to create equivalent implantation-peak depths. The CL spectra of the 4H-SiC:P and 4H-SiC:Ar samples indicated no other radiative defect sites. Beam energy dependency measurements indicated no significant depth dependence. Sample temperature dependent measurements indicated

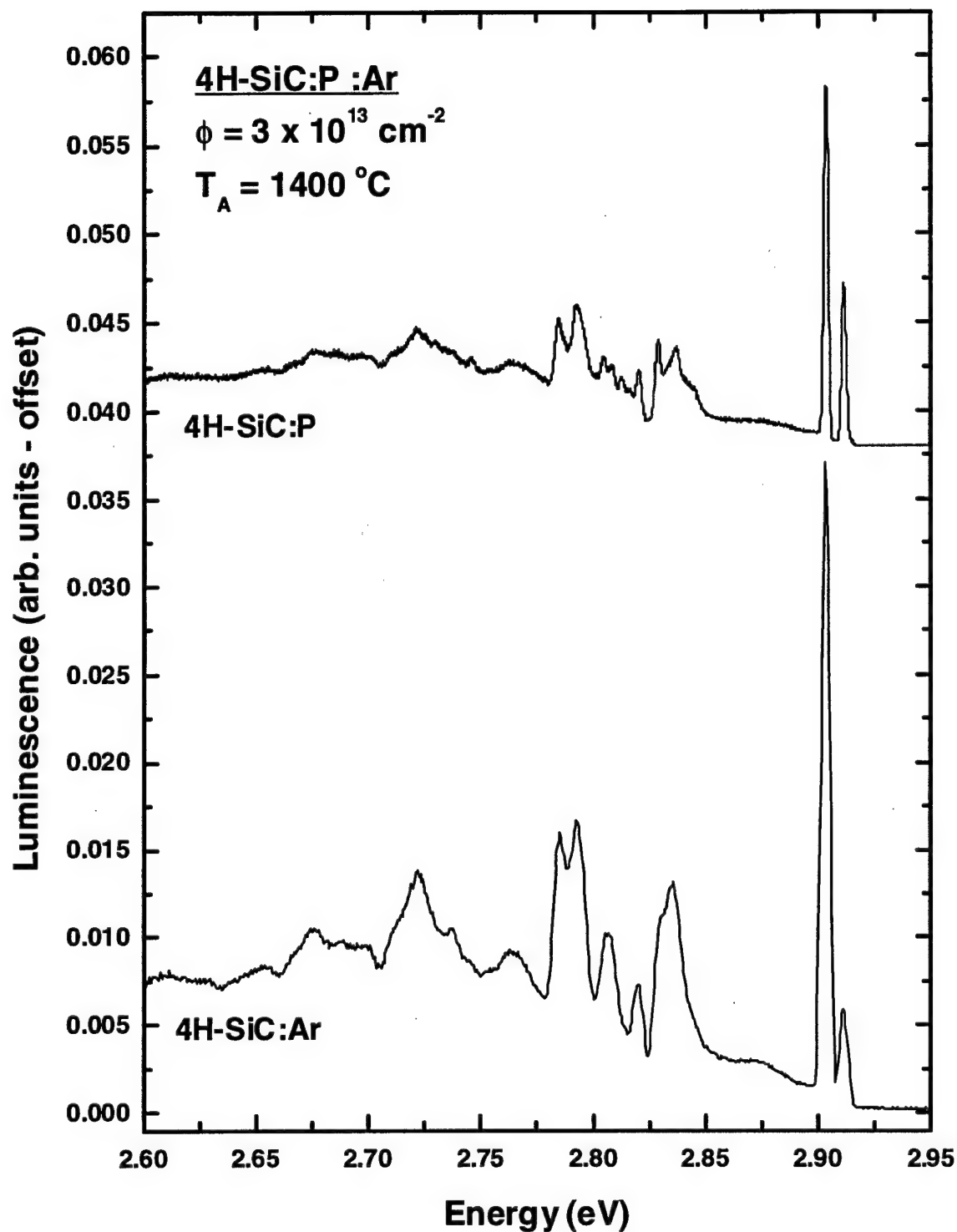


Figure VI-38. Cathodoluminescence spectra of 1400 °C annealed 4H-SiC:P and 4H-SiC:Ar samples. Spectrum of 4H-SiC:P is offset for clarity. Identical ZPLs and associated phonon replicas suggests this defect to be damage-related and that phosphorus is not one of the defect constituents. The electron-beam energy used for both spectra was 10 keV.

that the ZPLs and replica lines are due to a common defect and that the radiative transitions are free-to-bound.

From the CL measurements of both 4H-SiC:P and 4H-SiC:N annealed at 1400, 1600, and 1800 °C, it appears that an elevated implantation temperature of 500 °C and high temperature annealing up to 1800 °C are not sufficient to significantly repair the damage generated by ion implantation including, perhaps, the damage at residual substitutional nitrogen sites. To further investigate the state of the ion-implanted and annealed material, Hall effect measurements were made on the nitrogen- and phosphorus-implanted 4H-SiC epilayers. Cathodoluminescence provides only indirect information of non-radiative defects.

## VI-2-B Hall Effect Measurements

Hall effect/sheet-resistivity measurements were made from 77 to 700 K on the nitrogen- and phosphorus-implanted 4H-SiC samples (SiC:N and SiC:P) using a van der Pauw method. Ohmic contacts were formed at the corners on the ion-implanted n-type epilayer using Ti/Ni evaporated 500  $\mu\text{m}$  diameter dots. Prior to evaporating the contact metals, a low-energy (50 keV) nitrogen implantation at the four corner areas was accomplished to produce high dose ( $1 \times 10^{19} \text{ cm}^{-3}$ ) corner regions on which the ohmic contacts were made. This ion implantation of the corner contact areas was required to form ohmic contacts due to the low donor concentration ( $5 \times 10^{15} \text{ cm}^{-3}$ ) of the n-type epilayer. The same procedure was also performed on the unimplanted and Ar-implanted n-type epilayer samples. However, these samples did not support the formation of ohmic contacts and thus, for these samples, Hall effect measurements were not possible. The Hall field strengths and current-voltage ranges were optimized for the tested samples over the entire temperature range. A Hall field of 5kG was used for both the mobility and free carrier concentration measurements. Hall effect voltage limits were set at 1.4 V to limit the current to under 10 mA over the entire sample temperature range (77 - 700 K).

### VI-2-B-1 Hall Effect Measurements of 4H-SiC:N

Hall effect/sheet-resistivity measurements were made for the high temperature (500 °C) nitrogen-implanted ( $\phi = 3 \times 10^{13} \text{ cm}^{-2}$ ) n-type epitaxial 4H-SiC samples. Shown in figure VI-39 is an Arrhenius plot of the sheet carrier concentration as a function of sample temperature for the 4H-SiC:N samples annealed at 1400, 1600, and 1800 °C. From the plotted curve, in Arrhenius format, the donor activation energy can be determined by the curve's slope. The slopes are consistent and linear over the lower portion of the sample temperature range of 77-300 K for all three samples and give a 63 meV value for the dominant donor level. This value falls within the 45 to 124 meV range of reported inequivalent lattice site nitrogen donor levels.(Ikeda, 1980; Scofield, 1996; Feldman, 1968) It is nearly identical to the 65 meV value reported by Ikeda *et al.* (Ikeda, 1980) by photoluminescence, which is believed to be associated with a donor located at the hexagonal-site. The deeper cubic-site level near 125 meV is observed only for the  $T_A=1400$  °C annealed sample, where the curve becomes steeper near 400 K. At the higher sample temperatures ( $> 500$  K), a deeper donor of  $\sim 250$  meV was also detected as indicated by the increased slope. It should be pointed out that an unidentified damage-related donor-like defect level of  $280 \pm 50$  meV has been reported in ion-implanted n-type 4H-SiC measured by deep level transient spectroscopy (Scofield, 1996).

At room temperature, the sample annealed at  $T_A = 1400$  °C had the highest free carrier concentration of  $7 \times 10^{12} \text{ cm}^{-2}$  while the sample annealed at  $T_A = 1800$  °C had the lowest free carrier concentration of  $3 \times 10^{12} \text{ cm}^{-2}$ . The 1600 °C annealed sample had only a

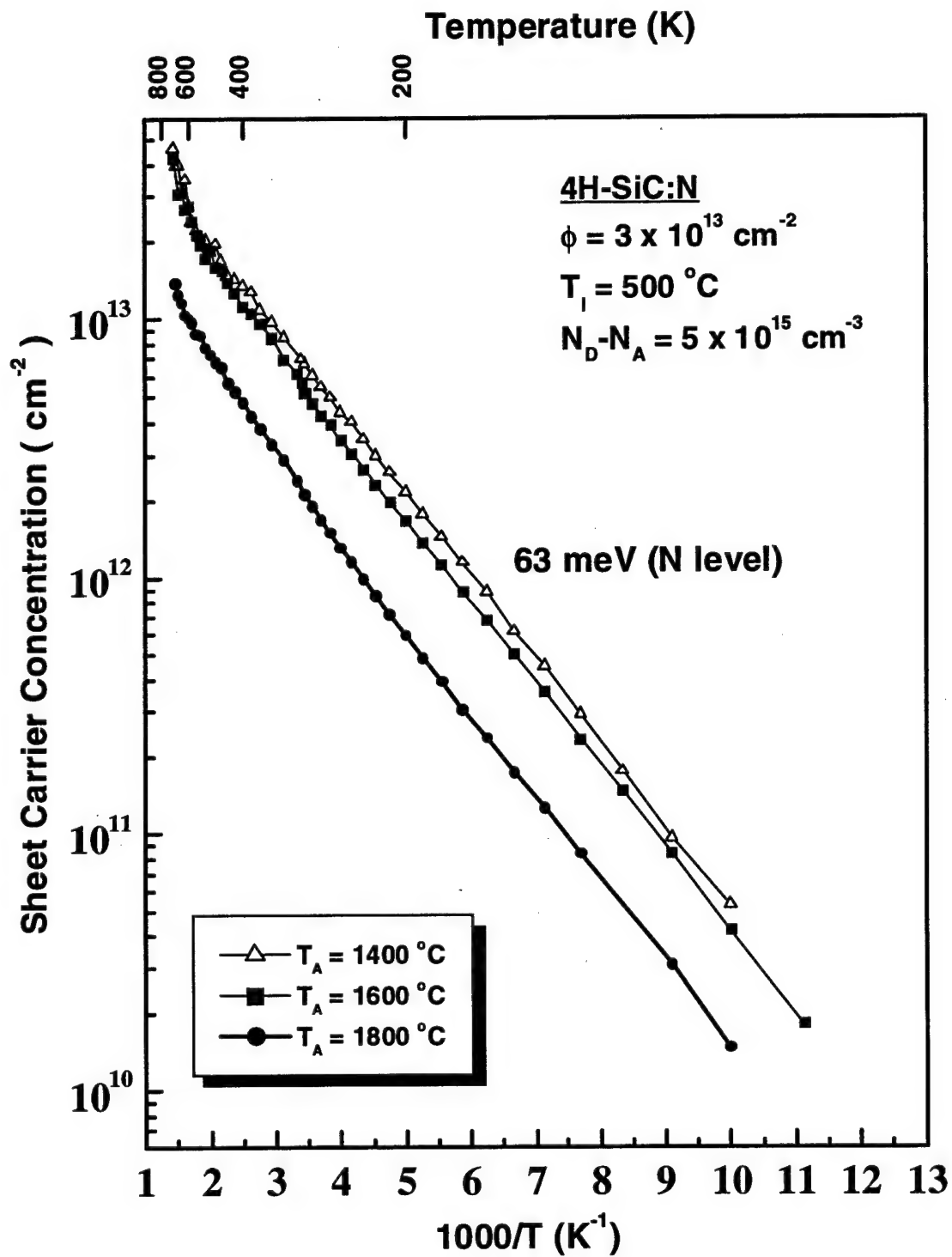


Figure VI-39. Sheet carrier concentration measurements of three N-implanted n-type 4H-SiC samples annealed at 1400, 1600 , and 1800 °C. A computed value of 63 meV is determined from the sheet carrier concentration slope and is associated to the shallow nitrogen donor level.



slightly smaller free carrier concentration of  $6 \times 10^{12} \text{ cm}^{-2}$  than the 1400 °C annealed sample.

The mobility for the same three 4H-SiC:N samples is illustrated in figure VI-40, where the mobility is plotted in  $\log_{10}$  scale versus sample temperature. From the 1800 °C annealed sample, a maximum mobility of  $120 \text{ cm}^2/\text{V}\cdot\text{sec}$  at 300 K was obtained. The mobilities (at 300 K) for the 1400 and 1600 °C annealed samples were only slightly less at  $100 \text{ cm}^2/\text{V}\cdot\text{sec}$ . The 400 °C increase in annealing temperature (1400 to 1800 °C) appears to have only a slight effect on reducing the total number of scattering sites in the high-temperature implanted 4H-SiC:N. The decreasing mobility with increasing sample temperature trend suggests that the dominant mechanism is lattice scattering. The two most important scattering mechanisms are impurity and lattice scattering. As the temperature of the sample increases, the mean free-electron velocity increases and impurity scattering becomes less since the electron remains near the impurity for a shorter time. At the same time, the lattice vibrations increase with increasing sample temperature and the mobility is reduced due to the increase exchange of energy between the free electrons and the lattice. The mobility due to lattice scattering decreases in proportion to  $T^{-3/2}$ . Shown in figure VI-40 is the theoretical  $T^{-3/2}$  curve associated with lattice scattering. The annealing trends suggests that the electrically-active implanted-nitrogen may be complexing with defects created during an 1800 °C anneal. This may explain the observed reduction in the carrier concentration (reduced activation) while the mobility increases (reduced scattering site concentration).

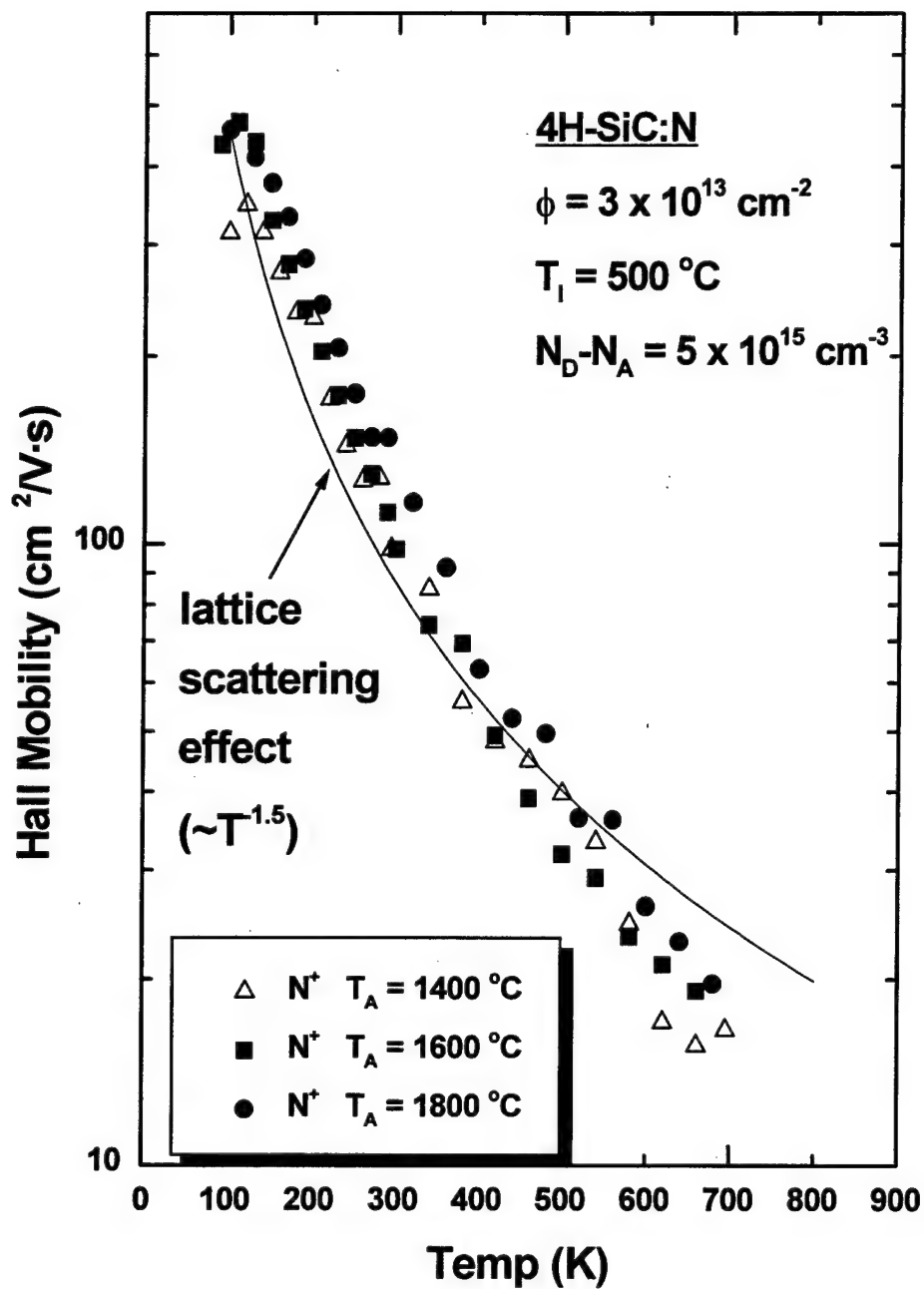


Figure VI-40. Hall mobility measurements of three N-implanted n-type 4H-SiC samples annealed at 1400, 1600, and 1800 °C. Increasing the anneal temperature had only the effect of slightly improving the mobility by approximately 20 %. The negative slope is determined by the lattice scattering effect.

## VI-2-B-2 Hall Effect Measurements of 4H-SiC:P

A similar set of data was obtained for the high temperature (500 °C) phosphorus-implanted ( $\phi = 3 \times 10^{13} \text{ cm}^{-2}$ ) n-type epitaxial 4H-SiC samples. In figure VI-41, the sheet carrier concentration is plotted versus sample temperature in Arrhenius format. The consistent linear slopes for the 1400, 1600, and 1800 °C annealed 4H-SiC:P samples indicate a 46 meV activation energy for the dominant donor level. No literature was discovered on phosphorus-implanted 4H-SiC to compare this value. To be consistent with the nitrogen donor levels, this relatively shallow level would be associated to a donor occupied at the cubic-site. The slope becomes dramatically steeper above 500 K indicating the presence of a significant concentration of a deeper level donor. The estimated activation energy of this deeper donor is between 250 and 380 meV. It is not known if this is the same donor that exists in the 4H-SiC:N samples.

If only a single donor level of significant concentration exists in the ion-implanted epilayer, then the curves would have a single slope. Additionally, if the donor site was fully ionized within the sample temperature range, the slope would "roll over" and remain nearly constant above the full-ionization temperature. This is not the case for 4H-SiC:P. In figure VI-42, hypothetical sheet carrier concentration curves are plotted - one for a single 46 meV level and the other for a 46 meV and a 300 meV level. Notice that the sheet carrier concentration curves differ significantly at the higher sample temperatures where the single 46 meV level is fully ionized by 500 K and the deeper 300 meV level is still only partially ionized. The deeper level detected by Hall effect measurements for 4H-

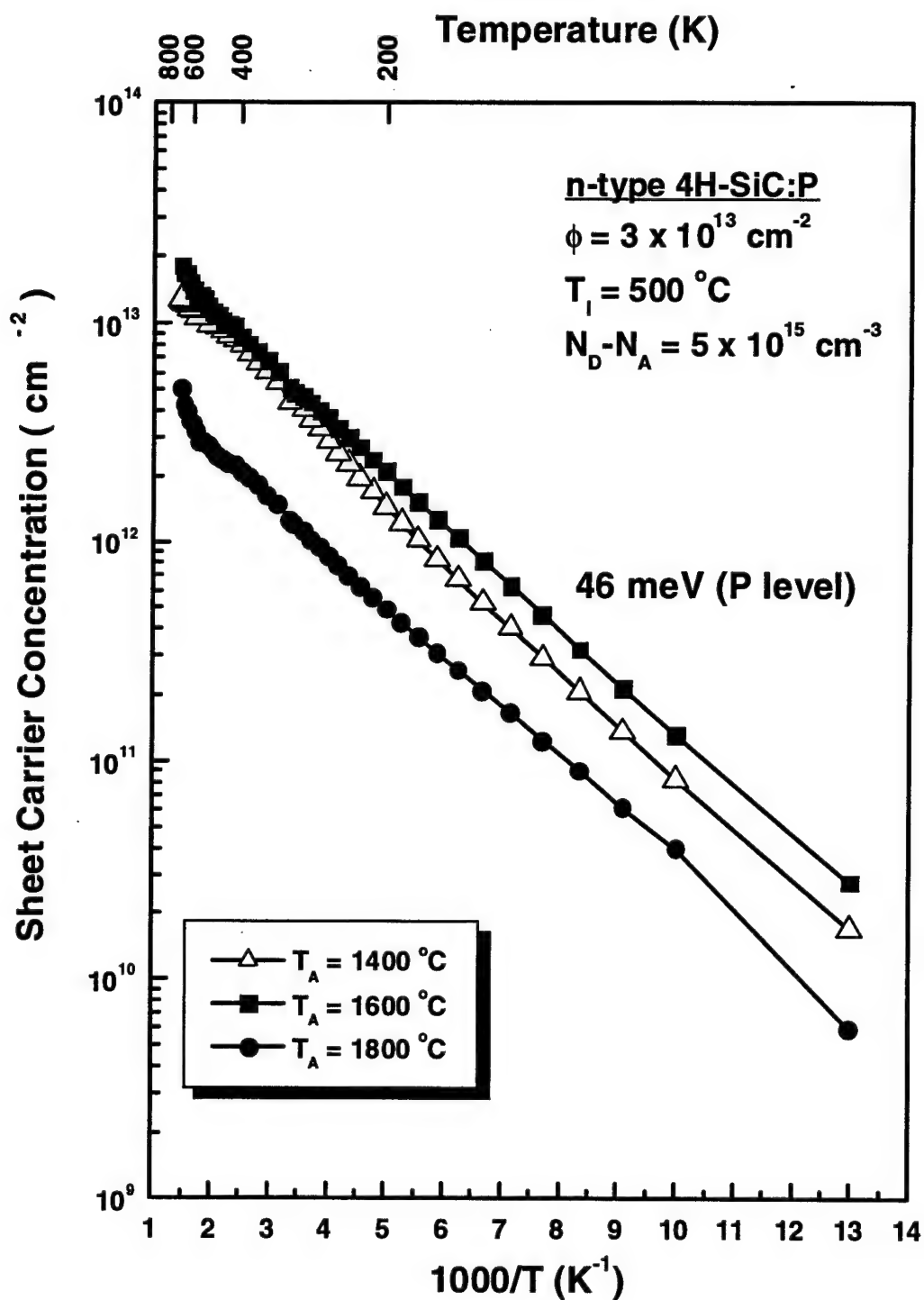


Figure VI-41. Sheet carrier concentration measurements of three P-implanted n-type 4H-SiC samples annealed at 1400, 1600, and 1800 °C. A computed value of 46 meV is determined from the sheet carrier concentration slope and is associated to the shallow phosphorus donor level.

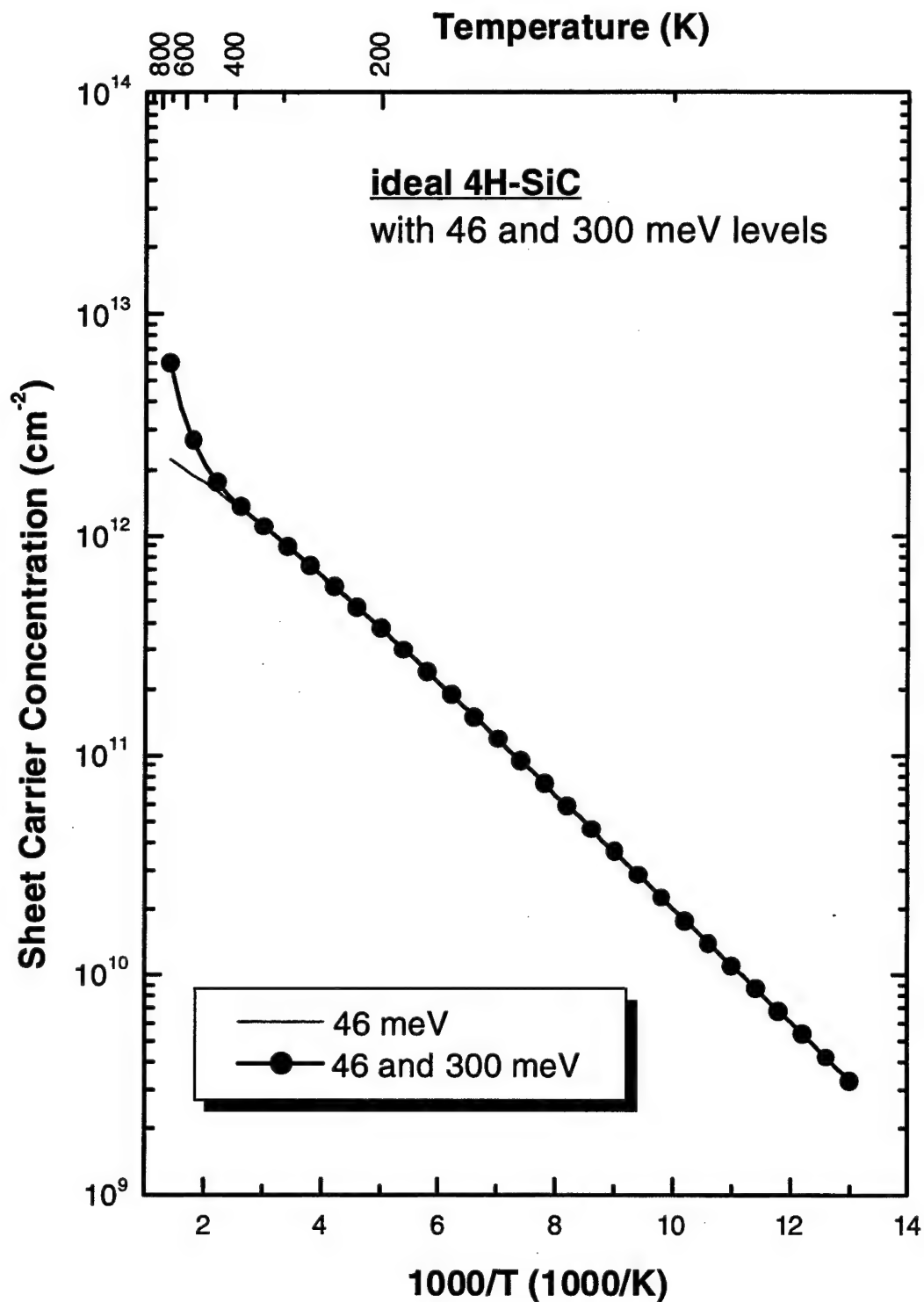


Figure VI-42. Computed sheet carrier concentration curves for an ideal 4H-SiC sample containing a single donor level at 46 meV, and containing two donor level at 46 and 300 meV. The concentration of the 300 meV levels was set at 10 times the concentration of the 46 meV level to  $6 \times 10^{13} \text{ cm}^{-2}$ .

SiC:P appears to be the same donor as that detected by cathodoluminescence (CL), because the activation energy of this level as measured by Hall effect is consistent with the activation energy measured by cathodoluminescence. Mobility measurements of 4H-SiC:P also indicate a reduction in the concentration of scattering sites as illustrated in figure VI-43 with the dominant scattering mechanism being lattice scattering. In this figure, the mobility of the free electrons increases significantly when the annealed temperature is raised to  $T_A = 1800\text{ }^{\circ}\text{C}$ . This indicates that the activation temperature for the large concentration defect lies in the 1600-1800  $^{\circ}\text{C}$  temperature range. Annealing would not effect the lattice scattering contribution.

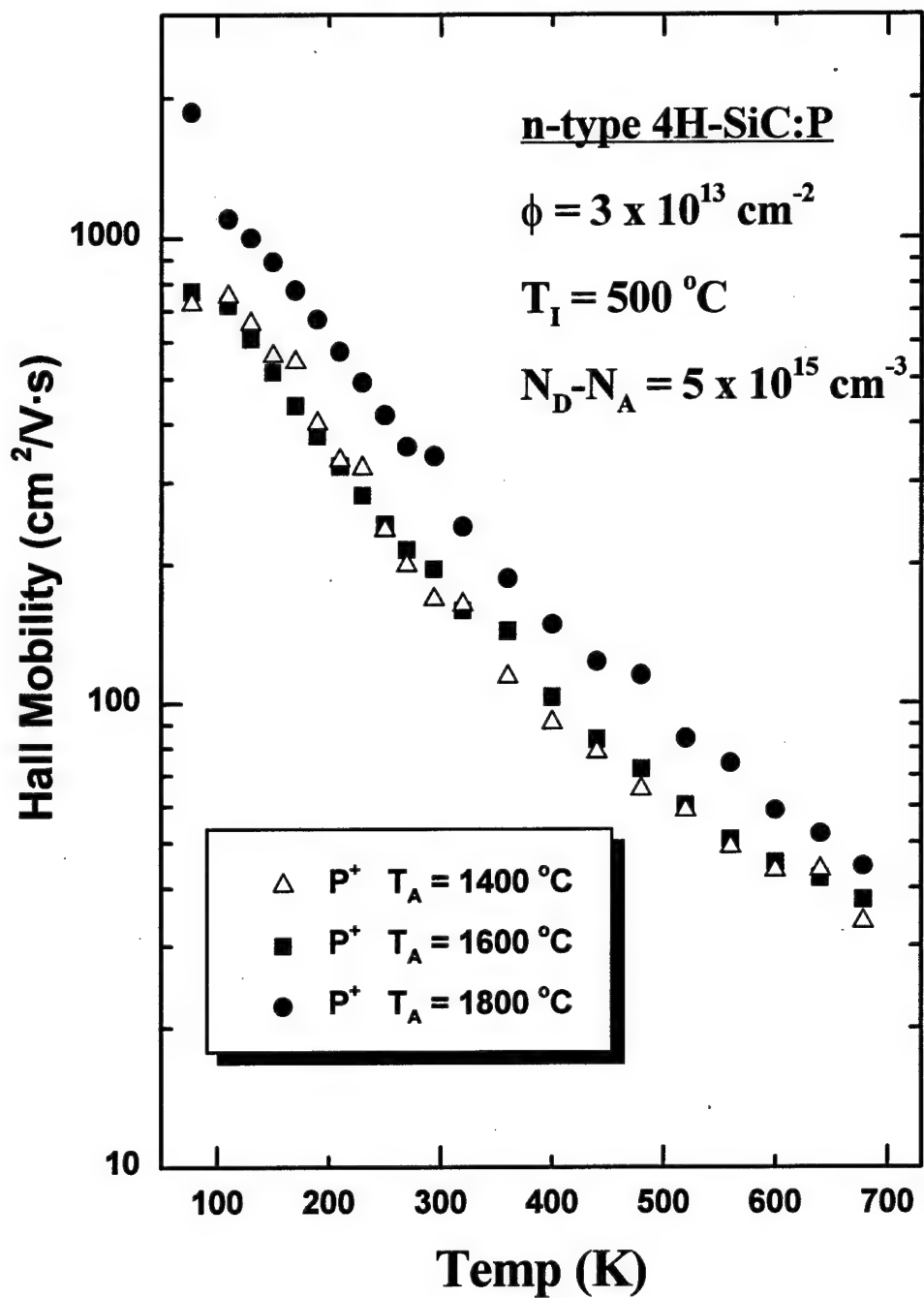


Figure VI-43. Hall mobility measurements of three P-implanted n-type 4H-SiC samples annealed at 1400, 1600, and 1800 °C.

### VI-2-B-3 Hall Effect Measurements Summary

Shown in figure VI-44 is the effect of anneal temperature on the activation efficiency of the dominant donor levels over the 77-500 K temperature range and the electron mobility at 300 K. The activation efficiency percentage was computed based on the calculated concentration of the shallow donor levels. The shallow donor levels are fully ionized at 600 K. The electrical activation of the N implant decreases slightly from 90 % when the anneal temperature is increased from 1400 to 1600 °C, and then decreases dramatically to approximately 30% after annealing at 1800 °C. Meanwhile, the mobility in 4H-SiC:N increases slightly from 100 to 120 cm<sup>2</sup>/V·sec. A similar trend exists for 4H-SiC:P. For the P-implant, the electrical activation increases slightly from 30 % as the anneal temperature increases from 1400 to 1600 °C, and then decreases dramatically to below 10 % after annealing at 1800 °C. The mobility in 4H-SiC:P increases significantly from 180 to 290 cm<sup>2</sup>/V·s following an 1800 °C anneal due to a reduction in the concentration of ionized donors. The mobility of 290 cm<sup>2</sup>/V·s for the 4H-SiC:P sample annealed at 1800 °C is only 20 % lower than the 370 cm<sup>2</sup>/V·s mobility value reported by Karmann *et al.* for CVD grown N-doped 6H-SiC (Karmann, 1992).

The optimum anneal temperature for high-temperature implanted 4H-SiC:N is near 1400 °C with a maximum activation efficiency of 90 %, while the optimum anneal-temperature for high temperature 4H-SiC:P is near 1600 °C with a maximum activation efficiency of 30 %. Certainly, an anneal temperature of 1800 °C is too high for both N- and P-implanted 4H-SiC. These two anneal-temperature trends of increased mobility



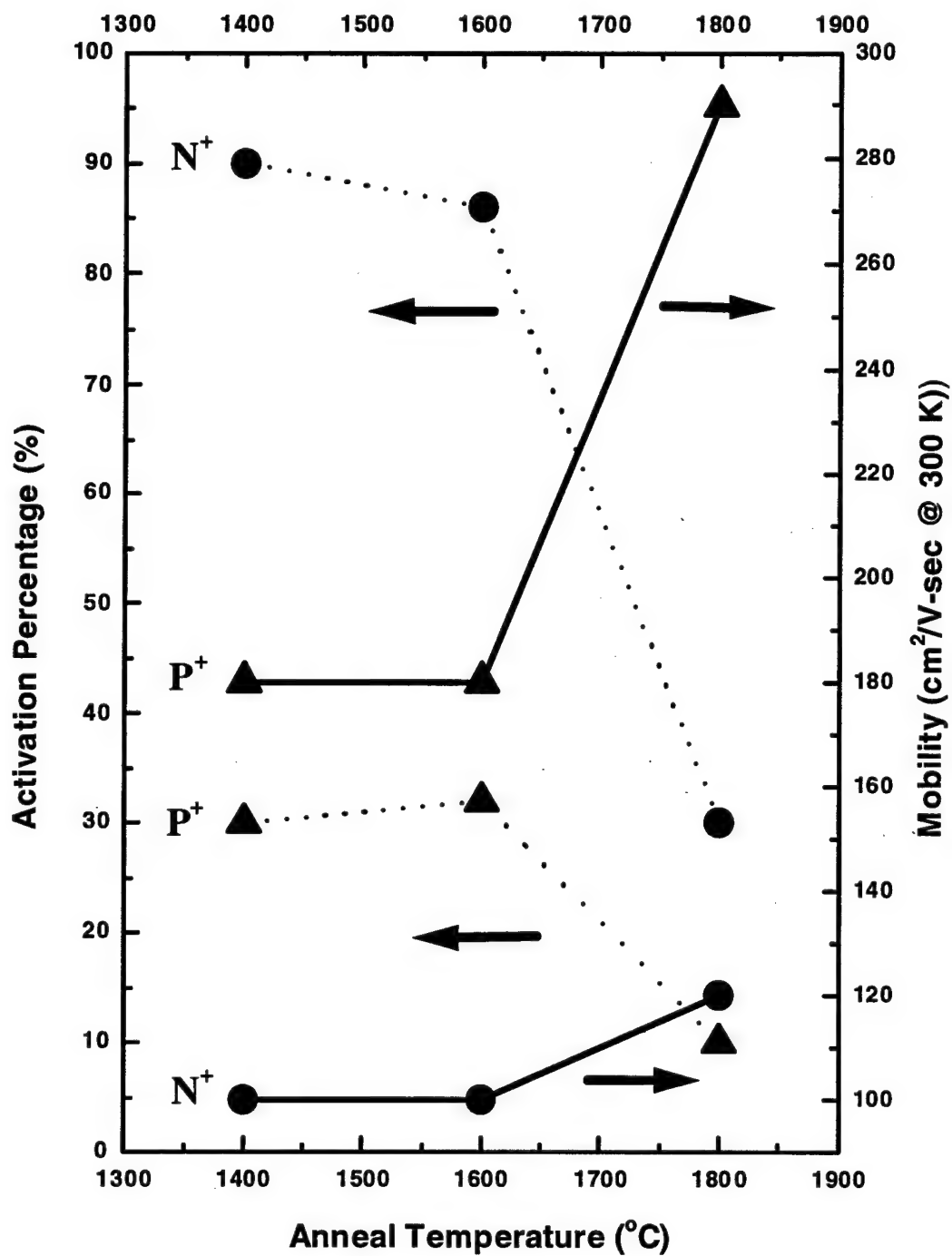


Figure VI-44. Activation efficiency and mobility dependence on anneal temperature on N- and P-implanted (500 °C) n-type 4H-SiC. Both implant types show improved mobility with increased anneal temperature. However, activation is dramatically reduced when the anneal temperature is raised to 1800 °C.

with decreasing activation suggest that the donor levels are complexing with defects during an 1800 °C anneal.

## VI-2-C Summary

Hall effect and cathodoluminescence measurements of high-temperature (500 °C) nitrogen- and phosphorus-implanted n-type 4H-SiC epilayers indicate that some of the defects created during ion-implantation are not being adequately repaired with thermal anneals of 1400, 1600, and 1800 °C. Shallow donor-like levels are being generated in both 4H-SiC:N and 4H-SiC:P samples at 63 and 46 meV, respectively. The 63 meV donor level found in 4H-SiC:N sample is believed to be due to a substitutional nitrogen at the hexagonal lattice site. The cubic-site 125 meV level was also observed. The 46 meV donor level observed in 4H-SiC:P may be due to a substitutional phosphorus at the hexagonal site. Additional deeper levels were detected in the ion-implanted samples. 4H-SiC:N has an additional donor level at 250 meV, and 4H-SiC:P has an additional level between 280 and 350 meV that may also be the radiative center observed by CL. We believe that the radiative center, 346 meV below the conduction band, is related to a damage center due to its additional presence in 4H-SiC:Ar. In 4H-SiC:N, a radiative level is detected at 626 meV from either the conduction or valence band. Figure VI-45 illustrates the possible levels existing in high temperature implanted 4H-SiC:N and 4H-SiC:P as measured by Hall effect and cathodoluminescence.

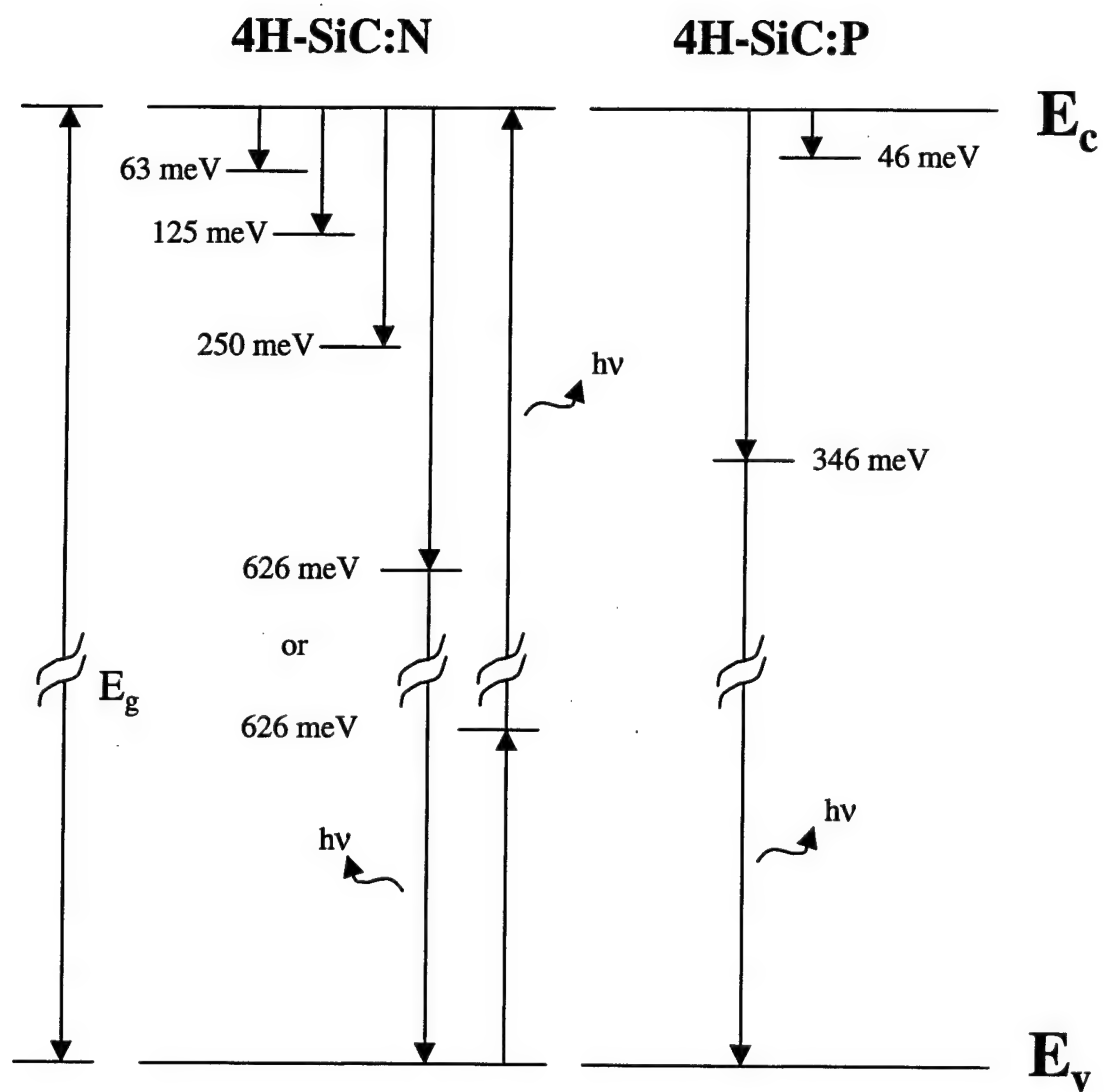


Figure VI-45. Observed levels in high temperature (500 °C) ion implanted and annealed 4H-SiC:N and 4H-SiC:P by Hall effect and cathodoluminescence measurements.

## VII CONCLUSIONS AND RECOMMENDATIONS

The goal of this research was to characterize the effect of high-temperature ion implantation and subsequent high-temperature annealing on the formation and evolution of damage- and species-related defects, both shallow and deep levels, in 6H and 4H polytype silicon carbide. In addition, optimum ion-implantation conditions were explored for these SiC samples.

From the deep level transient spectroscopy (DLTS) measurements of both room- and high-temperature ion-implanted 6H-SiC, 12 new deep level defect pairs were found and characterized, including their trap parameter values and categorization as either damage- or species-related (as listed in Table VI-7). The pairing of trap levels is due to the inequivalent lattice sites in the 6H-polytype material. In the Cr-implanted 6H-SiC samples, four Cr-related electron trap levels were formed at 683, 732, 785 and 840 meV, with a common optimum activation temperature of 1400 °C. In the Mg-implanted 6H-SiC samples, five Mg-related electron trap levels were formed at 679, 760, 897, 968 and 1107 meV, with a common optimum activation temperature of 1600 °C. In addition, the  $E_1$  and  $E_2$  damage-related traps reported by Pensl were observed and characterized, and the previously reported 615 meV electron trap was assigned to a  $V_{Si}-N_C$  complex based on trap behavior and comparisons with published data. Trap concentration dependencies on net donor concentration, implant species and dose, implantation temperature, and anneal temperature were observed, with the most notable being the sensitivity of the trap concentrations to the ion-implantation temperature. Damage-related trap concentrations

were higher in room-temperature ion-implanted samples and species-related trap concentrations were higher in 475 °C ion-implanted samples. Both Mg- and Cr-related trap pairs showed increased activation with increased implantation temperature. In addition, increasing either the implantation or anneal temperatures in Cr- and Mg-implanted samples significantly reduced the leakage current of the test diodes - an indication of a significant reduction in the concentration of near midgap defects. Of all the detected damage-related defects, only the anneal-resistant 435 meV damage-related electron trap was found to increase in concentration with increasing anneal temperature. Near-surface trap levels were identified, showing a significant change in the trap concentration with depth. This includes an indication of out-diffusion of ion-implanted magnesium toward the surface. I-V-T measurements of both ion-implanted and unimplanted samples indicated that the leakage current was dominated by generation due to a relatively high concentration of near midgap energy level defects.

From the Hall effect measurements of the high-temperature (500 °C) nitrogen- and phosphorus-implanted 4H-SiC samples, optimum anneal temperatures were determined. The optimum anneal temperature for 4H-SiC:N was near 1400 °C with an activation efficiency of 90 % for the 63 meV nitrogen-related donor level. The Hall mobility continued to improve following 1600 and 1800 °C anneals. The deeper 125 meV nitrogen donor level was also detected. The optimum anneal temperature for 4H-SiC:P was near 1600 °C with an activation efficiency of only 30 % for the 46 meV phosphorus-related donor level. Like 4H-SiC:N, the mobility was also improved following an 1800 °C anneal. Deeper donor levels between 250 and 380 meV were also observed for both

4H-SiC:N and 4H-SiC:P samples. The identity of these deeper level defects are unknown.

Cathodoluminescence (CL) measurements of the 4H-SiC samples indicated that the high-temperature implantation and high-temperature annealing was effective in repairing a significant portion of the lattice damage created by ion implantation. However, deep level traps were formed in both 4H-SiC:N and 4H-SiC:P. In 4H-SiC:N, a radiative 626 meV donor or acceptor level was formed, which is believed to be nitrogen-related. The intensity of the luminescence increased with increasing anneal temperature. The zero-phonon lines (ZPLs) associated with the bound exciton at substitutional nitrogen sites were observed at 3.23 eV along with their phonon replicas for the as-grown samples but were not detectable for the 4H-SiC:N samples. Phonon energies of 37, 68, 95, and 108 meV were calculated and compared well with published values. Also observed in the as-grown samples was an above bandgap CL peak pair at 3.36 eV. This observation indicates the existence of a higher energy level conduction band minimum, 130 meV above the lower energy level conduction band minimum. This is only the second reported detection of this level in 4H-SiC, with the first being in 1998. From the 4H-SiC samples implanted with phosphorus ions, a damage-related radiative level was detected at 346 meV below the conduction band. This energy level coincides with the energy level of the deep donor defect observed in the 4H-SiC:P samples from Hall effect measurements.

It was observed that an elevated ion-implantation temperature, near 500 °C, had a significant effect in the formation of deep level defects, both damage- and species-related. However, the desired dramatic restoration of the homogeneity of the crystalline structure

and complete activation of the implanted ions did not occur even after annealing to temperatures as high as 1800 °C. This suggests that a higher-temperature implantation might be worthwhile to be carried out on SiC. High-temperature ion-implantation also had a positive effect on activation implanted nitrogen.

Considering these results, I recommend that the following research be completed.

- 1) The effects of ion-implantation temperature on damage recovery and activation of implants in SiC should be further studied using an implantation temperature of 750 °C for 6H-SiC:Ar, :Mg, and :Cr.

- 2) DLTS measurements should be made on high- and room-temperature helium-implanted 6H-SiC to form damage-related defects from light-atom ion-implantation. These defects should then be compared with the defects formed in high- and room-temperature magnesium-implanted 6H-SiC to identify the defects in the magnesium-implanted samples as either damage- or species-related.

- 3) DLTS and Hall effect studies should be done on co-implanted 6H-SiC, using chromium and nitrogen, and magnesium and nitrogen, to assess the ability of co-implanting to produce n-type SiC with a low concentration of midgap defects. If successful, highly rectifying diodes could be created that could be operated at temperature greater than 700 K.

- 4) Hall effect measurements should be made on 500 °C ion-implanted 4H-SiC:N and annealed at 1000, 1200, 1300, and 1400 °C to determine to optimum anneal temperature to activate the implanted nitrogen. Due to the anneal temperature range used in this research, the optimum anneal temperature could only be upper bounded at 1400 °C.



Before SiC-based electronic devices can be commercially produced, ion-implantation techniques must first be developed for SiC, which permit the exploitation of this semiconductor's extraordinary electrical and physical properties.

## Appendix A

### Publication Summary

The following is the complete list of presentations and publications resulting from this doctoral research.

#### Presentations:

1. "Deep Level Trap Analysis of Ion Implanted n-type 6H-SiC by Double Correlated Deep Level Transient Spectroscopy," M.B. Scott, Y.K. Yeo, R.L. Hengehold, and J.D. Scofield, presented at the March 1997 Meeting of the American Physical Society, held on 17-21 March 1997 in Kansas City, Missouri.
2. "Deep Level Defect Study of Ion Implanted (Ar, Mg, Cr) n-Type 6H-SiC by Deep Level Transient Spectroscopy," M.B. Scott, J.D. Scofield, Y.K. Yeo, and R.L. Hengehold, presented at the International Conference on SiC, III-Nitrides and Related Materials (ICSC III-N'97), held on 31 August-5 September 1997 in Stockholm, Sweden.
3. "Implantation Temperature and Anneal Temperature Effects on Deep Level Traps in Cr and Mg Implanted 6H-SiC," M.B. Scott, Y.K. Yeo, R.L. Hengehold, and J.D. Scofield, presented at the Fall 1996 Meeting of the Ohio Section of the American Physical Society held on 1-2 November 1996 in Athens, Ohio.
4. "Cathodoluminescence Studies of As-Grown and Ar<sup>+</sup>-, P<sup>+</sup>-, and N<sup>+</sup>-Implanted 4H-SiC, M.B. Scott, Y.K. Yeo, R.L. Hengehold, and J.D. Scofield, presented at the March 1998 Meeting of the American Physical Society, held on 16-20 March 1998 in Los Angeles, California.
5. "Activation of P<sup>+</sup> and N<sup>+</sup> Ions in Epitaxial n-Type 4H-SiC Implanted at High Temperature, M.B. Scott, Y.K. Yeo, R.L. Hengehold, and J.D. Scofield, presented at the 24<sup>th</sup> International Conference on the Physics of Semiconductors, held on 2-7 August 1998 in Jerusalem, Israel.
6. "High Temperature (500 °C) Implantation Study of P<sup>+</sup> and N<sup>+</sup>-Implanted Epitaxial n-Type 4H-SiC, M.B. Scott, Y.K. Yeo, R.L. Hengehold, and J.D. Scofield, presented at the International Symposium on Compound Semiconductors, held on 12-16 Oct 1998 in Nara, Japan.

**Refereed Conference Proceedings:**

1. "Deep Level Defect Study of Ion Implanted (Ar, Mg, Cr) n-Type 6H-SiC by Deep Level Transient Spectroscopy," M.B. Scott, J.D. Scofield, Y.K. Yeo, and R.L. Hengehold, Mater. Sci. Forum 264-268, 549-552 (1998).
2. "High Temperature (500 °C) Implantation of P+ and N+ Implanted Epitaxial n-Type 4H-SiC," M.B. Scott, Y.K. Yeo, R.L. Hengehold, and J.D. Scofield, Compound Semiconductors 1998, Nara, Japan, 1998; Inst. Phys. Conf. Ser. no. 162, (Institute of Physics, Bristol and Philadelphia, 1999), pp. 763-768.

## Appendix B

### Sample Processing Procedures

The inert chemical nature of SiC makes sample preparation difficult. Through trial and error the following procedures were developed and refined to prepare the SiC surface for device fabrication. Process I involves a sacrificial thermal oxide growth for Schottky devices. The oxide is grown in a quartz tube furnace heated to 1100 °C, with a wet O<sub>2</sub> atmosphere introduced by bubbling O<sub>2</sub> through water maintained at 90 °C. During the SiO<sub>2</sub> growth, a thin SiC surface layer is consumed in order to liberate the Si required to complete the growth chemistry. As a result, when the grown SiO<sub>2</sub> layer is subsequently etched away with concentrated hydrofluoric acid, a fresh SiC surface for metal deposition is realized. Processes II is a chemical-only process, which was identified as sufficient for preparation of SiC surfaces. This process was primarily used for the preparation of surfaces, which were intended for ohmic contact metallization. For all SiC samples, the ohmic contact metallizations used were Ti/N/Au for n-type 4H-SiC, Al for p-type 4H-SiC, and Ni for n-type 6H-SiC. Schottky contacts were formed using Al for n-type 6H-SiC. Anneals were done for the ohmic contacts at 1050 °C for 10 minutes in flowing argon gas.

## **Process I. Oxide Growth/Etch Removal for Schottky Devices**

### **Step 1) Organic Solvent Degrease**

- i) Acetone (5 min @ 30 °C)
- ii) TCE (trichloroethylene) (5 min @ 30 °C)
- iii) Acetone (5 min @ 30 °C)
- iv) Methanol (5 min @ 30 °C)
- v) Propanol (5 min @ 30 °C)
- vi) H<sub>2</sub>O rinse N<sub>2</sub> dry

### **Step 2) Acid Cleanse**

- i) H<sub>2</sub>SO<sub>4</sub> (5 min @ 50 °C)
- ii) NH<sub>4</sub>OH:H<sub>2</sub>O<sub>2</sub> (1:1) (5 min @ 30 °C)
- iii) HF (1 min @ 30 °C)
- iv) H<sub>2</sub>O rinse N<sub>2</sub> dry

### **Step 3) Wet Oxide Growth**

- i) Heat tube furnace 1050 to 1100 °C
- ii) Place samples in tube with wet O<sub>2</sub> gas flow
- iii) Inset tube in pre-heated furnace
- iv) Duration 3 to 5 hours

### **Step 4) Oxide Removal (performed immediately before metal deposition)**

- i) HF (5 min @ 30 °C)
- ii) K<sub>2</sub>CO<sub>3</sub> (10 min @ 50 °C) (20 % solution 5 g K<sub>2</sub>CO<sub>3</sub> powder with 25 g H<sub>2</sub>O)
- iii) HCL:H<sub>2</sub>O (1:9, 10 % solution) (5 min @ 30 °C)
- iv) H<sub>2</sub>O rinse N<sub>2</sub> dry

### **Step 5) Device Processing backside ohmic contacts**

- i) spin/bake PR (photo-resist) on front surface of samples
- ii) deposit ohmic metal
- iii) remove PR front surface
- iv) anneal (for nickel, 5 min @ 1050 °C)

### **Step 6) Process diode contacts**

- i) clean front surface using step 2) above and substitute 1 min for 5 min acid dips
- ii) pattern PR on front surface
- iii) deposit metal
- iv) liftoff PR

## **Process II. Chemical Surface Prep for Schottky Devices**

### **Step 1) Organic Solvent Degrease**

- i) Acetone (5 min @ 30 °C)
- ii) TCE (5 min @ 30 °C)
- iii) Acetone (5 min @ 30 °C)
- iv) Methanol (5 min @ 30 °C)
- v) Propanol (5 min @ 30 °C)
- vi) H<sub>2</sub>O rinse N<sub>2</sub> dry

### **Step 2) Acid "Etch"**

- i) H<sub>2</sub>SO<sub>4</sub>:H<sub>2</sub>O<sub>2</sub> (1:1) (15 min @ 30 °C)
- ii) H<sub>2</sub>O rinse
- iii) Buffered HF (5 min @ 30 °C)
- iv) NH<sub>4</sub>OH:H<sub>2</sub>O<sub>2</sub>: H<sub>2</sub>O (1.5:1.5:5) (5 min @ boil)
- v) H<sub>2</sub>O rinse
- vi) HCl:H<sub>2</sub>O<sub>2</sub>:H<sub>2</sub>O (1.5:1.5:5) (5 min @ boil)
- vii) H<sub>2</sub>O rinse

### **Step 3) Device Processing ohmic contacts**

- i) spin/bake PR on front surface of sample
- ii) deposit ohmic metal
- iii) remove PR from front surface
- iv) anneal (Ni 5 min @ 1050 °C)

### **Step 4) Process diode contacts**

- i) clean front surface using step 2) above and substitute 1 min for 5 min acid dips
- ii) pattern PR on front surface
- iii) deposit metal
- iv) liftoff PR

## Appendix C

### Modulating Function Error

In an attempt to reverse engineer the rate window curves from the trap parameters, I wrote a Mathcad<sup>®</sup> routine, which generated the DLTS transient capacitance data from trap parameter inputs. Once that data were generated, I ran the data through the Arrhen6.bas program to generate the trap parameters. This program is part of the DLTS laboratory setup and is used to compute the trap parameters from the DLTS capacitance data. This was done to verify that the Arrhen6.bas program was properly computing the trap parameters.

I found that a different set of trap parameters were generated from my Mathcad<sup>®</sup> routine, which were slightly off from the trap parameters used as the initial inputs. After searching for the reason for this disconnect, I resolved all the unknown variables done to a single term, designated as  $\gamma$ , the emission rate coefficient.

To compute the trap parameters from DLTS transient capacitance data, the  $\gamma$  factor term in the equation must first be properly computed. The expression for this term is

$$\gamma(T) = v(T) \cdot N_c(T) / T^2,$$

where  $v(T)$  is the mean free electron velocity, and  $N_c(T)$  is the effective electron density of states. These terms were computed using 6 as the number of conduction band minima and  $0.27 \cdot m_e$  as the effective electron mass. These two choices were based on published values from Suttrop *et al.* in an Applied Physics article (Suttrop, 1992). This produced a  $\gamma$  value of  $5.27 \times 10^{18}$  [1/cm<sup>2</sup>K<sup>2</sup>msec] at 300 K, which is different from the  $1.25 \times 10^{18}$

[1/cm<sup>2</sup>K<sup>2</sup>msec] required to get the Arrhen6.bas program to generate the same trap parameters.

To reproduce the rate window curve found in Dr. Scofield's Kyoto, Japan paper, p.331 (upper graph), I had to set the emission rate coefficient  $\gamma$  to  $1.25 \times 10^{18}$  [1/(cm<sup>2</sup>\*K<sup>2</sup>\*msec)]. The reported

trap parameters that accompanied this rate window plot were

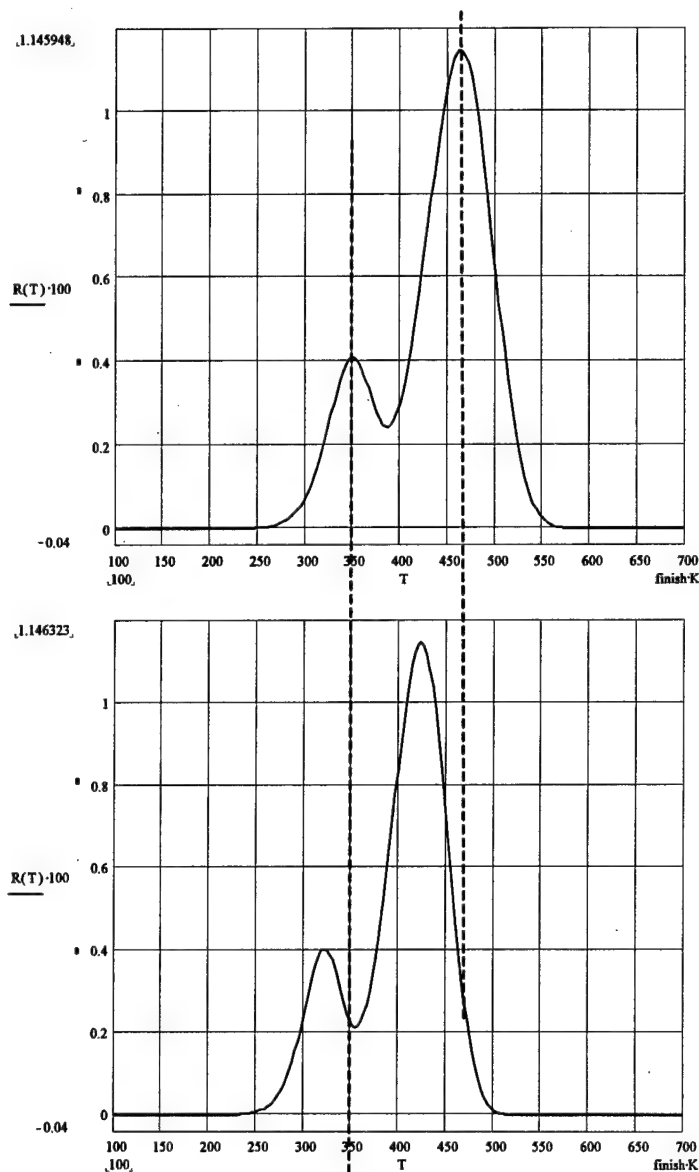
$$E_1 = 510 \text{ meV} \quad \sigma_1 = 8e-19 \text{ cm}^2$$

and

$$E_2 = 440 \text{ meV} \quad \sigma_1 = 1e-17 \text{ cm}^2.$$

If these trap parameter values are used to generate DLTS data, the resulting rate window curve is shifted to a slightly lower

temperature (lower graph). Meaning that the  $\gamma$  term used in the Arrhen6.bas was too small. The  $\gamma$  coefficients used in this program could not be edited, which resulted in restricting the use of the program to just qualitative data assessments.





## Bibliography

- Achtziger N. and Witthuhn W., Appl. Phys. Lett. **71** (1), 110-112 (1997).
- Ahmed S., Barbero C.J., and Sigmon T.W., Appl. Phys. Lett. **66** (6), 712-714 (1995).
- Anikin M.M., Lebedev A.A., Syrkin A.L., and Suvorov A.V., Sov. Phy. Semicond. **19** (1), 69-71 (1985).
- Baraff G. and Schluter M., Phys. Rev. B **28**, 2296 (1983).
- , Bull. Am. Phys. Soc. **29**, 250 (1984).
- Bar-Yam Y. and Joannopoulos J. D., Phys. Rev. B **52**, 1129 (1984).
- Bethe, H., Ann. Phys. **76**, 325 (1932).
- Blakemore, J.S. Semiconductor Statistics. New York: Dover Pub., 1987.
- Blood P. and Orton J.W. The Electrical Characterization of Semiconductors: Majority Carriers and Electron States. New York: Academic Press, 1992.
- Bohr, N., Phil. Mag. **30**, 581(1915).
- Brice, D.K., Rad. Effects **11**, 227 (1971).
- Campbell A.B., Shewchun J., and Thompson D.A. "Nitrogen Implantation in SiC: Lattice Disorder and Foreign-Atom Location Studies," in Ion Implantation in Semiconductors. Ed. Susumu Namba. New York: Plenum Press, 1974.
- Carter G. and Grant W. Ion Implantation of Semiconductors. London: Edward Arnold, 1976.
- Chadderton L.T. and Eisen F.H. "On the Annealing of Damage Produced by Boron Implantation of Silicon Single Crystals," in Ion Implantation. Ed. Fred Eisen and Lewis Chadderton. London: Gordon and Breach, 1971.
- Choyke W.J. and Patrick L., Phys. Rev. **105**, 1721 (1957).
- , Phys. Rev. **127**, No. 6, 1868 (1962).
- , Phys. Rev. **172**, No. 3, 769 (1968).
- Choyke W.J., Hamilton D.R., and Patrick L., Phys. Rev. **117**, 1430 (1968).

Davis R.F. "Deposition and characterization of diamond, silicon carbide, and gallium nitride thin films," J. of Crystal Growth **137**, pp. 161-169 (1994).

-----, "III-V Nitrides for electronic and optoelectronic applications," IEEE Proc. **79**, 702 (1991).

Dean P.J. and Hartman R. L., Phys. Rev. B **5** (12), 4911 (1972).

Evwaraye A.O., Smith S.R., and Mitchel W.C., J. Appl. Phys. **76** (10), 5769 (1994).

Feldman D.W. *et al.*, Phys. Rev. **173**, 787 (1968).

Fontaine F. *et al.*, Appl. Phys. Lett. **68** (16), 2264 (1996).

Furukawa, S. and Ishiwara, H., J. Appl. Phys. **43**, 1268 (1972).

Hassler C. *et al.*, Diffus. Defect Data B, Solid State Phenom. **37**, 195 (1993).

Hobgood H. McD. *et al.*, Appl. Phys. Lett. **66** (11), 1364 (1995).

Ikeda, M., Matsunami H., and Tanaka T., Phys. Rev. B **22**, 2842 (1980).

Itoh J., Appl. Phys. **66**, 4529 (1989).

-----, Electron Mater. **21**, 707 (1992).

Jenny J. R. and Skowronski M., J. Appl. Phys. **78** (6), 3839 (1995).

Kaczer B., *et al.*, Phys. Rev. **B57** (7), 4027 (1998).

Kawasuso A., Itoh H., and Okada S., J. Appl. Phys. **80** (10), 5639 (1996).

Knippenberg W.F. and Verspui G., Phillips Res. Report **21**, pp. 113-121 (1966).

Kroko L.J. and Milnes A.G., Solid State Electron. **9**, 1125 (1966).

Lang, D.V. *et al.*, "Deep Level Transient Spectroscopy: A new method to characterize traps in semiconductors", J. Appl. Phys. **45** (7), 3023 (1974).

Lely J. A., "Darstellung von Einkristallen von Silicium Carbid und Beherrschung von Art und Menge der Eingebauten Verunreinigungen," Ber. Deut. Keram. Ges. **32**, 229 (1955).

Lindelfelt U., Phys. Rev. B **28**, 4510 (1983).

Lindelfelt U. and Zunger A., Phys. Rev. B **30**, 1102 (1984).

Lindhart J., Scharff M., Schiøtt H.E., Kgl. Danske Videnskab. Selskab., Mat.-Fys. Medd. **33** (14), (1963).

Linus P. The Nature of the Chemical Bond, Cornell Univ. Press, pp. 247-248, (1988).

Madelung O. Semiconductors Group IV Elements and II-V Compounds, New York: Springer-Verlag, 1991.

Maier K., Schneider J., and Wilkening W., Mat. Sci. and Eng. **B11**, 27 (1992).

Marsh O.J. and Dunlap H.L. "Ion-Implanted Junctions and Conducting Layers in SiC," in Ion Implantation. Ed. Fred Eisen and Lewis Chadderton. London: Gordon and Breach, 1971.

McLean F.B. *et al.*, IEEE Trans. Nucl. Sci. **41** (12), 2465 (1994).

Morkoç H. *et al.*, J. Appl. Phys. **76** (3), 1363 (1994).

Neudeck P.G. and Fazi C., J. Appl. Phys. **80** (2), 1219 (1996).

Nilsson, H. E., Sannemo U., and Petersson C.S., J. Appl. Phys. **80** (16), 3365 (1996).

O'Connor J.R. and Smiltens J. Silicon Carbide, A High Temperature Semiconductor. New York: Peramon Press, 1960.

Palmour J.W., Kong H.S., and Carter Jr. C., "Field Effect transistors in 6H-SiC," unpublished report, CREE Research, Inc., Durham N.C. 27713, (1997).

Palmour J.W., *et al.*, Physica B **185**, 461 (1993).

Pensl G. and Choyke W.J., Physica B **185**, 264 (1993).

Prins J.F., Phys. Rev. B **44**, 2470 (1991).

-----, Mater. Sci. Rep. **7**, 271 (1992).

Przybylko S., "High Temperature Electronics for Aircraft Engines," Proc. AIAA/SAE/ASME/ASEE 26<sup>th</sup> Joint Propulsion Conference, (1990).

Ryssel H. and Ruge I. Ion Implantation. Chichester: John Wiley & Sons, 1986.

Scheffler M. *et al.* Phys. Rev. Lett. **49**, 1756 (1982).

Scofield, J.D., Yeo Y.K., and Hengehold R.L., Inst. Phys. Conf. Ser. No 145: Ch. 3, 22nd Int. Symp. Compound Semiconductors, Cheju Island, Korea, 28 Aug - 2 Sep 1995.

Scofield, J.D., Yeo Y.K., and Hengehold R.L., Inst. Phys. Conf. Ser. No 142: Ch. 2,

Silicon Carbide and Related Materials 1995 Conf., Kyoto, Japan, 1995.

Scofield, J.D. Electrical Characterization of Intrinsic and Induced Deep Level Defects in Hexagonal SiC. Dissertation, AFIT/DS/ENP/96-08. Graduate School of Engineering and Management, Air Force Institute of Technology (AU), Wright-Patterson AFB OH, November 1996.

Shockley, W., U.S. Patent No. 2,787,564 (1957).

Strack, H., *Trans. Metallurgical Soc. AIME* **239**, 381 (1967).

Suttrop W., Pensl G., Choyke W. J., Stein R., and Leibenzeder S., *J. Appl. Phys.* **27**, 37 (1992).

Suttrop W. *et al.*, *J. Appl. Phys.* **72** (8), 3708 (1992).

Suttrop W., Pensl G., and Lanig P., *Appl. Phys. A* **51**, 231 (1990).

Swonger J.W. Briefing handout, "High Temperature Silicon Microelectronics," Harris Semiconductor, Military & Aerospace Division, Oct. 1992.

Sze S.M. Semiconductor Devices, Physics and Technology, New York: John Wiley & Sons, 1985.

Thome F., and King D. Internal memo, "High Temperature Electronics Survey," Sandia National Laboratory, 1988.

Vainer V.S. and Il'in V.A., *Sov. Phys. Solid State* **23**, 2126 (1981).

Verna A.R. and Krishna P. Polymorphism and Polytypism in Crystals. New York: Wiley, 1966.

Wolf C.M. *et al.*, *J. Appl. Phys.* **41**, 504 (1970).

Woodbury H. H. and Ludwig G. W., *Phys. Rev.* **124** (4), 1083 (1961).

REPORT DOCUMENTATION PAGE			Form Approved OMB No. 0704-0188	
Public reporting burden for this collection of information is estimated to average 1 hour per response, including the time for reviewing instructions, searching existing data sources, gathering and maintaining the data needed, and completing and reviewing the collection of information. Send comments regarding this burden estimate or any other aspect of this collection of information, including suggestions for reducing this burden, to Washington Headquarters Services, Directorate for Information Operations and Reports, 1215 Jefferson Davis Highway, Suite 1204, Arlington, VA 22202-4302, and to the Office of Management and Budget, Paperwork Reduction Project (0704-0188), Washington, DC 20503.				
1. AGENCY USE ONLY (Leave blank)		2. REPORT DATE 10-08-1999		3. REPORT TYPE AND DATES COVERED Sep 94 - Sep 99
4. TITLE AND SUBTITLE Electrical and Optical Characterization of Intrinsic and Ion-Implantation Induced Defects in 6H- and 4H-SiC			5. FUNDING NUMBERS	
6. AUTHOR(S) Michael B. Scott, Major, USAF Yung K. Yeo, Professor, AFIT, USAF				
7. PERFORMING ORGANIZATION NAME(S) AND ADDRESS(ES) Air Force Institute of Technology Department of Engineering Physics 2750 P Street Wright-Patterson AFB, OH 45433-6583			8. PERFORMING ORGANIZATION REPORT NUMBER  AFIT/DS/ENP/99-04	
9. SPONSORING/MONITORING AGENCY NAME(S) AND ADDRESS(ES) Dr. James D. Scofield (phone: 255-3014) AFRL/PRPE Wright-Patterson, OH 45433			10. SPONSORING/MONITORING AGENCY REPORT NUMBER	
11. SUPPLEMENTARY NOTES				
12a. DISTRIBUTION AVAILABILITY STATEMENT APPROVED FOR PUBLIC RELEASE; DISTRIBUTION UNLIMITED			12b. DISTRIBUTION CODE	
13. ABSTRACT (Maximum 200 words) Deep level transient spectroscopy (DLTS), Hall effect, and cathodoluminescence (CL) measurements are used to characterize the intrinsic and ion-implantation induced defects in high-temperature (475 and 500 C) ion-implanted epitaxial n-type 6H- and 4H-SiC, ion-implanted with Cr, Mg, Ar, N, and P atoms. Comparison of room-temperature and high-temperature ion-implanted 6H-SiC:Mg and :Cr indicate the significance of high-temperature ion implantation on the activation of the ion-implanted atoms and damage-recovery of the crystalline lattice. The effects of high-temperature annealing on both damage-recovery and implanted ion activation are detected and analyzed, from 1200 to 1800 degrees C. Trap parameters of both damage-related and species-related defects are determined by curve-fitting of DLTS rate window plots, including the identification of a 615 meV silicon-vacancy-substitutional-nitrogen defect. Double-correlated DLTS measurements indicate a one-dimensional distribution of various defects along the implantation axis and slight surface diffusion of ion-implanted magnesium during high-temperature annealing. Current-voltage-temperature measurements of 6H-SiC:Mg :Cr indicate the effect of annealing temperature and ion species on the concentration of near midgap defects. Optimum anneal temperatures are determined for activation of ion-implanted nitrogen and phosphorus. CL measurements indicate the formation of deep radiative centers in 500 degrees C ion-implanted 4H-SiC:P and :N. CL measurements also indicate the presence of a 130 meV higher energy level conduction band minimum.				
14. SUBJECT TERMS silicon carbide, SiC, ion implantation, high-temperature annealing, epitaxial, defects, deep level transient spectroscopy, Hall effect, cathodoluminescence, activation, mobility			15. NUMBER OF PAGES 251	
			16. PRICE CODE	
17. SECURITY CLASSIFICATION OF REPORT  U		18. SECURITY CLASSIFICATION OF THIS PAGE  U		19. SECURITY CLASSIFICATION OF ABSTRACT  U
				20. LIMITATION OF ABSTRACT  UL